Adsorption of Astrochemically Relevant Molecules on Interstellar Dust Analogues

Amandeep Singh Bolina

Thesis for the degree of Doctor of Philosophy

University College London
University of London

2005

ProQuest LLC
789 East Eisenhower Parkway
P.O. Box 1346
Ann Arbor, MI 48106-1346

Abstract

In the last few decades, astronomers have found that interstellar clouds are chemical factories, in which atoms are processed into more complex chemical species in reactions energized by starlight and fast particles. Many of the identified molecules are formed in networks of ion-molecule and neutral-neutral reactions and, at the low temperatures in the interstellar medium (~15 K), can accrete on the surface of interstellar dust grains to form ices. However, it is widely speculated that some of these interstellar ices can only form sufficiently rapidly if the more abundant atoms, and carbon monoxide, are hydrogenated on the surface of dust grains. Hence, there is an urgent need for data concerning gas-grain interactions, especially with regard to whether addition reactions can take place on dust grains.

This thesis presents detailed information on the adsorption and desorption of water, methanol and ammonia on suitable dust grain analogue surfaces, using a combination of temperature programmed desorption (TPD) and reflection absorption infrared spectroscopy (RAIRS). All three adsorbates show evidence for molecular adsorption in a physisorbed state. In addition, various degrees of hydrogen bonding are observed in the multilayer. Crystallisation is also observed to take place during the desorption of the ices in both RAIRS and TPD studies. Detailed analysis of the TPD spectra has been performed for all adsorption systems to give desorption energies, desorption orders and pre-exponential factors.

The information obtained from these experiments has been incorporated into simple simulations under astrochemically relevant conditions (i.e. low heating rates and appropriate ice thicknesses). These simulations can be directly incorporated into astronomical models. This in turn helps to lead to a greater understanding of star formation, and hence of the Universe in which we live.

Acknowledgements

I would like to thank the following people, without whom this thesis would never have made it to print:

Wendy Brown - for the best possible supervision. Thank you for the innumerable hours spent explaining the intricacies of surface science and the much needed pep talks when things were not going my way. Without her enthusiasm the kit would probably have had a few spanner injuries.

Robin Mukerji - for everything I know about flanges, venting, baking and so forth.
Angela Wolff - for helping around the lab and introducing me to life beyond Excel.
All members of the Physical Chemistry group, past and present, for making the last four years such good fun.

All my friends, including those in the Hockey Club - for providing much needed relief and refreshment.

And most importantly my family, especially my mother and father. Without their unconditional love and support I would never have been in a position to undertake a PhD, let alone contemplate completion. Thank you.

Contents

Chapter 2: Experimental Apparatus

Chapter 3: Experimental Methods

Chapter 4: Water Adsorption on HOPG

List of Figures

Chapter 3

Chapter 4

Chapter 5

Chapter 6

Chapter 7

Chapter 8

List of Tables

Chapter 7

Chapter 8

Chapter 1: Interstellar Chemistry

1.1 The Interstellar Medium

Up until the 1920s, it was thought that our Galaxy was the entire Universe, and that everything in the Universe belonged to it [1]. However, it is now known that the dimensions of the visible Universe are 10^5 times larger than our Galaxy, and it is by studying neighbouring galaxies that information has been gathered about our own Galaxy.

The majority of matter in our Galaxy is locked up in the 10^{11} stars that are spread over a disk of diameter of approximately 10^6 light years by a thickness of about 6000 light years. Observations with the naked eye would lead us to believe that the regions between these stars are empty and void of matter, however this is not the case. Approximately 10% of the mass of our Galaxy is found in the regions between the stars, the so called Interstellar Medium (ISM). The ISM consists of a large variety of different types of gas, from tenuous plasmas (~10^3 atoms, ions and electrons m^{-3} at ~10^6 K) to cold dense clouds (~10^9 atoms and molec m^{-3} at 10 K) [2]. The gas is predominantly neutral hydrogen, either in atomic or molecular form (93.38%), and helium (6.49%). The remaining component (0.13%) is made up of larger atoms including oxygen, carbon and nitrogen and some simple molecules [3]. In addition to the gas, dust grains are also present in the ISM making up approximately 1% of the mass. The dust plays a vital role in the chemistry of the ISM.

The majority of the volume of the ISM is very hot (> 10^4 K) and therefore does not contain any molecules at all. Hence, the gas and dust in the ISM is not uniformly distributed, but clumped. These clumps, or gas clouds, can be categorised into three main groups on the basis of their physical characteristics and the state of hydrogen, the most abundant element [4]. These three types of gas clouds are known as H II regions, diffuse clouds and dark clouds.

H II regions occur near bright hot stars and contain about 1% of the mass of the ISM. They have a temperature of around 30 K and densities of 10^{12} molec m^{-3}. In this region hydrogen is predominantly ionised.

Diffuse clouds have relatively low number densities of 10^{6} - 10^{9} atoms m^{-3} and high gas temperatures of 100 – 120 K. They are known as diffuse clouds since interstellar ultraviolet radiation (UV) can easily penetrate them. UV photons play an important part in the chemistry of diffuse clouds, since they can photodissociate several molecules. Additionally, species with an ionisation potential less than that of atomic hydrogen, such as atomic carbon and sulphur, can be photoionised. Species such as atomic oxygen and nitrogen, with ionisation potentials greater than atomic hydrogen, are found to be neutral since shorter wavelength radiation is absorbed by the dominant hydrogen. Hence, diffuse clouds tend to consist of atomic hydrogen, simple molecules and dust grains.

Figure 1.1: A picture of a Bok Globule. The dark cloud consisting of molecules and dust obscures the starlight of distant stars in the Milky Way. ***Photo Credit & Copyright: J. Alves (ESO), E. Tolstoy (Groningen), R. Fosbury (ST-ECF), & R. Hook (ST-ECF), VLT.***

Dark clouds are characterised by number densities of 10^9 - 10^{10} molec m^{-3} and temperatures of only 10 - 15 K [5]. In contrast to diffuse clouds, molecules are shielded from UV radiation by the presence of dust grains. A direct result of this shielding effect is the obscuration of light from stars lying behind the dust cloud. Hence, dark clouds often appear as dark patches as shown in *Figure 1.1*. A further result of dust shielding is the larger variety of molecules detected in dark clouds, compared with diffuse clouds.

1.2 Identification of Molecules in the ISM

More than 137 different molecules have been detected in the ISM to date, varying from the simplest molecular hydrogen (H_2) to more complicated hydrocarbons and nitriles. *Table 1.1* lists some of the molecular species identified in the ISM to date. Larger molecules have also been identified in the ISM, such as polycyclic aromatic hydrocarbons (PAHs) [6-10], glycoaldehyde ($HOCH_2CHO$) [11] and possibly even the amino acid glycine (H_2NCH_2COOH) [12, 13].

Detection of molecules takes place in several ways, either through earth based observations, the use of satellites or through the observation of tracer molecules [14]. The majority of observations rely on spectroscopy, in which atoms, molecules and ions either emit or absorb radiation corresponding to transitions between their various energy levels. Early work focused on diffuse interstellar clouds, in which absorption lines of the electronic transitions in atoms and simple molecules could be observed at visible and ultraviolet wavelengths, superposed on the spectra of background stars. The rich variety of molecules present in dark clouds was only detected in the 1970s, following the developments of millimetre wave telescopes [14]. Using these telescopes, the rotational emission lines of molecules present in dark clouds could be observed.

Table 1.1: Table listing the molecules detected in the ISM to date (adapted from *http://www.ajmarkwick.com/achemnet/stats.php?mode=1&flat=0*).

2 atoms	3 atoms	4 atoms	5 atoms	6 atoms	7 atoms	>7 atoms
AlF	C_3	c-C_3H	C_5	C_5H	C_6H	CH_3C_3N
AlCl	C_2H	l-C_3H	C_4H	C_5O	CH_2CHCN	$HCOOCH_3$
C_2	C_2O	C_3N C_3O	C_4Si	C_2H_4	CH_3C_2H	CH_3COOH
CH	C_2S	C_3S	l-C_3H_2	CH_3CN	HC_5N	CH_3C_4H
CH^+	CH_2	C_2H_2	c-C_3H_2	CH_3NC	$HCOCH_3$	CH_3CH_2CN
CN	HCN	CH_2D^+	CH_2CN	CH_3OH	NH_2CH_3	$(CH_3)_2O$
CO	HCO	HCCN	CH_4	CH_3SH	c-C_2H_4O	CH_3CH_2OH
CO^+	HCO^+	$HCNH_+$	HC_3N	HC_3NH^+	CH_2CHOH	HC_7N
CP	HCS^+	HNCO	HC_2NC	HC_2CHO		C_8H
CS	HOC^+	HNCS	HCOOH	$HCONH_2$		CH_3C_5N
CSi	H_2O	$HOCO^+$	H_2CHN	l-H_2C_4		$(CH_3)_2CO$
HCl	H_2S	H_2CO	H_2C_2O	C_5N		NH_2CH_2COOH
H_2	HNC	H_2CN	H_2NCN			HC_9N
KCl	HNO	H_2CS	HNC_3			$HC_{11}N$
NH	MgCN	H_3O^+	SiH_4			CH_8
NO	MgNC	NH_3	H_2COH_+			CH_2OHCHO
NS	N_2H^+	SiC_3				C_7H
NaCl	N_2O					H_2C_6
OH	NaCN					
PN	OCS					
SO	SO_2					
SO^+	c-SiC_2					
SiN	CO_2					
SiO	NH_2					
SiS	H_3^+					
HF	AlCN					
SH						

1.3 Molecular Formation in the ISM

Molecules in the ISM play a vital role in star formation, hence an understanding of molecular formation is crucial for an understanding of star formation. A star forms when a cloud of gas molecules collapses under its own gravity, so that the density becomes high enough for nuclear fusion to take place and the star can ignite [2]. However, cloud collapse results in a decrease in volume, which in turn increases the number of molecular collisions. The kinetic energy released from these collisions manifests itself as an increase in the cloud's temperature, which provides resistance to

further collapse. In order for star formation to occur, this resistance to collapse must be overcome. This is achieved by radiation of the excess energy by emissions from molecules and dust found in the collapsing gas clouds. In this manner, interstellar molecules act as coolants in star formation. Hence an understanding of the formation of molecules in the ISM, and an understanding of the interaction between dust grains and gas is essential for understanding star formation. The relevance of the gas-grain interaction in star forming regions and in hot cores will be discussed in depth later.

Many of the molecules shown in *Table 1.1* can be formed by reactions involving ions and neutral species in the gas phase. H_2 is the most abundant molecule in the ISM and is the driving force behind all of the gas phase chemistry in the ISM. Once formed H_2 reacts with various different species (e.g. O, C, N) and hence the formation of all molecules can be traced back to the simplest molecule, H_2.

In both diffuse and dark clouds gas phase chemistry is initiated by cosmic rays, CR, ionising H_2 to H_3^+:

$$H_2 + CR \rightarrow H_2^+ + e^-$$

$$H_2^+ + H_2 \rightarrow H_3^+ + H$$

Since H_2 has a low proton affinity, H_3^+ readily donates H^+ to a large variety of atoms and molecules to form larger molecules. Despite the importance of H_3^+, it has only recently been detected in the ISM [15, 16]. Once formed, H_3^+ takes place in a large number of reactions including reactions with carbon atoms.

The nature of carbon chemistry is dependent upon the type of gas cloud being considered. In diffuse clouds the majority of atomic carbon is in the form of C^+. The reaction between C^+ and H_2 is highly endothermic and unlikely to proceed at the low temperatures of the ISM. However it is suggested that slow radiative association can take place [17]:

$$C^+ + H_2 \rightarrow CH_2^+ + h\nu$$

In dark clouds, impenetrable to UV radiation, carbon chemistry is initiated by reaction with H_3^+.

$$C + H_3^+ \rightarrow CH^+ + H_2$$

$$CH^+ + H_2 \rightarrow CH_2^+ + H$$

In both diffuse and dark clouds, the CH_2^+ ion can then react with H_2:

$$CH_2^+ + H_2 \rightarrow CH_3^+ + H$$

Further hydrogen abstraction is endothermic, so competing reactions occur. The capture of an electron leads to CH_2 and thus the formation of the first hydrocarbons.

$$CH_3^+ + e^- \rightarrow CH_2 + H$$

Alternatively reaction with an oxygen atom leads to the formation of CO:

$$CH_3^+ + O \rightarrow HCO^+ + H_2$$

$$HCO^+ + e^- \rightarrow CO + H$$

CO is the second most abundant molecule in the ISM and plays a vital role in star formation. CO molecules possess a dipole moment and hence rotational transitions are permitted. This allows the excited gas molecules in an interstellar cloud a mechanism by which they can radiate energy away, hence cooling the clouds and allowing the process of star formation to continue.

1.4 Molecular Formation Problems in the ISM

Despite the detailed gas phase chemistry models built over the last thirty years, there are still several problems related to molecular formation in the ISM. Simulations that only include gas phase chemical reactions are successful in producing most (~ 80%) of the molecules observed in the gas phase of the ISM [18]. However, this leads to a significant percentage of chemistry being unaccounted for. There are two particular problems, in which gas phase reaction schemes alone cannot account for the observed abundances.

1.4.1 Hydrogen Formation Problem

It has been demonstrated that not only is H_2 the most abundant molecule in the ISM, but it is also the driving force behind the majority of chemistry. Hence, the mechanism responsible for the formation of H_2 needs to be extremely efficient. This efficiency is required since UV radiation from background stars destroys H_2 in the ISM. In fact, it turns out that for the interstellar radiation field, approximately 10% of absorptions of UV radiation by H_2 lead to dissociation of the molecule. This gives H_2, unshielded by dust grains, a lifetime of less than a thousand years if exposed to the average UV radiation field [2]. Hence formation of H_2 needs to be very efficient to account for the observed abundances.

In the early Universe, H_2 was formed in reactions involving electrons and protons as catalysts. However, electrons and protons are relatively minor components of the ISM, and lead to inefficient formation of H_2 [19]. Utilising reaction mechanisms involving electrons and protons as catalysts alone therefore leads to an abundance of H_2 slightly greater than one part per billion of the atomic hydrogen abundance. Observations of interstellar clouds show a variation in the ratio of H_2 molecules to atomic hydrogen from one part per million in some regions, to other regions in the ISM where the abundances of H_2 and hydrogen atoms are comparable [19]. Therefore, even in the regions where H_2 is at its least abundant, mechanisms involving electrons and protons result in predicted abundances a thousand times smaller than observed abundances.

An alternative reaction pathway for H_2 formation is a two body process involving two hydrogen atoms:

$$H + H \rightarrow H_2 + h\nu$$

For this to occur, the H_2 molecule needs to radiate away some of its binding energy of 4.5 eV. The contact time for the two colliding hydrogen atoms is comparable to the period of vibrational oscillation in the molecule, typically 10^{-13} s. However, the largest transition probability is typically 10^{-8} s^{-1}, implying that only one in 10^5 collisions would lead to the formation of a H_2 molecule [19].

Stabilisation of the colliding pair may be enhanced if a third body is used to radiate some of the binding energy:

$$H + H + M \rightarrow H_2 + M$$

However the number density of the ISM is very low, and hence the probability of stabilisation of H_2 by a third body is negligible.

Hence there are two problems in the formation of H_2. Primarily a formation mechanism needs to be found which is at least a thousand times faster than radiative and ion-molecule exchange. Secondly an explanation needs to be found for why the ratio of H_2 with respect to atomic hydrogen varies so widely in differing regions of the ISM. In fact, the solution to both of these problems is that a catalytic process can occur on the surface of interstellar dust grains [18, 20]. At the low temperatures in the ISM, hydrogen atoms accrete on the surface of interstellar dust grains, where they can react to form H_2. This is discussed in depth later.

1.4.2. Composition of Interstellar Ices

A second problem that cannot be explained by gas phase chemistry alone is the observation of interstellar ices. At the low temperatures in the ISM, simple molecules

freeze out on the surface of dust grains and accumulate in icy mantles. This is especially prevalent in dark clouds. The ice composition varies from one interstellar location to another but includes molecules such as H_2O, CO, CH_3OH, NH_3 and CH_4 [21]. Of these detected species, only CO is sufficiently abundant in the gas phase that CO ice can be deposited in a short enough timescale on dust grain surfaces [21]. This implies that an alternative formation mechanism for species detected in interstellar ices is required. It has been suggested that, similar to H_2 formation, chemistry explicitly on the surface of dust grains again provides the solution to this problem. Simple atoms and molecules accrete on the surface of dust grains, where reactions then occur to form more complex species.

1.5 Interstellar Dust

Clearly, interstellar dust grains play a vital role in the chemistry of the ISM, despite making up only approximately 1% of the mass of the ISM. The grains are believed to be active sites for molecular formation. Furthermore, they are critical components in both establishing the thermal equilibrium in interstellar clouds and in the collapse of clouds leading to star formation, and ultimately planet formation [1, 18, 22].

1.5.1 Evidence for and Properties of Dust Grains

Interstellar dust grains were first observed in 1784 by William Herschel, who noted the existence of regions of the night sky which were completely devoid of stars. Herschel called these regions "holes in the sky" [18, 23]. At the time it was unclear whether these were regions of space devoid of stars, or whether some agent was obscuring the light from the background stars. Today it is known that these holes in the sky are caused by the obscuration of light as a result of dust grains extinguishing most of the background visible starlight. An example of a "hole in the sky" is shown in *Figure 1.2*, which shows the "Black Cloud" B68. Since the initial observation of dust grains as "holes in the sky", several further pieces of evidence point to the existence of dust grains.

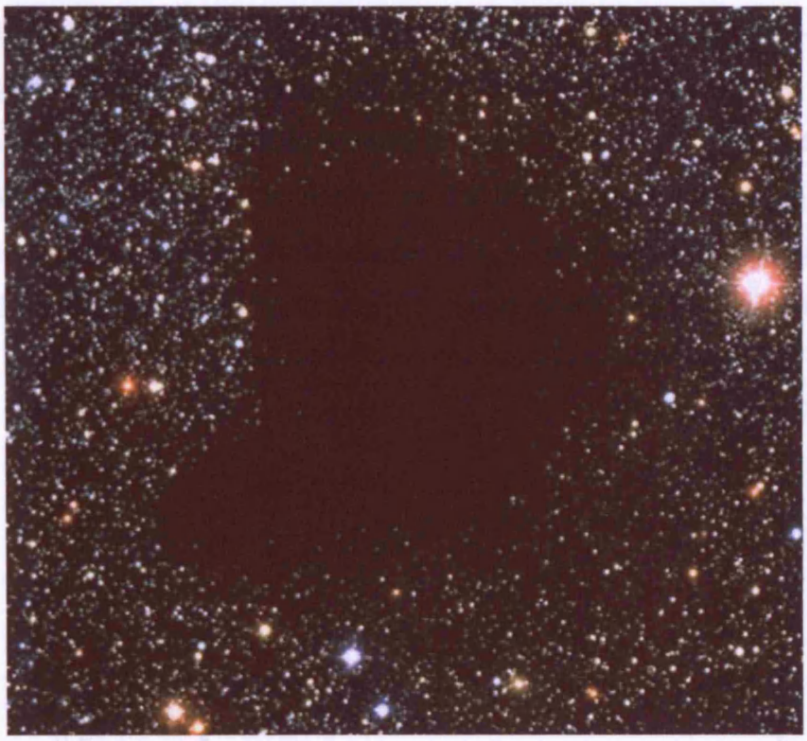

Figure 1.2: A figure showing the "Black Cloud" B68. Interstellar dust grains obscure most of the visible light from background stars. *Photo Credit & Copyright:* http://antwrp.gsfc.nasa.gov/apod/ap990511.html

The obscuration of starlight by an intervening agent, as described above, is called extinction. The average interstellar extinction curve (*Figure 1.3*) shows the normalised rate of extinction as a function of wavelength λ. Initially a slow steady rise is observed from the infrared through to the visible region, where extinction is proportional to $1/\lambda$. A prominent bump is observed at approximately 4.6 μm^{-1}, after which the curve continues to rise strongly into the ultraviolet. Some differences are found in different regions of the galaxy, such as the width and position of the bump; however the general shape is as shown in *Figure 1.3* [1, 24]. It has been shown that obscuration of light is most effective when there is an approximate match of particle size to wavelength [4], hence extinction is believed to be caused by particles ranging from a few nanometres to approximately 1 μm across [18], with an average grain radius of 0.1 μm. The bump observed in the extinction curve (*Figure 1.3*) is attributed to grains of 10 to 100 times smaller than the average grain size [23, 24].

The interstellar extinction curve also provides information concerning the constitution of the dust grains. In order to correctly simulate extinction curves, several models are employed using various dielectric materials such as silicates and carbonaceous materials. However, a unique solution cannot be offered due to the large number of parameters in such calculations. For example, it has been suggested that the 4.6 μm^{-1} bump is attributed to small graphite grains [25], however this has been disputed.

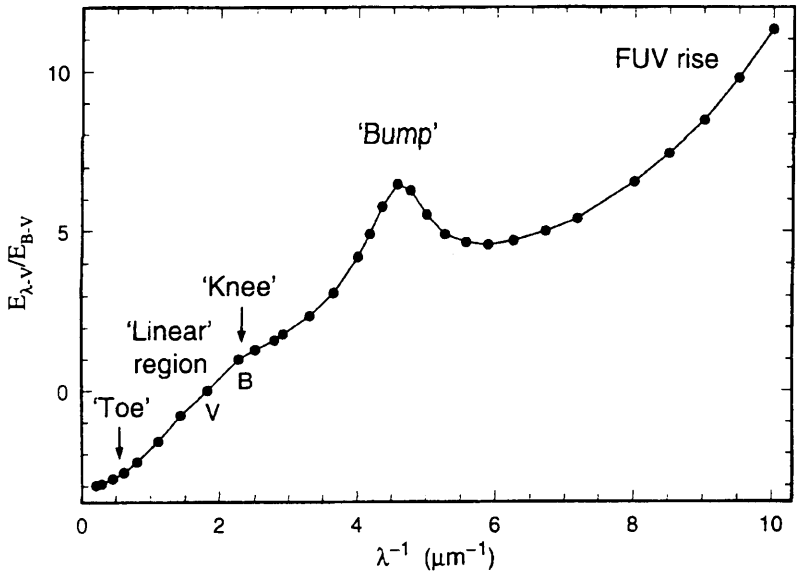

Figure 1.3: A typical interstellar extinction curve [26]. The curve shows the normalised extinction, E with respect to the change in extinction at wavelengths B and V (indicated on the diagram).

Complementing the evidence from the interstellar extinction curve are observations that starlight is polarised by a few percent. The amount of polarisation observed seems to be proportional to the amount of extinction, since the mechanism of polarisation is one of preferential extinction [1]. In order for starlight to be polarised, two constraints must be met. Dust grains, behaving in an isotropic manner, causing the polarisation, cannot be spherical but must be elongated. In addition, the elongated dust grains must be aligned to some degree. If these constraints are met, then components of radiation parallel to the longer axes of the grains will be more heavily extinguished than the component perpendicular to the elongated axes of the grain and polarisation can occur [1]. A known magnetic field exists within the ISM, which aligns dust grains which in turn are believed to be paramagnetic in nature. Polarisation only exists to a few percent since the grains will normally be rotating and hence only a partial alignment of the axes of

rotation can occur. In addition, randomisation of orientation will occur through collisions.

Evidence for the existence and composition of dust grains also arises through elemental depletion observed in the ISM [18]. Due to the proximity of our Sun, it is often thought of as a typical star, especially in terms of observed relative abundances of certain elements. Whether this assumption is true or not is still highly debated [1]. However, comparing relative abundances of elements in the Sun with those in interstellar clouds has led to widely differing relative abundances, with several elements severely depleted in certain stars compared to the Sun. Elements such as titanium have been observed to be depleted by a factor of 1000 and silicon by a factor of 10 towards the star ζ Ophiuchi [27] compared to standard stellar models. It is suggested that, as gas cools and moves away from stars, these missing elements form refractory solids which are removed from the gas as solid particles [28, 29]. An example of this is the formation of silicates from silicon, oxygen, magnesium and iron. It therefore follows that the most depleted elements are likely to form the constituents of dust grains. *Figure 1.4* shows a chart of the most depleted elements with respect to total dust mass [26]. Carbon and oxygen are particularly depleted and therefore considered key constituents of dust grains.

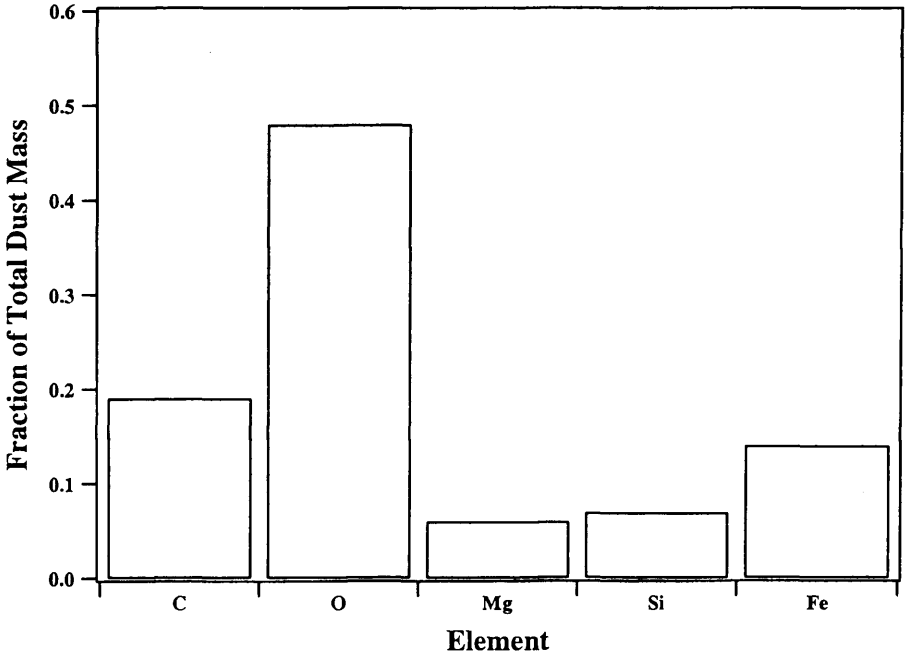

Figure 1.4: A bar chart showing the fractional masses of the elements which are most depleted with respect to total dust mass [26].

Dust grains are also believed to be responsible for the scattering of diffuse starlight. The source of scattering of the diffuse starlight, not directed from any particular source, cannot be attributed to atoms or molecules but to species the size of dust grains. In addition to the diffuse starlight, reflection nebulae exist where stars are sufficiently near to dust and gas clouds that scattered light can be observed by the naked eye [1]. An example of a reflection nebula is shown in *Figure 1.5*.

Figure 1.5: The Witch Head Nebula. Scattering of starlight by dust grains causes the appearance of the nebula. (*Photo*: www.astro.cz/apod/ap990829.html)

Ground based observations have also noted a broad band emission centred on the red or near infrared from interstellar regions of high extinction [1, 18]. This emission is thought to occur due to the absorption of UV and visible light by materials with appropriate bandgap energies (~ 2 eV), so that leakage can occur into other modes from

the newly populated states. The leakage leads to emission across the bandgap. Possible materials with appropriate bandgaps include H-rich amorphous hydrocarbons, which are also believed to be a constituent of dust grains.

A further piece of information about dust grains is gained from the collection of interplanetary dust (shown in *Figure 1.6*), from sources such as asteroids, as it falls to the Earth. The majority of interplanetary dust is heavily affected by the physical processing that it has undergone, however a certain component appears to be unmodified. This unmodified component may be similar to interstellar dust [18, 25]. The interplanetary dust, obtained on various space missions [30], has been found to contain glasses with embedded metals and sulphides (GEMS), which have physical and chemical properties very similar to those expected for interstellar dust [31].

The principle method for the identification of the components of interstellar dust grains is through the study of solid state spectral lines. Absorption of infrared radiation from background stars by foreground solid species leads to the appearance of solid state spectral features. However, carrying out these observations from the ground is fraught with difficulties because of the constitution of the Earth's atmosphere. The most accurate measurements have been made by a European satellite, the Infrared Space Observatory (ISO) [32-34]. The observed spectral features can then be compared with laboratory based samples and identification of the components giving rise to the features can be made. In this manner it has been determined that interstellar dust grains consist of silicates and carbonaceous material [18, 23, 35]. Additionally, infrared observations by ISO have shown interstellar ices present in dark clouds [21, 32-34, 36]. H_2O appears to account for 60 to 70% of ice composition while other species detected include CO, CO_2, $^{13}CO_2$, OCS, CH_3OH, CH_4, H_2CO and HCOOH and NH_3 [21, 26]. Not all observed spectral features can be assigned confidently, with disagreement occurring over several assignments [33].

By using the evidence for the existence of interstellar dust grains, it is possible to construct a model for the nature of the grains. Interstellar dust grains are thought to vary in size from approximately 1 nm up to 10 μm [18]. The cores of the grains are believed

to consist of metallic silicates, carbonaceous materials and GEMS. In dark clouds the dust grains are coated in interstellar ices consisting of a variety of molecules such as H_2O, CO, CO_2 and CH_3OH. This composition is shown schematically in *Figure 1.6*.

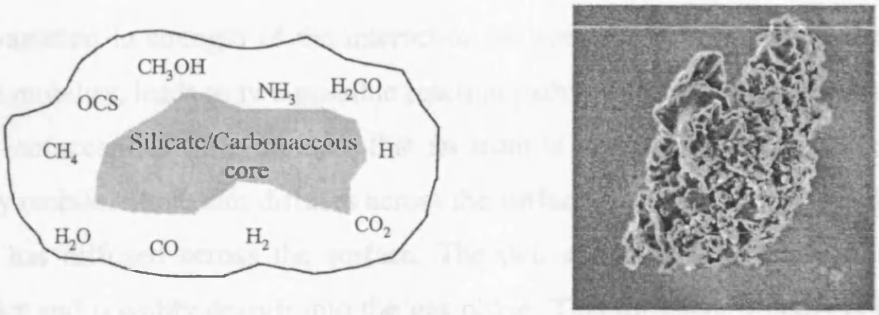

Figure 1.6: The figure on the left shows a schematic diagram of the composition of interstellar dust grains. The picture on the right is of collected interplanetary dust (picture from *http://news-info.wustl.edu/tips/2003/science-tech/dust.html*).

1.5.2 Surface Processes on Dust Grains

Astronomers believe that the surfaces of dust grains act as active sites for molecular formation in the ISM [18, 23]. Hence, in order to understand molecular formation mechanisms a fundamental understanding of chemical processes on the surface of dust grains is required. Chemistry on the surface of dust grains can be broken down into several steps: accretion on the surface, diffusion across the surface, surface reaction, mantle accumulation and processing and finally desorption [37]. At the low temperatures in the ISM, the majority of atoms, molecules and ions that collide with a dust grain stick to the surface of the grain. This is a result of the high sticking probability of a variety of surfaces representative of the ISM [18, 38]. In fact, theoretical models of chemistry on dust grain surfaces have assumed a sticking probability of unity [39, 40]. Once the atom or molecule is adsorbed on the surface, the question of surface mobility arises. The mobility of the adsorbate depends on several factors including the strength of the interaction between the adsorbate and the surface and the size of the adsorbate. For example, a light adsorbate such as a hydrogen atom is

expected to be highly mobile. A further question is the nature of the motion across the surface, be it thermal hopping or quantum tunnelling. The nature of the motion has been investigated by several groups, and appears to be sensitive to the constitution of the surface [41-43].

The variation in strength of the interaction between the surface and the adsorbate, and hence mobility, leads to two possible reaction pathways for molecular formation on dust grain surfaces. Consider the case that an atom is weakly adsorbed on the surface and highly mobile. This atom diffuses across the surface until it meets a second atom, which itself has diffused across the surface. The two atoms can then react to form a new product and possibly desorb into the gas phase. This diffusive process is known as the Langmuir-Hinshelwood mechanism and is shown schematically in *Figure 1.7*.

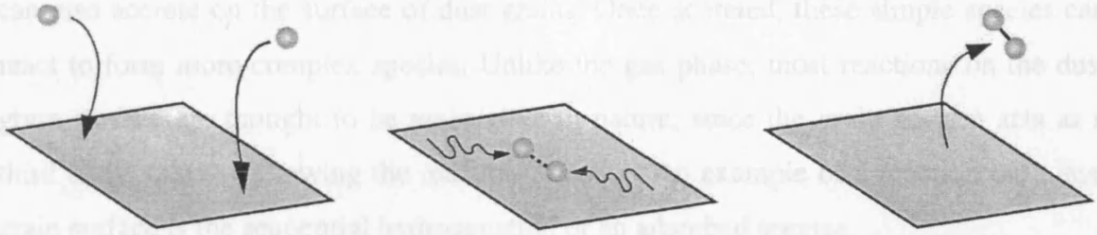

Figure 1.7: A schematic of the Langmuir-Hinshelwood mechanism on the surface of dust grains.

An alternative to the Langmuir-Hinshelwood mechanism is a scenario where atoms are bound to the surface sufficiently strongly that diffusion is not competitive. Hence, over a period of time, surface adsorption sites become occupied with adatoms. In this case, an atom direct from the gas phase lands atop the adatom and reacts to form a new molecule, which can in turn desorb from the surface. This is known as the Eley-Rideal mechanism and is shown schematically in *Figure 1.8*.

The formation of molecules on the surface of dust grains could proceed either via the Langmuir-Hinshelwood or the Eley-Rideal mechanism. An example of this is the formation of H_2. The dust grain provides an opportunity for two hydrogen atoms to meet and react to form H_2. In this manner, the dust grain acts as a third body and can be

used to dissipate some of the excess energy produced during the reaction [20, 44, 45]. It is currently not clear whether the Langmuir-Hinshelwood or the Eley-Rideal mechanism is the dominant mechanism for the formation of H_2.

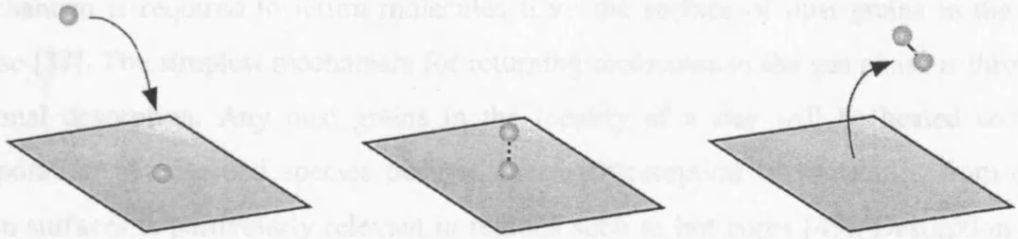

Figure 1.8: A schematic of the Eley-Rideal mechanism on the surface of dust grains.

Dust grains can also act as a site for the formation of molecules larger than H_2 [46]. As has been demonstrated, atoms such as C, O, N and S, and simple molecules such as CO, can also accrete on the surface of dust grains. Once accreted, these simple species can react to form more complex species. Unlike the gas phase, most reactions on the dust grain surface are thought to be associative in nature, since the grain surface acts as a third body, thereby allowing the reaction to occur. An example of a reaction on a dust grain surface is the sequential hydrogenation of an adsorbed species

$$H + X \rightarrow HX$$

where X could be O, C or N to form H_2O, CH_4, NH_3 respectively. Similarly, addition reactions may occur not involving H atoms

$$X + Y \rightarrow XY$$

where X and Y could be, for example, the reaction between CO and O to form CO_2.

Molecular formation and chemical change may also occur as a result of mantle processing. Interstellar ices accreted on the surface of dust grains are subjected to substantial energetic processing by UV radiation and by collisions with CR particles

[47, 48]. It is believed that the UV radiation leads to chemical modification of the ices, while the CR particles return the modified molecules back to the gas phase [23].

In order to prevent complete freeze out of molecules from the gas phase, an efficient mechanism is required to return molecules from the surface of dust grains to the gas phase [37]. The simplest mechanism for returning molecules to the gas phase is through thermal desorption. Any dust grains in the locality of a star will be heated so that evaporation of adsorbed species occurs. Thermal desorption of molecules from dust grain surfaces is particularly relevant in regions such as hot cores [49]. Desorption can also occur as a result of chemical reaction. If a chemical reaction is sufficiently exothermic, reaction may lead to the ejection of the products and possibly neighbouring species. Alternatively, desorption may take place due to CR heating or due to sputtering of dust as a result of interstellar gas being shocked. (Shocking is a process where by a rapid temperature rise occurs in a volume of gas).

1.5.3 Hot Cores

Hot cores are small, compact clumps found within molecular clouds in the vicinity of newly formed massive stars [49]. They are found to be optically thick, relatively warm in temperature and are characteristically rich in the range of molecular species detected [50]. This variety in observed molecules, from small saturated hydrocarbons to large organic molecules [51], is believed to be a result of evaporation of interstellar ices accumulated on dust grains during cloud collapse in star formation [52]. Furthermore, recent observations have indicated the existence of precursors of hot cores [53]. Hence, the precursors and the hot cores can be considered as a record of the collapse process in the chemistry of the ices deposited during the collapse [49]. The time taken for a pre-stellar core to evolve towards the main sequence is brief on astronomical scales, hence this "turn-on" time has been considered to be instantaneous [54]. Similarly, conventional models of hot core chemistry have treated the sublimation of ices as an instantaneous process, due to the lifetime of the hot core being comparable to the turn-on time of the hot star. However, recent observations have indicated the possibility of non-instantaneous sublimation [55]. Incorporating finite sublimation rates for the

molecules present in the interstellar ices has been shown to have a significant effect on the chemistry of the hot cores [56]. Hence, a detailed understanding of the sublimation kinetics of interstellar ices is required to accurately model the chemistry of hot cores and the process of star formation.

1.5.4 Data Needs on Gas-Grain Interactions

It is now widely accepted that dust grains play an important role in the chemistry of the ISM. However, significant gaps still exist pertaining to exactly what extent dust grains are involved in molecular formation and ultimately star formation. For this reason a detailed knowledge of the gas-grain interaction is needed to allow a complete understanding of the chemistry that occurs in star forming regions. In particular information about the following processes is required:

- the sticking probability of molecules on astronomically relevant surfaces
- the residence time of molecules on dust grain surfaces in different interstellar environments
- the feasibility of reaction mechanisms in molecular formation
- the kinetics and rate coefficients of steps in these reaction mechanisms
- retention and ejection of intermediate products in reaction mechanisms
- the effects of surface morphology on the reaction mechanisms
- the energy budget of reaction mechanisms
- the effects of irradiation on interstellar ices

1.6 Previous Studies on Molecular Formation

Over the last decade several studies, both theoretical and experimental, have taken place concerning molecular formation on astrochemically relevant surfaces. The majority of these concern the formation of molecular H_2 and include thermally reactive processes and photochemistry driven by UV radiation [57-60] (not discussed here).

Experiments concerning the formation of molecular H_2 can be divided into two broad categories, those determining the internal and translational energy of the product molecule and those measuring the rate and mechanism of reaction. Perry and co-workers measured the energy budget of molecular H_2 formed on a graphite surface using resonance enhanced multiphoton ionisation (REMPI) [61], while Roser and co-workers took similar measurements on a water-ice surface employing simple time of flight (TOF) mass spectrometry [62]. In both studies it was found that the majority of the 4.5 eV of energy is dissipated into the grain surface rather than the internal modes of the product molecule. Theoretical calculations have also been carried out for the formation of molecular H_2. Takahashi and co-workers [63] reported the formation of highly vibrationally excited molecular H_2 on water-ice surfaces, via both the Eley-Rideal and Langmuir-Hinshelwood mechanisms. Farebrother and co-workers [39, 64] and Meijer and co-workers [40], employed Density Functional Theory (DFT) and scattering calculations to evaluate the rotational and vibrational populations of molecular hydrogen formed via an Eley-Rideal mechanism on a graphite surface. Once again, population of highly excited states was reported.

Theoretical studies of hydrogen recombination on graphitic surfaces have also been carried out by Sha and co-workers [65-67]. These investigations studied hydrogen recombination via the Eley-Rideal mechanism using DFT. Morriset and co-workers have also investigated the recombination of hydrogen on graphite [68-70]. These studies focussed on recombination via both the Eley-Rideal and the Langmuir-Hinshelwood mechanisms.

The mechanism of H_2 formation has been studied experimentally by Pirronello and co-workers on olivine (a poly-crystalline silicate) [71, 72] and on amorphous carbon [73], and on water-ice by Manico and co-workers [74] and by Roser and co-workers [75]. In all cases TPD measurements were taken, and involved using H and D atoms to improve signal to noise ratio. For the olivine and the carbonaceous surfaces it was reported that molecular formation took place following thermal activation (by thermal hopping) rather than tunnelling. Molecular formation on a water-ice surface was shown to be

more complicated with a strong dependence on the manner in which the water-ice was deposited [75].

Molecular H_2 formation has also been investigated on/in a water-ice surface by Hornekaer and co-workers [76]. This study, in direct contrast to Roser and co-workers [75], found that molecular formation took place immediately following deposition, possibly by tunnelling. It should be noted that both studies measured HD formation, which could have a significant impact on the reaction mechanism. In fact it has been shown that there is an isotopic segregation effect in the adsorption and desorption of hydrogen on water ice at low temperatures [77].

Roser and co-workers have also studied the formation of CO_2 in TPD experiments [78, 79]. CO and O atoms were co-adsorbed on a Cu substrate at 5 K and then dosed with water-ice. In this manner an appreciable signal of CO_2 was recorded by the mass spectrometer. Hiraoka and co-workers investigated NH_3 formation by reacting H atoms with N atoms trapped in a solid N_2 matrix [80] using electron spin resonance experiments. In this study it was observed that H atoms diffuse into the N_2 matrix and react with the N atoms to form NH_3 molecules.

Several studies have also been reported for the reaction of H atoms with simple molecules such as C_2H_2, C_2H_4, C_2H_6 and CO [41, 42, 80-85]. Of all of these reactions, the most interesting and controversial is the reaction of CO with H atoms. Initial reports indicated that this reaction led to the formation of both H_2CO and CH_3OH, albeit in relatively low yields [81]. However, subsequent similar studies by the same group showed that no CH_3OH could be detected and in certain cases abstraction (instead of addition) of H atoms from intermediates occurred [41, 42, 82, 84, 85]. Conversely, the most recent study by the same group has focussed on the reaction of H and D atoms with H_2CO and CH_3OH and has shown that both CH_3OH and CO are formed by reaction of H with H_2CO i.e. both addition and abstraction reactions take place [83].

Watanabe and co-workers have also performed a series of experiments investigating the hydrogenation of CO to produce both H_2CO and methanol [86-89]. This group, once

again using RAIRS and TPD, observed appreciable yields of both H_2CO and CH_3OH when a CO-H_2O ice mixture was dosed with H atoms. The experiments were carried out as a function of surface temperature, film thickness [88] and H atom beam temperature [89]. Further hydrogenation experiments were carried out on pure solid CO ice and showed that hydrogenation was efficient below a temperature of 12 K. The discrepancies between the studies of Watanabe and co-workers and Hiraoka and co-workers show that hydrogenation of CO under interstellar conditions requires further study.

The Nottingham Surface Astrophysics Experiment (NoSAE) [90] has studied the thermal desorption of astrochemically relevant molecules from molecular ices [49, 50]. These studies are fundamental in understanding the chemistry behind hot cores found within molecular clouds, in the vicinity of newly formed massive stars. Furthermore, Collings and co-workers have observed the trapping of CO molecules within the porous structure of amorphous water [91, 92]. These studies have aided the understanding of several problems in the field of astronomy including the non-detection of a spectral band at 2152 cm^{-1} in interstellar ices [93]. A new experiment based at Leiden, The SURFace REaction SImulation DEvice (SURFRESIDE), has recently studied the trapping of CO in methanol [94] using TPD. Preliminary results indicate that methanol can trap CO in a similar manner to water.

1.7 The UCL Surface Science Experiment

New experiments are currently taking place at the UCL Centre for Cosmic Chemistry and Physics designed to aid understanding of gas-grain interactions. The aim of the UCL Surface Science Experiment is to investigate the role of the surface in several processes that occur in the ISM. Initially the investigations have focused on the adsorption and desorption of astrochemically relevant molecules on suitable dust grain analogues. The experiment is also designed to study addition reactions involving simple species.

This thesis presents complete investigations of the adsorption and desorption of water, methanol and ammonia on highly oriented pyrolitic graphite (HOPG). HOPG is a high purity form of carbon and can therefore be considered a suitable dust grain analogue (*Chapter 2*). This study is particularly important for an understanding of the chemistry on bare dust grain surfaces, i.e. in diffuse interstellar clouds or in dark clouds where interstellar ices have not yet accreted [95]. The adsorption and desorption of water and methanol on these bare grain surfaces is crucial for an understanding of the chemistry of interstellar ices, due to the high abundance of both molecules in ices. Few studies have focused on the adsorption and desorption of ammonia on dust grains, hence the chemistry of ammonia (and in turn nitrogen) in the ISM is poorly understood. The importance of each adsorbate molecule in the ISM is discussed individually in *Chapters 4* to *7*. The data presented in this thesis can be applied to aiding the understanding of gas-grain interactions. This is particularly important for a complete model of the chemistry occurring in regions such as hot cores, and in turn the process of star formation.

The investigation, presented here, uses a piece of ultrahigh vacuum (UHV) apparatus to mimic the low pressures of the ISM. Furthermore, the chamber is equipped with a liquid helium cryostat to perform experiments at astronomically relevant temperatures. The study uses two well established surface science techniques, reflection absorption infrared spectroscopy (RAIRS) and temperature programmed desorption (TPD) (*Chapter 3*). By using these two techniques in tandem, it is possible to gain a complete understanding of the adsorption system being studied. Information can be gained on the kinetic parameters of adsorption and desorption (including desorption orders, desorption energies and pre-exponetial factors), whether adsorbates have any preference in adsorption sites, and if any surface catalysed chemistry occurs.

An atom source has also been designed so that addition reactions can be studied (*Chapter 2*). An example of such a reaction mechanism is the sequential hydrogenation of CO to form methanol.

$$CO + H \rightarrow HCO$$

$$HCO + H \rightarrow H_2CO$$

$$H_2CO + H \rightarrow H_3CO$$

$$H_3CO + H \rightarrow CH_3OH$$

It is currently unclear whether hydrogenation occurs until the fully saturated species, methanol, is formed, which of the four equations is the rate determining step and how efficiently CO is converted to methanol [41, 80, 81, 84, 86-89].

The adsorption studies presented in this thesis will provide a useful tool in the analysis of future addition reaction investigations. Since both RAIRS and TPD are fingerprinting techniques, an intimate knowledge of the spectral signatures of species of interest is required for accurate identification of reactants, intermediates and products in reaction schemes.

1.8 References

[1] Dyson, J.E. and Williams, D.A., *The Physics of the Interstellar Medium.* 1997: Institute of Physics Publishing.

[2] Hartquist, T.W. and Williams, D.A., *The Chemically Controlled Cosmos.* 1995: Cambridge University Press.

[3] Kaiser, R.I., Chem. Rev., **102** (2002) p. 1309.

[4] Krugel, E., *The Physics of Interstellar Dust.* Series in Astronomy and Astrophysics, ed. M. Birkinshaw, M. Elvis, and J. Silk. 2003: IoP.

[5] Charnley, S.B., Ehrenfreund, P., and Kuan, Y.J., Spectroc. Acta Pt. A-Molec. Biomolec. Spectr., **57** (2001) p. 685.

[6] Allamandola, L.J., Tielens, A.G.G.M., and Barker, J.R., Astrophys. J., **290** (1985) p. L25.

[7] Allamandola, L.J., Tielens, A.G.G.M., and Barker, J.R. in *Interstellar Processes.* 1987: D. Reidel Publishing.

[8] Tielens, A.G.G.M., in *Dust and Chemistry in Astronomy*, T.J. Millar and D.A. Williams, Editors. 1993, Institute of Physics Publishing.

[9] Tielens, A.G.G.M., Van Kerckhoven, C., Peeters, E., and Hony, S. in *Astrochemistry: From Molecular Clouds to Planetary Systems*. 2000: Astronomical Society of the Pacific.

[10] Leger, A. and Puget, J.L., Astron. Astrophys., **137** (1984) p. L5.

[11] Butler, R.A.H., De Lucia, F.C., Petkie, D.T., Mollendal, H., Horn, A., and Herbst, E., Astrophys. J. Suppl. Ser., **134** (2001) p. 319.

[12] Kuan, Y.J., Charnley, S.B., Huang, H.C., Tseng, W.L., and Kisiel, Z., Astrophys. J., **593** (2003) p. 848.

[13] Snyder, L.E., Orig. Life Evol. Biosph., **27** (1997) p. 115.

[14] Van Dishoeck, E.F., in *The Molecular Astrophysics of Stars and Galaxies*, T.W. Hartquist and D.A. Williams, Editors. 1998, Oxford Science Publications.

[15] Geballe, T.R., McCall, B.J., Hinkle, K.H., and Oka, T., Astrophys. J., **510** (1999) p. 251.

[16] Geballe, T.R. and Oka, T., Nature, **384** (1996) p. 334.

[17] Black, J.H. and Dalgarno, A., Astrophys. J. Lett., **15** (1973) p. 79.

[18] Williams, D.A. and Herbst, E., Surf. Sci., **500** (2002) p. 823.

[19] Duley, W.W. and Williams, D.A., *Interstellar Chemistry*. 1984, London: Academic Press.

[20] Hollenbach, D. and Salpeter, E.E., Astrophys. J., **163** (1971) p. 155.

[21] Whittet, D.C.B., in *Dust and Chemistry in Astronomy*, T.J. Millar and D.A. Williams, Editors. 1993, Institute of Physics Publishing.

[22] Millar, T.J. and Williams, D.A., in *Dust and Chemistry in Astronomy*, T.J. Millar and D.A. Williams, Editors. 1993, Institute of Physics Publishing.

[23] Greenberg, J.M., Surf. Sci., **500** (2002) p. 793.

[24] Li, A. and Greenberg, J.M., Astron. Astrophys., **323** (1997) p. 566.

[25] Williams, D.A., Astron. Geophys., **41** (2000) p. 8.

[26] Whittet, D.C.B., *Dust in the Galactic Environment*. Series in Astronomy and Astrophysics. 2003: Institute of Physics Publishing.

[27] Snow, T.P. and Whittet, D.C.B., Astrophys. J., **468** (1996) p. L65.

[28] Greenberg, J.M., in *Cosmic Dust*, J.A.M. McDonnell, Editor. 1978, Wiley: New York.

[29] Gehrz, R.D. in *Interstellar Dust*. 1989: Kluwer Academic Publishers.

[30] Grun, E., Gustafson, B., Mann, I., Baguhl, M., Riemann, R., Horanyi, M., and Polanskey, C., Astron. Astrophys., **286** (1994) p. 915.

[31] Bradley, J.P., Keller, L.P., Snow, T.P., Hanner, M.S., Flynn, G.J., Gezo, J.C., Clemett, S.J., Brownlee, D.E., and Bowey, J.E., Science, **285** (1999) p. 1716.

[32] Whittet, D.C.B., Schutte, W.A., Tielens, A.G.G.M., Boogert, A.C.A., de Graauw, T., Ehrenfreund, P., Gerakines, P.A., Helmich, F.P., Prusti, T., and Van Dishoeck, E.F., Astron. Astrophys., **315** (1996) p. L357.

[33] Gibb, E.L., Whittet, D.C.B., Boogert, A.C.A., and Tielens, A., Astrophys. J. Suppl. Ser., **151** (2004) p. 35.

[34] Ehrenfreund, P., Space Sci. Rev., **90** (1999) p. 233.

[35] Witt, A.N. in *Astrochemistry: From Molecular Clouds to Planetary Systems*. 2000: Astronomical Society of the Pacific.

[36] Duley, W.W. and Grishko, V.I., Astrophys. Space Sci., **285** (2003) p. 699.

[37] Williams, D.A., in *Dust and Chemistry in Astronomy*, T.J. Millar and D.A. Williams, Editors. 1993, Institute of Physics Publishing.

[38] Williams, D.A., Astron. Geophys., **44** (2003) p. 14.

[39] Farebrother, A.J., Meijer, A.J.H.M., Clary, D.C., and Fisher, A.J., Chem. Phys. Lett., **319** (2000) p. 303.

[40] Meijer, A.J.H.M., Farebrother, A.J., Clary, D.C., and Fisher, A.J., J. Phys. Chem. A, **105** (2001) p. 2173.

[41] Hiraoka, K. and Sato, T., Rad. Phys. Chem., **60** (2001) p. 389.

[42] Hiraoka, K., Sato, T., and Takayama, T., Science, **292** (2001) p. 869.

[43] Katz, N., Furman, I., Biham, O., Pirronello, V., and Vidali, G., Astrophys. J., **522** (1999) p. 305.

[44] Hollenbach, D. and Salpeter, E.E., J. Chem. Phys., **53** (1970) p. 79.

[45] Hollenbach, D., Werner, M.W., and Salpeter, E.E., Astrophys. J., **163** (1971) p. 165.

[46] Hasegawa, T.I., Herbst, E., and Leung, C.M., Astrophys. J. Suppl. Ser., **82** (1992) p. 167.

[47] Pirronello, V., in *Dust and Chemistry in Astronomy*, T.J. Millar and D.A. Williams, Editors. 1993, Institute of Physics Publishing.

[48] Greenberg, J.M., Mendoza-Gomez, C.X., S., d.G.M., and Breukers, R., in *Dust and Chemistry in Astronomy*, T.J. Millar and D.A. Williams, Editors. 1993, Institute of Physics Publishing.

[49] Viti, S., Collings, M.P., Dever, J.W., McCoustra, M.R.S., and Williams, D.A., Mon. Not. R. Astron. Soc., **354** (2004) p. 1141.

[50] Collings, M.P., Anderson, M.A., Chen, R., Dever, J.W., Viti, S., Williams, D.A., and McCoustra, M.R.S., Mon. Not. Roy. Astron. Soc., **354** (2004) p. 1133.

[51] Walmsley, C.M. and Shilke, P., in *Dust and Chemistry in Astronomy*, T.J. Millar and D.A. Williams, Editors. 1993, Institute of Physics Publishing.

[52] Millar, T.J., in *Dust and Chemistry in Astronomy*, T.J. Millar and D.A. Williams, Editors. 1993, Institute of Physics Publishing.

[53] Molinari, S., Testi, L., Rodriguez, L.F., and Zhang, Q., Astrophys. J., **570** (2002) p. 758.

[54] Bernasconi, P.A. and Maeder, A., Astron. Astrophys., **307** (1996) p. 829.

[55] Hofner, P., Wiesemeyer, H., and Henning, T., Astrophys. J., **549** (2001) p. 425.

[56] Viti, S. and Williams, D.A., Mon. Not. R. Astron. Soc., **305** (1999) p. 755.

[57] Bernstein, M.P., Moore, M.H., Elsila, J.E., Sandford, S.A., Allamandola, L.J., and Zare, R.N., **582** (2003) p. L25.

[58] Gerakines, P.A., Moore, M.H., and Hudson, R.L., Icarus, **170** (2004) p. 202.

[59] Kaiser, R.I. and Roessler, K., Astrophys. J., **503** (1998) p. 959.

[60] Mennella, V., Palumbo, M.E., and Baratta, G.A., Astrophys. J., **615** (2004) p. 1073.

[61] Perry, J.S.A. and Price, S.D., Astrophys. Space Sci., **285** (2003) p. 769.

[62] Roser, J.E., Swords, S., Vidali, G., Manico, G., and Pirronello, V., Astrophys. J., **596** (2003) p. L55.

[63] Takahashi, J., Masuda, K., and Nagaoka, M., Astrophys. J., **520** (1999) p. 724.

[64] Meijer, A., Fisher, A.J., and Clary, D.C., J. Phys. Chem. A, **107** (2003) p. 10862.

[65] Sha, X.W. and Jackson, B., Surf. Sci., **496** (2002) p. 318.

[66] Sha, X.W., Jackson, B., Lemoine, D., and Lepetit, B., J. Chem. Phys., **122** (2005) p. art. no.

[67] Sha, X.W., Jackson, B., and Lemoine, D., J. Chem. Phys., **116** (2002) p. 7158.

[68] Morisset, S., Aguillon, F., Sizun, M., and Sidis, V., Phys. Chem. Chem. Phys., **5** (2003) p. 506.

[69] Morisset, S., Aguillon, F., Sizun, M., and Sidis, V., J. Phys. Chem. A, **108** (2004) p. 8571.

[70] Morisset, S., Aguillon, F., Sizun, M., and Sidis, V., J. Chem. Phys., **121** (2004) p. 6493.

[71] Pirronello, V., Biham, O., Liu, C., Shen, L.O., and Vidali, G., Astrophys. J., **483** (1997) p. L131.

[72] Pirronello, V., Liu, C., Shen, L.Y., and Vidali, G., Astrophys. J., **475** (1997) p. L69.

[73] Pirronello, V., Liu, C., Roser, J.E., and Vidali, G., Astron. Astrophys., **344** (1999) p. 681.

[74] Manico, G., Raguni, G., Pirronello, V., Roser, J.E., and Vidali, G., Astrophys. J., **548** (2001) p. L253.

[75] Roser, J.E., Manico, G., Pirronello, V., and Vidali, G., Astrophys. J., **581** (2002) p. 276.

[76] Hornekaer, L., Baurichter, A., Petrunin, V.V., Field, D., and Luntz, A.C., Science, **302** (2003) p. 1943.

[77] Dulieu, F., Amiaud, L., Baouche, S., Momeni, A., Fillion, J.H., and Lemaire, J.L., Chem. Phys. Lett., **404** (2005) p. 187.

[78] Roser, J.E., Vidali, G., Manico, G., and Pirronello, V., Astrophys. J., **555** (2001) p. L61.

[79] Vidali, G., Roser, J.E., Manico, G., and Pirronello, V., Adv. Space. Res., **33** (2004) p. 6.

[80] Hiraoka, K., Yamashita, A., Yachi, Y., Aruga, K., Sato, T., and Muto, H., Astrophys. J., **443** (1995) p. 363.

[81] Hiraoka, K., Ohashi, N., Kihara, Y., Yamamoto, K., Sato, T., and Yamashita, A., Chem. Phys. Lett., **229** (1994) p. 408.

[82] Hiraoka, K., Takayama, T., Euchi, A., Handa, H., and Sato, T., Astrophys. J., **532** (2000) p. 1029.

[83] Hiraoka, K., Wada, A., Kitagawa, H., Kamo, M., Unagiike, H., Ueno, T., Sugimoto, T., Enoura, T., Sogoshi, N., and Okazaki, S., Astrophys. J., **620** (2005) p. 542.

[84] Hiraoka, K., Sato, T., Sato, S., Sogoshi, N., Yokoyama, T., Takashima, H., and Kitagawa, S., Astrophys. J., **577** (2002) p. 265.

[85] Hiraoka, K., Sato, T., and Takayama, T., in *Astrochemistry: From Molecular Clouds to Planetary Systems*. 2000, Astronomical Society of the Pacific.

[86] Watanabe, N. and Kouchi, A., Astrophys. J., **571** (2002) p. 1173.

[87] Watanabe, N., Nagaoka, A., Shiraki, T., and Kouchi, A., Astrophys. J., **616** (2004) p. 638.

[88] Watanabe, N., Shiraki, T., and Kouchi, A., Astrophys. J., **588** (2003) p. L121.

[89] Hidaka, H., Watanabe, N., Shiraki, T., Nagaoka, A., and Kouchi, A., Astrophys. J., **614** (2004) p. 1124.

[90] Fraser, H.J., Collings, M.P., and McCoustra, M.R.S., Rev. Sci. Instrum., **73** (2002) p. 2161.

[91] Collings, M.P., Dever, J.W., Fraser, H.J., and McCoustra, M.R.S., Astrophys. Space Sci., **285** (2003) p. 633.

[92] Collings, M.P., Dever, J.W., Fraser, H.J., McCoustra, M.R.S., and Williams, D.A., Astrophys. J., **583** (2003) p. 1058.

[93] Fraser, H.J., Collings, M.P., Dever, J.W., and McCoustra, M.R.S., Mon. Not. Roy. Astron. Soc., **353** (2004) p. 59.

[94] Fraser, H.J. and van Dishoeck, E.F., Adv. Space. Res., **33** (2004) p. 14.

[95] Fraser, H.J., Bisschop, S.E., Pontoppidan, K.M., Tielens, A., and van Dishoeck, E.F., Mon. Not. Roy. Astron. Soc., **356** (2005) p. 1283.

Chapter 2: Experimental Apparatus

2.1 Introduction

Chapter 1 described the harsh conditions that exist in the Interstellar Medium (ISM), and the problems that need to be overcome for chemistry to occur, namely the extremely low pressures and low temperatures present in the ISM. In order to fully understand the chemical processes that occur on the surface of dust grains, these extreme conditions need to be recreated in the laboratory. Realistically, the lowest achievable pressure in the laboratory is 1×10^{-11} mbar, still several orders of magnitude higher than typical pressures in the ISM. However experiments can be carried out with surface temperatures of ~10 K, which is comparable to temperatures in the ISM. To recreate these conditions in the laboratory, experiments are carried out in an ultrahigh vacuum (UHV) chamber equipped with a liquid helium cooled manipulator.

The experiments presented in this thesis were carried out at ~90 K, as opposed to the 10 – 20 K regime of dust grains in the ISM, but can still provide detailed information about the formation of ices on dust grains and the subsequent desorption of these ices from the grains.

2.2 The UHV system

The experimental apparatus consists of a UHV chamber equipped with a liquid helium cooled manipulator, a Fourier transform infrared (FTIR) spectrometer and infrared optics for reflection absorption infrared spectroscopy (RAIRS). The RAIRS set-up is described in detail in *Chapter 3*.

The vacuum chamber consists of two experimental levels, between which the sample can be moved by a high precision manipulator (Omniax Translator, MX Series, Vacuum Generators, UK). The manipulator allows the sample to move in all three directions, x, y

and z, with micrometer precision. Additionally, it is fitted with a differentially pumped rotary feedthrough, allowing the sample to be rotated through 360°. Hence, the sample position can be identified to a high level of accuracy, which is essential for the surface analysis techniques employed in this study.

The experimental chamber rests on a stainless steel "T-section", to which the vacuum pumps used to obtain UHV are fitted. In order to pump the chamber from atmospheric pressure to high vacuum (approximately 10^{-8} mbar) a 145 l s^{-1} turbo-molecular pump (TMP) (Turbovac 151, Leybold Ltd.) is used. The TMP is backed by a 5 m^3 hr^{-1} rotary pump (Trivac D5E, Leybold). To attain UHV, the chamber is baked and an additional vacuum pump is used. This is a combined ion and titanium sublimation pump (Captorr ion pump & Boostivac TSP, Physical Electronics). The TMP and the combined ion and TSP are individually connected to the T-section by a pair of gate valves. The experimental chamber is fitted with an ion gauge to allow pressure measurement down to UHV. The UHV chamber has a base pressure of 1.2×10^{-10} mbar.

The experimental chamber is also equipped with a fine control leak valve (LVM Series Leak Valve, Vacuum Generators) for leaking sample gas into the chamber in a controlled manner. The sample gas is handled via a stainless steel manifold, which allows several gases to be admitted to the chamber in succession. The gas manifold is evacuated using a 55 l s^{-1} air cooled TMP (Leybold Turbovac 50), backed by a 2.5 m^3 hr^{-1} rotary pump (Leybold Trivac D2.5E). *Figure 2.1* shows a schematic of the experimental chamber and the gas handling manifold and all associated vacuum pumps and gauges.

The UHV chamber consists of two experimental levels. The upper level is equipped with an argon ion gun (Physical Electronics Inc.) for sputtering the sample, Low Energy Electron Diffraction (LEED) optics (ErLEED-1000A, Specs GmbH) for surface electron diffraction experiments and an ion gauge (ITL Ltd.) for pressure measurement down to UHV. The lower level is equipped with a quadrupole mass spectrometer (HAL 201, Hiden Analytical Ltd.) for temperature programmed desorption (TPD) experiments and residual gas analysis (RGA). The lower level is also used for performing RAIRS

experiments, which require differentially pumped infrared windows. The chamber also has several viewing ports, which can be used to observe the sample whilst it is being positioned. *Figure 2.2* shows a side on view of the chamber [1].

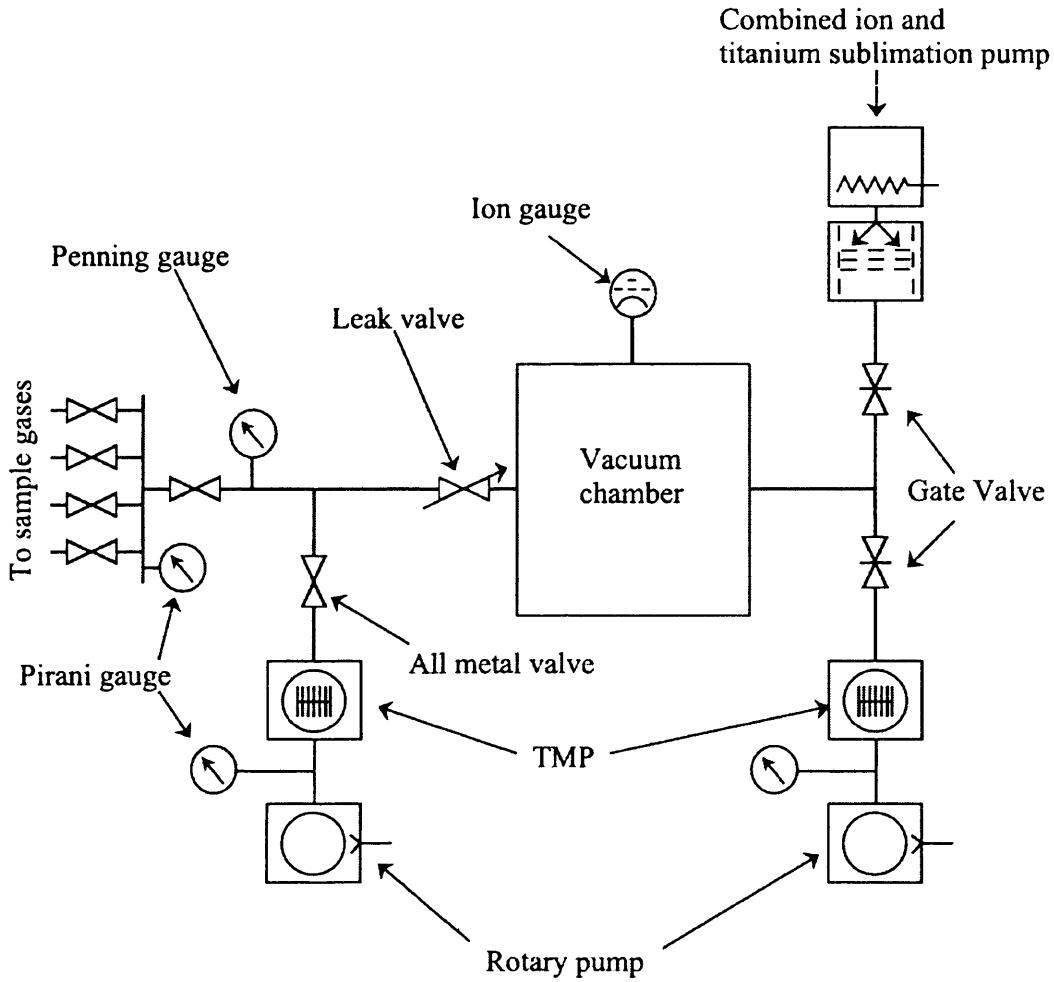

Figure 2.1: Diagram showing the layout of the experimental chamber and the gas handling manifold and all associated vacuum pumps and gauges.

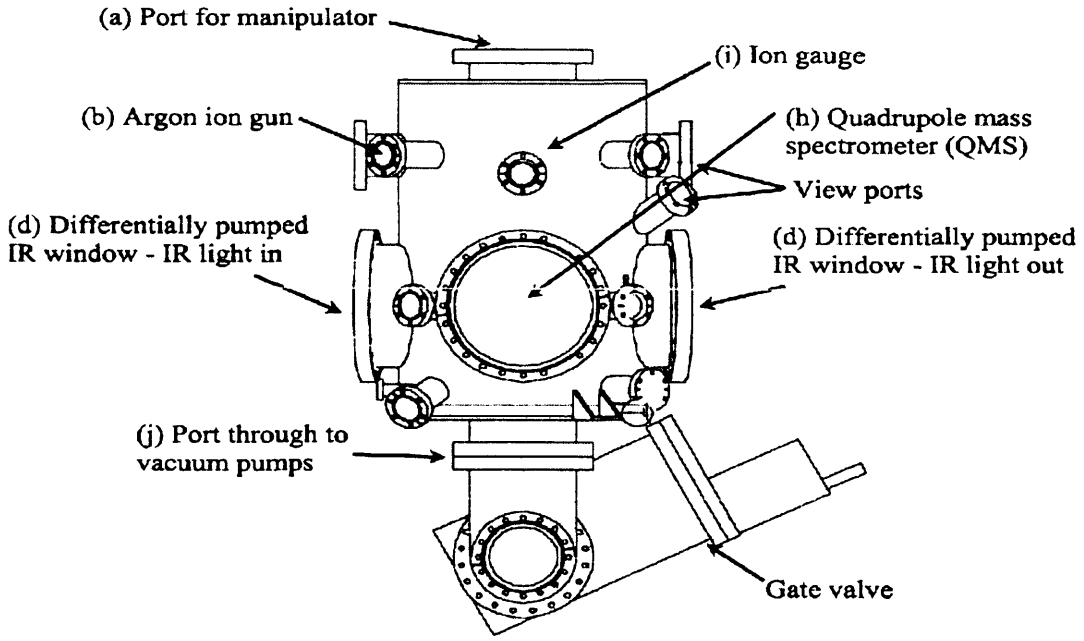

Figure 2.2: A schematic diagram of the experimental chamber used in these studies. The upper level contains the Ar ion gun, the ion gauge and the LEED optics (on the reverse of the chamber). The lower level contains the QMS and the infrared windows used in RAIRS experiments.

2.3 Sample Heating and Cooling

An important aspect of the experimental set-up is the ability to both heat and cool the sample to desired temperatures in suitable timescales. The ability to cool the sample down to low temperatures is especially crucial from an astrochemical viewpoint due to the low temperatures present in the ISM. Similarly, it must be possible to anneal the sample to a high enough temperature to ensure that it is clean. Furthermore, it is necessary to cool the sample from its annealing temperature down to the base temperature in as short a time as possible to prevent residual gases in the chamber adsorbing onto the clean sample surface. Another consideration in designing the sample heating mechanism is the ability to maintain a well controlled and constant heating rate, so that TPD studies may be performed.

The sample is heated using a resistive heating mechanism. This involves passing a large current through a set of filaments which are directly attached to the sample. This large

current causes joule heating within the filaments, elevating their temperature in a very short period of time. In this manner only the sample is heated.

To achieve sufficient cooling, a continuous flow liquid helium cryostat (A.S. Scientific Products Ltd.) is used. The cryostat was designed to operate at liquid helium temperatures, although only liquid nitrogen temperature experiments are described in this thesis. The cryostat consists of a 1 m long double-walled duct with a copper heat exchanger at one end. Liquid nitrogen is poured down the cryostat and passes through the central duct to the copper heat exchanger at the bottom of the cryostat. Once the liquid nitrogen has passed through the heat exchanger, the boil-off gas is returned to waste via the outer duct. Hence the outer duct acts a radiation shield for the inner duct. This arrangement allows the end of the cryostat to reach a temperature of ~79 K, when liquid nitrogen is poured into the coldfinger. The whole cryostat is mounted on a CF63 flange and passes down the manipulator into the experimental chamber.

The CF63 flange, on which the cryostat is mounted, also has four CF16 ports. Two of these ports are mounted with power feedthroughs, used to power the resistive heating mechanism. Each of the power feedthroughs is connected to two 2 m lengths of (0.6 mm diameter) silver plated copper wire, insulated with Kapton® (Caburn Ltd.), which form part of the resistive heating circuit. A third CF16 port is mounted with an N-type thermocouple feedthrough, which is used to monitor the sample temperature. N-type thermocouple consists of a Nicrosil (a nickel, chromium and silicon alloy) positive wire and a Nisil (a nickel, silicon and magnesium alloy) negative wire and has a working temperature range between 3 and 1500 K. The final CF16 port is mounted with a standard electrical feedthrough, used to earth the sample during LEED experiments. This feedthrough is connected to a 2 m length of (0.6 mm diameter) silver plated copper wire insulated with Kapton® (Caburn Ltd.)

2.4 The Sample Mount

The sample is attached to the end of the heat exchanger via the sample mount. The original sample mount was used for single metal crystal samples [1] and was based on

an original design by Schlichting and Menzel [2]. This sample mount had the capability of heating a metal sample up to 1100 K and could be cooled down to ~105 K. However, this mount was unsuitable for the experiments presented in this thesis for several reasons. A major shortcoming of the original sample mount was that the metal sample was spot welded to the mount. In all of the experiments presented in this thesis, a highly oriented pyrolitic graphite (HOPG) sample is used, which cannot be spot welded. Hence, a major experimental consideration was how to hold the sample in place on the sample mount. Furthermore, the original sample mount used the filaments of the resistive heating circuit to thermally connect the sample to the heat exchanger on the end of the cryostat. This led to a conflict between achieving good thermal conductivity between the heat exchanger and the sample, and being able to anneal to high temperatures. This play-off was determined by the need to anneal the metal sample to high enough temperatures (~1100 K) so that the surface was clean. The HOPG sample does not need to be annealed to such a high temperature to ensure cleanliness. Therefore the sample mount was re-designed to ensure that the sample could be cooled to lower temperatures and be held in place without spot welding.

The purpose of the sample mount is to connect the heat exchanger on the end of the cryostat to the HOPG sample. In order to achieve this successfully, several factors needed to be taken into account during the re-design of the sample mount. Good thermal conductivity was needed between the heat exchanger and the sample to ensure that the sample could be cooled down to the required low temperature; however heat could not be transferred from the sample to the cryostat, whilst the sample was being annealed. Additionally, as a resistive heating mechanism is employed, certain parts of the sample mount needed to be electrically isolated from one another and from the heat exchanger. An ideal mounting material, which fulfils all of the above criteria, is sapphire. At very low temperatures (< 80 K) the thermal conductivity of sapphire is high, however at elevated temperatures (> 80 K) the thermal conductivity of sapphire is poor [3]. This is shown graphically in *Figure 2.3*. Furthermore, sapphire is an electrical insulator, ideal for use in sample mounts using resistive heating.

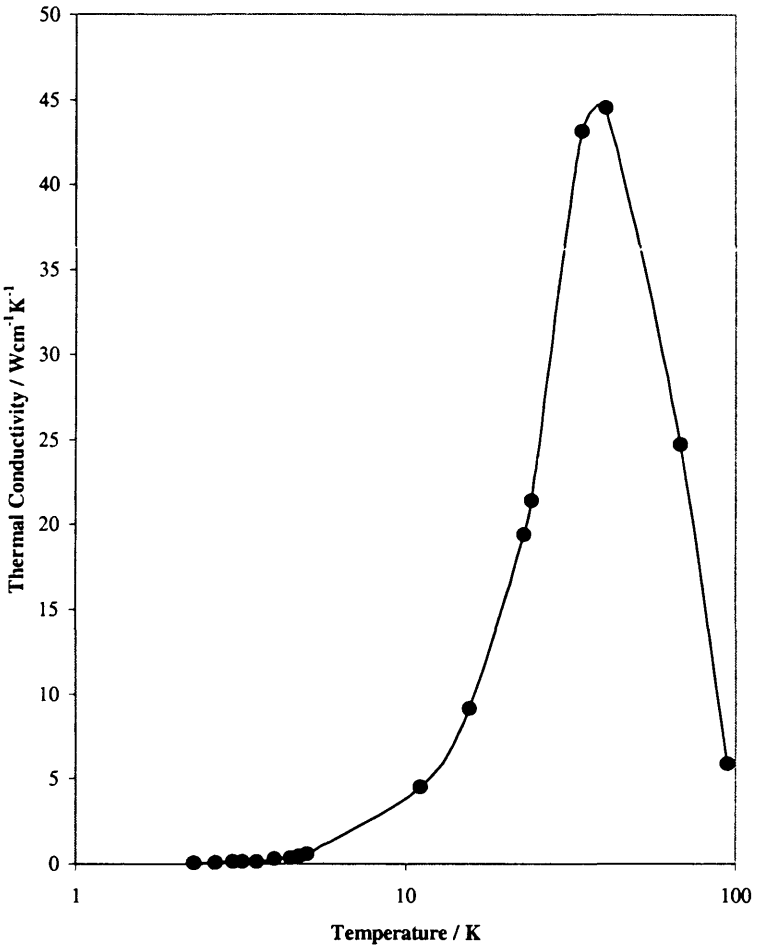

Figure 2.3: A graph showing the variation in thermal conductivity of sapphire with temperature [1].

Figure 2.4 shows a diagram of the sample mount, which is attached to the heat exchanger. The sample mount is made of a 28 mm diameter oxygen free high conductivity (OFHC) copper block. The block is composed of two halves, which are separated by a 1 mm thick piece of sapphire, 28 mm across and 60 mm long. The two halves are screwed together using a molybdenum screw and are insulated from each other using a ceramic top hat. The copper block is bolted to the heat exchanger via three molybdenum screws, which in turn are insulated from the copper block by ceramic top hats. Between the heat exchanger and the sample mount is a 28 mm diameter by 1 mm thick disk of sapphire. 0.05 mm thick silver foil is sandwiched on either side of both pieces of sapphire to improve the thermal contact between the sample mount and the heat exchanger.

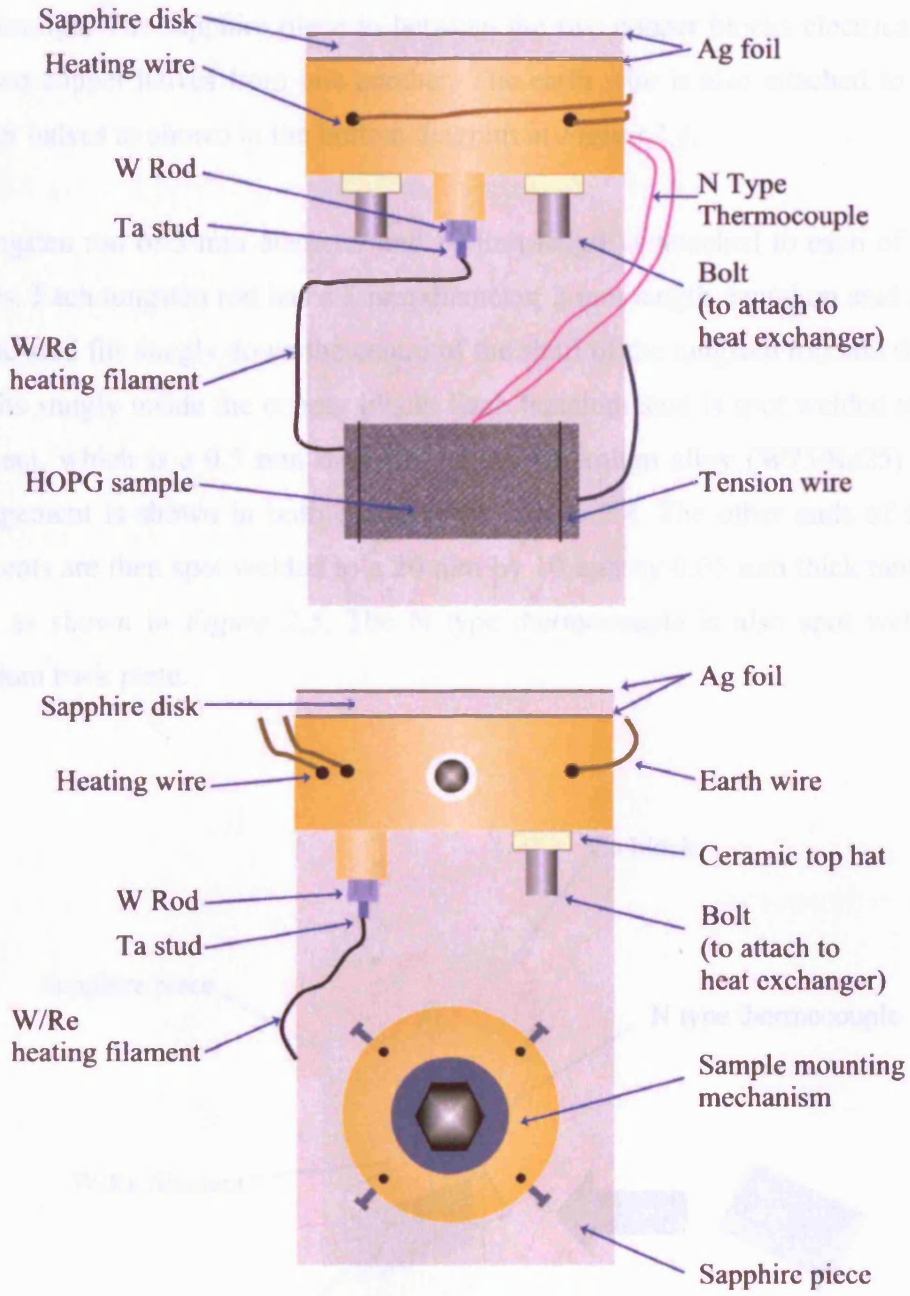

Figure 2.4: Diagram showing the layout of the sample mount attached to the heat exchanger. The sample is held in place by a pair of tension wires. The top diagram shows the front of the sample mount and the bottom diagram shows the rear of the sample mount.

Each half of the copper block is attached to a set of heating wires from a power feedthrough. The sapphire piece in between the two copper blocks electrically isolates the two copper halves from one another. The earth wire is also attached to one of the copper halves as shown in the bottom diagram in *Figure 2.4*.

A tungsten rod of 3 mm diameter and 10 mm length is attached to each of the copper halves. Each tungsten rod has a 1 mm diameter, 2 mm length, tantalum stud attached to it. The stud fits snugly down the centre of the shaft of the tungsten rod and the tungsten rod fits snugly inside the copper block. Each tantalum stud is spot welded to a heating filament, which is a 0.5 mm diameter tungsten/rhenium alloy (W75/Re25) wire. This arrangement is shown in both diagrams in *Figure 2.4*. The other ends of the heating filaments are then spot welded to a 20 mm by 10 mm by 0.05 mm thick tantalum back plate as shown in *Figure 2.5*. The N type thermocouple is also spot welded to the tantalum back plate.

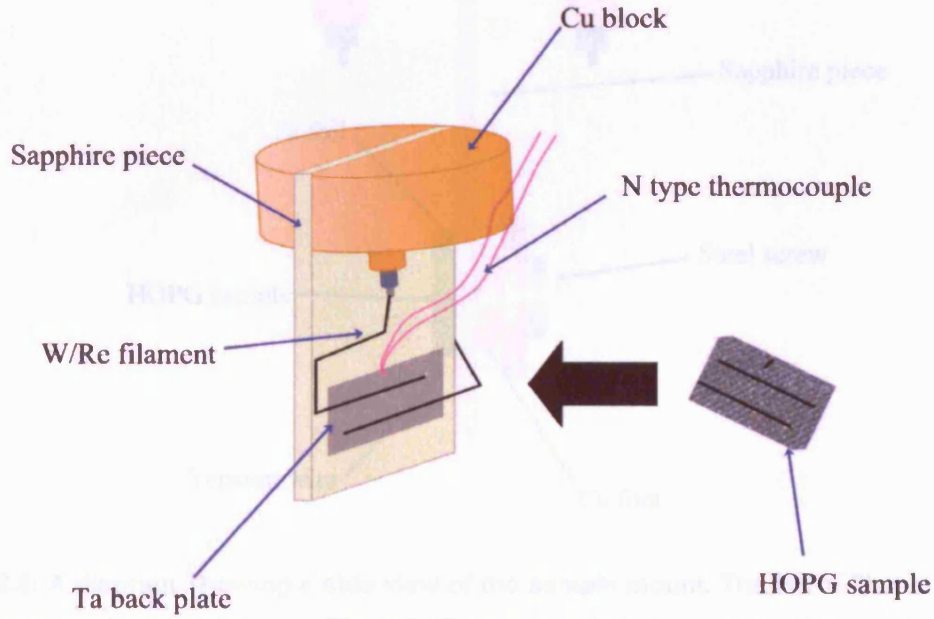

Figure 2.5: Diagram showing the position of the W/Re filaments and the N type thermocouple on the tantalum back plate. Both filaments and the thermocouple are spot welded to the tantalum back plate. Also shown is the position of the grooves on the back of the HOPG sample, in which the filaments and the thermocouple rest. The whole assembly is held in place by tension wires.

The HOPG sample (Goodfellow Ltd, UK) is 20 mm by 10 mm by 2 mm thick and is held in place on top of the tantalum back plate, tungsten/rhenium filaments and the thermocouple by a pair of tension wires. In order to ensure good thermal contact, the HOPG sample needs to be pressed against the tantalum back plate as tightly as possible. To aid thermal contact, grooves are created in the back of the HOPG sample corresponding to the position of the two filaments and the thermocouple. The grooves are the same size as the filaments and the thermocouple to create a snug fit. The positioning of the grooves is shown in *Figure 2.5*. Furthermore, by creating these grooves, the majority of the heat from the filaments is passed directly to the HOPG sample. The tension wires used are N type thermocouple wire and hold the sample in place on the sample mounting. The tension wires can be seen in *Figure 2.6*.

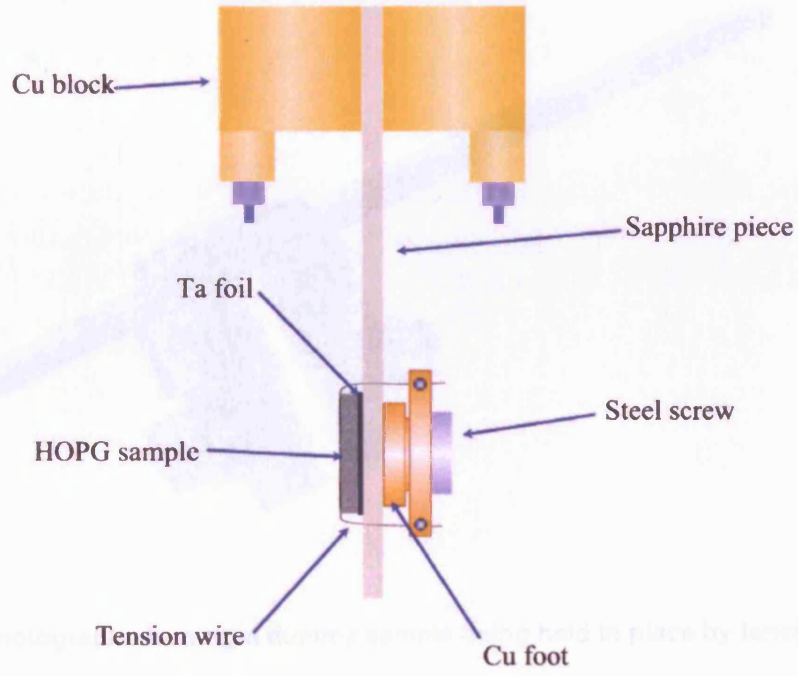

Figure 2.6: A diagram showing a side view of the sample mount. The W/Re filaments and the thermocouple are not shown. The HOPG sample is held in place on the tantalum back plate by a pair of tension wires, which pass through two pairs of holes in the sapphire and into the sample mounting mechanism.

Each tension wire is looped over the HOPG sample (~2 mm from the edge of the sample) and passes through a pair of holes in the sapphire. The four ends of the two tension wires are then held equal distances apart on the sample mounting mechanism. A stainless steel screw passes through the centre of the sample mounting mechanism, which rests against a copper foot, which in turn rests against the back of the sapphire (*Figure 2.6*). When the screw is tightened, the sample mounting mechanism moves away from the copper foot, tightening the tension wires, and holds the HOPG sample in place. *Figure 2.7* shows a photograph of the sample mounting mechanism, holding a dummy sample against a piece of Perspex similar in dimension to the sapphire piece. This modified sample mount allows the HOPG sample to be cooled from 500 K to below 90 K in less than 5 minutes.

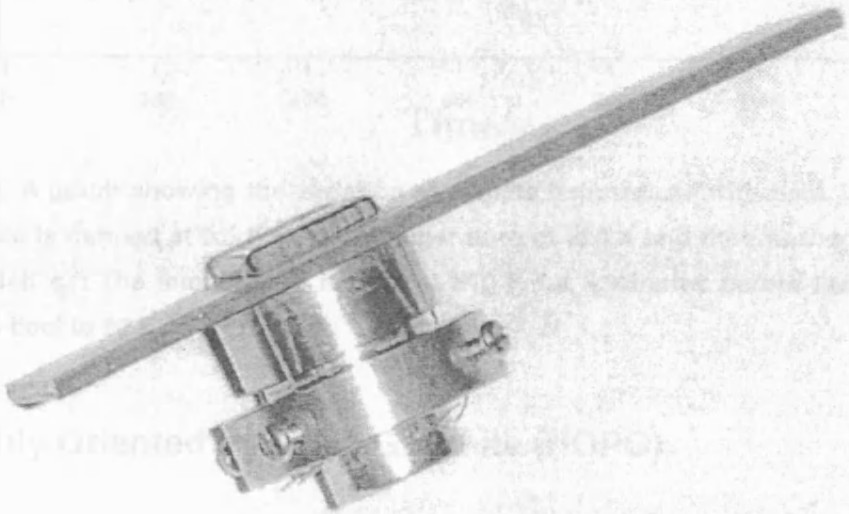

Figure 2.7: A photograph showing a dummy sample being held in place by tension wires.

To control the sample heating during annealing and experimentation, a Eurotherm temperature control module (ε2408, Eurotherm Ltd.) and Itools (Eurotherm Ltd.) software is used. The Itools software is capable of programming the ε2408 module and controlling a power supply (Xantrex 30-70, Thurlby Thandar Ltd.) to heat the sample at a constant rate or to heat to, and maintain, a constant temperature. *Figure 2.8* shows the sample temperature being controlled by the Eurotherm unit and Itools software.

Initially, the temperature is ramped at 0.5 K s^{-1} to a temperature of 220 K and then further ramped to 510 K at 1 K s^{-1}. The temperature is held constant at 510 K for 3 minutes before the sample is allowed to cool to 90 K.

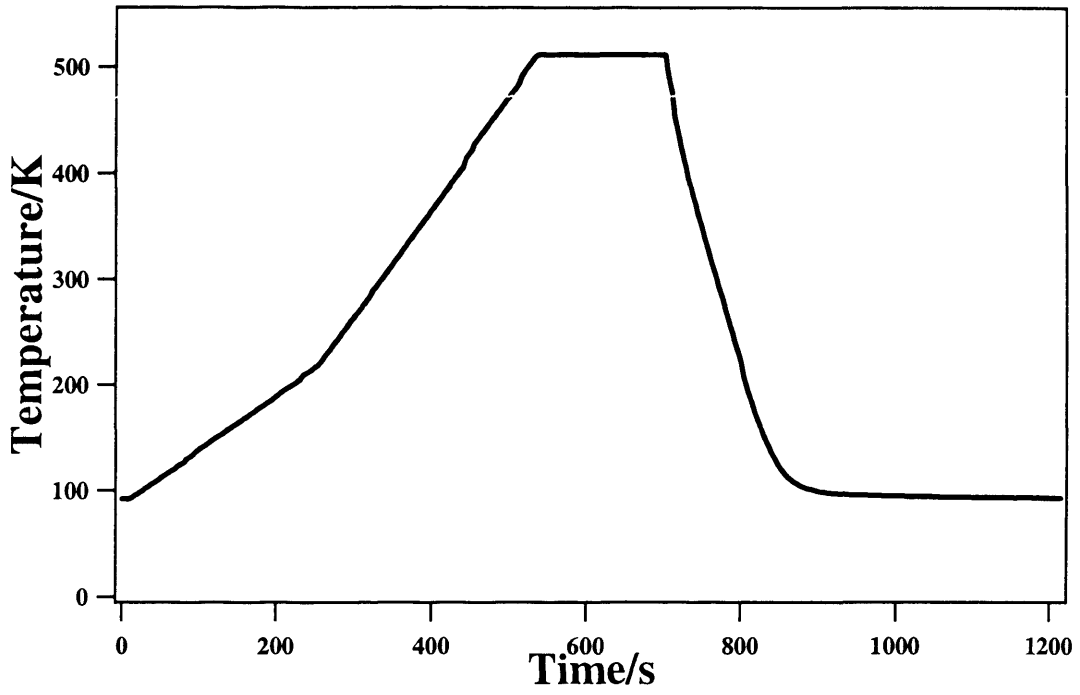

Figure 2.8: A graph showing the variation of sample temperature with time. Initially, the temperature is ramped at 0.5 K s^{-1} to a temperature of 220 K and then further ramped to 510 K at 1 K s^{-1}. The temperature is held at 510 K for 3 minutes before the sample is allowed to cool to 90 K.

2.5 Highly Oriented Pyrolitic Graphite (HOPG)

Since it is not possible to use actual interstellar dust grains, a suitable analogue is used to represent the dust grain surface. The experiments described in this thesis use a HOPG sample, which is a high purity form of carbon. HOPG is considered a suitable analogue for interstellar dust grains, since grains have been shown to contain a large carbonaceous component (see *Chapter 1*). Furthermore, HOPG is an excellent substrate for use in RAIRS experiments since it obeys the metal surface selection rule (see *Chapter 3*).

The HOPG (Goodfellow Ltd. UK) samples used are 20 mm × 10 mm × 2 mm, and are mounted in the manner described above. The samples used have a mosaic spread of 3.5° ± 1.5°. The mosaic spread measures how ordered the HOPG surface is, with a more ordered surface having a lower mosaic spread. *Figure 2.9* shows the structure of the HOPG surface. The carbon atoms are arranged in a honeycomb structure with every corner of each hexagon representing an individual atom. Also indicated on the figure is the unit cell for the HOPG surface, which is a parallelogram with a lattice constant, *a*, of 2.46 Å and an angle, γ, of 60°.

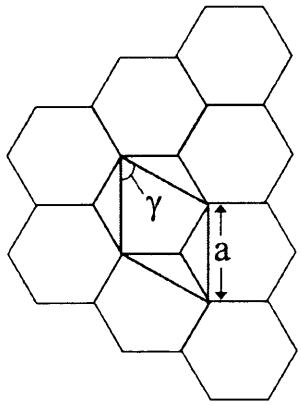

Figure 2.9: A diagram showing the honeycomb structure of HOPG. Every corner of each hexagon indicates the position of a carbon atom. Also indicated is the unit cell for HOPG. the lattice constant, a, and the corresponding angle, γ.

Planes of carbon atoms are then stacked on top of each other as shown in *Figure 2.10* to produce a three dimensional structure.

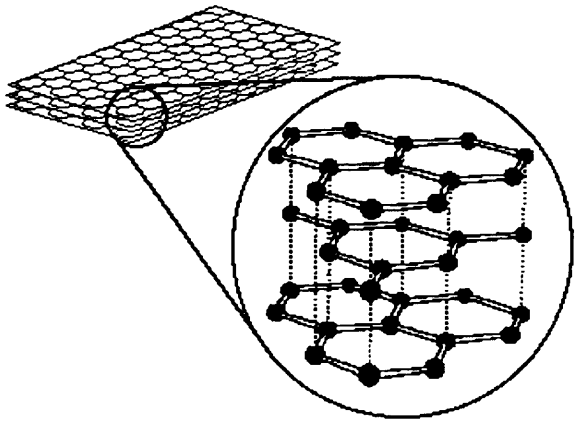

Figure 2.10: A diagram showing the layered structure of HOPG (from *http://www.chem.wisc.edu/~newtrad/currRef/BDGTopic/BDGtext/BDGGraph.html*).

Subsequent layers in the HOPG structure are weakly bound; hence the surface can easily be cleaved. By cleaving the surface (as described in *Chapter 3*) a fresh surface can be created with relative ease.

2.6 The Atom Source

To successfully study addition reactions on cosmic dust analogues, as discussed in *Chapter 1*, an atomic beam is required. To create a useable atomic beam, a second UHV chamber, known as the atom source chamber, has been designed. The chamber consists of two sections, the atom source region and the differentially pumped orifice/flag region. The atom source region is based upon the design of Perry and co-workers [4].

2.6.1 Principle of Operation

An atomic beam can be produced by the microwave dissociation of molecular gas. High purity molecular gas is flowed through a Pyrex discharge cell, 260 mm in length, outer diameter 25.5 mm and wall thickness 2 mm [4]. The Pyrex cell is surrounded by a 5 mm thick cylindrical slotted copper radiator, with a 26 mm internal diameter to ensure a snug fit around the cell [5]. The copper radiator is in two pieces, which are screwed together around the cell. Each half of the radiator has two pairs of 2 mm wide, 54 mm length, slots which are connected as shown in *Figure 2.11*.

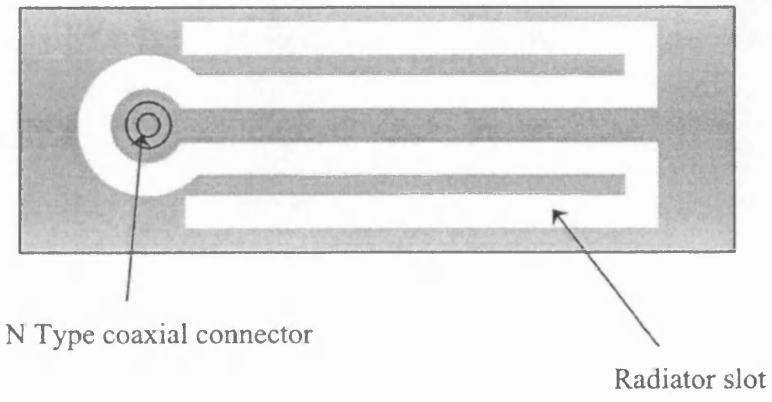

Figure 2.11: A diagram showing one half of the copper radiator as if laid out flat. The microwaves are fed into the radiator through the N type coaxial connector.

Microwaves are fed into the slotted radiator, through the N type coaxial connector, which establishes a potential difference between the slot walls. The positioning of the four radiator slots leads to a superposition of the potential differences and creates an electric field within the Pyrex cell. A plasma is created within the electric field by oscillating electrons, which in turn dissociates the molecular gas by a series of collisions. The separation and the positioning of the radiator slots are set so that a standing wave is set up in the Pyrex cell and microwave power is used in an efficient manner. To this end, the length of the radiator slots is chosen so that the midpoints of the two slots on each of the radiators are half a wavelength apart and the ends of each slot are a quarter of a wavelength from the midpoint of the adjacent slot [4].

Microwaves are fed into the radiator by Sucoflex waveguides from a 300 W Microwave Generator System (Testbourne Ltd.). The lengths of the waveguides are chosen to make the two halves of the radiator 180° out of phase, since this further increases power coupled into the discharge tube and reduces reflected microwave power to less than 10% [4]. The radiator is held between two water cooled flanges in order to keep the Pyrex tube cool, since the rate of recombination of molecules increases with temperature [6]. A diagram of the atom source assembly is shown in *Figure 2.12*.

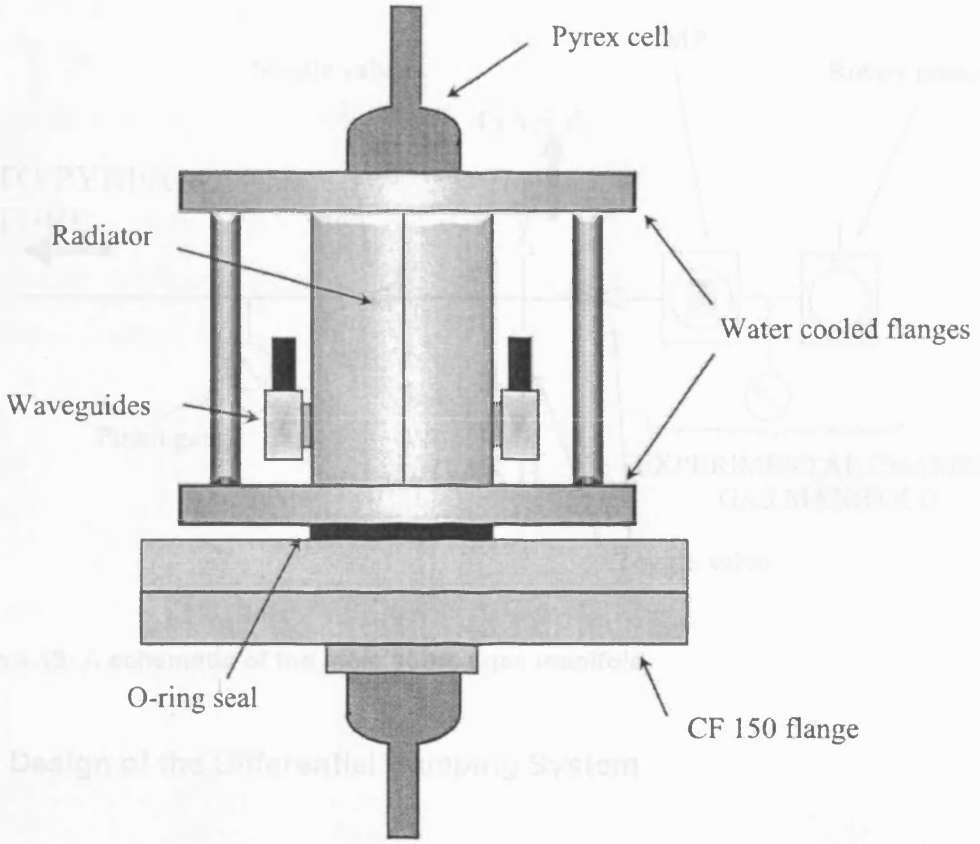

Figure 2.12: A diagram of the atom source assembly.

2.6.2 Atom Source Gas Manifold

A simple gas manifold has been created to allow the molecular gas into the Pyrex cell. This manifold is shown schematically in *Figure 2.13*. The Pyrex cell is connected to the atom source manifold via ¼ inch PTFE tubing and a Cajon O-ring seal. The manifold consists of a combination of stainless steel and copper piping with Swagelok fittings.

The manifold has the benefit of switching between two different gases so that the atomic beam can be altered depending on which addition reaction system is being studied. The atom source manifold is evacuated using the TMP on the experimental chamber manifold since one of the gas lines, shown in *Figure 2.1*, is connected to the atom source manifold shown in *Figure 2.13*.

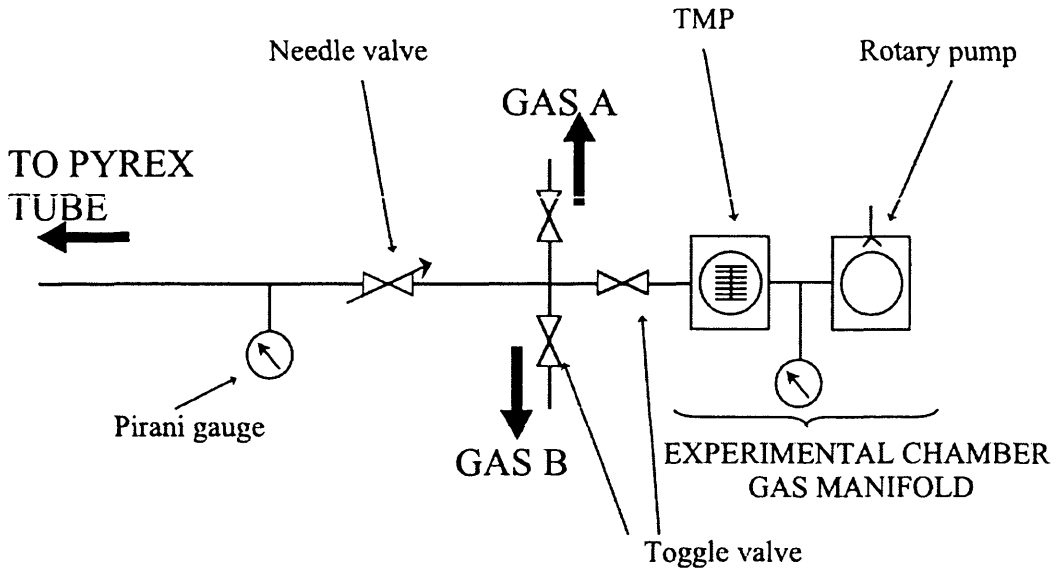

Figure 2.13: A schematic of the atom source gas manifold.

2.6.3 Design of the Differential Pumping System

The atomic beam has to be introduced into the main experimental chamber without degradation of the UHV within the chamber. To achieve optimum working conditions for the atom source, the source needs to be run continuously [4], however the atomic beam itself would only be required to run in short pulses. To achieve this, an orifice and flag arrangement was designed. Calculations were carried out to estimate the extent of any pressure rise in the main experimental chamber when the atom beam was being admitted.

Once the molecules have dissociated in the Pyrex cell, the atomic beam exits the cell through a 1 mm wide capillary of length 20 mm. This capillary is connected to PTFE tubing, of 5.4 mm internal diameter, which transports the atomic beam up to the orifice. The rate of pressure rise in the experimental chamber, whilst dosing the atomic beam, can be altered by changing the size of the orifice. To ensure that the atomic beam dose can be controlled, an aluminium flag is positioned in between the end of the PTFE

tubing and the orifice. The flag effectively acts as an on/off switch for the beam and the end of the PTFE tubing acts as a nozzle.

To calculate the load of the atomic beam on the experimental chamber, and hence the pressure rise in the chamber, the solid angle, ω, of the orifice at the nozzle and the intensity of the beam need to be evaluated [7, 8]. Assuming the distance between the nozzle and the orifice is given by $n - s$, and r is the radius of the orifice, the solid angle is given by *Equation 2.1*.

$$\omega = \frac{\pi r^2}{4\pi(n-s)^2} \times 4\pi \qquad \textit{Equation 2.1}$$

If the nozzle to orifice distance is 20 mm and the orifice aperture is 1 mm, the solid angle of the orifice at the nozzle is

$$\omega = \frac{\pi(1^2)}{(20)^2} = 7.9\times10^{-2}\ Sr.$$

To evaluate the intensity of the beam, the volume of gas per unit time being supplied by the atom source region needs to be calculated. Assuming that no gas is escaping through the orifice, the volume of gas per unit time is

$$\textit{Amount of gas per unit time} = p \times v \qquad \textit{Equation 2.2}$$

where p is the pressure in the source chamber and v is the pumping speed of the source chamber. Using a source chamber pressure of 7.5×10^{-7} mbar [9] and a chamber pumping speed of 345 l s^{-1}, gives an amount of gas per unit time of

$$\textit{Amount of gas per unit time} = 7.5\times10^{-7} \times 345 = 2.4\times10^{-4}\ mbar\, l\, s^{-1}.$$

If the atomic beam is highly directional, it can be assumed that the distribution of the beam is of cosine form. Hence the intensity per unit solid angle is

$$Intensity = \frac{dose}{\pi} \qquad \textit{Equation 2.3}$$

where the dose is the amount of gas per unit time being supplied by the atom source. Hence, the intensity is

$$Intensity = \frac{2.4\times10^{-4}}{\pi} = 7.6\times10^{-5}\ mbar\,l\,Sr^{-1}\,s^{-1}.$$

The load of the atomic beam is determined by the solid angle of the orifice at the nozzle; therefore the load is given by *Equation 2.4*.

$$Load = Intensity\times\omega \qquad \textit{Equation 2.4}$$

$$Load = 7.6\times10^{-5}\times7.9\times10^{-2} = 6.0\times10^{-7}\ mbar\,l\,s^{-1}.$$

In addition to the load created by the atomic beam, some background effusion will also take place through the orifice. To evaluate the rate of the background effusion, the size of the orifice is compared to the size of the aperture at the throat of the pump. Assuming that background effusion is solely due to the bombardment of atoms at these apertures, the background effusion is given by *Equation 2.5*, where r is the radius of the orifice, R is the radius of the aperture at the pump and the *dose* is calculated from *Equation 2.2*.

$$Background\ Effusion = \frac{\pi r^2}{\pi R^2}\times dose \qquad \textit{Equation 2.5}$$

Using a 1 mm radius for the orifice and a 75 mm radius aperture for the pump, the background effusion is

$$Background\ Effusion = \frac{(1)^2}{(75)^2}\times2.4\times10^{-4} = 4.3\times10^{-8}\ mbar\,l\,s^{-1}.$$

Hence, the total rate of gas dose into the main chamber with the atom source on is equal to the beam load added to the background effusion.

$$Total\ rate\ of\ gas\ dose = Load + Background\ Effusion \qquad Equation\ 2.6$$

Using the values calculated above

$$Total\ rate\ of\ gas\ dose = 6.0\times10^{-7} + 4.3\times10^{-8} = 6.4\times10^{-7}\ mbar\,l\,s^{-1}.$$

The rise in pressure in the main experimental chamber, as a result of dosing with the atom source, is given by the total rate of gas dose divided by the pumping speed of the main experimental chamber. The main experimental chamber has a pumping speed of 320 l s^{-1} so the pressure rise in the chamber is

$$pressure\ rise = \frac{6.4\times10^{-7}}{320} = 2.0\times10^{-9}\ mbar.$$

A pressure rise of approximately 2.0 × 10^{-9} mbar, whilst dosing with the atom beam, is tolerable and allows the main experimental chamber to maintain UHV.

2.6.4 Design of the Atom Source Chamber

The atom source chamber consists of two sections, the atom source region described above, and the differentially pumped chamber, which houses the orifice/flag mounting and connects to the main experimental chamber. A schematic of the complete atom source is shown in *Figure 2.14*.

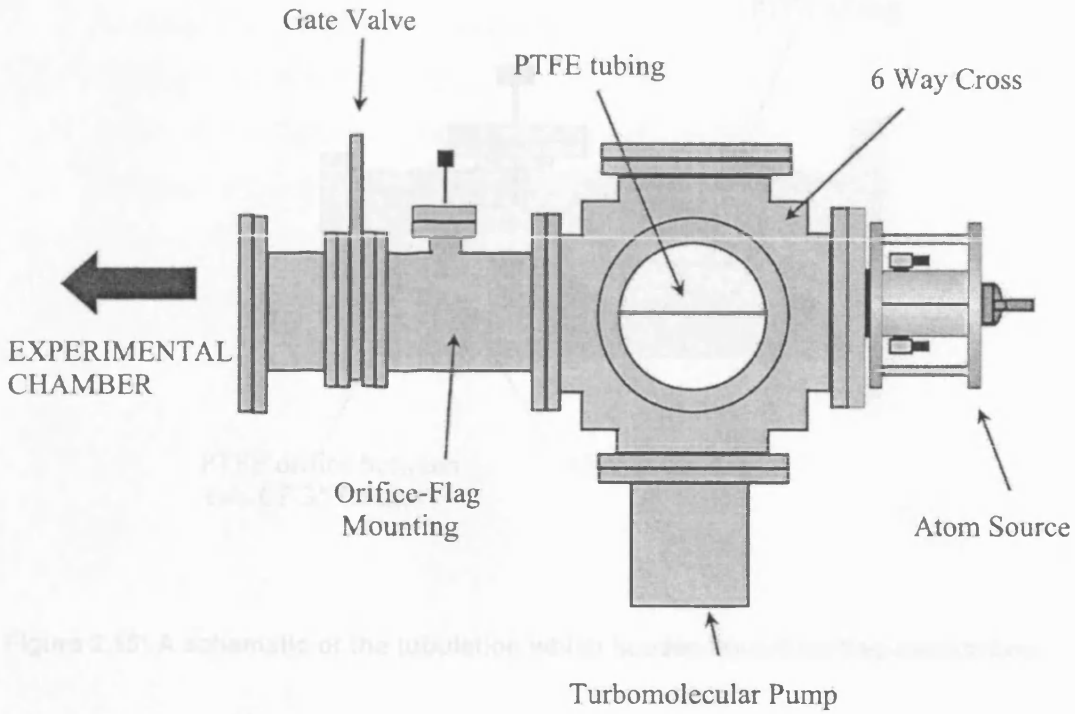

Figure 2.14: A schematic diagram of the atom source chamber. The atomic beam is piped from the atom source through the six way cross up to the orifice/flag mounting. The atom source is connected to the experimental chamber by a tubulated bellows. The whole atom source rests on a movable metal frame.

The atom source region is seated on a CF 150 flange, which is horizontally attached to a six way cross as shown in *Figure 2.14*. The capillary at the end of the Pyrex tube is attached to PTFE tubing, which pipes the atomic beam through the six way cross, and the opposite port, up to the orifice/flag mount. The PTFE tubing is supported inside the six way cross by two PTFE spacers, which pass through the central axis of the six way cross in the orientation of the atom source region. One of the ports on the six way cross is connected to a 345 l s^{-1} TMP (Turbovac 361, Leybold Ltd.). The TMP is backed by a 16 m^3 hr^{-1} rotary pump (Trivac B D16B, Leybold Ltd.). A second port is fitted with an ion gauge to monitor the pressure inside the atom source chamber. The port opposite the atom source is fitted with a custom made stainless steel tubulation, which houses the orifice/flag mount. A cross section of this tubulation is shown in *Figure 2.15*.

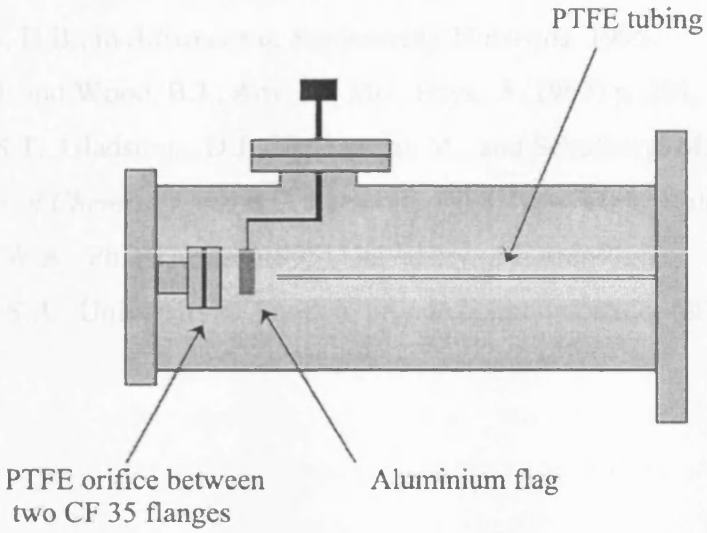

Figure 2.15: A schematic of the tubulation which houses the orifice/flag mechanism.

The atomic beam emerges from the end of the PTFE tubing, which pipes the beam up to a 1 mm orifice centred in a PTFE disk, 30 mm in diameter and 5 mm thickness. The PTFE disk is held in place by two custom made CF35 flanges. The atom source needs to run constantly, so an aluminium flag can be moved into the path of the beam, between the end of the PTFE nozzle and the orifice, to control the dose. Having passed through the orifice, the atoms enter the main experimental chamber via a short stainless steel tubulation. A gate valve is positioned between the two chambers to prevent background effusion from the atom source chamber into the main experimental chamber when not dosing. Additionally the rate of dosing into the experimental chamber can be adjusted by altering the radius of the orifice or by moving the position of the nozzle.

2.7 References

[1] Mukerji, R.J., PhD Thesis, (2003) University of London.

[2] Schlichting, H. and Menzel, D., Rev. Sci. Instrum., **64** (1993) p. 2013.

[3] Berman, R., Foster, E.L., and Ziman, J.M., **231** (1955) p. 130.

[4] Perry, J.S.A., Gingell, J.M., Newson, K.A., To, J., Watanabe, N., and Price, S.D., Meas. Sci. Technol., **13** (2002) p. 1414.

[5] Higgins, D.P., McCullough, R.W., Geddes, J., Woolsey, J.M., Schlapp, M., and Gilbody, H.B., in *Advances in Engineering Materials*. 1995.

[6] Wise, H. and Wood, B.J., Adv. At. Mol. Phys., **3** (1967) p. 291.

[7] Ceyer, S.T., Gladstone, D.J., McGonigal, M., and Schulberg, M.T., *Physical Methods of Chemistry*, ed. R.C. Baetzold. 1988, New York: Wiley.

[8] Brown, W.A., PhD Thesis, (1995) University of Cambridge.

[9] Perry, J.S.A., University of London, private communication, (2002).

Chapter 3: Experimental Methods

3.1 Introduction

This chapter describes how the experiments presented in this thesis were performed. A description is given of how the sample was prepared prior to mounting in the UHV chamber, and before each experiment was carried out. A detailed account of the Reflection Absorption Infrared Spectroscopy (RAIRS) and Temperature Programmed Desorption (TPD) set-ups for the experiments described in this thesis is also presented. The underlying principles of RAIRS and TPD are briefly described.

3.2 Sample Preparation

All of the studies presented in this thesis were performed using the equipment described in *Chapter 2*. Despite experiments being performed in a UHV chamber, the sample surface was cleaned prior to insertion in the UHV chamber and between each experiment. In this way any impurities adsorbed on the sample surface from the atmosphere, or in the UHV chamber, were removed.

Immediately prior to insertion into the vacuum chamber, the highly oriented pyrolitic graphite (HOPG) sample was cleaved using the scotch tape method [1]. This ensured that a fresh plane of carbon atoms was exposed before the sample was mounted in the chamber. The sample was then routinely cleaned before an experiment, and between experiments, to ensure that no contaminants were present on the surface. To achieve sample cleanness, the HOPG was annealed to 500 K and held at that temperature for 3 minutes. The sample was then allowed to cool to its base temperature. The base temperature, of less than 90 K, was usually achieved in approximately 5 minutes. Sample cleanness was confirmed by the absence of any desorbing species during TPD experiments with no dosage. Once sample cleanness was established, RAIRS and TPD

experiments were performed to investigate the adsorption of water, methanol and ammonia on the HOPG surface.

3.3 Reflection Absorption Infrared Spectroscopy (RAIRS)

RAIRS is a non-destructive vibrational spectroscopic technique usually used to study adsorbates on metal surfaces. It allows the identification of surface species and also provides information concerning the molecular geometry and the chemical environment. The use of RAIRS in adsorbate-surface systems, especially on the surface of single crystal metals, has been the subject of a number of reviews [2-6]. The experiments presented in this thesis have all been carried out on a HOPG sample, which obeys surface selection rule in a similar way to metal surfaces [7]. Hence, the theory of RAIRS on metal surfaces can be applied to RAIRS on HOPG samples.

3.3.1 Theory of RAIRS

In conventional transmission infrared spectroscopy, spectra are compared before and after passing infrared radiation through a sample. This results in a set of absorption bands characteristic of the constituents of the sample. However, the application of transmission infrared spectroscopy to surface studies is severely limited since the substrate must be both very thin (< 200 μm) and infrared transparent. Furthermore, changes in transmission that occur due to absorption of infrared radiation by molecules at the surface are only a small proportion of the total absorption. Therefore reflectance techniques are used to study the adsorption of species on surfaces [8]. For reflectance techniques to be successful the substrate surface must be a very good reflector, hence RAIRS is predominantly used on single crystal metal surfaces.

In RAIRS, infrared light passes through a thin layer of adsorbates and is reflected off a plane substrate surface. The reflected light loses intensity, due to absorption in the adsorbed layer, at frequencies corresponding to the vibrational modes of the adsorbed species or the vibrational modes resulting from the interaction between the adsorbate and the surface [8]. The loss in intensity of the reflected light is a direct result of the

interaction of the electric field of the incident infrared light with the dipole moment of the adsorbed molecule. Since the electric field of the infrared light and the dipole moment of the vibrating molecule interact strongly with the electrons in the substrate surface, the absorption of infrared light is strongly dependent on the dielectric behaviour of the surface [9].

The degree to which infrared light is absorbed by species adsorbed on a metal surface can be evaluated by considering the electric fields produced by radiation at a bare metal surface. The electric field of the incident radiation can be separated into two polarisations: p-polarised, which is perpendicular to the surface, in the plane of incidence, and s-polarised, which is in the plane of the surface [9]. This is shown in *Figure 3.1*. E_s and E_p are the s-polarised and p-polarised components of the incident radiation, and E_s' and E_p' are the respective components of the reflected radiation. The plane of incidence is the xy plane.

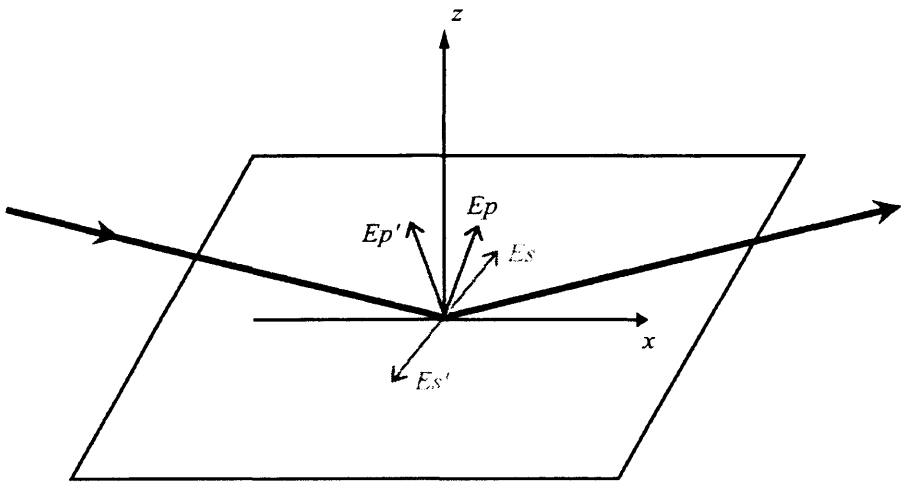

Figure 3.1: A diagram showing the electric fields associated with the reflection of infrared radiation, E_o, at a bare metal surface. E_s and E_p are the s-polarised and p-polarised components of the incident radiation, and E_s' and E_p' are the respective components of the reflected radiation. The plane of incidence is the xy plane [9].

At all angles of incidence, θ, the reflected component of s-polarised radiation, E_s', reverses in phase by 180°, and since the reflection coefficient for infrared radiation at metal surfaces is near unity this results in a near zero vector sum for E_s and E_s'. As a result, the s-polarised component cannot interact with the dipoles of adsorbed

molecules. Conversely, the p-polarised component undergoes a phase shift that is strongly dependent on the angle of incidence. Hence, the vector sum of E_p and E_p' is dependent upon the angle of incidence. This is shown in *Figure 3.2* [10]. *Figure 3.2* shows that at grazing angles of incidence, the vector sum of the incident and reflected p-polarised component is nearly twice the amplitude of the incident p-polarised component.

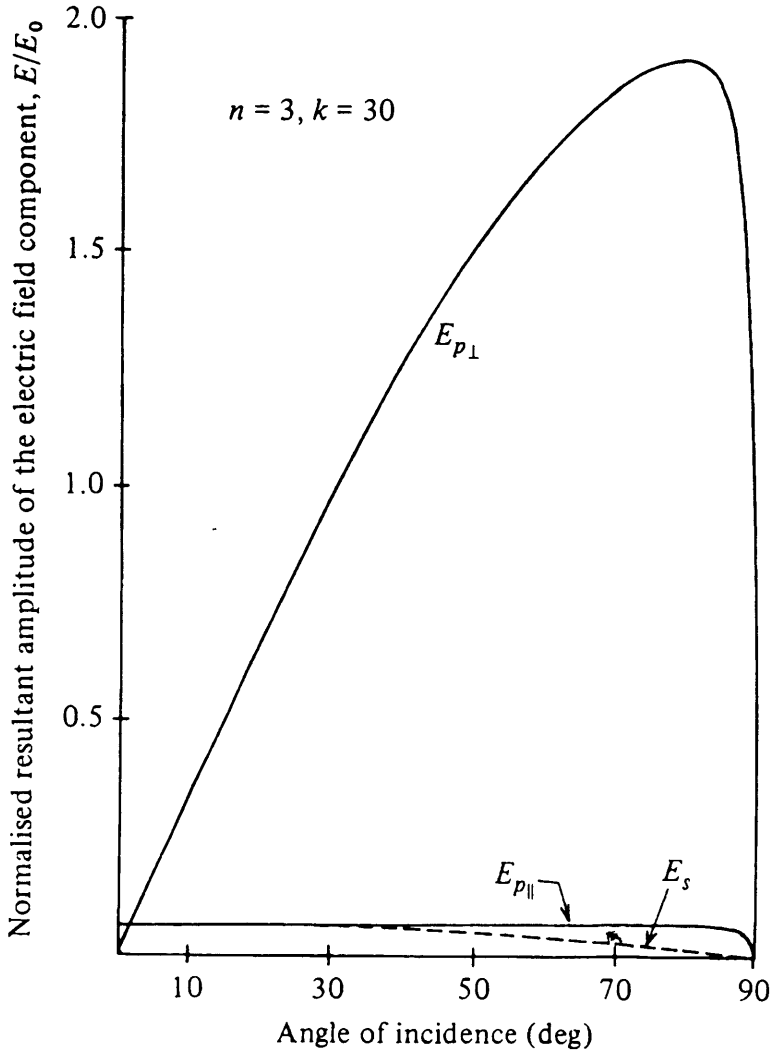

Figure 3.2: A graph showing the angular dependence of the resultant amplitude of the electric field components of incident radiation at a bare metal surface. $E_{p\perp}$ and $E_{p\parallel}$ indicate the perpendicular and the parallel components of p-polarised radiation respectively [10].

Figure 3.2 also shows that it is the perpendicular component of the p-polarised radiation, $E_{p\perp}$, which enhances the amplitude of radiation at grazing angles, while the

tangential component, $E_{p\parallel}$, remains insignificant at all angles. Therefore, the p-polarised component interacts strongly with dipoles that are perpendicular to the surface and negligibly with dipoles parallel to the surface. This difference between interactions with dipoles perpendicular or parallel to the surface can be explained by considering the effect of image charges, induced in the surface by the dipoles themselves. *Figure 3.3* shows the formation of image charges produced by a dipole perpendicular to the surface and by a dipole parallel to the surface.

For the dipole perpendicular to the surface, the vector sum of the dipole and the image charge results in a reinforcement of the dipole moment, while the vector sum of the dipole parallel to the surface, and its image charge, is near zero [4]. Hence, dipoles which are perpendicular to the surface absorb the p-polarised component of radiation and can be observed, while dipoles parallel to the surface do not and are not observed in RAIRS. Note that the adsorbate only requires a component of the dipole moment to be perpendicular to the surface for it to be observed in RAIRS.

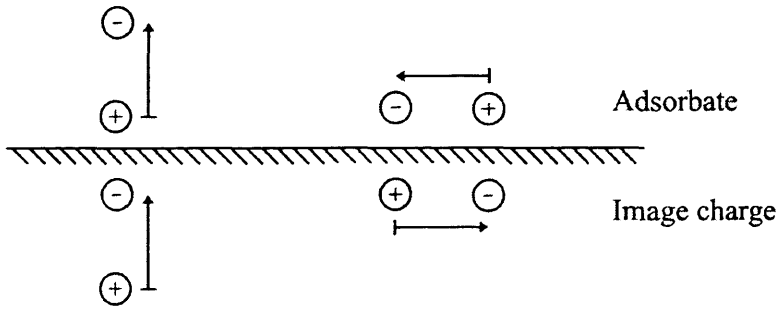

Figure 3.3: A diagram showing the image charges induced within a metal surface by a dipole perpendicular to, and parallel to, the surface.

A further consideration in RAIRS is that an increase in the incidence angle of radiation leads to an increase in the area of the sample irradiated, and hence an increase in the number of adsorbed species sampled [8]. The increase in the number of adsorbed species sampled directly results in an increase in absorption strength. The area of irradiation varies as sec θ, where θ is the angle of incident radiation. Hence the total

absorption intensity is proportional to E^2 sec θ. The angular dependence of the total absorption intensity is shown in *Figure 3.4* [10]. Once again it is shown that a maximum intensity occurs at grazing angles.

Figures 3.2 and *3.4* show that there are two important considerations in RAIRS experiments on metal surfaces:

1. The p-polarised component of the incident radiation will only excite dipoles which have a component perpendicular to the surface. This is commonly known as the metal surface selection rule.
2. The absorption intensity is greatly increased using grazing angles of incidence.

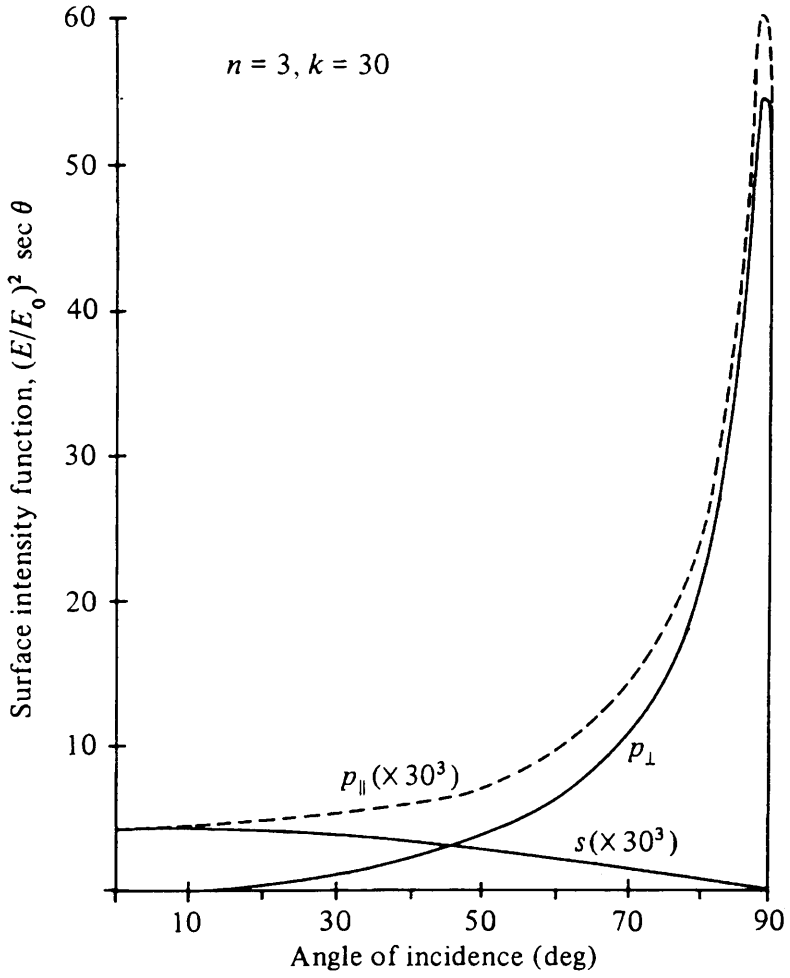

Figure 3.4: A graph showing the angular dependence of the surface intensity function for the electric field components of incident infrared radiation at a bare metal surface [10].

As previously mentioned, HOPG behaves similarly to metal surfaces in RAIRS experiments, but with a maximum absorption intensity achieved using an incident angle of 73°. This is shown in *Figure 3.5* [7].

The UHV chamber was previously used to study adsorption on single crystal metal surfaces, so a grazing angle of 5° was used. This was incorporated into the design of the chamber by angling the two ports, through which the infrared light passes, at 5°. In order to achieve optimum absorption intensities for HOPG, the grazing angle of the optical system was altered to 15°. This was achieved by re-designing the two ConFlat flanges, within which the infrared windows are held. Each flange was recessed by an additional 10° so that the infrared window and the port upon which the flange was fitted had a combined grazing angle of 15°.

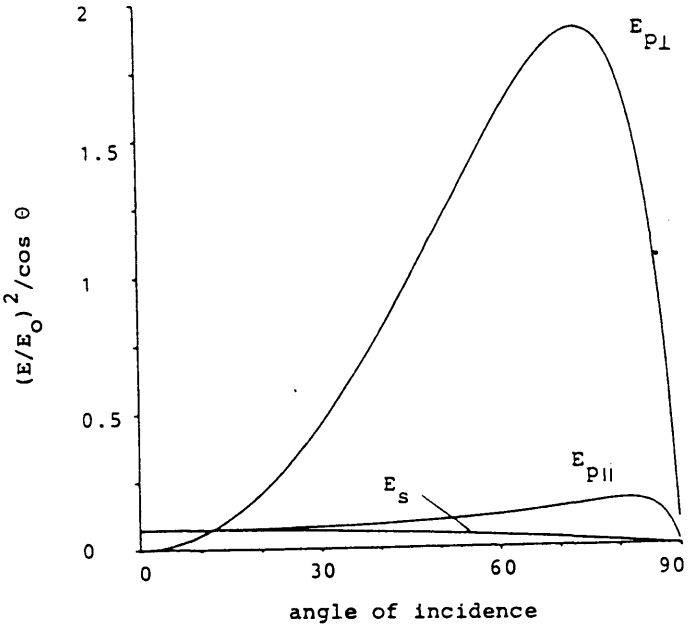

Figure 3.5: A graph showing the angular dependence of the surface intensity function for the electric field components of incident infrared radiation on HOPG [7].

3.3.2 RAIRS Experimental Set-up

During RAIRS experiments, infrared light from a Fourier transform infrared spectrometer (RS1 Research series, Mattson Instruments) is focussed onto the HOPG sample using a series of mirrors. The reflected light is then refocused onto the infrared detector using a further set of mirrors. This is shown schematically in *Figure 3.6* [11].

detector using a further set of mirrors. This is shown schematically in *Figure 3.6* [11].

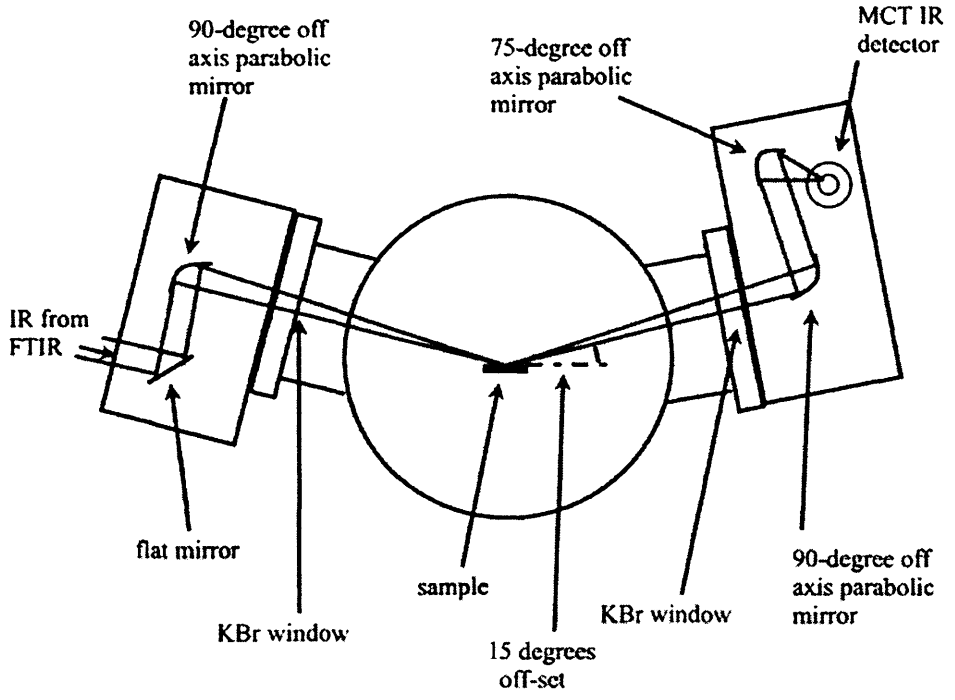

Figure 3.6: A diagram showing the RAIRS system used to perform the experiments presented in this thesis [11].

The infrared light from a FTIR spectrometer is initially reflected off a polished flat aluminium mirror (Aero Research Ltd.) and focused off a 90° off-axis parabolic mirror (Aero Research Ltd.) through a differentially pumped KBr window and onto the HOPG sample. Once the light has been reflected off the sample, it passes through a second KBr window and is refocused onto the detector by another 90° off-axis parabolic mirror and a 75° off-axis parabolic mirror. The detector used is a narrow band liquid nitrogen cooled mercury cadmium telluride (MCT) detector (EG&G, Optoelectronics). This detector is highly sensitive over a frequency range of 700 – 4000 cm^{-1}. Any signal

received by the MCT detector is fed back to the FTIR spectrometer and is converted to an infrared absorption spectrum using the Win-First software (Mattson).

The infrared optics shown in *Figure 3.6* are housed in a pair of custom built sealed aluminium boxes. The optics boxes and the FTIR spectrometer are all purged with dry, carbon dioxide free, air. It is essential to purge the optical path outside the UHV chamber, since water and carbon dioxide in the atmosphere are strong absorbers in the frequency range of interest, and would swamp any signal observed from surface species.

3.3.3 RAIRS Experiments

In order to cool the MCT detector with liquid nitrogen, the purge was temporarily broken at least half an hour before any experimentation. This half hour period allowed enough time for the optical path to re-establish a suitably stable purge. Prior to experimentation, the HOPG sample was approximately positioned at the infrared focal length in order to gain a signal at the MCT detector. The sample position was then adjusted to gain a maximum peak-to-peak signal. A typical peak-to-peak voltage of approximately 2.8 V was obtained in the experiments described in this thesis. The sample was then cleaned in the manner described above.

All RAIR spectra are the result of the co-addition of 256 scans at a resolution of 4 cm^{-1}, taking approximately 3 minutes. Initially a background spectrum of a clean surface was recorded. Dosing of the sample gas was achieved by back filling the chamber via a high precision leak valve. A RAIR spectrum was recorded of the sample and the adsorbed species. Absorption spectra were then generated by subtracting the background spectrum from the sample spectrum, and then ratioing the result with the background spectrum. A resultant plot of $\Delta R/R$ against wavenumber was then created.

After the adsorption sequence, the sample was heated in a controlled manner to determine the effect of annealing on the spectra. The sample was heated to a pre-designated temperature, held at that temperature for 3 minutes, and then allowed to cool back down to the base temperature. Once the base temperature was reached, the RAIR

spectrum was recorded. This process was repeated with increasing temperature until no absorption peaks were observed in the spectrum.

3.4 Temperature Programmed Desorption (TPD)

TPD or thermal desorption spectroscopy (TDS) is conceptually one of the simplest forms of surface analysis. It can provide kinetic information about an adsorption system by noting the temperature at which adsorbates desorb from a surface. However, the process is destructive, since the adlayer is completely desorbed from the surface. Furthermore, there are several potential pitfalls in both performing the experiments and the quantitative analysis of TPD spectra. These will be discussed in detail later.

3.4.1 Principles of TPD

The simplicity of TPD lies in that it only requires the sample and a mass spectrometer to perform the experiments. The sample is heated in a known linear manner, while desorbing species are recorded by a mass spectrometer as a function of temperature. *Figure 3.7* shows the arrangement of a typical TPD experiment.

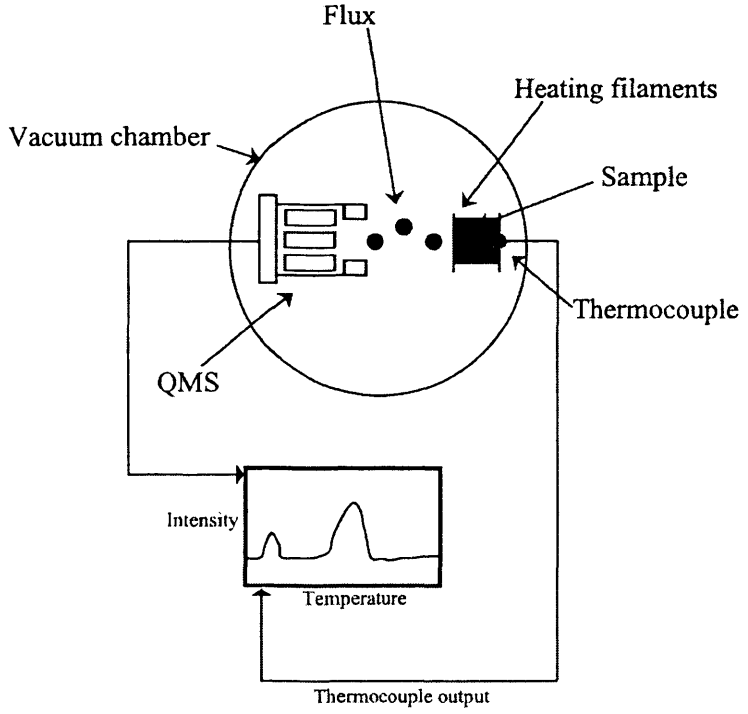

Figure 3.7: A schematic diagram of a typical TPD experimental set-up.

In TPD experiments, the gas is adsorbed onto the sample surface. Any adsorbed species must be bound to the surface with a specific amount of energy and will desorb at a rate determined by a Boltzmann factor [9]. As the sample is heated, the adsorbates acquire enough energy to desorb from the surface. This desorption leads to a change in the rate of gas evolution in the UHV chamber. This change is recorded by a mass spectrometer, which is set to detect any species of interest.

The rate of desorption in a TPD experiment is described by the Polanyi-Wigner equation [12] (*Equation 3.1*).

$$r_{des} = -\frac{\partial \theta}{\partial t} = \upsilon_n \theta^n \exp\left[\frac{-E_{des}}{RT_S}\right] \qquad \textit{Equation 3.1}$$

The Polanyi-Wigner equation relates the rate of desorption, or the rate of change in coverage as a function of time, r_{des}, to the pre-exponential factor, υ_n, the desorption order, n, the coverage, θ, the desorption activation energy, E_{des}, the gas constant, R, and the surface temperature, T_s. Further discussion of the application of the Polanyi-Wigner equation to the analysis of TPD spectra is discussed in *Chapters 4* to *7*.

3.4.2 TPD Experiments

As previously mentioned, care has to be taken while performing and setting up TPD experiments. A major problem encountered in the experiments was ensuring that the desorbing species monitored by the quadrupole mass spectrometer (QMS) (HAL 201, Hiden Analytical Ltd.) arose only from the sample surface. This was achieved in several ways. First, the set-up of the sample mount described in *Chapter 2* is such that any adsorbing species will only stick to the HOPG surface. The other possible adsorption sites on the front of the sample mount are the tungsten/rhenium heating filaments and the tension wires. However, the surface area of the heating filaments and tension wires is significantly less than the sample surface area, so any desorption from these wires during TPD experiments is negligible. Secondly, the HOPG sample was placed directly in line of sight of the QMS. This ensured that the signal received by the QMS was from

the HOPG sample and not from the copper mounting blocks or heat exchanger on the cryostat. The HOPG sample was positioned approximately 15 mm from the end of the QMS and was placed in the same position for all experiments to ensure that spectral intensities were comparable.

Another experimental consideration is that occasionally temperature gradients may occur across the sample when using a resistive heating mechanism. This led to spurious readings in the QMS. To prevent a temperature gradient across the sample, the heating filaments rest across the whole width of the back of the HOPG sample as described in *Section 2.4*. Additionally the heating filaments rest in grooves created in the back of the sample so that it is heated in a uniform manner. This mounting also ensures that heat is transferred effectively from the filaments to the sample. To ensure that an accurate sample temperature is recorded, the N-type thermocouple is in direct contact with the HOPG sample. While the sample is being heated the QMS records the intensities of the masses of any desorbing species as a function of time. The intensity versus time data and the temperature versus time data are then combined to give an intensity versus temperature profile for the two masses.

The following procedure was adopted for TPD experiments carried out following dosing at higher temperatures. The sample was cleaned in the manner described above. The sample was then heated to the pre-determined temperature and the sample exposed to the desired exposure. After dosing, the sample was held at the dosing temperature until the background pressure in the UHV chamber had returned to its usual base pressure. This took approximately 3 minutes. The sample was then allowed to cool to a base temperature (~90 - 100 K) and the TPD spectrum was recorded in the same manner as described above. By following this procedure, it was ensured that any additional adsorption onto the surface as it cools to its base temperature was negligible.

3.5 References

[1] Wiesendanger, R., Eng, L., Hidber, H.R., Oelhafen, P., Rosenthaler, L., Staufer, U., and Guntherodt, H.J., Surf. Sci., **189** (1987) p. 24.

[2] Hoffmann, F.M., Surf. Sci. Rep., **3** (1983) p. 106.

[3] Hirschmugl, C.J., Surf. Sci., **500** (2002) p. 577.

[4] Bradshaw, A.M. and Schweizer, E., in *Spectroscopy of Surfaces*, R.E. Hester, Editor. 1988, John Wiley & Sons Ltd.

[5] Horn, A., in *Spectroscopy for Surface Science*, R.E. Hester, Editor. 1998, John Wiley & Sons.

[6] Chabal, Y.J., Surf. Sci. Rep., **8** (1988) p. 211.

[7] Heidberg, J. and Warskulat, M., J. Elec. Spec. Rel. Phenom., **54/55** (1990) p. 961.

[8] Riviere, J.C., *Surface Analytical Techniques*. 1990, Oxford: Oxford University Press.

[9] Woodruff, D.P. and Delchar, T.A., *Modern Techniques of Surface Science*. 1990, Cambridge: Cambridge University Press.

[10] Greenler, R.G., J. Chem. Phys., **44** (1966) p. 310.

[11] Mukerji, R.J., PhD Thesis, (2003) University of London.

[12] de Jong, A.M. and Niemantsverdriet, J.W., Surf. Sci., **233** (1990) p. 355.

Chapter 4: Water Adsorption on Highly Oriented Pyrolitic Graphite

4.1 Introduction

Water (H_2O) is possibly the most essential molecule on our planet and, as a result, has received much attention with respect to interactions occurring at the interfaces of solid surfaces. The motivation for these studies arises from a variety of areas including catalysis, astronomy, electrochemistry, sensors and atmospheric chemistry. Thorough reviews of the fundamental interactions of water with solid surfaces have been presented by Henderson [1] and Thiel and Madey [2]. As described in *Chapter 1*, water ice plays a significant role in the chemistry of the interstellar medium (ISM), since it accounts for 60 to 70% of the composition of interstellar ices [3, 4]. Hence, a clear understanding of the adsorption and desorption of water from dust grain surfaces is crucial in understanding gas-grain interactions and in turn the chemistry of the ISM. This is especially relevant in regions such as hot cores [5] (*Chapter 1*). Furthermore, it has been shown that the desorption of all species accreted on dust grain surfaces, such as methanol, carbon dioxide and ammonia, is predominantly controlled by the presence and behaviour of water ice [6]. This chapter presents a combined RAIRS and TPD study of water adsorption on, and desorption from, highly oriented pyrolitic graphite (HOPG).

There have been several previous studies, both theoretical and experimental, of the adsorption of water on graphitic surfaces. Phelps and co-workers investigated the adsorption of water on HOPG at 88 K using high resolution electron energy loss spectroscopy (HREELS) [7]. Loss features were observed at 235 cm^{-1}, 735 cm^{-1} and 3340 cm^{-1} along with a weak feature at 1600 cm^{-1}. These were assigned to frustrated translational, frustrated rotational, O-H stretching and HOH scissor modes respectively. All spectral features were broad, relative to the elastic peak, especially the O-H stretching feature. The frequencies of the adsorbate peaks were independent of the water exposure. The study also showed that water adsorption was associative in nature, that

the adlayer formed hydrogen bonded clusters rather than uniform overlayers, and that these clusters showed vibrational spectra equivalent to that of bulk ice [7].

Similar findings were reported in a HREELS study of water adsorbed on HOPG at 85 K by Chakarov and co-workers [8, 9]. Loss features, typical of condensed water ice, were noted at 200 cm^{-1} (frustrated translation), 710 cm^{-1} (frustrated rotation), 1595 cm^{-1} (HOH scissors mode) and 3345 cm^{-1} (symmetric stretch). However, in contrast to Phelps and co-workers, a frequency shift was noted for increasing exposures of water. It was noted that the collective modes, such as the frustrated rotation, undergo a faster frequency shift than the intermolecular vibrations. This was identified as being indicative of a weak interaction with the surface and an increase in hydrogen bonding with increasing exposure. This led to clustering of water molecules and a Stranski-Krastanov growth mode of water ice on HOPG [9].

Chakarov and co-workers have also investigated the adsorption of water on HOPG using TPD [8, 9]. Water was observed to desorb molecularly in a single peak at 148 K, which increased in desorption temperature with increasing exposure. This peak could not be saturated and demonstrated a linear increase in peak area with increasing exposure, implying a constant sticking probability [8]. The peak showed characteristics of zero order desorption and was assigned to the sublimation of water ice with a desorption energy of 43.4 kJ mol^{-1}. This was described as either a strongly physisorbed or a very weakly chemisorbed species. Furthermore, a small percentage of water was noted to desorb as several small peaks at approximately 180 K. This was tentatively assigned to the desorption of intercalated water. Additionally, a series of isothermal TPD experiments were performed for varying water exposures. These involved ramping the surface temperature to 142 K at a constant rate and then holding the surface at that temperature. These experiments confirmed the observation of zero order desorption kinetics in bulk ice.

Isothermal TPD experiments have also been carried out to investigate the crystallisation kinetics of water on a HOPG surface [10, 11]. The structure of water adsorbed on a surface is highly dependent on the deposition conditions and the surface temperature. If

deposition occurs below 135 K, ice grows as amorphous solid water (ASW) [12-14], whose exact morphology depends on the dosing conditions [15, 16]. ASW has a glass transition temperature, T_g, at ~135 K [17, 18], above which it undergoes a phase transition to cubic crystalline ice (CI) [14, 19]. This phase transition has been reported to occur over a temperature interval from 130 to 160 K [11] and is accompanied by a reduction in vapour pressure (and hence desorption rate) by a factor of $3 - 10^0$ [10, 14, 20]. Isothermal TPD studies of water adsorbed on HOPG at ~100 K by Lofgren and co-workers [10, 11] have shown the transition of ASW to CI as a function of film thickness by monitoring the change in desorption rate associated with the transition. They also showed that water does not wet the surface but tends to form 3D droplets, which grow in size with increasing deposition [11].

Chakarov and co-workers have also investigated the photoinduced crystallisation of ASW on a HOPG surface. The ASW was irradiated with ultraviolet (UV) light and resulted in the formation of crystalline water [21]. This study was part of a larger study which investigated the effects of UV irradiation of co-adsorbed water and alkali metals on a HOPG surface [9, 21, 22].

A density functional theory (DFT) calculation has been performed by Sanfelix and co-workers concerning the structure of water on a graphite (0001) surface [23]. This study showed that water molecules were physisorbed on the surface at all coverages, lying at least 3.5 Å above the surface. It was also inferred that, at low coverages, water molecules showed little preference for orientation. However as the coverage was increased the water showed a preference for orientation of molecules such that the dipole was parallel to the surface. Further increases in coverage led to the formation of extended ice-like layers.

4.2 Experimental

All experiments were performed in the UHV chamber described in *Chapter 2*. Sample cleanness was achieved using the techniques described in *Chapter 3*. RAIRS and TPD experiments investigating the adsorption of water (distilled, deionised water) were

performed by back filling the chamber via a high precision leak valve, in a controlled manner. All exposures are measured in Langmuir (L), where an exposure of 1 L is equivalent to back filling the chamber to a pressure of 1×10^{-6} mbar for 1 second. Exposures were not corrected for ion gauge sensitivity. Both RAIRS and TPD experiments were performed as already described in *Chapter 3*. All TPD spectra were recorded at a heating rate of 0.50 (± 0.01) K s^{-1}. For isothermal TPD experiments the sample was heated to 142 K at 0.5 K s^{-1} and then held constant at that temperature until no further desorbing species were observed with the mass spectrometer.

4.3 Results and Discussion

4.3.1 TPD Results

A series of TPD spectra for increasing exposures of water on HOPG at 92 K are shown in *Figures 4.1*, *4.2* and *4.3*. At the lowest exposures, between 0.04 L and 0.3 L, a single peak is observed, *Peak A*. As the exposure is increased, between 0.04 L and 0.3 L, this peak shifts up in desorption temperature from approximately 132 K up to 138 K. Further increase in exposure leads to the appearance of a second peak, *Peak B*, initially as a shoulder on *Peak A*, at 146 K (*Figure 4.1*). For a 2 L exposure *Peak B* can be clearly distinguished from *Peak A* and is the dominant species in the spectrum (*Figure 4.1*). Increasing the exposure to 7 L and through to 15 L leads to *Peak B* dominating *Peak A* until the two peaks can no longer be distinguished from each other (*Figure 4.2*). This combined peak, labelled as *Peak B'*, shifts up in desorption temperature with increasing coverage.

At the highest recorded exposures, *Peak B'* continues to shift up in desorption temperature with increasing exposure, with a desorption temperature of 164 K for a 275 L exposure (*Figure 4.3*). This peak cannot be saturated with increasing exposure and is the dominant feature in the desorption spectra (*Figure 4.3*). *Figure 4.3* shows two further desorption features labelled *Peaks C* and *D*. *Peak C* is seen following exposures of 50 L upwards and is a distinctive bump on the low temperature side of *Peak B'*. It is particularly prominent in spectra following exposures of 100 and 275 L, with a

desorption temperature of 152 K. Similarly, *Peak D* is observed following exposures of 50 L and above. *Peak D* is initially observed as a tail on *Peak B'* following a 50 L exposure, but is a distinct peak following exposures of 100 L and 275 L. This peak increases in intensity and shifts to higher desorption temperatures as the exposure is increased. Once again this peak could not be saturated with increasing exposure.

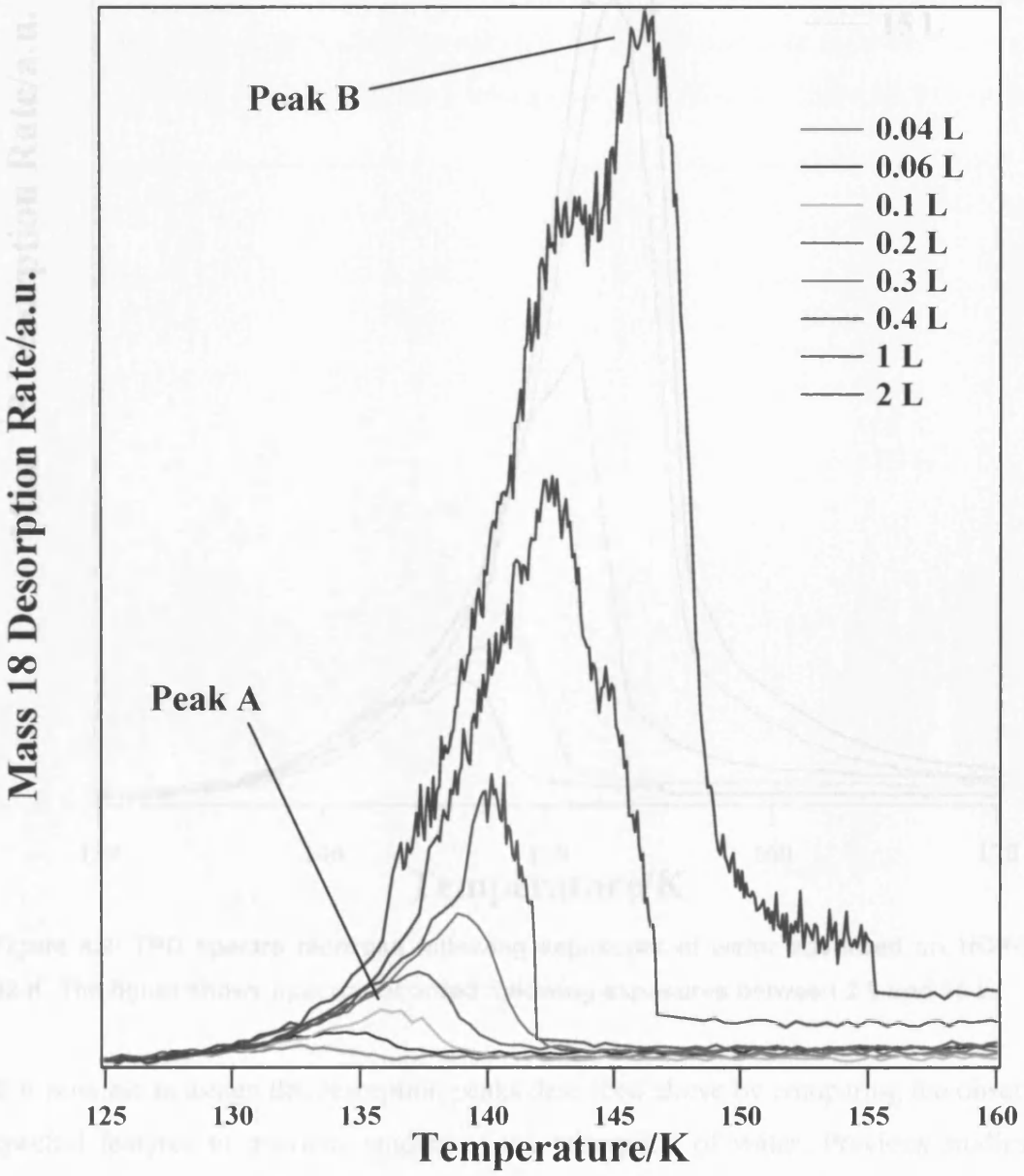

Figure 4.1: TPD spectra recorded following exposures of water adsorbed on HOPG at 92 K. The figure shows spectra recorded following exposures between 0.04 L and 2 L.

desorption temperature of 152 K. Similarly, *Peak D* is observed following exposures of 50 L and above. *Peak D* is initially observed as a tail on *Peak B'* following a 50 L exposure, but is a distinct peak following exposures of 100 L and 275 L. This peak increases in intensity and shifts to higher desorption temperatures as the exposure is increased. Once again this peak could not be saturated with increasing exposure.

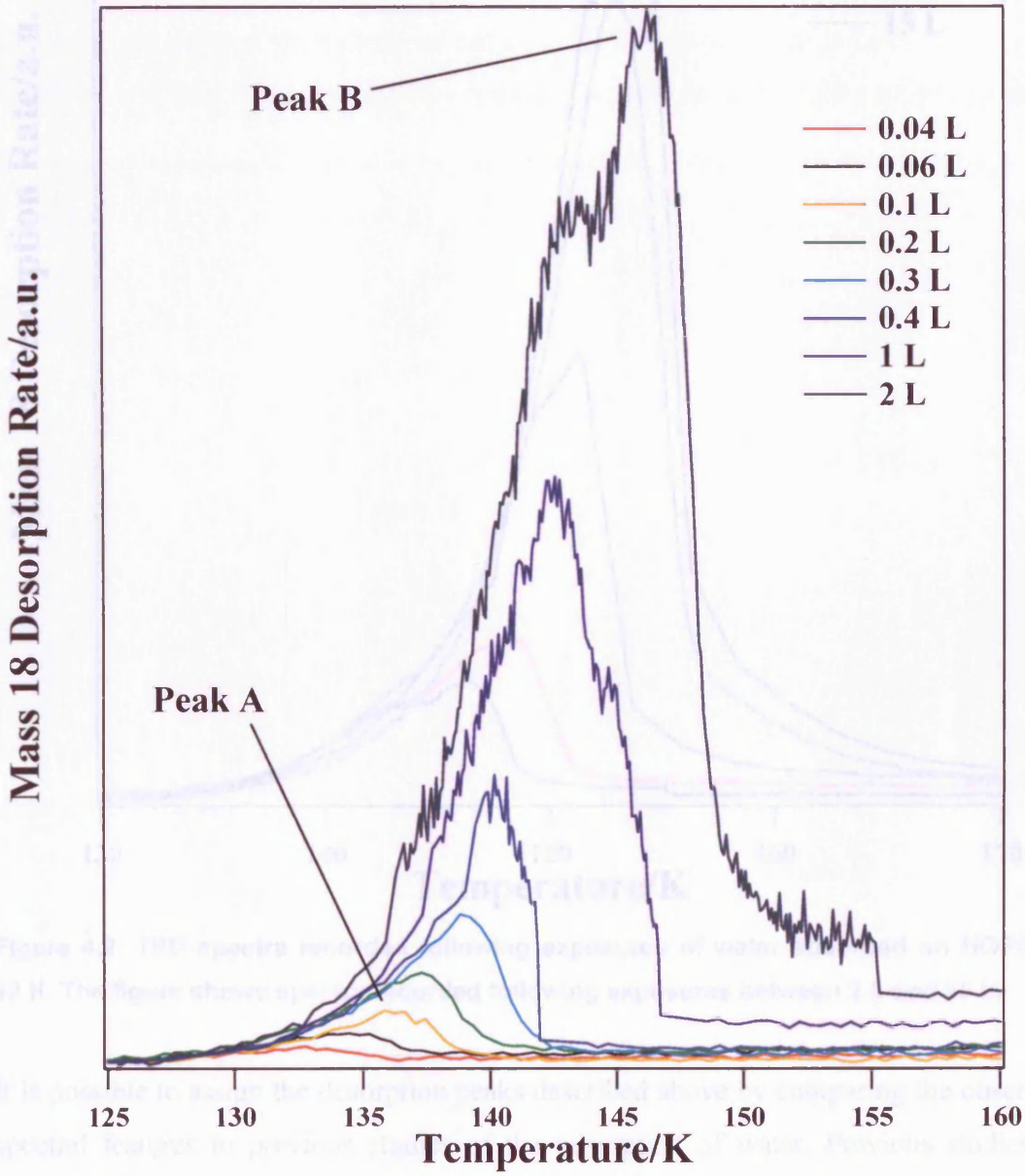

Figure 4.1: TPD spectra recorded following exposures of water adsorbed on HOPG at 92 K. The figure shows spectra recorded following exposures between 0.04 L and 2 L.

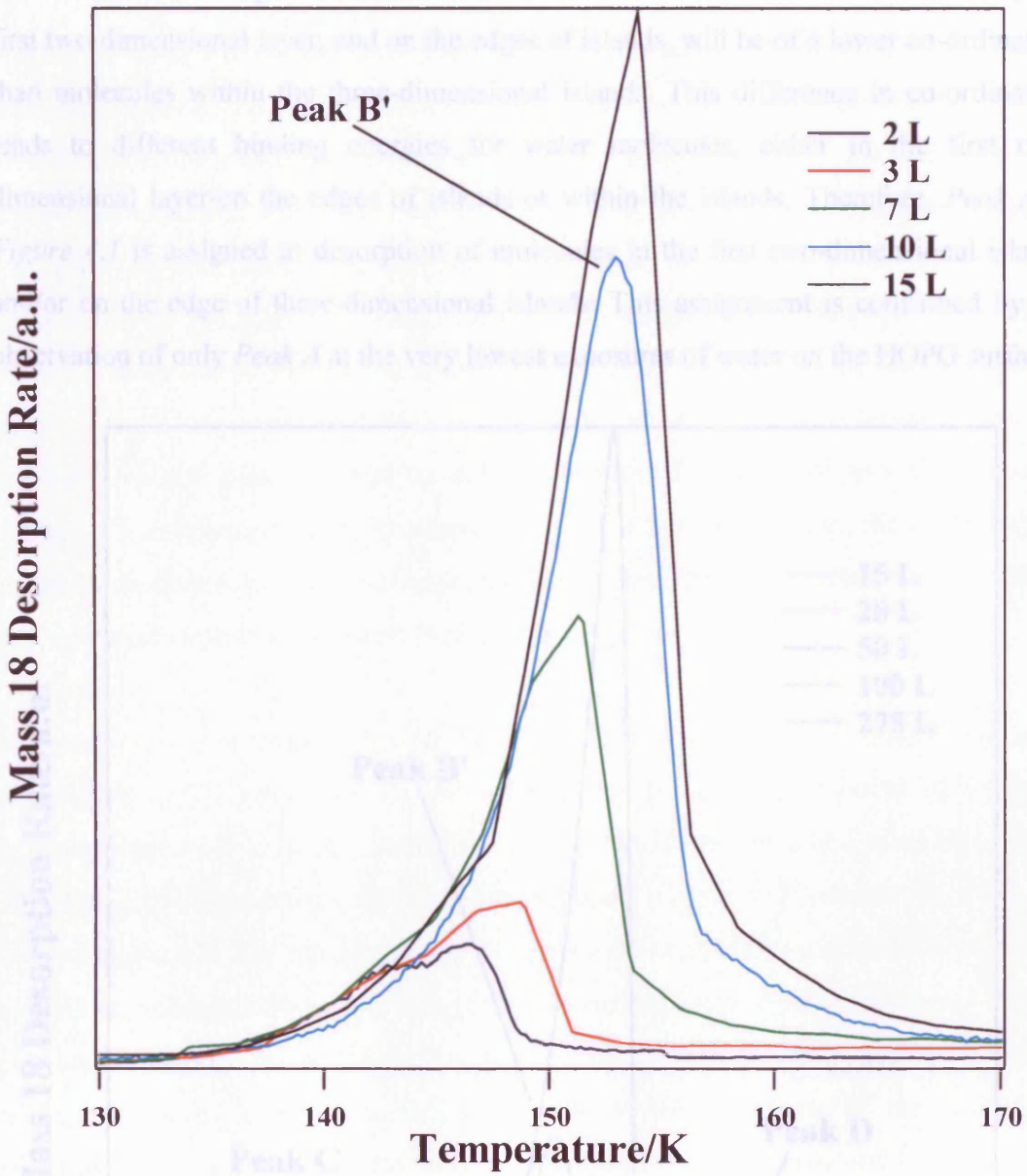

Figure 4.2: TPD spectra recorded following exposures of water adsorbed on HOPG at 92 K. The figure shows spectra recorded following exposures between 2 L and 15 L.

It is possible to assign the desorption peaks described above by comparing the observed spectral features to previous studies of the adsorption of water. Previous studies of water adsorption on HOPG [8, 9, 21] have shown a cluster growth mechanism of ice layers. In Stranski-Krastanov growth, initial growth is layer by layer, but at some point the ordered sequence, where complete layers form, gives way to the formation of bulk crystallites [24]. With this growth mode, island formation can occur. This results in

water molecules being bonded in two different co-ordinations. Water molecules in the first two-dimensional layer, and on the edges of islands, will be of a lower co-ordination than molecules within the three-dimensional islands. This difference in co-ordination leads to different binding energies for water molecules, either in the first two-dimensional layer/on the edges of islands or within the islands. Therefore, *Peak A* in *Figure 4.1* is assigned to desorption of molecules in the first two-dimensional islands and/or on the edge of three-dimensional islands. This assignment is confirmed by the observation of only *Peak A* at the very lowest exposures of water on the HOPG surface.

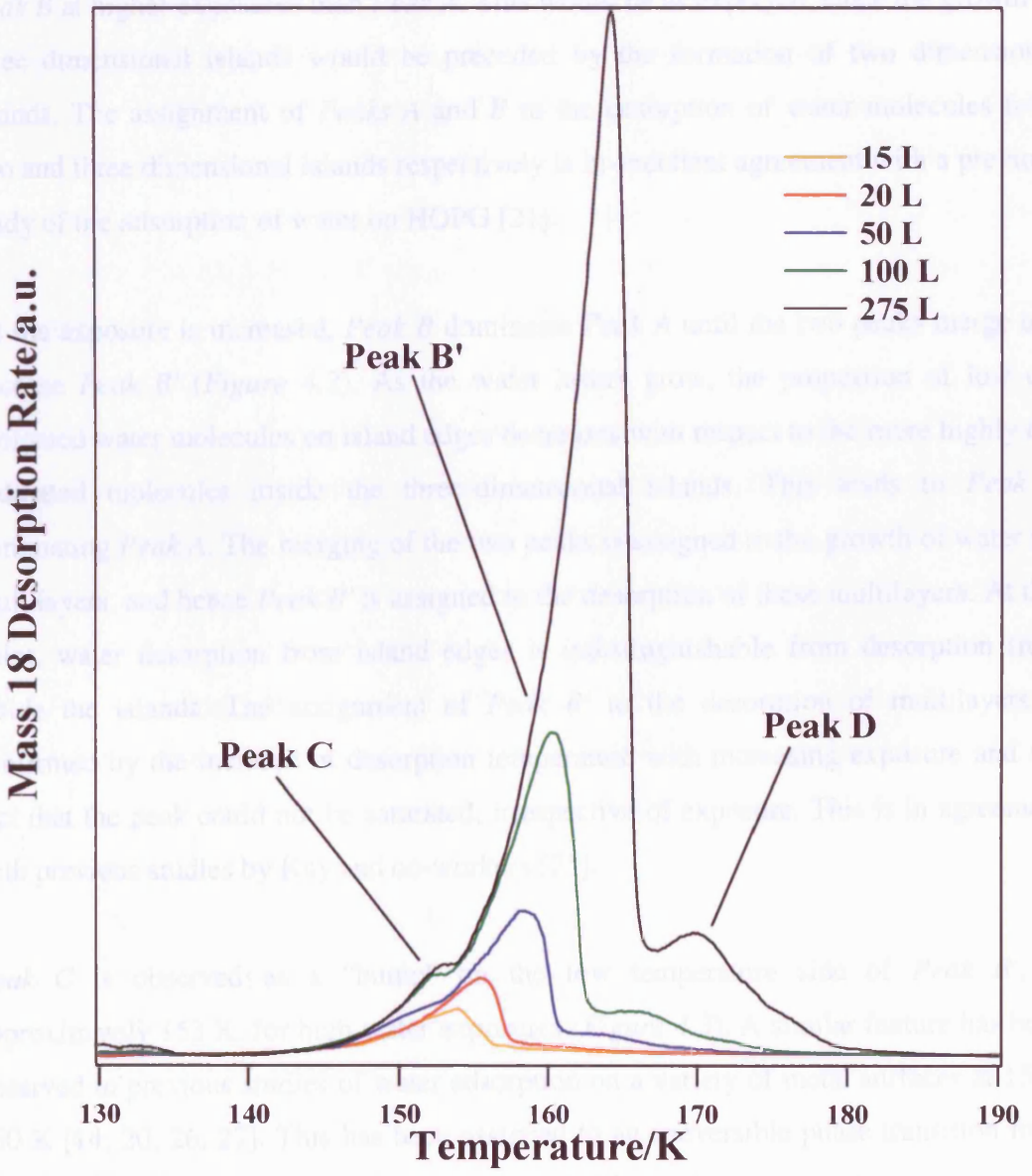

Figure 4.3: TPD spectra recorded following exposures of water adsorbed on HOPG at 92 K. The figure shows spectra recorded following exposures between 15 L and 275 L.

Peak B is assigned to the desorption of water molecules from within the three dimensional islands i.e. from multilayers of water. As previously mentioned, water molecules within the islands are more highly co-ordinated than water molecules on the edges of islands, and would therefore be expected to have a higher desorption energy and hence higher desorption temperature. *Peak B* has a desorption temperature approximately 6 K higher than *Peak A* and can be assigned to the desorption of water molecules from within the islands. This assignment is confirmed by the appearance of *Peak B* at higher exposures than *Peak A*. This would be as expected, since the growth of three dimensional islands would be preceded by the formation of two dimensional islands. The assignment of *Peaks A* and *B* to the desorption of water molecules from two and three dimensional islands respectively is in excellent agreement with a previous study of the adsorption of water on HOPG [21].

As the exposure is increased, *Peak B* dominates *Peak A* until the two peaks merge and become *Peak B'* (*Figure 4.2*). As the water layers grow, the proportion of low co-ordinated water molecules on island edges decreases with respect to the more highly co-ordinated molecules inside the three-dimensional islands. This leads to *Peak B* dominating *Peak A*. The merging of the two peaks is assigned to the growth of water ice multilayers, and hence *Peak B'* is assigned to the desorption of these multilayers. At this point, water desorption from island edges is indistinguishable from desorption from inside the islands. The assignment of *Peak B'* to the desorption of multilayers is confirmed by the increase in desorption temperature with increasing exposure and the fact that the peak could not be saturated, irrespective of exposure. This is in agreement with previous studies by Kay and co-workers [25].

Peak C is observed as a "bump" on the low temperature side of *Peak B'*, at approximately 153 K, for high water exposures (*Figure 4.3*). A similar feature has been observed in previous studies of water adsorption on a variety of metal surfaces at 150 - 160 K [14, 20, 26, 27]. This has been assigned to an irreversible phase transition from ASW to CI. The phase transition is accompanied by a change in vapour pressure and hence a change in the desorption rate which manifests itself as a "bump" in the TPD

spectra. The phase transition from ASW to CI is a direct consequence of the temperature ramp applied during the TPD process. The phase transition is believed to occur for all exposures in which multilayers are present, however can only be observed for exposures above 50 L using the experimental ramp rate (0.5 K s^{-1}). For exposures below 50 L, the water adlayer is completely converted from ASW to CI in a timescale comparable to the experimental ramp, hence no "bump" is observed. For exposures greater than 50 L, some desorption occurs from the residual ASW, that has not undergone a phase change in the timescale of the TPD experiments. Similar findings have been reported by Dohnalek and co-workers [28]. It should be possible to observe the phase transition at the lower exposures if a faster ramp rate was used in the experiment. This has previously been shown by Smith and co-workers, who clearly observed the ASW "bump" in their spectra [29]. The phase transition from ASW to CI has not been observed in previous TPD studies of water adsorption on HOPG. However, these studies involved films of water ice that were too thin for the transition to be observed [8, 21].

To confirm the assignment of *Peak C* to the phase transition from ASW to CI, a series of experiments were carried out in which water was adsorbed on HOPG as a function of sample temperature. If water is adsorbed on a surface held above T_g, the adlayer will be CI in structure. Hence, spectra recorded following adsorption above T_g would not show the "bump" (*Peak C*) seen in *Figure 4.3*. *Figure 4.4* shows TPD spectra recorded following 100 L exposures of water on HOPG, with the sample held at 100 K and at 130 K. It can clearly be seen that adsorption at 130 K leads to the loss of the "bump" attributed to ASW. Note that the desorption spectra shown in *Figure 4.4* are shifted up in temperature with respect to the spectra shown in *Figure 4.3*. This is due to the different heating rate used in the TPD experiments shown in *Figure 4.4* (1 K s^{-1}) compared to the spectra shown in *Figure 4.3* (0.5 K s^{-1}).

The appearance of *Peak D* in *Figure 4.3* has not been observed in any previous TPD studies of the adsorption of water on HOPG. *Peak D* is only observed for exposures greater than 50 L and is assigned to a further phase transition from CI to hexagonal ice, HI. HI is the only naturally found stable form of ice and is formed at a temperature of

~200 K [30]. It is believed that HI is not formed upon adsorption of the water adlayer but is a result of the temperature ramp, applied in the TPD experiment.

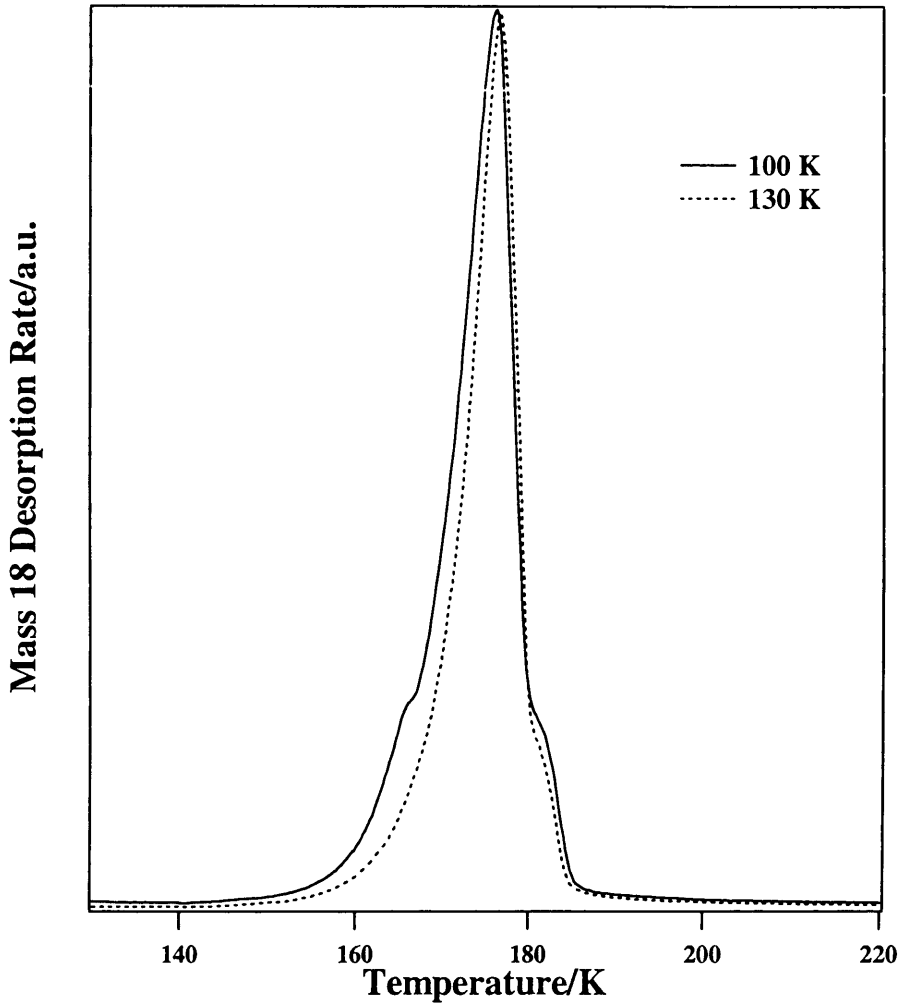

Figure 4.4: TPD spectra recorded following a 100 L exposure of water on HOPG as a function of sample temperature.

4.3.2 RAIRS Results

In order to gain a clearer understanding of the crystallisation of ASW to CI, RAIRS experiments were also performed. RAIR spectra following adsorption of water on the HOPG sample at 100 K are shown in *Figure 4.5*. At low exposures, no spectral features are observed. This is in direct contrast to the TPD spectra shown in *Figures 4.1* and *4.2*, where desorption peaks are observed at low exposures (< 7 L). At an exposure of 11 L, a broad band is observed centred at a frequency of ~3405 cm^{-1} with a width of

~280 cm^{-1}. As the exposure is increased, this band grows in intensity but does not undergo a frequency shift. Following an exposure of 50 L this peak has broadened to approximately 450 cm^{-1} and appears to be developing into two peaks. This splitting of peaks is clearest in spectra following exposures of 100 L and 300 L of water. A shallow shoulder is also observed at ~3180 cm^{-1} for exposures greater than 100 L. Following a 300 L exposure, the region between 3100 cm^{-1} and 3600 cm^{-1} clearly shows three spectral features, as indicated in the bottom spectrum in *Figure 4.5*.

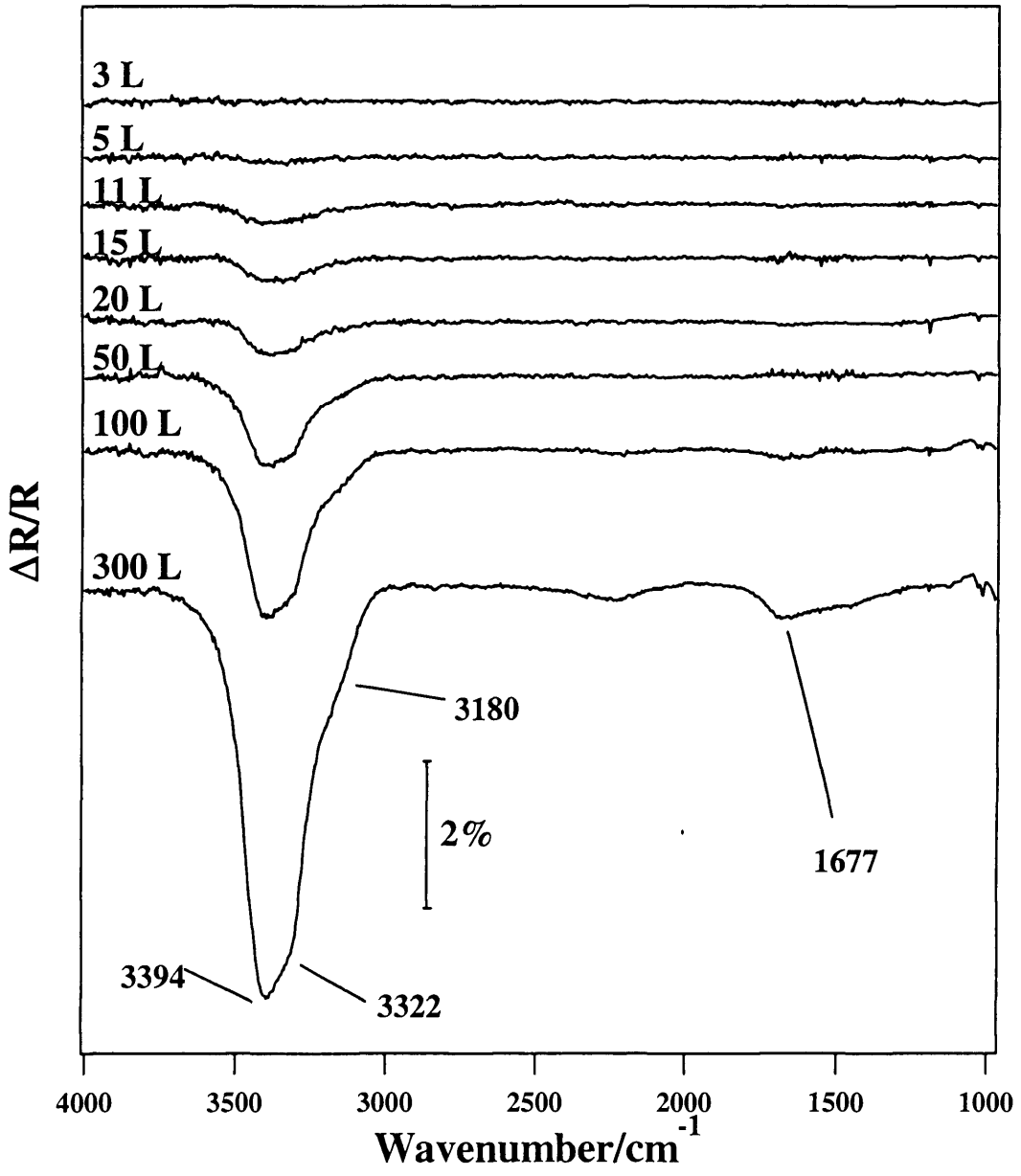

Figure 4.5: RAIR spectra of increasing exposures of water adsorbed on HOPG at 100 K. Exposures of water are indicated on the individual spectra.

A second feature is also observed at ~1677 cm^{-1} for exposures above 100 L. This feature is relatively low in intensity but can clearly be seen in the spectrum recorded following a 300 L exposure. A further increase in exposure leads to an increase in intensity of all features but does not lead to the observation of any additional bands. No frequency shift is observed for any of the vibrational features, nor is it possible to saturate any of the spectral features.

The bands observed in *Figure 4.5* can be assigned confidently by comparing the observed frequencies with previous studies of water adsorbed on HOPG at similar temperatures [7, 8]. The bands observed between 3100 and 3600 cm^{-1} are assigned to O-H stretching modes, and the band observed at 1677 cm^{-1} is assigned to the HOH scissors mode. The observed features are comparable to those recorded for multilayer water adsorbed on a variety of metal surfaces and for solid water [1] (*and references therein*). Hence, the spectral features shown in *Figure 4.5* are assigned to physisorbed multilayers of water-ice. The multilayers of water are believed to exist in hydrogen bonded networks, which is demonstrated by the broadness of the O-H stretching bands shown in *Figure 4.5*. Broad O-H stretching bands have previously been observed for hydrogen bonded networks of water multilayers adsorbed on a variety of surfaces [1, 2].

The assignment of the vibrational features observed in *Figure 4.5* to water multilayers is confirmed by the TPD spectra presented in *Figures 4.2* and *4.3*. The TPD spectra show that at comparable exposures (> 11 L) the TPD peaks observed are due to the desorption of multilayers of water. Note that the island growth observed in the TPD spectra could not be observed in the RAIR spectra shown here. Previous vibrational studies of island growth of water on HOPG have been performed using EELS [8, 9] and have followed the frequency shift of the frustrated rotational and frustrated translational modes. However, these modes are too low in frequency to be observed with the RAIRS set-up described in this thesis.

It is possible to determine the phase of water present on the surface by monitoring the appearance of the O-H stretch [31-33]. The shape and structure of the vibrational band alters, depending on whether the water is ASW or CI in nature. The shape of the O-H

stretch shown in the bottom spectrum in *Figure 4.5* is in excellent agreement with previous spectra recorded of ASW on Cu{110} [32] and on Pt{533} [33]. Previous RAIRS studies of the O-H stretching region of ASW have generally shown a broad feature with two distinct peaks and a shallow shoulder [32, 33]. The shoulder is observed on the low frequency side of the peaks, and the lower frequency peak is less intense than the higher frequency peak. The two peaks are separated by ~90 cm^{-1}. All of these characteristics are clearly shown in the bottom spectrum in *Figure 4.5*, hence the water adlayer is assigned as ASW. It should be noted that the TPD spectra shown in *Figures 4.1* to *4.3* appear to contradict this assignment since the majority of the adlayer desorbs as the CI peak. However, this anomaly can be explained by the TPD process itself, which converts the ASW to CI.

In order to observe the phase change from ASW to CI, experiments were performed where multilayers of water adsorbed on HOPG were annealed to various temperatures. *Figure 4.6* shows a series of spectra resulting from the annealing of the adsorbed water layer (300 L exposure) to various temperatures. Annealing the adlayer causes a marked change in the appearance of the bands in the O-H stretching region, which is discussed in depth later.

No changes in the spectra were observed following annealing to temperatures between 100 K and 135 K. No additional spectral bands are observed when the adlayer is annealed. Annealing the adlayer to 165 K leads to a significant loss in intensity in both the O-H stretching region and the HOH scissors mode, implying desorption of the water adlayer. All spectral features have disappeared by 175 K, implying complete desorption of the water adlayer. This desorption temperature is in agreement with the desorption temperature of water multilayers in the TPD study shown above, confirming the observation of multilayers of water in the RAIR spectra.

Figure 4.7 shows a close up of the O-H stretching region of a series of RAIR spectra resulting from the annealing of a water adlayer (300 L exposure) to various temperatures.

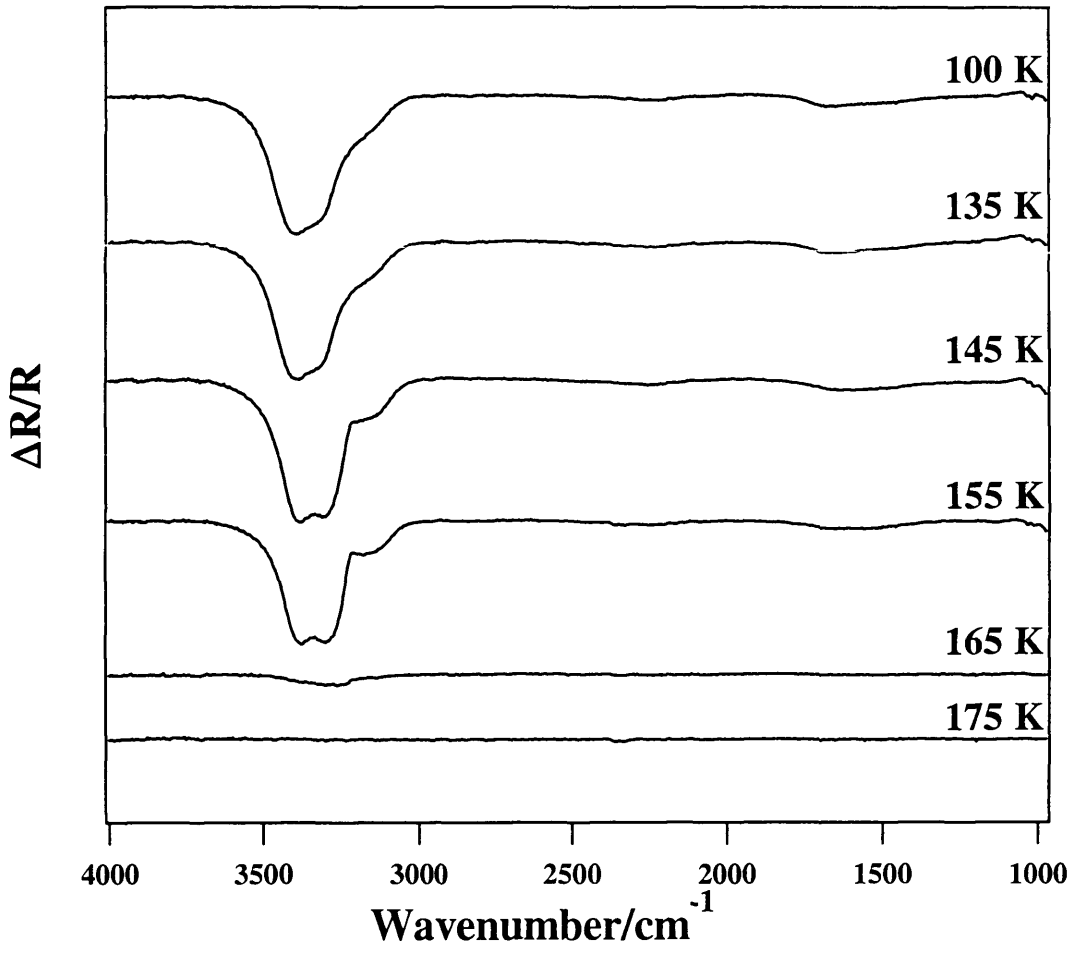

Figure 4.6: RAIR spectra showing the sequential heating of a water adlayer (300 L exposure) adsorbed on HOPG at 100 K. The temperatures to which the water adlayer was annealed are indicated on the individual spectra.

Annealing the adlayer from 100 K to 155 K causes a marked change both in the shape and structure of the O-H stretching mode. This change in shape is also accompanied by a slight down shift (~20 cm^{-1}) in frequency of the entire spectral feature. Annealing the adlayer to 135 K leads to the two peaks observed at 3394 cm^{-1} (*Peak Y*) and 3322 cm^{-1} (*Peak Z*) becoming more pronounced and distinct. Note that following both adsorption at 100 K and annealing to 135 K, *Peak Z* has approximately 90% of the amplitude of *Peak Y*. Further annealing to 145 K leads to a clear separation of the peaks and a change in the ratio of the amplitudes of the two peaks, so that the amplitude of *Peak Z* is 94% of the amplitude of *Peak Y*. This trend continues as the adlayer is annealed to 155 K when the two peaks become almost comparable in amplitude (*Peak Z* has an amplitude

of 98% of *Peak Y*). This change in amplitude of *Peak Z* with respect to *Peak Y*, as a function of annealing temperature, is shown in *Figure 4.8*. Additionally, the low frequency shoulder at 3180 cm^{-1} becomes more pronounced when the adlayer is annealed. Annealing the adlayer to 165 K and above leads to a loss in the vibrational feature since the water adlayer desorbs at this temperature.

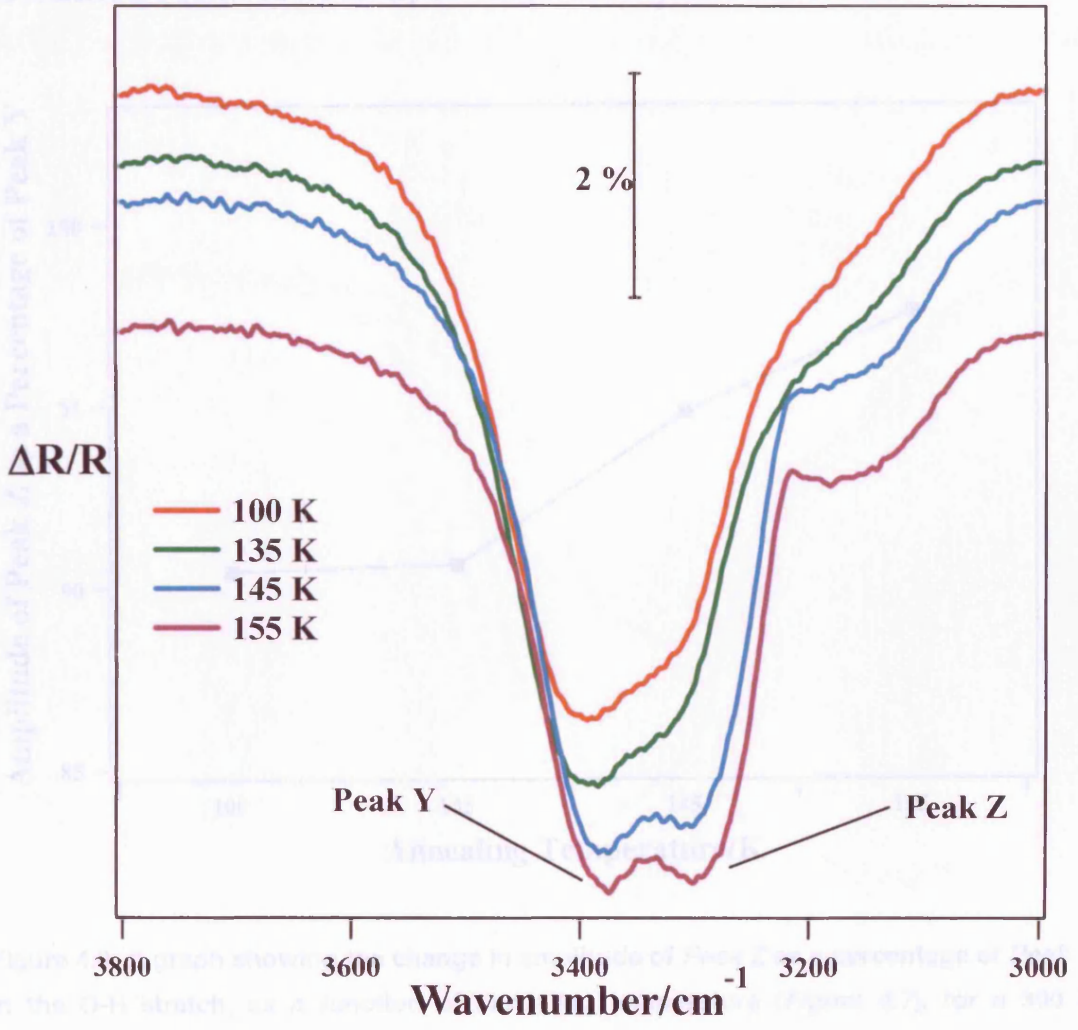

Figure 4.7: RAIR spectra between 3000 cm^{-1} and 3800 cm^{-1} showing the sequential heating of a 300 L water adlayer adsorbed on HOPG at 100 K.

To complement the annealing experiments, and to test this hypothesis further, RAIRS experiments were also carried out to determine the effect of adsorption temperature on the water layer adsorbed on HOPG. *Figure 4.9* shows the effect of adsorption

temperature on a 300 L exposure of water on HOPG in the O-H stretching region. The only other vibrational feature observed in the spectrum is the HOH scissors mode at approximately 1615 cm^{-1}. This band does not change in frequency as a function of adsorption temperature, but loses intensity with increasing temperature. The HOH scissors mode cannot be observed for spectra recorded following adsorption above 145 K. No additional spectral features are observed at any adsorption temperature, and no features are observed for adsorption temperatures greater than 150 K.

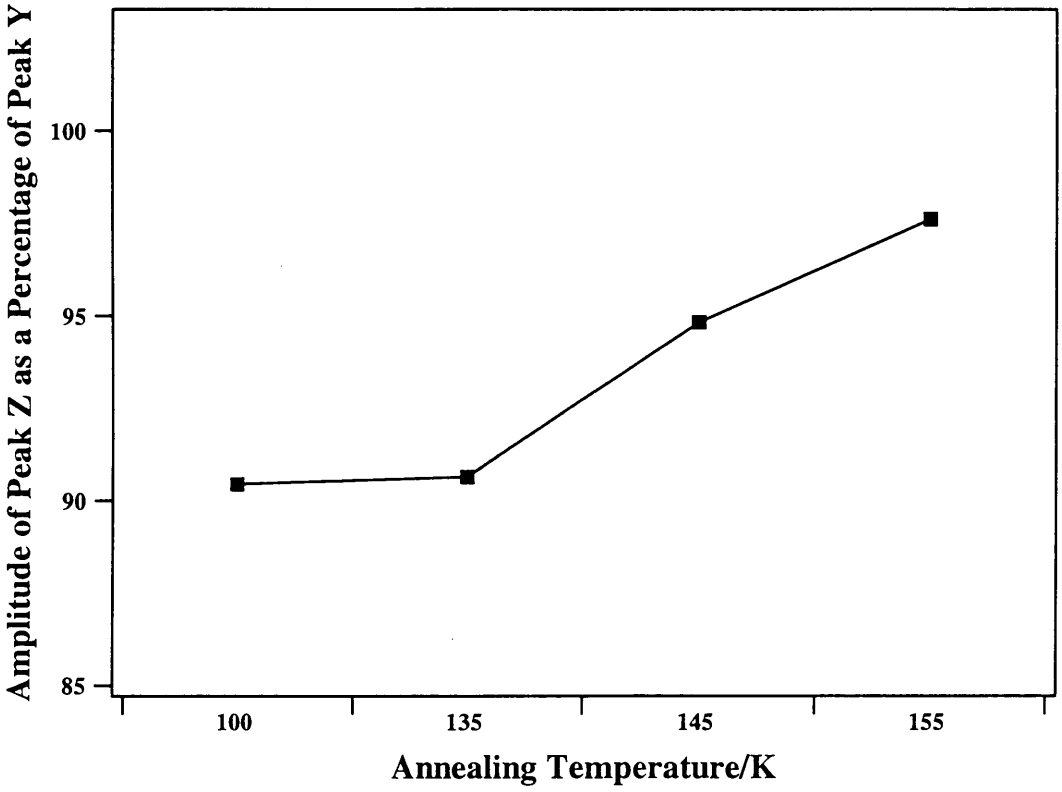

Figure 4.8: A graph showing the change in amplitude of *Peak Z* as a percentage of *Peak Y* in the O-H stretch, as a function of annealing temperature (*Figure 4.7*), for a 300 L exposure of water on HOPG.

Figure 4.9 shows that the adsorption temperature has a marked effect on the shape and structure of the O-H stretch. An increase in adsorption temperature leads to a down shift in the frequency of the two peaks at 3394 cm^{-1} and 3322 cm^{-1} by approximately 40 cm^{-1}. As previously mentioned, adsorption at 100 K leads to *Peak Z* having an amplitude approximately 90% of that of *Peak Y*. Adsorption at 130 K leads to a sharpening of the

two features, but does not alter the ratio between the amplitudes of the two peaks (*Figure 4.10*). Increasing the adsorption temperature to 145 K alters the amplitude ratio between *Peaks Y* and *Z* so that *Peak Z* has larger amplitude than *Peak Y*, and becomes the dominant peak within the O-H stretch. Further increasing the adsorption temperature to 150 K sees a continuation of this trend, with *Peak Z* now having an amplitude 30% greater than *Peak Y*. The change in the amplitude of *Peak Z* as a percentage of *Peak Y*, as a function of adsorption temperature, is shown in *Figure 4.10*. No change is observed in the low frequency shoulder at 3180 cm^{-1} as function of adsorption temperature.

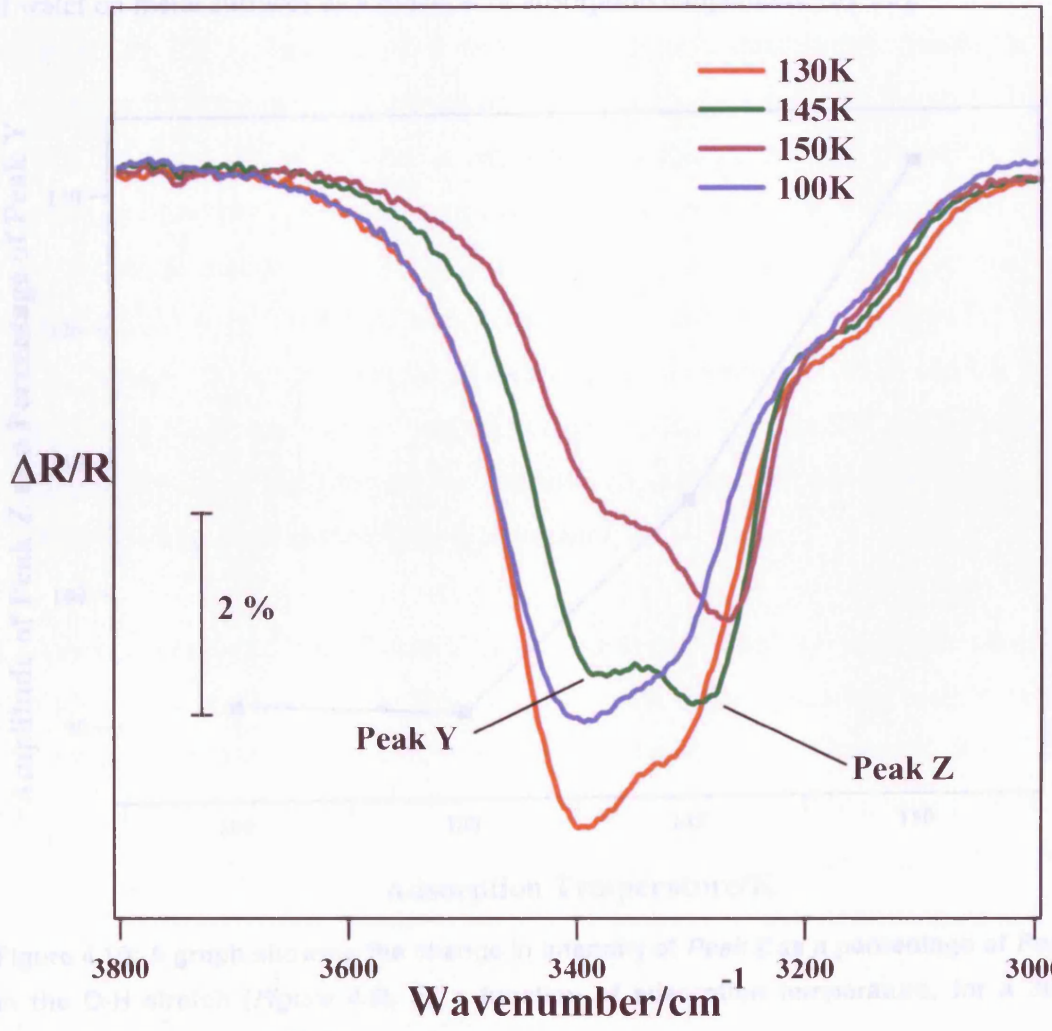

Figure 4.9: RAIR spectra between 3000 cm^{-1} and 3800 cm^{-1} recorded following a 300 L exposure of water on HOPG as a function of adsorption temperature.

As previously mentioned, water ice takes on an ASW structure below ~130 K and a CI structure above ~130 K. It has already been demonstrated that there is a marked change

in the shape and structure of the O-H stretching mode as a function of annealing and adsorption temperature. Hence, the changes observed in the spectra, shown in *Figures 4.7* and *4.9*, are assigned to the phase change from ASW to CI in the water adlayer. The spectra shown in *Figure 4.9* are assigned as ASW, CI or a combination of ASW and CI, depending on the adsorption temperature. Adsorption at 100 K and at 130 K results in the water taking on an ASW structure, while adsorption at 150 K results in a CI structure (*Figure 4.9*). Adsorption at 145 K leads to a mixture of both ASW and CI. These assignments are confirmed by comparison with previous studies of the adsorption of water on metal surfaces as a function of adsorption temperature [31-35].

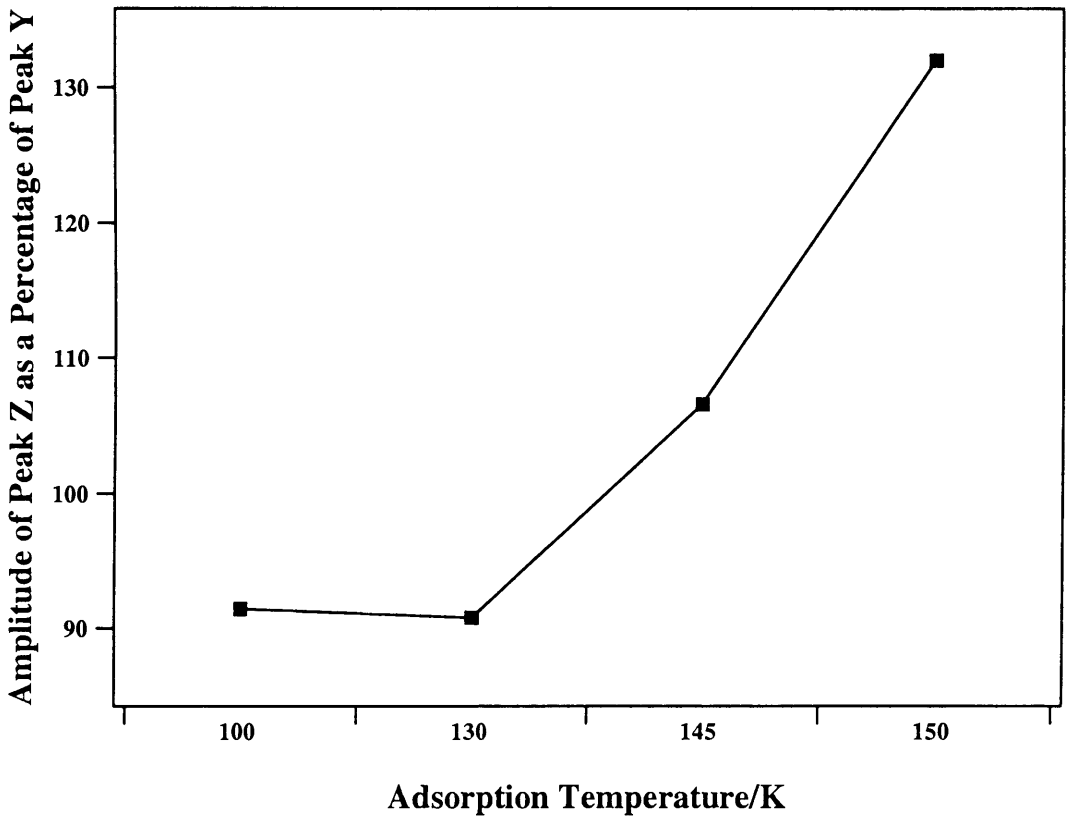

Figure 4.10: A graph showing the change in intensity of *Peak Z* as a percentage of *Peak Y* in the O-H stretch (*Figure 4.9*), as a function of adsorption temperature, for a 300 L exposure of water on HOPG.

It is clear by comparing *Figures 4.7* and *4.9* that annealing the water adlayer, adsorbed at 100 K, to a certain temperature does not lead to the same water structure as for adsorption at that temperature. This is in contrast to a previous study where RAIR

spectra obtained by dosing at a set temperature and those obtained by isothermal crystallisation of ASW dosed at 100 K were identical [33]. The apparent disagreement between the study by Backus and co-workers [33] and this study can be explained by considering how the experiments in this study were performed. The spectra shown in *Figure 4.9* were recorded following adsorption at a specified temperature with the sample held at that temperature throughout the adsorption process. In this manner the phase of the adlayer depends solely on the adsorption temperature. Hence the spectra shown in *Figure 4.9* are a true reflection of which phase of water is present on the surface. Alternatively, the spectra shown in *Figure 4.7* were recorded following adsorption at 100 K, heating the sample to the desired temperature, holding at that temperature for 3 minutes and then allowing the sample to cool back down to 100 K. Hence, the phase of the adlayer is dependent on the temperature to which it was annealed and for how long it was annealed. For these experiments, adsorption at 100 K leads to the formation of ASW and subsequent annealing to higher temperatures converts the ASW to CI. Hence, the spectra recorded following annealing to 145 K and 155 K (*Figure 4.7*) are believed to be indicative of a mixture of ASW and CI, rather than pure CI. This is a result of incomplete conversion of the ASW to CI during the annealing process. If the adlayer was annealed for longer, complete conversion from ASW to CI could occur at the higher temperatures.

A further difference between *Figures 4.7* and *4.9* is the manner in which the integrated intensity of the O-H stretching band changes with either annealing temperature or adsorption temperature. *Figure 4.11* shows how the integrated intensity of the O-H stretch changes as a function of adsorption temperature and annealing temperature. For spectra recorded following annealing, there is little change in the integrated intensity of the O-H stretching band between adsorption at 100 K and annealing to 145 K. Annealing to 155 K leads to a decrease in intensity and this is attributed to desorption of some of the adlayer. This continues with annealing to 165 K and desorption is completed by 175 K (shown in *Figure 4.5*). However, *Figure 4.11* shows that there is a marked difference in the integrated intensity of the peak as a function of adsorption temperature. An increase in integrated intensity occurs when the adsorption temperature is increased from 100 K to 130 K. This is attributed to the increased presence of CI,

which is more ordered than ASW, and hence would have more intense absorption features. As the adsorption temperature is increased to 145 K the overall intensity of the band decreases and further decreases as the adsorption temperature is increased to 155 K. This decrease in overall intensity is attributed to a reduction in sticking probability with increasing temperature, despite the increasing presence of CI.

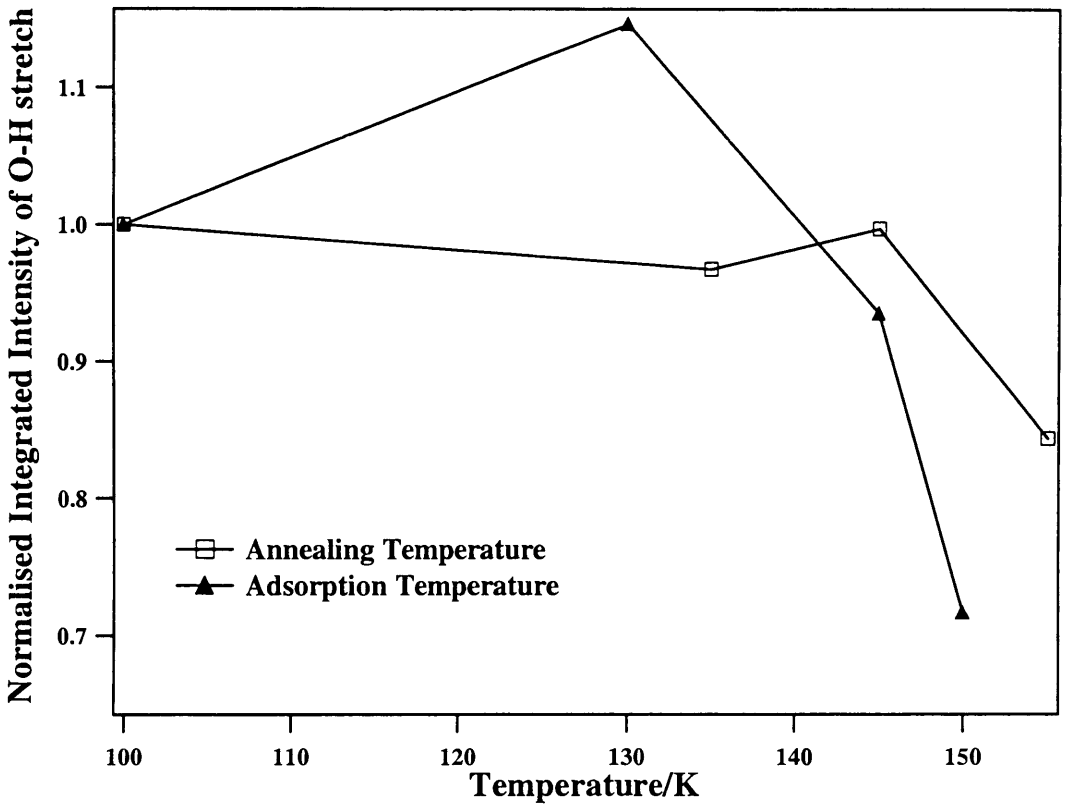

Figure 4.11: Graph showing the effect of adsorption temperature and annealing temperature on the normalised integrated intensity of the O-H stretch. The integrated intensities have been normalised against adsorption at 100 K.

4.3.3 Isothermal TPD Results

A series of isothermal TPD experiments have also been carried out so that a clearer understanding of the ASW to CI transition can be gained. Water was initially adsorbed on the HOPG surface at 93 K. The sample was then annealed to 142 K at 0.5 K s^{-1} and held at that temperature until the desorption signal from the QMS was comparable to the background signal. A temperature of 142 K was chosen in accordance with previous

isothermal TPD studies of water on HOPG [8, 10, 11]. *Figure 4.12* shows the isothermal TPD spectrum recorded following a 40 L exposure of water on HOPG. The spectrum is divided into three regions, labelled *A*, *B* and *C*. Initially there is an increase in the desorption rate as desorption of the adlayer takes place during both the initial temperature ramp and with the sample held at 142 K. The desorption rate then rapidly decreases. At approximately 190 s, the desorption rate slows down considerably. This marks the end of region *A*. The desorption rate then decreases slowly until 760 s, when the desorption rate changes drastically again. The region between 190 s and 760 s is labelled as region *B*. The final region of the spectrum, region *C*, signifies the final desorption of the remaining water adlayer.

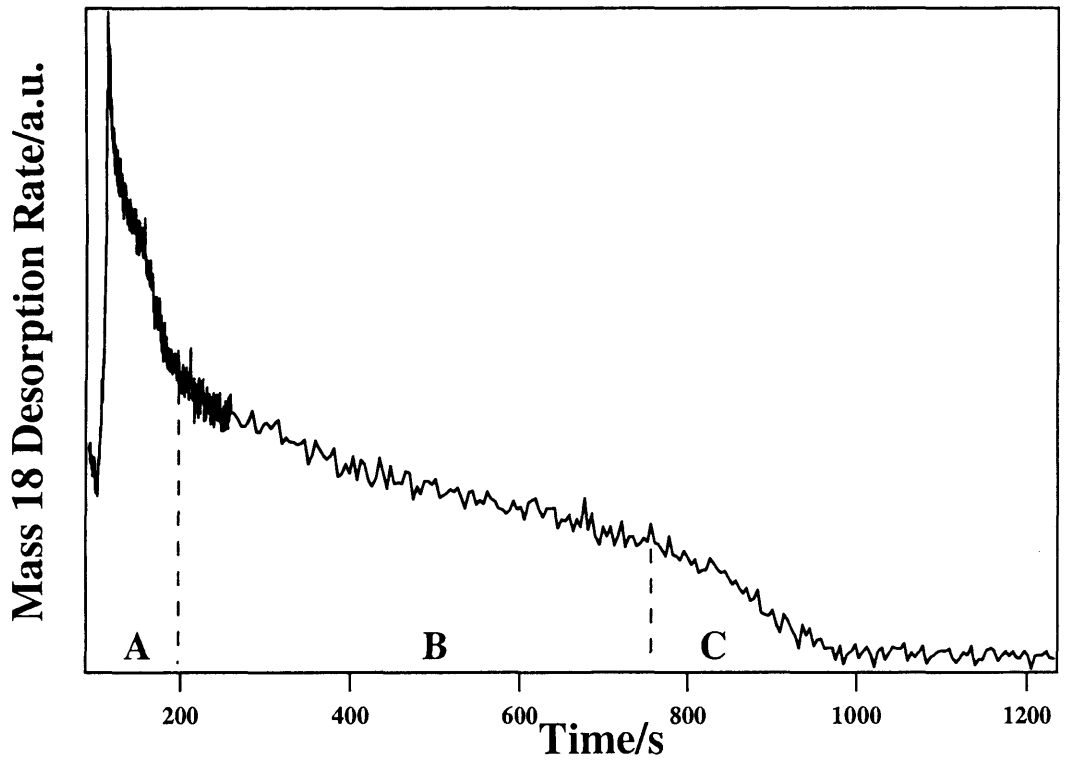

Figure 4.12: Isothermal TPD spectrum recorded following a 40 L exposure of water adsorbed on HOPG at 93 K. The sample was ramped to 142 K at 0.5 K s^{-1} and then held at that temperature. The spectrum is divided into 3 regions: region *A*, where ASW is converted to CI, region *B*, where the desorption of multilayers of CI occurs and region *C*, corresponding to the desorption of water islands and the appearance of bare patches on the HOPG surface.

It is possible to assign the three regions to different kinetic regimes by comparing *Figure 4.12* with previous isothermal TPD studies of water on HOPG [10, 11] and on single crystal metal surfaces [14]. It has been shown above that when water is adsorbed at 93 K the overlayer formed is ASW. In region *A*, two thermodynamically driven, parallel, processes are occurring in the ASW [11], namely the desorption of the ASW film and the crystallisation of ASW to CI. The initial high desorption rate observed in region *A* is a result of the high vapour pressure of the desorbing ASW compared to the CI. As crystallisation occurs, the rate of desorption rapidly decreases until the adlayer has been completely transformed from ASW to CI. This is equivalent to the "bump" observed in the TPD spectra shown in *Figure 4.3*. Once the phase change has occurred, the rate of desorption levels out to an almost constant value. This marks the end of region *A* and the onset of region *B*. Region *B* corresponds to the desorption of multilayers of the annealed adlayer, which are CI in structure. Note that, if desorption of the multilayer obeyed perfect zero order kinetics, the desorption rate would be constant in region *B* and a plateau would be observed. It is clear from *Figure 4.12* that this is not the case for the desorption of multilayers of water from HOPG. This will be confirmed later when the desorption order of multilayers of water from the HOPG surface is calculated.

Region *C* indicates the kinetic region where the water adlayer does not cover the whole surface. In this region, islands of water ice alternate with "bare" areas of the HOPG surface [10, 11]. Sublimation of the ice causes a monotonic decrease in island size and effective island surface area. This leads to the monotonic decrease in desorption rate observed in region *C*. Note that region *B* will only be observed if the water ice film is sufficiently thick for multilayers to form. If the ice film is not thick enough, region *A* will be followed directly by region *C*.

A series of isothermal TPD spectra for varying exposures, and hence film thickness, are shown in *Figure 4.13*. *Figure 4.13* clearly shows that region *A*, the time taken for the ASW to crystallise, increases with increasing film thickness. Previous isothermal TPD studies of the adsorption of water on HOPG and Pt{111} have shown that the time taken for crystallisation, τ, becomes independent of film thickness for sufficiently thick

films [11]. However, this was not observed for the adsorption of water on HOPG as shown in *Figure 4.13*. Note that for low exposures (6 L), region *A* is followed directly by region *C*. This implies that, for exposures 6 L, desorption of any multilayers takes place simultaneously with the crystallisation of the ASW. For exposures greater than 6 L, crystallisation takes place before all the multilayers have desorbed. It can also be seen in *Figure 4.13* that the desorption of water multilayers, region *B*, is not a perfect zero order process for thick ice multilayers as already seen in *Figure 4.12*. Region *B* has a downward slope for all coverages indicating a fractional order desorption process. This is confirmed in *Section 4.4.1*.

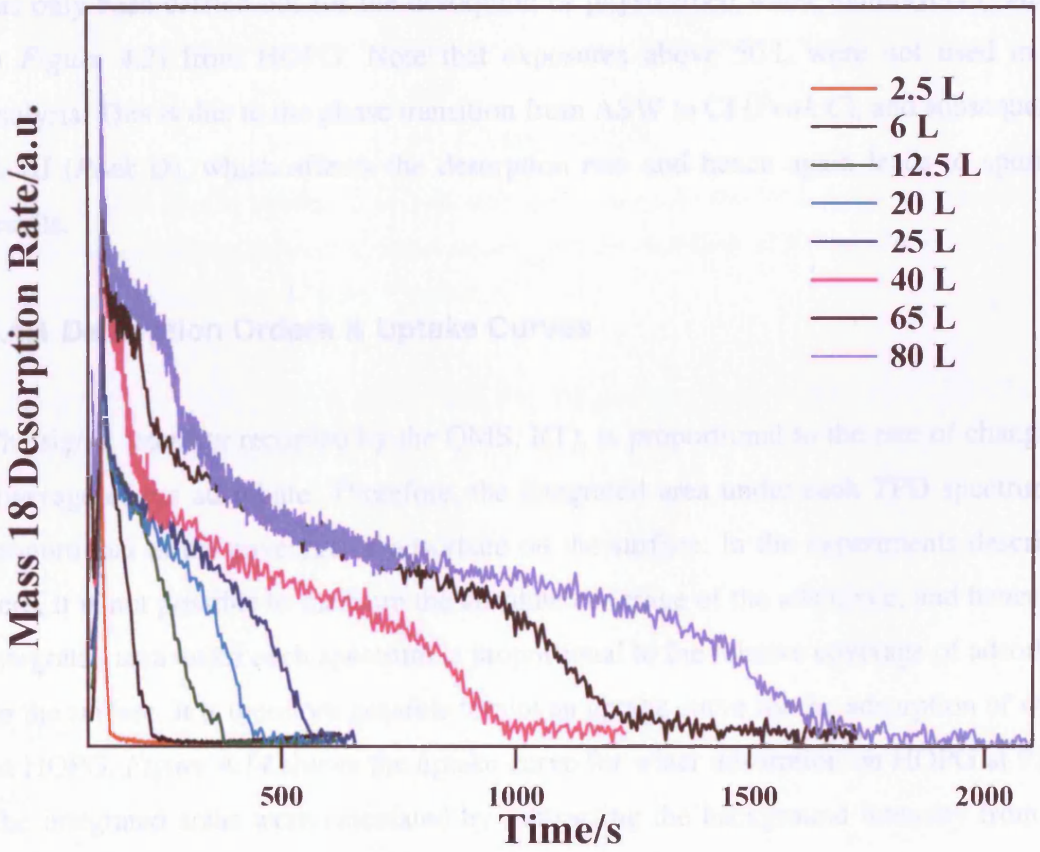

Figure 4.13: Isothermal TPD spectra recorded following various exposures of water adsorbed on HOPG at 93 K. The adlayer was ramped to 142 K at 0.5 K s^{-1} and then held constant at 142 K.

4.4 Quantitative Analysis of TPD Spectra

In order to acquire an understanding of the desorption kinetics of water adsorbed on HOPG, desorption orders, desorption energies and pre-exponential factors were calculated. These calculations used the TPD data shown in *Figures 4.1* to *4.3*. An attempt was made to separate the TPD spectra into contributions from *Peaks A* to *D* using a fitting programme, by simulating the spectra, in order to confirm the assignments made in *Section 4.3.1*. However, the quality of the fits was deemed insufficient. An attempt was also made to carry out analysis for *Peak A* alone, but this led to spurious results due to an insufficient number of data points. Therefore analysis has only been carried out for the desorption of physisorbed water multilayers (*Peak B'* in *Figure 4.2*) from HOPG. Note that exposures above 50 L were not used in the analysis. This is due to the phase transition from ASW to CI (*Peak C*), and subsequently to HI (*Peak* D), which affects the desorption rate and hence again leads to spurious results.

4.4.1 Desorption Orders & Uptake Curves

The signal intensity recorded by the QMS, I(T), is proportional to the rate of change of coverage of the adsorbate. Therefore, the integrated area under each TPD spectrum is proportional to the coverage of adsorbate on the surface. In the experiments described here, it is not possible to measure the absolute coverage of the adsorbate, and hence the integrated area under each spectrum is proportional to the relative coverage of adsorbate on the surface. It is therefore possible to plot an uptake curve for the adsorption of water on HOPG. *Figure 4.14* shows the uptake curve for water adsorption on HOPG at 92 K. The integrated areas were calculated by subtracting the background intensity from the spectrum and using the trapezium rule over a temperature range where the peak intensity is appreciable. Note that *Figure 4.14* uses the data from all TPD curves shown in *Figures 4.1* to *4.3*. The data in *Figure 4.14* can be fitted with a single straight line with an R^2 value of 0.999, indicating a constant sticking probability for physisorbed water adsorbed on HOPG at 92 K.

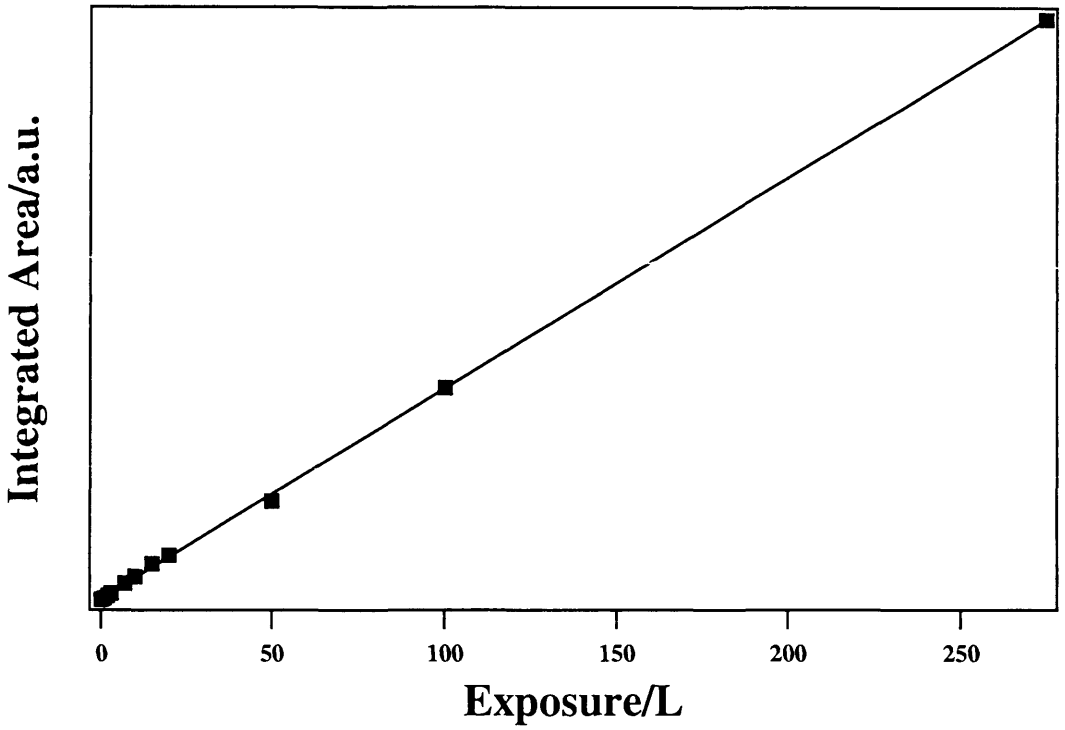

Figure 4.14: A graph showing, as a function of exposure, the total integrated area of the TPD curves obtained following water adsorption on HOPG at 92 K. The data can be fitted by a single straight line with an R^2 value of 0.999.

The desorption order can be calculated for the desorption of water from HOPG using the Polanyi-Wigner equation [36]:

$$r_{des} = -\frac{\partial\theta}{\partial t} = \upsilon_n \theta^n \exp\left[\frac{-E_{des}}{RT_S}\right] \qquad \textit{Equation 4.1}$$

where r_{des} is the rate of desorption, or the rate of change of coverage as a function of time, υ_n is the pre-exponential factor of the desorption process of order n, θ is the coverage, E_{des} is the desorption activation energy, R is the gas constant and T_s is the surface temperature. The rate of change of coverage with respect to time can be linked to the rate of change of coverage with respect to temperature via the heating rate during the TPD experiment, β.

$$\frac{\partial\theta}{\partial t} = \frac{\partial\theta}{\partial T}\frac{\partial T}{\partial t} = \frac{\partial\theta}{\partial T}\beta \qquad \textit{Equation 4.2}$$

Since the heating rate is constant, *Equation 4.2* becomes

$$\frac{\partial\theta}{\partial t} \propto \frac{\partial\theta}{\partial T} \qquad \textit{Equation 4.3}$$

In TPD studies, the rate of change of coverage with respect to temperature is proportional to the intensity of the measured TPD trace, *I(T)*.

$$I(T) \propto \frac{\partial\theta}{\partial T} \qquad \textit{Equation 4.4}$$

It is not possible to measure an absolute coverage in the experiments described here, however a relative coverage can be obtained. Hence *Equation 4.1* now becomes

$$I(T) \propto \upsilon_n \theta_{rel}^n \exp\left[\frac{-E_{des}}{RT_S}\right] \qquad \textit{Equation 4.5}$$

Re-arranging and taking logs of *Equation 4.5* leads to

$$\ln[I(T)] \propto n\ln[\upsilon_n\theta_{rel}] - \frac{E_{des}}{RT_s} \qquad \textit{Equation 4.6}$$

Desorption orders, and hence a confirmation of the peak assignments, can be obtained from *Equation 4.6* by plotting a graph of $\ln[I(T)]$ against $\ln[\theta_{rel}]$ at a fixed temperature, T_x. The gradient of such a plot is *n*, the order of desorption [36]. Note that it has been assumed that the pre-exponential factor does not vary with coverage or temperature, since all of the adsorbed water is physisorbed on the surface. Furthermore, it has also been assumed that the desorption energy does not vary with coverage or temperature. The validity of these assumptions will be demonstrated later. *Figure 4.15* shows a plot

of $\ln[I(T)]_x$ against $\ln[\theta_{rel}]_x$ for a T_x of 148 K for water adsorption on HOPG at 92 K. This process was repeated for a range of fixed temperatures and the gradients obtained from the plots, and hence desorption orders, for multilayers of water ice adsorbed on HOPG are given in *Table 4.1*.

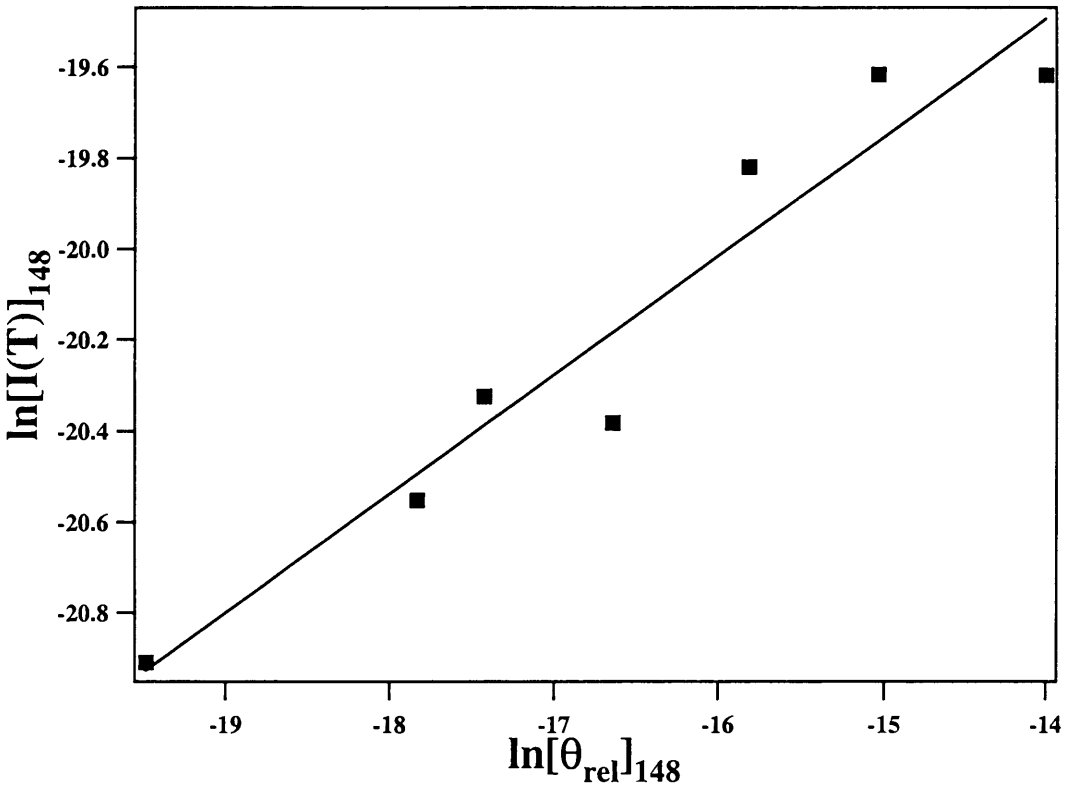

Figure 4.15: A plot of $\ln[I(T)]_x$ against $\ln[\theta_{rel}]_x$ for a T_x of 148 K for various exposures of water adsorption on HOPG at 92 K.

Table 4.1 shows that multilayers of water have a desorption order of 0.24 ± 0.03. This fractional desorption order is in excellent agreement with the isothermal TPD results presented in *Figures 4.12* and *4.13*. The fractional order desorption is attributed to the hydrogen bonded network, which exists in the water multilayer. It has been previously shown that hydrogen bonded systems exhibit fractional order desorption kinetics [37, 38]. Evidence for a hydrogen bonded network within the water adlayer has also been shown in the broadness of the observed O-H stretching bands presented in the RAIRS data (*Figure 4.5*).

Further evidence for a non-zero order desorption process arises from the TPD spectra themselves, shown in *Figures 4.2* and *4.3*. The spectra do not share perfect leading edges for varying exposures of water, as is expected for zero order desorption. It has already been shown in *Section 4.3.3* that the desorption kinetics of water are influenced by the rate of crystallisation of ASW, which is in turn influenced by the thickness of the adlayer. A previous TPD study of the adsorption of water on HOPG concluded a zero order desorption process for multilayers of water from the TPD peak shape [8]. This is clearly in disagreement with the results presented here. It should be noted that no quantitative analysis was carried out with respect to desorption orders by Chakarov and co-workers, nor was the ASW to CI phase transition observed in the TPD spectra.

Table 4.1: Table showing calculated desorption orders for multilayers of water ice adsorbed on HOPG at 92 K.

T_x value/K	Desorption order for multilayer water
148	0.26
153	0.21
156	0.23
158	0.25

4.4.2 Desorption Energy

It is also possible to calculate the desorption energy for water multilayers adsorbed on HOPG. In this way it is possible to gain an indication of the binding strength within the water multilayer. The desorption energy has been calculated using the complete analysis technique [36, 39], a method which uses the family of desorption spectra shown in *Figure 4.2* and is based on rigorous application of the Polanyi-Wigner equation (*Equation 4.1*) [36, 39]. Rearrangement of *Equation 4.6* leads to

$$\ln I(T) \propto n \ln \upsilon_n + n \ln \theta_{rel} - \frac{E_{des}}{RT_S} \qquad \textit{Equation 4.7}$$

The essence of the method is that TPD traces are converted to a give a plot of coverage against temperature. The relative coverage is then fixed at some chosen value θ'_{rel} and the corresponding temperatures are then read off at that chosen value of θ'_{rel}, across all exposures. As a result, the relative coverage across all exposures becomes constant and *Equation 4.7* becomes

$$\ln I(T) \propto n \ln \upsilon_n - \frac{E_{des}}{RT_S} \qquad \textit{Equation 4.8}$$

The temperatures for each exposure, at this fixed relative coverage value θ'_{rel}, are then related to the corresponding desorption intensity, *I(T)*, for the family of TPD curves shown in *Figure 4.2*. An Arrhenius plot of ln *I(T)* against $1/T_s$ for all exposures at θ'_{rel} then gives a straight line with a gradient of $-E_{des}/R$. An example of the conversion of the family of TPD curves, shown in *Figure 4.2*, into relative coverage against temperature traces is given in *Figure 4.16*.

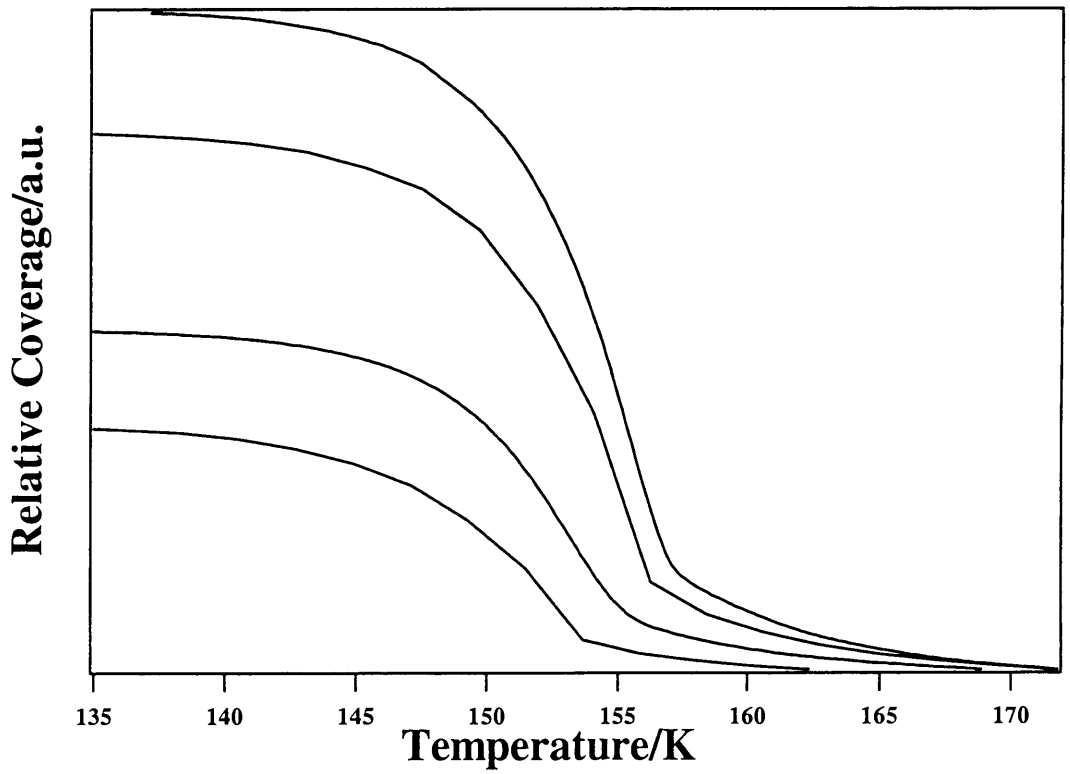

Figure 4.16: Figure showing the relative coverage plotted as a function of surface temperature for water adsorbed on HOPG at 92 K. The plots (from top to bottom) correspond to exposures of 20 L, 15 L, 10 L and 7 L.

The only assumptions made in this analysis are that the pre-exponential factor and the desorption energy do not vary with either coverage or temperature.

Figure 4.17 shows an Arrhenius plot for a relative coverage value of 1.4×10^{-8} a.u. The resulting desorption energy, obtained from the gradient of this graph, is 36.2 kJ mol^{-1}. This process was repeated for several values of θ'_{rel} and *Table 4.2* lists the desorption energies obtained. It can be seen from *Table 4.2* that good agreement in the calculated desorption energies for multilayers of water adsorbed on HOPG is obtained for a range of fixed relative coverage values. From *Table 4.2* an average value of 39.9 ± 2.5 kJ mol^{-1} is obtained for the desorption energy of the water multilayer adsorbed on HOPG at 92 K. This corresponds to a strongly physisorbed or weakly chemisorbed adsorbate and is in excellent agreement with a previously reported value of 43.4 ± 2.9 kJ mol^{-1} for multilayers of water adsorbed on HOPG [8]. This desorption value is also comparable to the sublimation enthalpy of ice, which has a reported value of 47.2 kJ mol^{-1} [40].

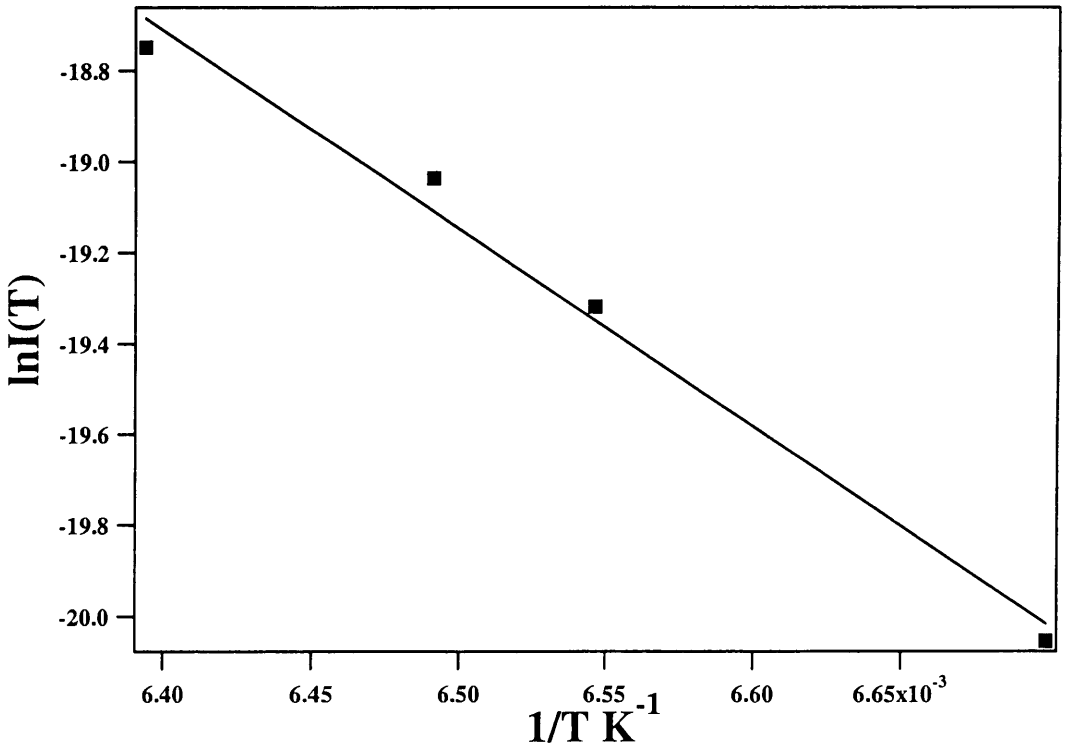

Figure 4.17: An Arrhenius plot used to obtain the desorption energy for multilayer water adsorbed on HOPG at 92 K. The intensity I(T) and the temperature T are measured for a fixed relative coverage of 1.4×10^{-8} a.u.

Table 4.2: Table showing desorption energies for multilayer water adsorbed on HOPG obtained by the complete analysis technique for a range of fixed relative coverage values.

Fixed Relative Coverage Value, θ_{rel}/a.u.	Desorption Energy/kJ mol^{-1}
1.4×10^{-8}	36.2
1.8×10^{-8}	42.3
2.0×10^{-8}	42.4
2.2×10^{-8}	38.6
2.35×10^{-8}	40.1

4.4.3 Pre-exponential Factor

It is also possible to evaluate a pre-exponential factor for the desorption of water from HOPG. These experimentally derived pre-exponential factors can then incorporated into computational models of star-forming regions [5]. For the data shown here it is not possible to determine the pre-exponential factor directly from an Arrhenius plot such as that shown in *Figure 4.17*, since the absolute coverage of the water on the surface is not known. However, it is possible to estimate the pre-exponential factor for water adsorbed on HOPG by converting the relative coverage and relative intensity into actual coverage and actual intensity respectively. This can be achieved by estimating the exposure at which there are no bare patches left on the HOPG surface i.e. monolayer saturation. It is then possible to estimate the number of adsorbates present, when saturation of the first adlayer is achieved. By using the fact that the sticking probability for water multilayers is constant (*Figure 4.14*), it is then possible to scale all relative coverages to absolute coverages.

Coverage is defined as

$$\theta = \frac{N_{ads}}{N_s} \qquad \textit{Equation 4.9}$$

where N_{ads} is the number of adsorbate molecules per unit area and N_s is the number of surface atoms per unit area [24]. N_s can be further defined as

$$N_s = \frac{atoms / unit\ cell}{area / unit\ cell} \qquad Equation\ 4.10$$

Figure 4.18 shows the honeycomb structure of the HOPG surface, with every corner of each hexagon representing a carbon atom. Also indicated in *Figure 4.18* is the unit cell for the HOPG surface, which is a parallelogram with a lattice constant, *a*, of 2.46 Å and an angle, γ, of 60 °. Each unit cell contains two atoms and has an area of

$$Unit\ Cell\ Area = (\sin 60^\circ \times 2.46\times10^{-10})\times 2.46\times10^{-10} = 5.24\times10^{-20}\, m^2$$

This gives a surface atom density of

$$Surface\ Atom\ Density = \frac{2}{5.24\times10^{-20}} = 3.82\times10^{19}\, atoms\, m^{-2}$$

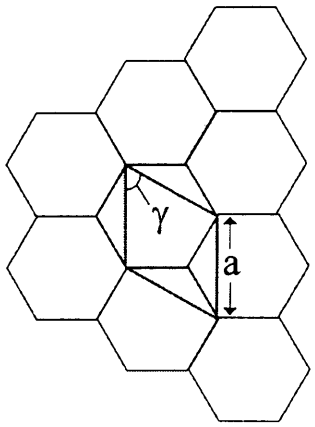

Figure 4.18: A diagram showing the honeycomb structure of HOPG. Every corner of each hexagon indicates the position of a carbon atom. Also indicated is the unit cell for HOPG and the lattice constant, a, and the corresponding unit cell angle, γ.

In order to calculate the number of adsorbates present on the surface, and hence estimate the coverage, a few approximations need to be made. By looking at the

isothermal TPD spectra in *Figure 4.13*, it is proposed that no bare patches are left on the HOPG surface for exposures greater than ~6 L. This is indicated by the lack of region *B* in isothermal TPD spectra recorded following exposures < 6 L. An exposure of 7 L in *Figure 4.2* is therefore approximated as a saturated first layer of water on HOPG. The validity of this assumption will be discussed later. The saturated first layer consists of an array of water molecules arranged in a hydrogen bonded network. To estimate the number of molecules present in this layer, each water molecule is treated as a sphere, with a radius corresponding to the O-H bond length. Each sphere is then hydrogen bonded to other spheres to form a two dimensional array. To compute the surface area occupied by each sphere, and hence each molecule, a O-H bond length of 0.957 Å and a hydrogen bond length of 1.97 Å are used [40]. This leads to the area occupied by each water molecule being

$$Area\,Occupied = \pi\left[0.957\times10^{-10} + \frac{1.97\times10^{-10}}{2}\right]^2 = 2.69\times10^{-19}\,m^2$$

and hence the number of adsorbates per unit area is

$$Adsorbates\,per\,Unit\,Area = \frac{1}{2.69\times10^{-19}} = 3.71\times10^{18}\,molec\,m^{-2}$$

The actual coverage, for a 7 L exposure is then given by

$$Coverage = \frac{3.71\times10^{18}}{3.82\times10^{19}} = 0.097 \approx 0.1\,ML$$

As shown in *Section 4.4.1*, the uptake of water molecules on HOPG is constant as a function of exposure, hence the number of adsorbates per unit area, as calculated above, can be directly related to the area under the 7 L TPD curve. In this way a scaling factor can be used to convert all QMS intensities, and hence relative coverages, to actual coverages. The area under the 7 L exposure curve (*Figure 4.2*) is 2.36×10^{-8} a.u., which corresponds to an absolute coverage of 3.71×10^{18} molec m^{-2}. Therefore all relative coverage values have been scaled by a factor of 1.6×10^{26} to allow conversion to

absolute coverage values. This allows calculation of the pre-exponential factor for the adsorption of multilayers of water on HOPG. Re-arrangement of *Equation 4.1* leads to

$$\upsilon_n = \frac{I(T)}{\theta^n \exp\left[\frac{-E_{des}}{RT_s}\right]} \qquad \textit{Equation 4.11}$$

where *I(T)* is the scaled QMS intensity signal, θ is the actual coverage derived from the scaled *I(T)*, *n* is the order of desorption calculated in *Section 4.4.1* and E_{des} is the desorption energy calculated in *Section 4.4.2*. By using *Equation 4.11* it is possible to evaluate the pre-exponential factor at every recorded temperature point in every TPD trace. The average value was then evaluated for each exposure. This process was repeated for all TPD spectra for exposures between 7 L and 20 L and a further average value obtained. No exposure dependence was noted for the calculated pre-exponential factors.

In order to verify the validity of the assumptions stated above, several checks were carried out. A possible source of error is the assumption that the saturation of a complete layer of water occurs for a 7 L exposure, which corresponds to a coverage of 0.1 ML. To test this assumption, a 0.1 ML coverage was assumed to have taken place for a variety of exposures from 3 L to 20 L. The outcome of this variation is shown in *Table 4.3*.

To further test the assumptions made above, the errors associated with the desorption orders and the desorption energies calculated in *Sections 4.4.1* and *4.4.2* were propagated through the calculations outlined above. The outcome of the errors associated with the order and desorption energy are shown in *Tables 4.4* and *4.5*.

Table 4.3: Table showing the effect of altering the exposure corresponding to a 0.1 ML coverage, which equates to saturation of the first layer, on the pre-exponential factor for water adsorbed on HOPG at 92 K.

Exposure/L	Pre-exponential Factor*/molec m^{-2} s^{-1}
3	9×10^{25}
7	4×10^{26}
15	3×10^{26}
20	2×10^{26}

Table 4.4: Table showing the effect of altering the desorption order on the pre-exponential factor for water adsorbed on HOPG at 92 K. It has been assumed that a 7 L exposure is equivalent to a coverage of 0.1 ML.

Desorption order	Pre-exponential Factor/molec m^{-2} s^{-1}
0.21	3×10^{27}
0.24	4×10^{26}
0.27	2×10^{26}

Table 4.5: Table showing the effect of altering the desorption energy on the pre-exponential factor for water adsorbed on HOPG at 92 K. It has been assumed that a 7 L exposure is equivalent to a 0.1 ML coverage.

Desorption Energy/kJ mol^{-1}	Pre-exponential Factor/molec m^{-2} s^{-1}
37.4	1×10^{26}
39.9	4×10^{26}
43.4	7×10^{27}

It can be seen from *Tables 4.3* to *4.5* that the pre-exponential factor for multilayer desorption of water from HOPG has a value of $10^{27.6\pm1.6}$ molec m^{-2} s^{-1}. The largest sources of error in the assumptions stated above arise in the propagation of errors in the

* The units for the pre-exponential factor are those expected for zero order desorption, despite the observation of a fractional desorption order.

desorption order and desorption energy. The estimate of the exposure at which saturation takes place is, surprisingly, the smallest source of error in the calculation, as shown in *Table 4.3*. This lack of sensitivity to the exact coverage is reassuring since the TPD data shown in *Section 4.1* point to the growth of irregular islands in the water adlayer rather than regular multilayers. This study is in good agreement with a previous study of the adsorption of water on a Au substrate at 10 K, which calculated a pre-exponential factor of $10^{34\pm2}$ molec m^{-2} s^{-1} [41].

4.5 Conclusions

A combined TPD and RAIRS study has been carried out to investigate the adsorption of water on HOPG at temperatures below 100 K. TPD studies (*Figures 4.1* to *4.3*) show the appearance of one peak at the lowest exposures at ~135 K, which shifts up in desorption temperature with increasing exposure. This peak is assigned to the desorption of water molecules from two dimensional islands and/or the edges of three dimensional islands. As the exposure is increased, a second peak is observed which is assigned to the desorption of water molecules within the three dimensional islands. Hence a Stranski-Krastanov growth mechanism is proposed for water adlayers on HOPG. The two peaks merge into one with increasing exposure, and are collectively assigned to the desorption of multilayers of water. This combined peak increases in desorption temperature with increasing exposure and cannot be saturated. At the highest exposures, two further peaks are observed in the TPD spectra which are assigned to phase changes occurring within the water multilayers. The ASW to CI phase transition is observed as a "bump" on the low temperature side of the main desorption peak, above the glass transition temperature of water at ~155 K. The CI to HI transition is observed as a separate peak at 175 K. A desorption order of 0.24 ± 0.03 and a pre-exponential factor of $10^{27.6\pm1.6}$ molec m^{-2} s^{-1} have been calculated for the desorption of multilayers of CI. A desorption energy 39.9 ± 2.5 kJ mol^{-1} has also been determined for multilayers of CI, which is in excellent agreement with previous studies. This desorption energy corresponds to a strongly physisorbed species.

RAIR spectra show the growth of physisorbed multilayers of water. Water adsorbs molecularly on the HOPG surface and does not undergo dissociation. Spectral features are assigned to the O-H stretching mode and HOH scissors mode. The observed bands do not undergo a frequency shift with increasing coverage, nor can the bands be saturated. The broadness of the O-H stretching bands indicates a high degree of hydrogen bonding within the multilayer. Annealing the adlayer has a marked effect on the O-H stretching band, which can be used to observe the phase change in the adlayer from ASW to CI. However, it is proposed that the adlayer was not annealed for long enough for the whole adlayer to be crystallised. Complete desorption took place when the adlayer was annealed above 175 K. This is consistent with the TPD studies shown above. RAIR spectra were also recorded as a function of adsorption temperature. Once again the phase transition from ASW to CI can clearly be observed via the O-H stretching band.

The ASW to CI phase change was also studied using isothermal TPD experiments. The phase transition is signalled by a rapid change in desorption rate. Once this irreversible phase change has occurred, desorption of multilayers occurs, provided that the ice layers are thick enough. For crystallisation to occur completely before the adlayer has desorbed, exposures of 6 L and above are required. The isothermal TPD experiments confirm the fractional desorption order of CI.

4.6 References

[1] Henderson, M.A., Surf. Sci. Rep., **46** (2002) p. 5.

[2] Thiel, P.A. and Madey, T.E., Surf. Sci. Rep., **7** (1987) p. 211.

[3] Whittet, D.C.B., in *Dust and Chemistry in Astronomy*, T.J. Millar and D.A. Williams, Editors. 1993, Institute of Physics Publishing.

[4] Whittet, D.C.B., *Dust in the Galactic Environment*. Series in Astronomy and Astrophysics. 2003: Institute of Physics Publishing.

[5] Viti, S., Collings, M.P., Dever, J.W., McCoustra, M.R.S., and Williams, D.A., Mon. Not. R. Astron. Soc., **354** (2004) p. 1141.

[6] Collings, M.P., Anderson, M.A., Chen, R., Dever, J.W., Viti, S., Williams, D.A., and McCoustra, M.R.S., Mon. Not. Roy. Astron. Soc., **354** (2004) p. 1133.

[7] Phelps, R.B., Kesmodel, L.L., and Kelley, R.J., Surf. Sci., **340** (1995) p. 134.

[8] Chakarov, D.V., Osterlund, L., and Kasemo, B., Vacuum, **46** (1995) p. 1109.

[9] Chakarov, D.V., Osterlund, L., and Kasemo, B., Langmuir, **11** (1995) p. 1201.

[10] Lofgren, P., Ahlstrom, P., Chakarov, D.V., Lausma, J., and Kasemo, B., Surf. Sci., **367** (1996) p. L19.

[11] Lofgren, P., Ahlstrom, P., Lausma, J., Kasemo, B., and Chakarov, D., Langmuir, **19** (2003) p. 265.

[12] Johari, G.P., Hallbrucker, A., and Mayer, E., J. Chem. Phys., **95** (1991) p. 2955.

[13] Jenniskens, P. and Blake, D.F., Science, **265** (1994) p. 753.

[14] Smith, R.S., Huang, C., Wong, E.K.L., and Kay, B.D., Surf. Sci., **367** (1996) p. L13.

[15] Stevenson, K.P., Kimmel, G.A., Dohnalek, Z., Smith, R.S., and Kay, B.D., Science, **283** (1999) p. 1505.

[16] Mayer, E. and Pletzer, R., Nature, **319** (1986) p. 298.

[17] Hallbrucker, A., Mayer, E., and Johari, G.P., J. Phys. Chem., **93** (1989) p. 4986.

[18] Handa, Y.P. and Klug, D.D., J. Phys. Chem., **92** (1988) p. 3323.

[19] Smith, R.S. and Kay, B.D., Nature, **398** (1999) p. 788.

[20] Smith, R.S. and Kay, B.D., Surf. Rev. Lett., **4** (1997) p. 781.

[21] Chakarov, D. and Kasemo, B., Phys. Rev. Lett., **81** (1998) p. 5181.

[22] Chakarov, D.V., Gleeson, M.A., and Kasemo, B., J. Chem. Phys., **115** (2001) p. 9477.

[23] Sanfelix, P.C., Holloway, S., Kolasinski, K.W., and Darling, G.R., Surf. Sci., **532** (2003) p. 166.

[24] McCash, E.M., *Surface Chemistry*. 2001, Oxford: Oxford University Press.

[25] Kay, B.D., Lykke, K.R., Creighton, J.R., and Ward, S.J., J. Chem. Phys., **91** (1989) p. 5120.

[26] Speedy, R.J., Debenedetti, P.G., Smith, R.S., Huang, C., and Kay, B.D., J. Chem. Phys., **105** (1996) p. 240.

[27] Dohnalek, Z., Ciolli, R.L., Kimmel, G.A., Stevenson, K.P., Smith, R.S., and Kay, B.D., J. Chem. Phys., **110** (1999) p. 5489.

[28] Dohnalek, Z., Kimmel, G.A., Ciolli, R.L., Stevenson, K.P., Smith, R.S., and Kay, B.D., J. Chem. Phys., **112** (2000) p. 5932.

[29] Smith, R.S., Huang, C., Wong, E.K.L., and Kay, B.D., Phys. Rev. Lett., **79** (1997) p. 909.

[30] Petrenko, V. and Whitworth, R., *Physics of Ice*. 1999, Oxford: Oxford University Press.

[31] Schaff, J.E. and Roberts, J.T., J. Phys. Chem., **100** (1996) p. 14151.

[32] Bensebaa, F. and Ellis, T.H., Prog. Surf. Sci., **50** (1995) p. 173.

[33] Backus, E.H.G., Grecea, M.L., Kleyn, A.W., and Bonn, M., Phys. Rev. Lett., **92** (2004) p. 236101.

[34] Nuzzo, R.G., Zegarski, B.R., Korenic, E.M., and Dubois, L.H., J. Phys. Chem., **96** (1992) p. 1355.

[35] Schaff, J.E. and Roberts, J.T., J. Phys. Chem., **98** (1994) p. 6900.

[36] de Jong, A.M. and Niemantsverdriet, J.W., Surf. Sci., **233** (1990) p. 355.

[37] Wu, M., Truoung, C.M., and Goodman, D.W., J. Phys. Chem., **97** (1993) p. 9425.

[38] Nishimura, S.Y., Gibbons, R.F., and Tro, N.J., J. Phys. Chem. B, **102** (1998) p. 6831.

[39] Kolasinski, K.W., *Surface Science: Foundations of Catalysis and Nanoscience*. 2002: John Wiley and Sons Ltd.

[40] Eisenberg, D. and Kauzmann, W., *The Structure and Properties of Water*. 1969, London: Oxford University Press.

[41] Fraser, H.J., Collings, M.P., McCoustra, M.R.S., and Williams, D.A., Mon. Not. R. Astron. Soc., **327** (2001) p. 1165.

Chapter 5: Methanol Adsorption on Highly Oriented Pyrolitic Graphite (HOPG): A RAIRS study

5.1 Introduction

Methanol (CH_3OH) is the second most abundant molecule in many interstellar ices [1] with an abundance of 5% to 50% of that of water. It has been shown in *Chapter 1* that in many areas of the interstellar medium (ISM), it is not possible to explain observed abundances of methanol by gas phase, ion-molecule chemistry alone. Instead, it is believed that methanol forms on the surface of dust grains and subsequently desorbs into the gas phase. Hence a clear understanding of the adsorption and desorption of methanol from the surface of dust grains is crucial in modelling regions such as hot cores [2]. Furthermore, the presence of methanol in such high abundances on dust grains has important implications for the chemical and physical properties of interstellar ices. For example water and methanol have been observed to form a clathrate structure at ~125 K and at low pressures [3]. This interaction has significant implications for the gas phase abundance of methanol [1]. Since methanol is high in abundance in interstellar ices, it also plays a vital role in the photoprocessing of ices by UV radiation [4]. However, there have been no previous studies of the adsorption of methanol on astrochemically relevant surfaces.

This chapter describes the first detailed RAIRS study of the adsorption of methanol on highly oriented pyrolitic graphite (HOPG), which can be considered a suitable dust grain analogue surface. A detailed TPD study of the adsorption of methanol on this surface is given in *Chapter 6*. The only previous study of the adsorption of methanol on a graphitic surface was carried out by Wang and co-workers [5], using atomic force microscopy. This study showed physisorbed multilayer growth of methanol on a HOPG surface. Furthermore, formation of irregular islands was observed within the multilayer [5].

In contrast the interaction of alcohols, especially methanol, with metal surfaces has been of considerable interest due to its widespread application in elementary catalytic processes [6] and in fuel cells [7, 8]. Methanol can be regarded as an excellent model molecule for the selective activation of different chemical bonds in heterogeneous catalysis, since it is relatively simple and yet contains C-H, C-O and O-H bonds. The adsorption and reaction of methanol with metal surfaces has been discussed in several review articles [9-11].

Methanol decomposes to form methoxy on a range of metal surfaces as shown in several studies [12-18]. The adsorption of intact methanol on a variety of single crystal metal surfaces has been studied using RAIRS and HREELS [16-21]. Methanol has been observed to adsorb both as a chemisorbed monolayer and a physisorbed multilayer on Pd{110} [20]. RAIR spectra indicate a crystalline structure within the multilayer in which hydrogen bonded chains of molecules lie parallel to the surface. Furthermore, a "sandwich" phase is identified consisting of several physisorbed layers between the chemisorbed layer and the crystalline phase. Crystalline methanol has also been observed on Pt{111} [21] and on polycrystalline platinum [19]. In both studies, adsorption of methanol at 90 K led to the observation of a chemisorbed monolayer and physisorbed amorphous multilayers. Annealing the adlayer to 125 K resulted in a phase transition from amorphous to crystalline methanol. This phase transition occured only if multilayers were present on the surface.

Spectra of physisorbed multilayer methanol ice have also been reported on Cu{100} [16]. Observed bands included the C-H stretching modes between 2750 - 3000 cm^{-1} and the C-O symmetric stretch at 1044 cm^{-1}. However, the expected O-H symmetric stretch of methanol was not clearly observed due to masking by the symmetric O-H stretch of water-ice, at 3282 cm^{-1}, built up in the MCT detector. High exposures of methanol also resulted in growth of multilayers on Ru{001} [17]. This study showed the O-H and C-O stretching features at 3285 cm^{-1} and 1045 cm^{-1} respectively. Methanol adsorption on Ru{001}has also been studied using EELS [18]. This study showed vibrational spectra of condensed multilayers of undissociated methanol, obtained after high exposure.

Vibrational modes were identified at 3190 cm^{-1}, 2900 cm^{-1} and 1055 cm^{-1} for the O-H, C-H and C-O stretches respectively.

5.2 Experimental

All experiments were performed in the UHV chamber described in *Chapter 2* and sample cleanliness was achieved using the techniques described earlier. RAIRS experiments investigated the adsorption of methanol (99.9% purity, BDH Laboratory Supplies) by back filling the chamber via a high precision leak valve, in a controlled manner. Prior to sample cleaning, methanol was flushed through the gas manifold several times, and admitted into the UHV chamber to a background pressure of 2×10^{-9} mbar for ten seconds, whilst monitoring the QMS in order to ensure no contaminants were being admitted during dosage. All exposures are measured in Langmuir (L), where an exposure of 1 L is equivalent to back filling the chamber to a pressure of 1×10^{-6} mbar for 1 second.

5.3 Results and Discussion

5.3.1 Methanol Adsorption on HOPG at 97 K

RAIR spectra following adsorption of methanol onto HOPG at 97 K are shown in *Figure 5.1*. Initial exposure of the surface to methanol leads to the appearance of one band at 1045 cm^{-1}. With increasing exposure this band is seen to grow in intensity, however there is no shift in frequency. This band remains the dominant feature in all spectra.

At an exposure of 5 L, a broad band appears centred at a frequency of 3260 cm^{-1} with a width of approximately 100 cm^{-1}. Similar to the lower frequency band, this band grows in intensity with increasing exposure but does not undergo a frequency shift. As the exposure is increased from 7 L upwards, several other spectral features are observed at 1132 cm^{-1}, 1468 cm^{-1}, 2833 cm^{-1}, 2908 cm^{-1}, 2956 cm^{-1} and 2983 cm^{-1} as highlighted in the bottom spectrum in *Figure 5.1*. A further increase in exposure leads to an increase in

intensity of these bands but does not lead to the observation of any additional spectral features (*Figure 5.2*). It is not possible to saturate the peaks with increasing exposure. This is characteristic of multilayer growth on the surface [18].

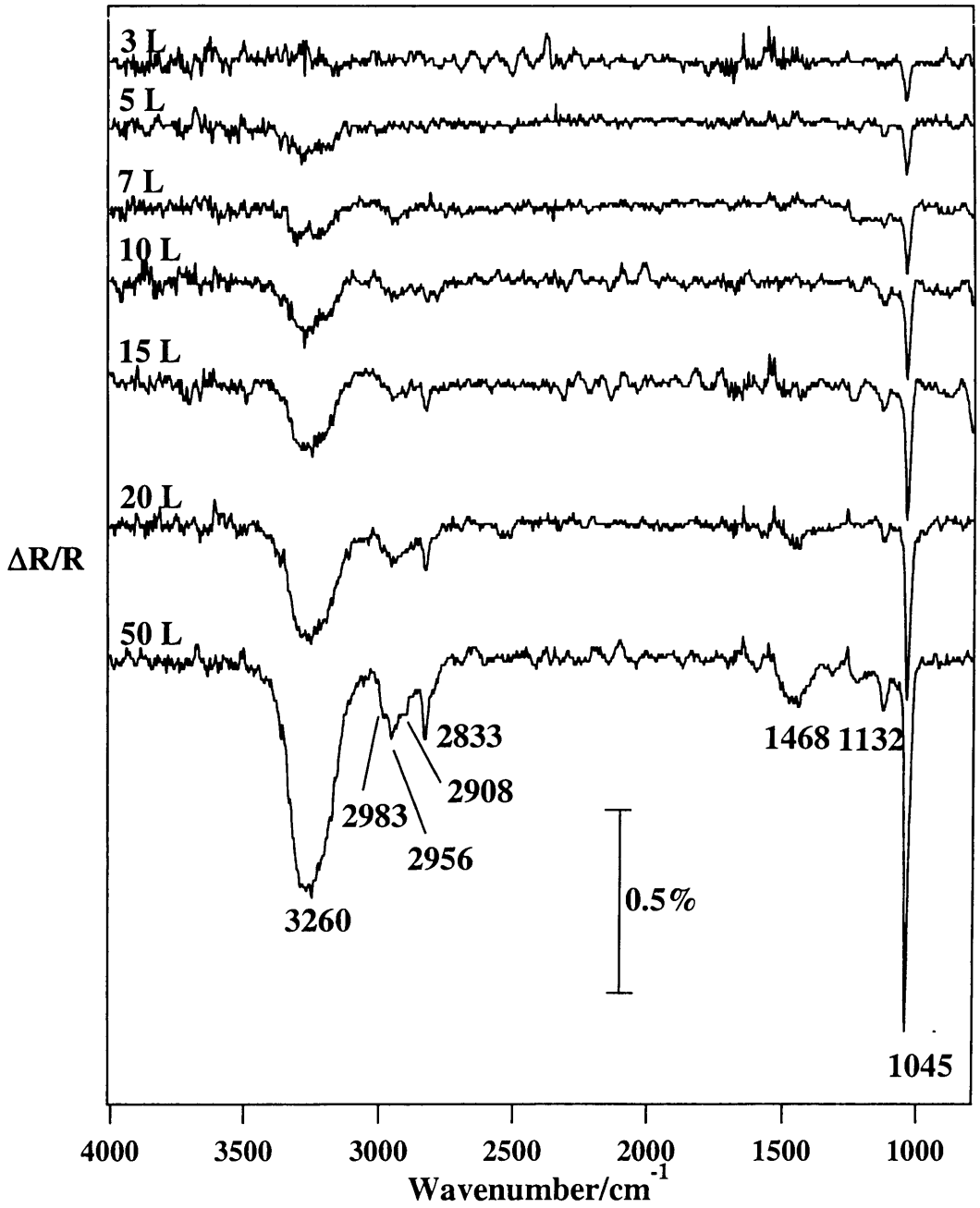

Figure 5.1: RAIR spectra of increasing exposures of methanol adsorbed on HOPG at 97 K.

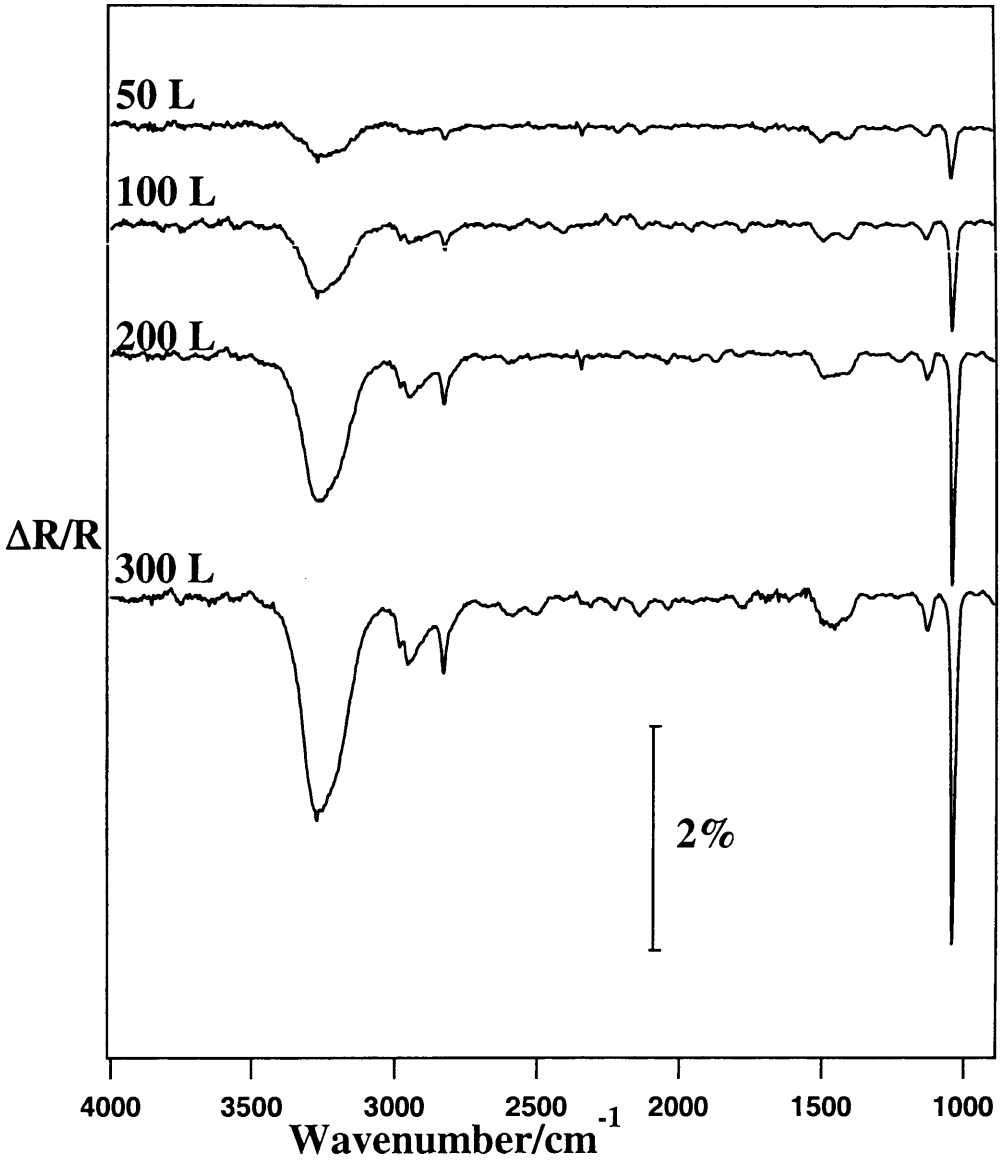

Figure 5.2: RAIR spectra of "high" exposures of methanol on HOPG adsorbed at 97 K. Exposures of methanol are indicated on individual spectra.

The bands observed in the spectra shown in *Figures 5.1* and 5.2 are comparable in frequency to those recorded for multilayer methanol on a number of metal surfaces [15-18, 20, 22, 23] and can be assigned confidently. *Table 5.1* shows the assignment of the vibrational bands observed for methanol adsorbed on HOPG in comparison to methanol adsorbed on Ru{001}[18], Rh{110}[23] and methanol in an argon matrix [24]. Comparison of the bands observed here with those previously observed confirms that methanol is adsorbed molecularly on the HOPG surface. The observed bands are also

comparable in frequency to those observed for gas phase and liquid methanol [12, 25], hence it is believed that methanol is physisorbed on the surface. Further evidence for this assignment is the lack of frequency shift of the bands with increasing exposure, implying weak lateral interactions within the adlayer. The two most intense bands at 1045 cm^{-1} and 3260 cm^{-1} are assigned to the symmetric C-O stretch, υ(CO) and the O-H stretch, υ(OH) of methanol respectively.

The multilayer exhibits strong intermolecular hydrogen bonding, demonstrated by the shift in frequency of the O-H stretch in condensed phases of methanol from that observed for gas phase methanol [25]. This downshift in frequency of the O-H stretch is from 3682 cm^{-1} in the gas phase to 3260 cm^{-1} for methanol multilayers on HOPG. This behaviour is also observed in other hydrogen bonded systems such as water and ice [26, 27]. Further evidence for the existence of hydrogen bonding within the multilayer is shown by the relative broadness of the O-H stretch.

The exposure dependent data in *Figure 5.1* give an indication of the possible orientation of the first few layers of adsorbed methanol. The selection rules, imposed by RAIRS, state that only vibrational bands with a component of the dipole moment perpendicular to the surface can be observed. Therefore, the observation of the C-O stretch and not the O-H stretch, at an exposure of 3 L, suggests that the O-H stretch is lying parallel to the surface. Two possible geometries for the methanol adsorbed at low exposure are given in *Figure 5.3*.

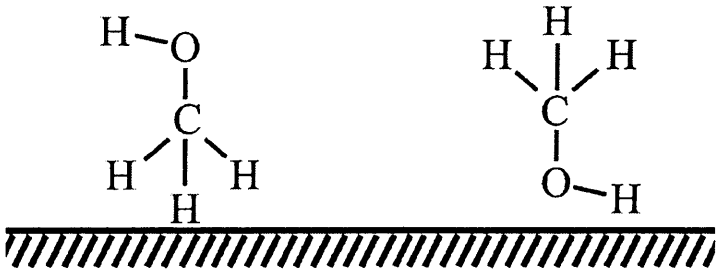

Figure 5.3: A diagram showing the possible orientation of methanol adsorbed at low exposures on a HOPG surface.

Table 5.1: Table showing the assignment of the vibrational bands observed for methanol adsorbed on HOPG at 97 K in comparison to methanol adsorbed on Rh{100} [23] and Ru{001} [18] and methanol in an Ar matrix [24].

Band assignment	**Multilayer methanol/HOPG /cm^{-1}**	Methanol Ar matrix [24] /cm^{-1}	Methanol/Rh{100} [23] /cm^{-1}	Methanol/Ru{001} [18] /cm^{-1}
υ(OH)	**3260**	3667	3245	3190
$\upsilon_a(CH_3)$	**2983**	3006 2962	2980	3000
$2\delta_a(CH_3)a'$	**2956** **2908**	2956 2921		
$\upsilon_s(CH_3)$	**2833**	2848	2905	2855
$\delta_a(CH_3)$		1473 1466		
$\delta_s(CH_3)$	**1468**	1452	1475	1470
δ(COH)		1334		
$\rho(CH_3)$	**1132**	1145 1077	1180	1145
υ(CO)	**1045**	1034	1040	1055

A series of spectra resulting from annealing of the methanol covered surface following adsorption at 97 K are shown in *Figures 5.4* and *5.5*. It can clearly be seen that annealing the methanol multilayer leads to immediate splitting of several of the bands. *Figure 5.4* shows a close up of the region between 800 cm^{-1} and 1600 cm^{-1} and *Figure 5.5* shows a close up of the region between 1500 cm^{-1} and 4000 cm^{-1}.

Figure 5.4 shows that the C-O stretch at 1045 cm^{-1} splits into a doublet on annealing to 129 K, with two peaks appearing at 1037 cm^{-1} and 1027 cm^{-1}. The broad band observed at 1468 cm^{-1} also splits into two distinct bands at 1475 cm^{-1} and 1521 cm^{-1}.

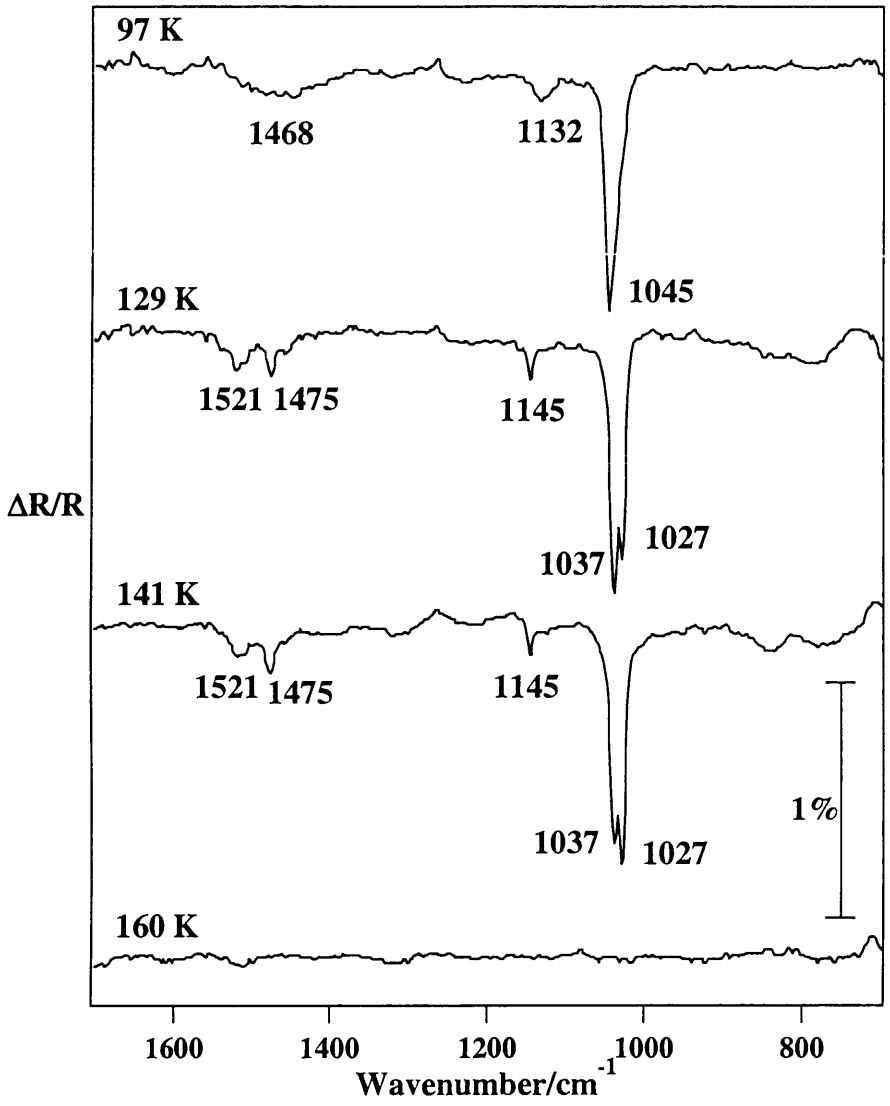

Figure 5.4: RAIR spectra between 800 cm^{-1} and 1600 cm^{-1} showing the sequential heating of methanol adlayers adsorbed on HOPG at 97 K. The temperatures to which the methanol adlayer was annealed are indicated on the individual spectra.

Similarly, *Figure 5.5* shows that the O-H stretch, centred at 3260 cm^{-1}, splits into two sharper bands at 3290 cm^{-1} and 3174 cm^{-1} after annealing to 129 K. Note that these two sharper bands seem to appear on top of a broader feature. This feature has a width of approximately 100 cm^{-1}, which is comparable to the width of the 3260 cm^{-1} band shown in the bottom spectrum in *Figure 5.1*. This splitting of spectral bands, which is observed as a result of annealing the methanol adlayer, can be attributed to the formation of crystalline methanol on the surface. Similar observations have been noted for

multilayers of methanol adsorbed on polycrystalline Pt [19], Pt{111} [21] and Pd{110} [20]. The observation of sharp crystalline bands on top of a broad band is in excellent agreement with studies on Pt{111} [21], which observed a mixture of amorphous and crystalline methanol on the surface. A further feature of the formation of crystalline methanol is the observation of the sharpening of several other bands as a result of ordering within the multilayer [20].

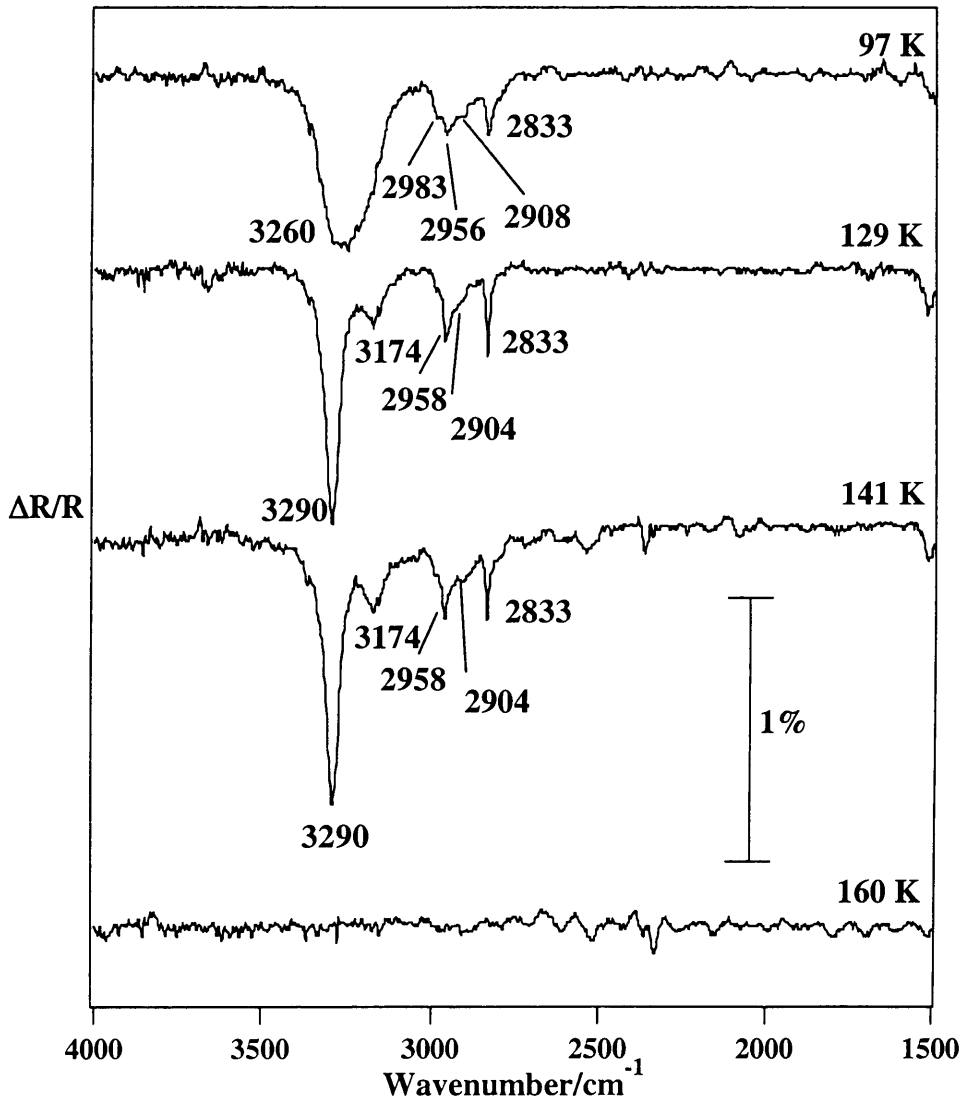

Figure 5.5: RAIR spectra between 1500 cm^{-1} and 4000 cm^{-1} showing the sequential heating of methanol adlayers adsorbed on HOPG at 97 K. The temperatures to which the methanol adlayer was annealed are indicated on the individual spectra.

Figure 5.5 clearly shows sharpening of the CH_3 stretching bands in the region between 2833 cm^{-1} and 2983 cm^{-1}. It is clear that the formation of crystalline methanol is a temperature dependent process since band splitting is only observed when the adlayer produced at 97 K is heated above 125 K. *Table 5.2* shows the good agreement of the bands observed in *Figures 5.4* and *5.5* with respect to the vibrational frequencies of crystalline forms of methanol [25].

Table 5.2: Table showing the assignment of vibrational bands of high exposures of methanol adsorbed on HOPG at 130 K in comparison to crystalline methanol.

Band assignment	**Multilayer CH_3OH/HOPG /cm^{-1}**	Crystalline α phase [25] /cm^{-1}
υ(OH)	**3290**	3284
	3174	3187
$\upsilon_a(CH_3)$	**2958**	2982
	2904	2955
$\upsilon_s(CH_3)$	**2833**	2829
$\delta_a(CH_3)$	**1475**	1458
		1426
δ(COH)	**1525**	1514
		1470
$\rho(CH_3)$		1256
		1162
	1145	1142
υ(CO)	**1037**	1046
	1027	1029

All vibrational bands have disappeared from the spectra after annealing the adlayer to 160 K, implying that the methanol has desorbed from the surface by this temperature. This is in good agreement with observations for the adsorption of methanol on Ru{001}, where the physisorbed multilayer completely desorbed by 190 K leaving only the dissociated chemisorbed methanol on the surface [18].

5.3.2 Crystalline Methanol

Crystalline methanol exists in hydrogen bonded chains in two distinct forms, the α and β phases [28–31]. Dilatation experiments have indicated that the α phase is stable below 156 K, and the β phase is stable between 156 K and the melting point of methanol at 175.4 K [32]. In both phases, it has been shown that the C atoms and/or the OH hydrogen atoms are out of plane with respect to the O atoms, since two O-H bending modes are observed out of plane [25, 33]. This results in differing distributions of the methyl group above and below the O atoms in the two crystalline chains. For the α chain, the methyl groups alternate above and below the O atoms allowing neighbouring chains to come closer together. In the β chain the methyl groups appear to be randomly distributed and may thermally flip between positions [33]. The chain structure for the α form of crystalline methanol is shown in *Figure 5.6* [20].

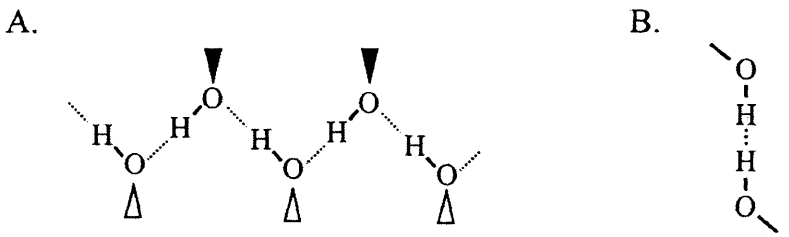

Figure 5.6: Diagram showing the chain structure of the α phase of crystalline methanol. Figure (a) shows the side view and Figure (b) shows the axial view [20].

The difference in distribution of the methyl groups in the α and β phases leads to different interchain interactions for the two phases, and therefore a difference in the orientation of intermolecular O-H bonds in adjacent chains. In the β phase, the O-H bonds point in the same direction as the chain axis, while in the α phase the bonds alternate in opposite directions [20]. This difference in orientation leads to the β form having a smaller primitive unit cell, containing just one chain and two molecules, compared to the α form, which contains two chains and four molecules. Furthermore,

adjacent chains are parallel in the β phase, but are rotated by almost 90° about the chain axis in the α phase [20].

For both the α and the β phases, interactions and coupling can take place within individual chains (between adjacent molecules) and also between adjacent chains. For both the inter- and intrachain interactions, the coupling can either be in-phase or out-of phase. Since chain stacking in the β phase appears to be disordered; only intrachain coupling can be considered. The expected intermolecular coupling for both the C-O and the O-H stretches of the β phase is shown in *Figure 5.7* [20].

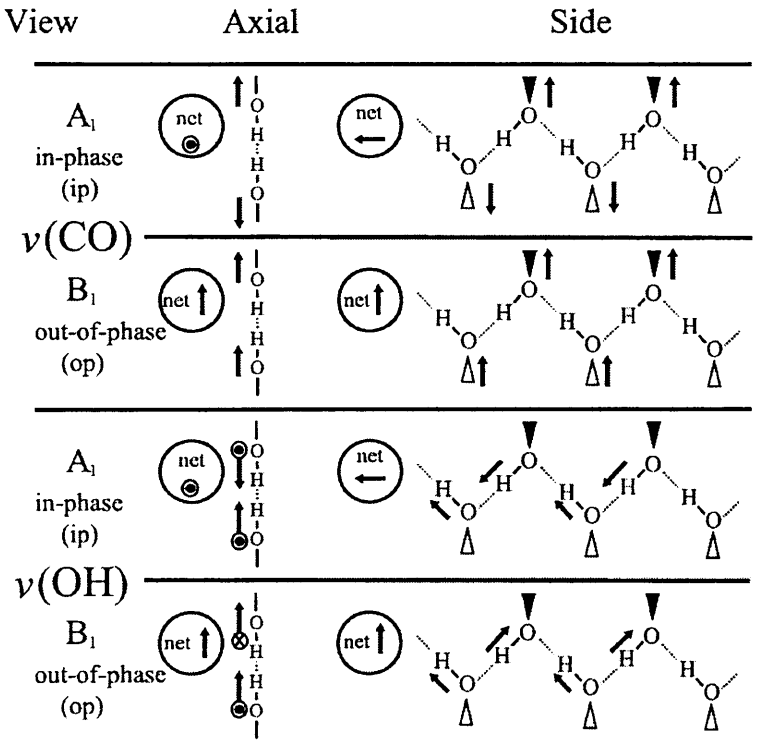

Figure 5.7: Figure showing the axial and side views of the expected coupling of the C-O and O-H stretching modes for the β phase of crystalline methanol. The net dipole moment is circled [20].

For both the C-O and the O-H stretching modes, coupling can either be in-phase (labelled A_1) or out-of-phase (labelled B_1). Both the in-phase and out-of-phase coupling modes are expected to be infrared active since a component of the net dipole moment is perpendicular to the surface as shown in *Figure 5.7*. Hence, if the crystalline methanol

adopts the β structure, two modes would be expected for each of the C-O and the O-H stretches.

For the α phase, which has ordered chain stacking, both inter- and intrachain coupling are possible. Hence, each internal mode will be split into four components [34]. The interactions of the C-O and the O-H stretches for the α phase of crystalline methanol are shown in *Figure 5.8* [20].

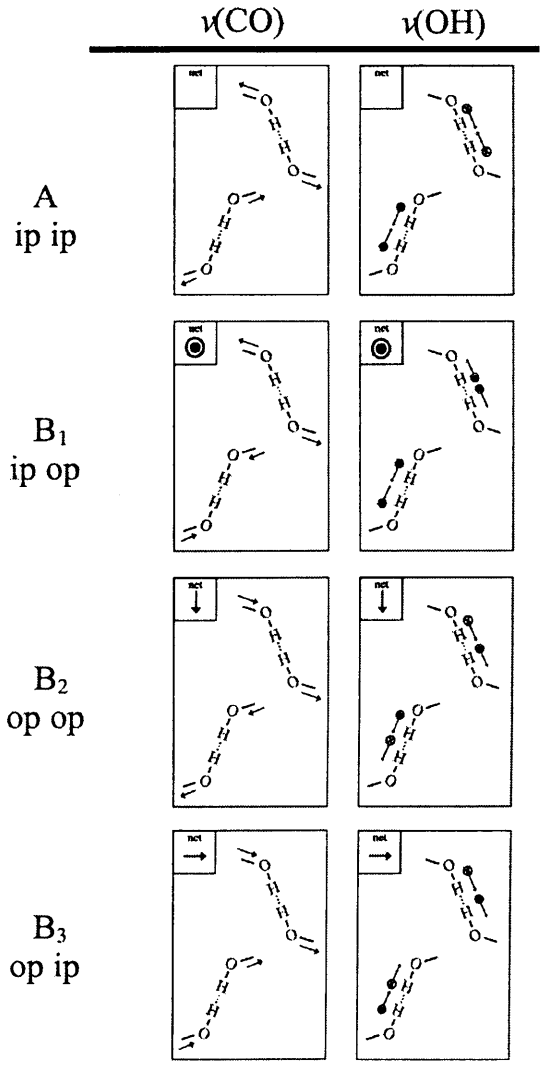

Figure 5.8: Axial view of the expected C-O and O-H stretching modes for the α phase of crystalline methanol. In-phase coupling and out-of-phase coupling have been abbreviated to ip and op respectively. The net dipole moment is shown in each figure [20].

In *Figure 5.8*, the top diagram, mode A, shows in-phase intrachain coupling with in-phase interchain interactions. This vibrational mode would not be observed in RAIRS since there is no net dipole moment change for the interaction. The modes B_1, B_2 and B_3 are however infrared active, and this would lead to the possibility of several modes in each of the C-O and the O-H bands being observed in RAIRS.

The possibility of different coupling between chains and within chains is manifested for crystalline methanol as splitting of bands in the infrared spectra into doublets [25, 33] as seen in *Figures 5.4* and *5.5*. This splitting, in direct comparison with the argon isolated-matrix monomer species, is known as correlation field band splitting (or Davydov splitting) and is a result of symmetry restricted intermolecular coupling [35]. The spectra in *Figures 5.4* and *5.5* show that the C-O and O-H stretching regions are the strongest in intensity and clearly demonstrate band splitting. It has been suggested that splitting may also be observed in other vibrational bands if infrared spectra were recorded at higher resolution, however there is no evidence for additional splitting in this study [20]. For the spectra shown in *Figures 5.4* and *5.5* it is not possible to determine whether crystalline methanol formed on HOPG adopts the α or the β phase since the correct structures of the two phases have only been determined recently and the vibrational structures have not yet been completely resolved.

5.3.3 Methanol Adsorption on HOPG at 130 K

The formation of crystalline methanol was initially observed when the adlayer, formed following adsorption at 97 K, was annealed above 125 K. Hence, experiments were also carried out with the surface at elevated temperatures to determine whether it was possible to form crystalline methanol directly following adsorption. RAIR spectra were recorded as a function of increasing exposure of methanol, with the surface held at 130 K. Initial adsorption of methanol at "lower" exposures (< 50 L) at 130 K led to essentially identical spectra to those recorded following adsorption at 97 K (*Figure 5.1*). The intensities of all the vibrational bands were slightly lower for adsorption at 130 K, in comparison to adsorption at 97 K, due to a lower sticking probability at the higher temperature. All vibrational bands of methanol identified for adsorption at 97 K were

present for adsorption at 130 K and no additional bands were observed. Hence methanol also adsorbs molecularly in a physisorbed state on HOPG at 130 K.

However, increasing exposures (≥ 50 L) of methanol adsorbed at 130 K show distinct differences compared to spectra recorded following adsorption at 97 K (*Figure 5.2*). "Higher" exposures, with the surface at 130 K, produce a similar effect to that observed following annealing of the adlayer formed at 97 K, with band splitting occurring in the C-O and O-H stretching modes (*Figures 5.9* and *5.10*).

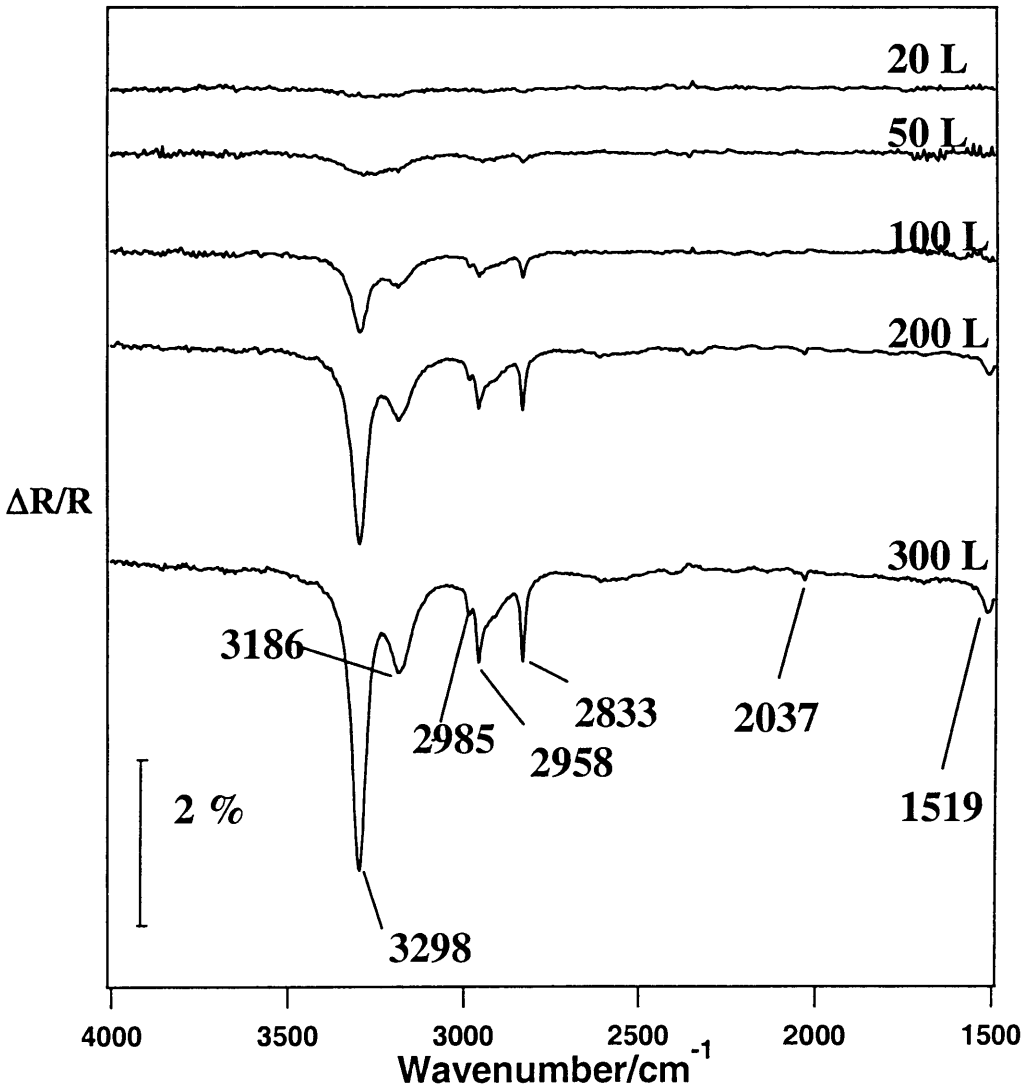

Figure 5.9: RAIR spectra of increasing exposures (between 20 L and 300 L) of methanol adsorbed on HOPG at 130 K. The figure shows the absorption region between 1500 cm^{-1} and 4000 cm^{-1}.

Furthermore, two distinct sharp bands can be seen at 1473 cm^{-1} and 1519 cm^{-1} in *Figure 5.10*, as opposed to one broad band over this frequency range as seen in *Figure 5.3*. A shift of approximately 10 cm^{-1} is noted for the O-H stretching mode between the annealed adlayer adsorbed at 97 K and the adlayer formed following adsorption at 130 K. This can be attributed to a difference in hydrogen bonding within the crystalline methanol formed following adsorption at 130 K, compared to that formed after annealing the adlayer adsorbed at 97 K. Since the splitting observed in *Figures 5.9* and *5.10* does not occur until high exposures, the formation of crystalline methanol requires not only specific temperature criteria, but also specific exposure criteria to be met.

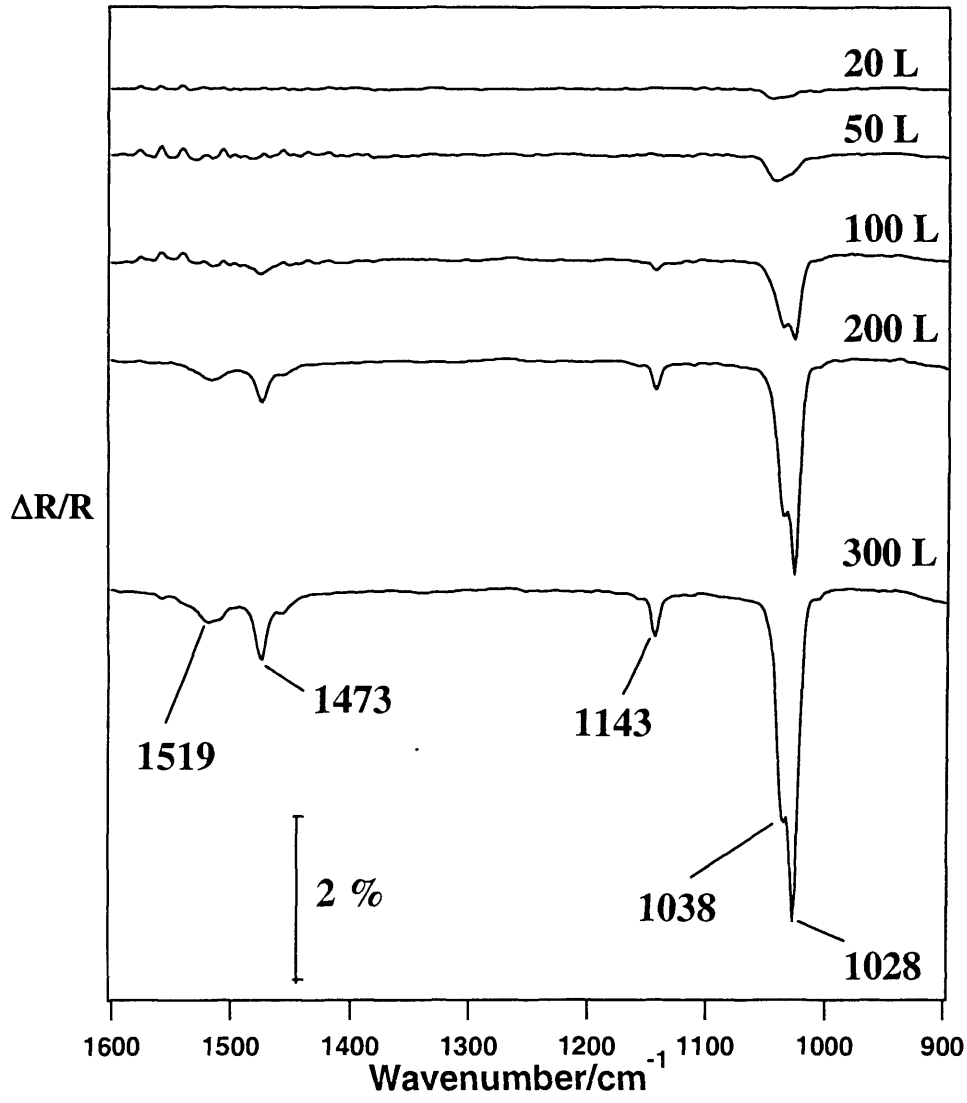

Figure 5.10: RAIR spectra of increasing exposures (between 20 L and 300 L) of methanol adsorbed on HOPG at 130 K. The figure shows the absorption region between 800 cm^{-1} and 1600 cm^{-1}.

To determine exactly what these specific exposure criteria were, further experiments were carried out annealing a "low" exposure (≤ 20 L) methanol adlayer adsorbed at 100 K. No splitting was observed during these experiments. Similarly, no splitting was observed after annealing a "low" exposure (≤ 20 L) methanol adlayer formed at 130 K. These experiments show that the formation of crystalline methanol, marked by correlation field band splitting, in the O-H and C-O stretching regions of the spectrum, is both a surface temperature and exposure dependent effect. Annealing the adlayer formed at 130 K did not lead to the observation of any new spectral features. In all cases, all vibrational bands had disappeared by 160 K implying that the methanol desorbed molecularly, similar to adsorption at 97 K.

5.4 Conclusions

RAIRS studies have been carried out to investigate the adsorption of methanol on HOPG at 100 K and 130 K. RAIR spectra show that methanol adsorbs molecularly in a physisorbed state on HOPG at 97 K. Increasing exposure leads to the formation of multilayers of methanol, and no new species are observed. Annealing the multilayer leads to correlation field splitting in several bands. This band splitting is attributed to the presence of crystalline methanol and arises due to the intra- and interchain coupling of two different phases of crystalline methanol. Adsorbing methanol to "low" exposures at 130 K leads to identical spectra to those seen for adsorption at 97 K, however "high" exposures lead to band splitting similar to that observed for the 97 K annealed adlayer. This is again attributed to interactions within crystalline phases of methanol. In both cases, at 97 K and 130 K, methanol desorbs molecularly after annealing to 160 K.

5.5 References

[1] Sandford, S.A. and Allamandola, L.J., Astrophys. J., **417** (1993) p. 815.

[2] Viti, S., Collings, M.P., Dever, J.W., McCoustra, M.R.S., and Williams, D.A., Mon. Not. R. Astron. Soc., **354** (2004) p. 1141.

[3] Blake, D., Allamandola, L.J., Sandford, S.A., Hudgins, D., and Freund, F., Science, **254** (1991) p. 548.

[4] Allamandola, L.J., Sandford, S.A., and Valero, G.J., Icarus, **76** (1988) p. 225.

[5] Wang, L., Song, Y.H., Wu, A.G., Li, Z., Zhang, B.L., and Wang, E.K., Appl. Surf. Sci., **199** (2002) p. 67.

[6] Rozovskii, A.Y. and Lin, G.I., Top. Catal., **22** (2003) p. 137.

[7] Masel, R.I., *Priniciples of Adsorption and Reactions on Solid Surfaces*. 1996, New York: John Wiley and Sons.

[8] Stoukides, M., Catal. Rev.-Sci. Eng., **42** (2000) p. 1.

[9] Netzer, F.P. and Ramsey, M.G., Crit. Rev. Sol. St. Mat. Sci., **17** (1992) p. 397.

[10] Shekhar, R. and Barteau, M.A., Catal. Lett., **31** (1995) p. 221.

[11] Barros, R.B., Garcia, A.R., and Ilharco, L.M., J. Phys. Chem. B, **108** (2004) p. 4831.

[12] Demuth, J.E. and Ibach, H., Chem. Phys. Lett., **60** (1979) p. 395.

[13] Mavrikakis, M. and Barteau, M.A., J. Mol. Cat. A: Chem., **131** (1998) p. 131.

[14] Wachs, I.E. and Madix, R.J., J. Catal., **53** (1978) p. 208.

[15] Sim, W.S., Gardner, P., and King, D.A., J. Phys. Chem., **99** (1995) p. 16002.

[16] Camplin, J.P. and McCash, E.M., Surf. Sci., **360** (1996) p. 229.

[17] Barros, R.B., Garcia, A.R., and Ilharco, L.M., J. Phys. Chem. B, **105** (2001) p. 11186.

[18] Hrbek, J., De Paola, R.A., and Hoffmann, F.M., J. Chem. Phys., **81** (1984) p. 2818.

[19] Peremans, A., Maseri, F., Darville, J., and Gilles, J.M., Surf. Sci., **227** (1990) p. 73.

[20] Pratt, S.J., Escott, D.K., and King, D.A., J. Chem. Phys., **119** (2003) p. 10867.

[21] Ehlers, D.H., Spitzer, A., and Luth, H., Surf. Sci., **160** (1985) p. 57.

[22] Bhattacharya, A.K., Chesters, M.A., Pemble, M.E., and Sheppard, N., Surf. Sci., **206** (1988) p. L845.

[23] Parmeter, J.E., Jiang, X.D., and Goodman, D.W., Surf. Sci., **240** (1990) p. 85.

[24] Serrallach, A., Meyer, R., and Gunthard, H.H., J. Mol. Spec., **52** (1974) p. 94.

[25] Falk, M. and Whalley, E., J. Chem. Phys., **34** (1961) p. 1554.

[26] Brosseau, R., Brustein, M.R., and Ellis, T.H., Surf. Sci., **294** (1993) p. 243.

[27] Brosseau, R., Brustein, M.R., and Ellis, T.H., Surf. Sci., **280** (1993) p. 23.

[28] Robyr, P., Meier, B.H., Fischer, P., and Ernst, R.R., J. Am. Chem. Soc., **116** (1994) p. 5315.

[29] Torrie, B.H., Binbrek, O.S., Strauss, M., and Swainson, I.P., J. Solid State Chem., **166** (2002) p. 415.

[30] Torrie, B.H., Weng, S.X., and Powell, B.M., Mol. Phys., **67** (1989) p. 575.

[31] Tauer, K.J. and Lipscomb, W.N., Acta. Crys., **5** (1952) p. 606.

[32] Staveley, L.A.K. and Hogg, M.A.P., J. Chem. Soc., (1954) p. 1013.

[33] Fischer, F. and Fuhrich, R., Z. Naturfors. Sect. A-J. Phys. Sci., **38** (1983) p. 31.

[34] Weng, S.X. and Anderson, A., Phys. Status Solidi B-Basic Res., **172** (1992) p. 545.

[35] Turrell, G., *Infrared and Raman Spectra of Crystals*. 1972: Academic Press Inc. 117.

Chapter 6: Methanol Adsorption on Highly Oriented Pyrolitic Graphite (HOPG): A TPD Study

6.1 Introduction

Methanol is an extremely important molecule in the interstellar medium (ISM), as already discussed in *Chapter 5*. An understanding of the adsorption and desorption of methanol is essential to aid our understanding of the chemistry of star forming regions of the ISM. With this in mind, this chapter describes the first detailed TPD study of the adsorption and desorption of methanol on highly oriented pyrolitic graphite (HOPG). Also presented is a model for the adsorption and desorption of methanol on HOPG using information from this TPD study and the RAIRS study already presented in *Chapter 5*.

The adsorption and decomposition of methanol on metal surfaces has been discussed in several reviews [1-3], and in the previous chapter. Methanol decomposes to form methoxy (H_3CO-) on most metal surfaces [4, 5] and this decomposition can be promoted by co-adsorbed oxygen [6-8]. Adsorption of methanol at low temperatures leads to the formation of physisorbed multilayers, adsorbed on top of the underlying chemisorbed layer [9-17]. A detailed review of previous vibrational studies of methanol adsorption was presented in *Chapter 5*.

In addition to the vibrational studies of methanol adsorption already discussed in, there have also been several previous TPD studies of methanol adsorbed on metal surfaces. On Ru{001} [12], two desorption peaks were observed at 155 K and 250 K. The lower temperature peak shifted up in temperature with increasing exposure and could not be saturated. This was assigned to desorption from the multilayer. The peak at 250 K shifted down in temperature with increasing exposure and was assigned to desorption of a chemisorbed monolayer species. By monitoring multiple masses during the experiment, it was determined that the monolayer dissociated upon adsorption, and re-

combined during the TPD process. Similar observations were noted for methanol adsorption on Al{111} [13].

On Pd{111} [2] and Pd{110} [9] a chemisorbed species was observed to desorb at approximately 225 K, while desorption from the multilayer took place at approximately 150 K. Reversible adsorption of methanol was also observed on NiO{100} by Wu and co-workers [18]. A desorption peak from the monolayer was seen at 298 K, while a multilayer desorption peak was observed at 150 K. It was also evident that population of multilayers began prior to completion of the monolayer. Furthermore, multilayer peaks did not share a common "leading edge" on the low temperature side, implying a non-zero order desorption process. This fractional order process demonstrated the existence of hydrogen bonding within the condensed multilayer phase. A similar fractional order desorption process has been reported for condensed multilayers on Pd{100} [19, 20]. This condensed multilayer was observed to grow on top of a physisorbed monolayer, which in turn grew on top of a chemisorbed monolayer.

TPD studies of methanol adsorption on Ag{111} have also been undertaken [14]. At low exposures, a single peak was observed, which was assigned to desorption from the monolayer. With increasing exposure, two further peaks were observed and assigned to desorption from multilayers of amorphous and crystalline phases of methanol. The observation of the crystalline phase was believed to be a result of the temperature ramp applied during the TPD process, converting some of the amorphous methanol to crystalline methanol.

6.2 Experimental

All experiments were performed in the UHV chamber described in *Chapter 2*. Sample cleanness was achieved using the techniques described in *Chapter 3*. TPD experiments investigated the adsorption of methanol (99.9% purity, BDH Laboratory Supplies) by back filling the chamber via a high precision leak valve, in a controlled manner. All exposures are measured in Langmuir (L), where 1 L is equivalent to back filling the chamber to a pressure of 1×10^{-6} mbar for 1 second.

All TPD spectra were recorded at a heating rate of 0.5 K s^{-1} and show desorption peaks for mass 31. Mass 31 is the major fragment ion created in the mass spectrometer and is not the result of any surface chemistry. To confirm this, the ratio of mass 32 to 31 was checked periodically during experiments and compared with the cracking pattern of methanol, shown in *Figure 6.1*. For all spectra reported here, the ratio of mass 32 to 31 was constant whatever the dosing conditions.

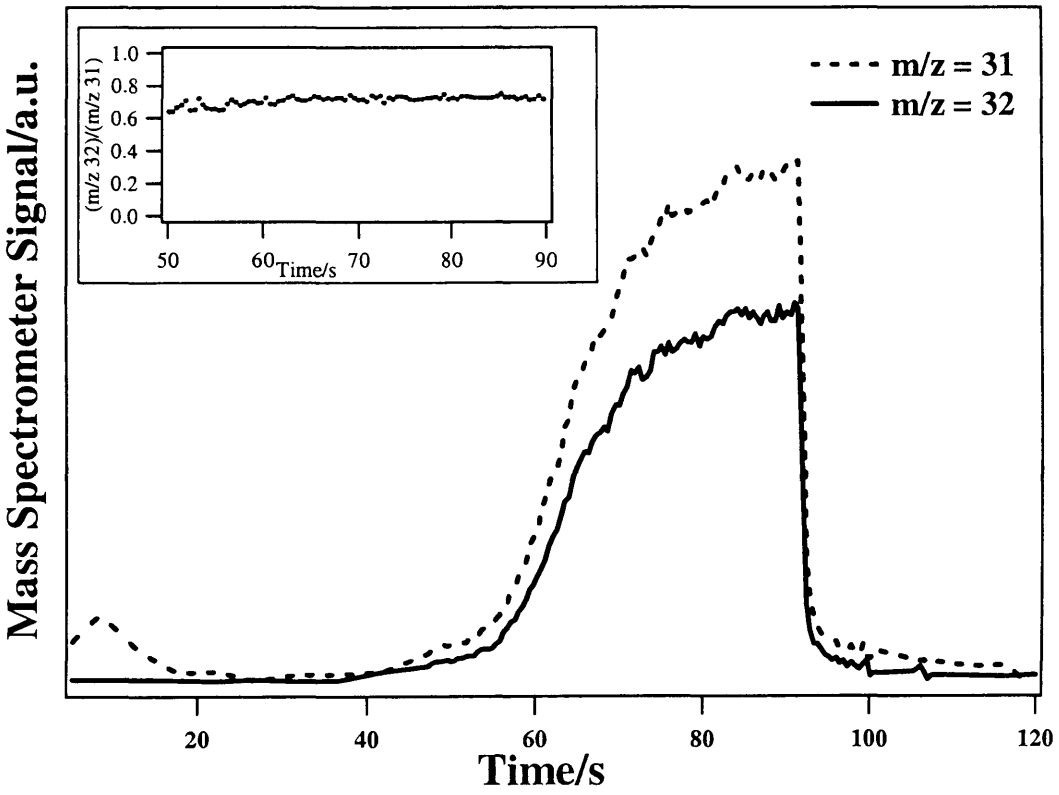

Figure 6.1: Mass spectrum resulting from dosing varying amounts of methanol into the UHV chamber. Relative intensities are shown for masses 31 and 32. Inset shows the ratio of mass 32 to mass 31 for the same mass spectrum.

6.3 Results and Discussion

TPD spectra were recorded for the adsorption of methanol on HOPG at 100 K and 130 K. A series of TPD spectra for increasing exposures of methanol on HOPG at 100 K are shown in *Figure 6.2*.

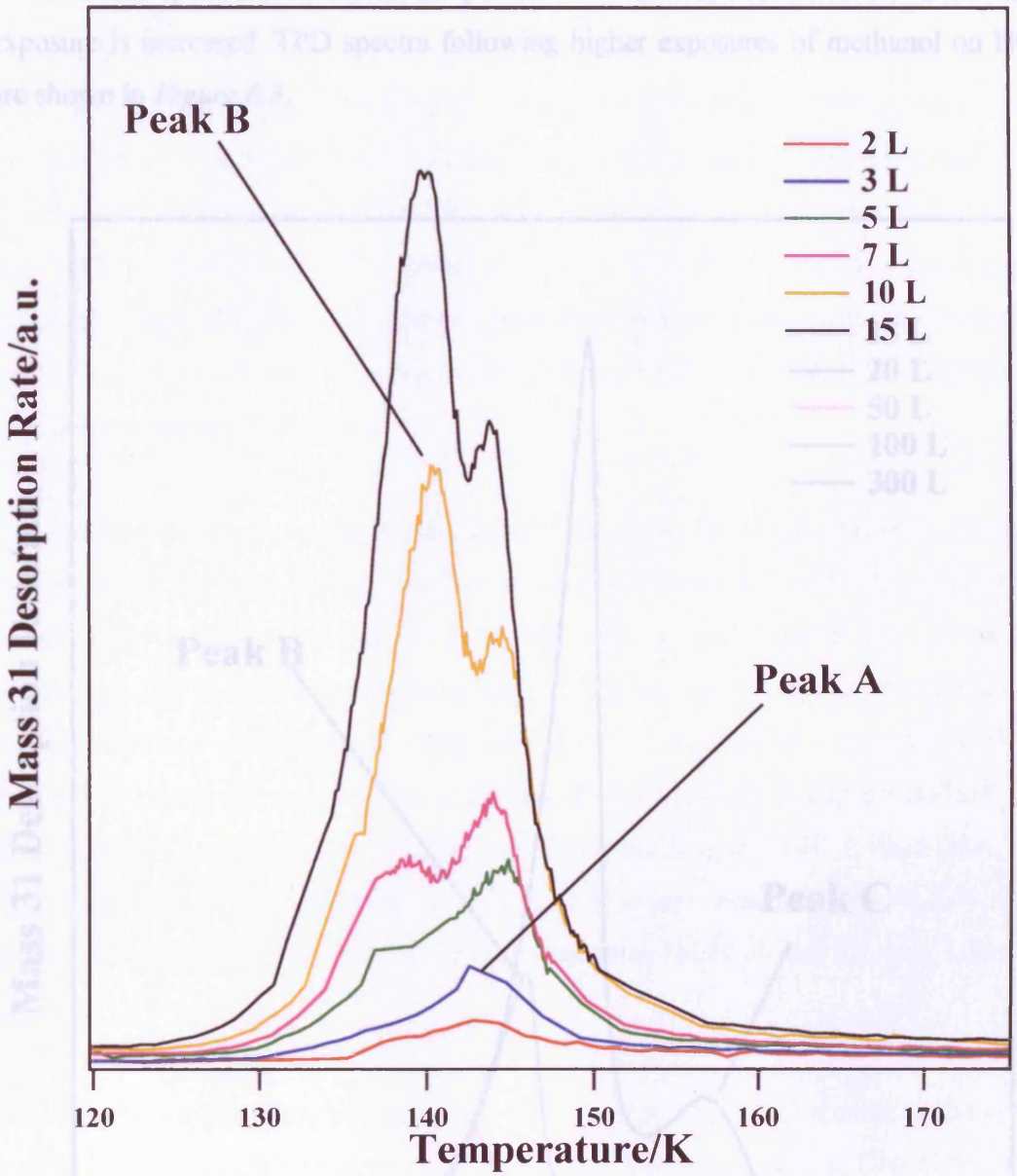

Figure 6.2: TPD spectra following exposures of methanol adsorbed on HOPG at 100 K. The figure shows spectra following exposures of 2 L, 3 L, 5 L, 7 L, 10 L and 15 L.

At the lowest exposures of methanol (2 L and 3 L) only one peak is observed with a desorption temperature of 144 K. This is labelled as *Peak A*. As the exposure is increased to 5 L a second, lower temperature, peak is observed, initially as a shoulder on *Peak A*. By 7 L this shoulder can be clearly identified at 139 K as a separate peak, labelled as *Peak B*. However, at this exposure, *Peak A* still has a higher intensity than *Peak B*. As the exposure is further increased to 10 L and 15 L *Peak B* begins to

dominate the spectrum. The peak temperature increases for both *Peaks A* and *B* as the exposure is increased. TPD spectra following higher exposures of methanol on HOPG are shown in *Figure 6.3*.

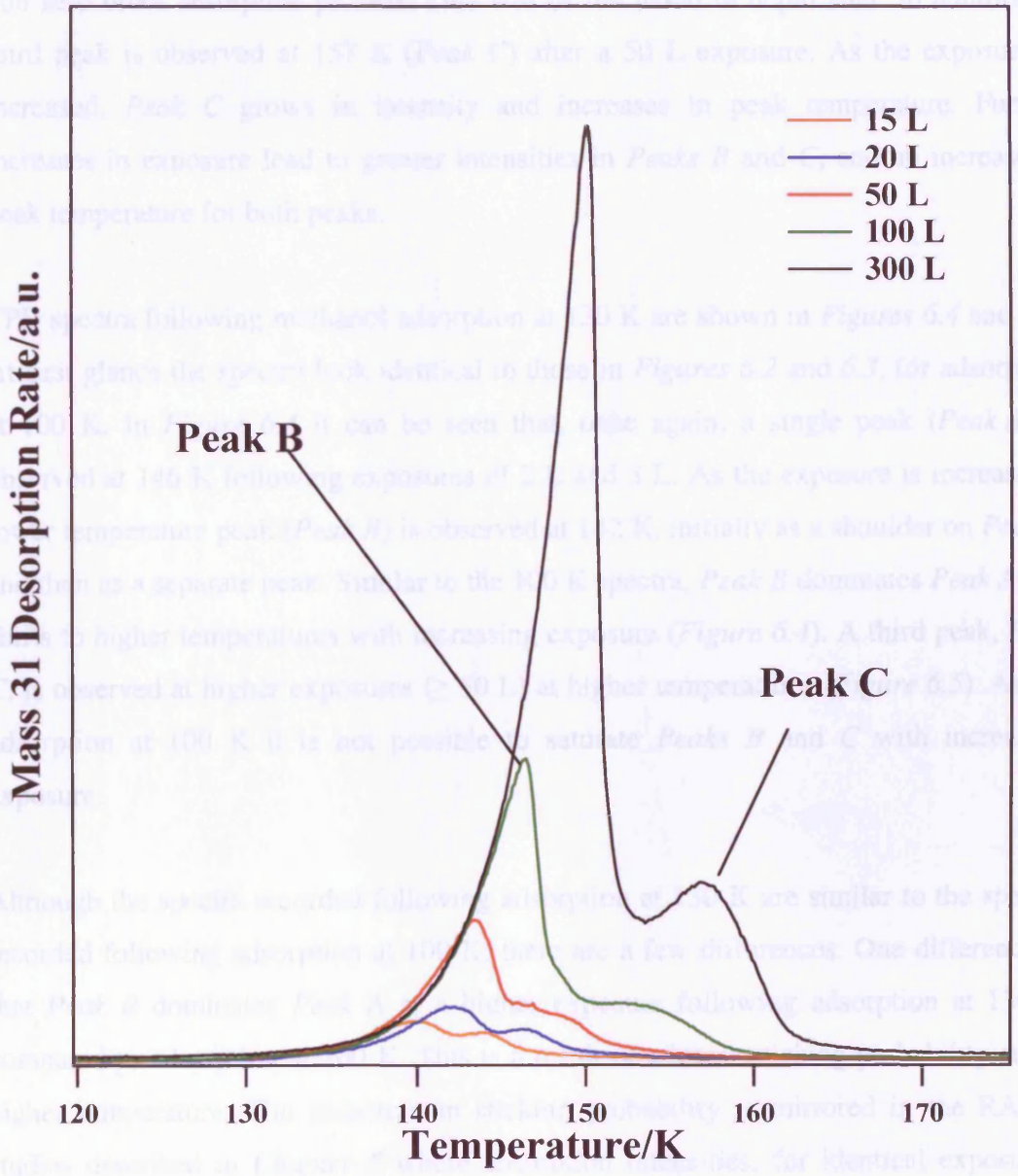

Figure 6.3: TPD spectra following exposures of methanol adsorbed on HOPG at 100 K. The figure shows spectra following exposures of 15 L, 20 L, 50 L, 100 L and 200 L.

Following 50 L methanol exposure, *Peak B* dominates *Peak A* and it is no longer possible to distinguish between the two peaks. As the exposure is increased further to 300 L, this combined peak shifts up in temperature (*Figure 6.3*). This combined peak does not share a perfect common leading edge with increasing exposure, implying a non-zero order desorption process. This will be discussed in depth later. In addition, a third peak is observed at 157 K (*Peak C*) after a 50 L exposure. As the exposure is increased, *Peak C* grows in intensity and increases in peak temperature. Further increases in exposure lead to greater intensities in *Peaks B* and *C*, and an increase in peak temperature for both peaks.

TPD spectra following methanol adsorption at 130 K are shown in *Figures 6.4* and *6.5*. At first glance the spectra look identical to those in *Figures 6.2* and *6.3*, for adsorption at 100 K. In *Figure 6.4* it can be seen that, once again, a single peak (*Peak A*) is observed at 146 K following exposures of 2 L and 3 L. As the exposure is increased a lower temperature peak (*Peak B*) is observed at 142 K, initially as a shoulder on *Peak A* and then as a separate peak. Similar to the 100 K spectra, *Peak B* dominates *Peak A* and shifts to higher temperatures with increasing exposure (*Figure 6.4*). A third peak, *Peak C*, is observed at higher exposures ($\geq$ 50 L) at higher temperatures (*Figure 6.5*). As for adsorption at 100 K it is not possible to saturate *Peaks B* and *C* with increasing exposure.

Although the spectra recorded following adsorption at 130 K are similar to the spectra recorded following adsorption at 100 K, there are a few differences. One difference is that *Peak B* dominates *Peak A* at a higher exposure following adsorption at 130 K compared to adsorption at 100 K. This is a result of a lower sticking probability at the higher temperature. The reduction in sticking probability is mirrored in the RAIRS studies described in *Chapter 5* where absorption intensities, for identical exposures, were lower for adsorption at 130 K compared to adsorption at 97 K. Another difference is that the TPD spectra appear to have shifted up by approximately 5 K following adsorption at 130 K. This is possibly a result of differing amounts of hydrogen bonding within the adlayers formed after adsorption at 130 K compared to at 100 K. This explanation is supported by the RAIR spectra seen in *Chapter 5*, which showed that the

O-H stretching mode (the mode most sensitive to changes in hydrogen bonding) had a slightly higher frequency following adsorption at 130 K than at 97 K. The final difference between TPD spectra recorded following adsorption at 100 K and 130 K is that *Peak C* is more pronounced following adsorption at 130 K compared to adsorption at 100 K. This will be discussed in more detail later.

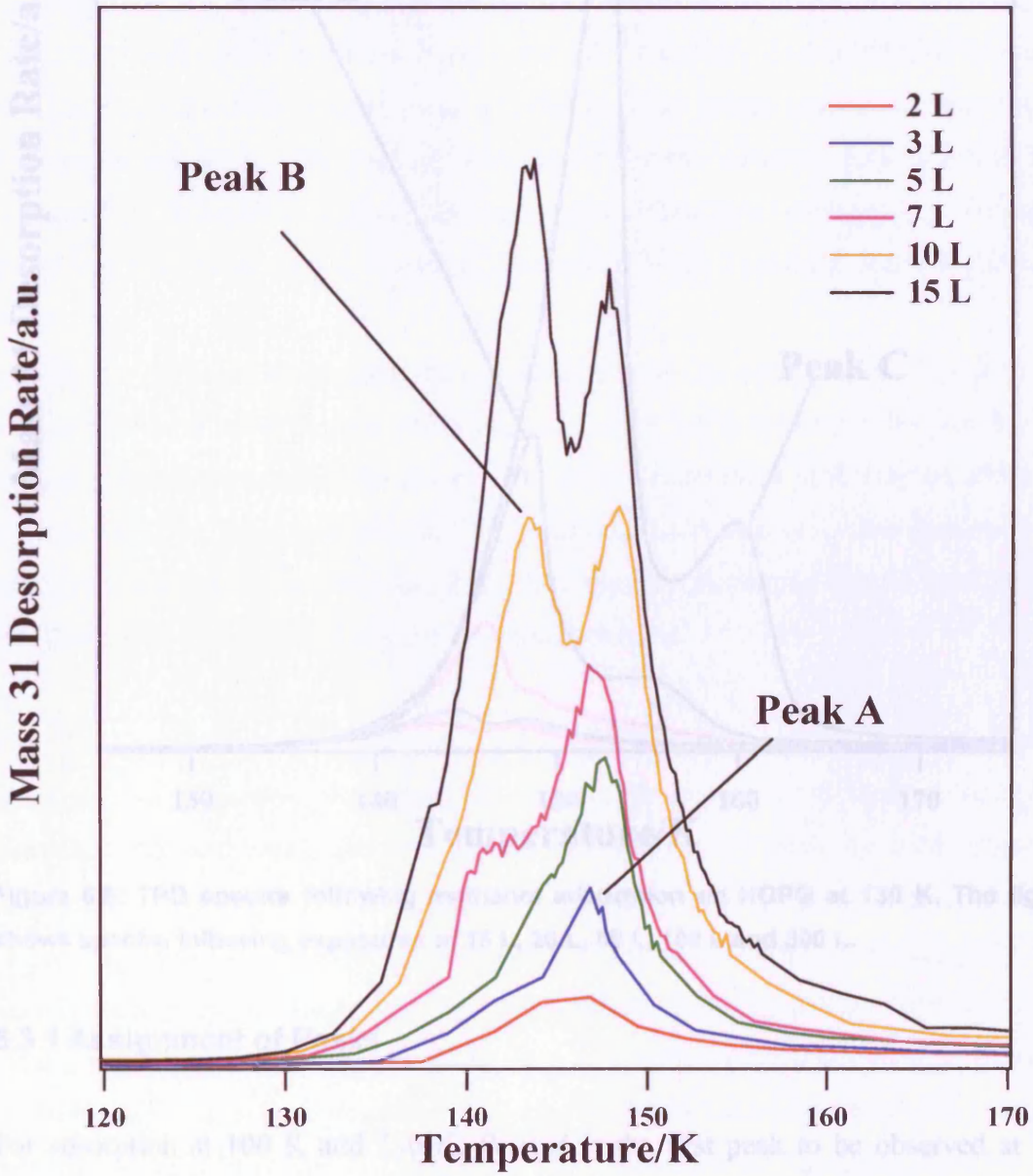

Figure 6.4: TPD spectra following methanol adsorption on HOPG at 130 K. The figure shows spectra following exposures of 2 L, 3 L, 5 L, 7 L, 10 L and 15 L.

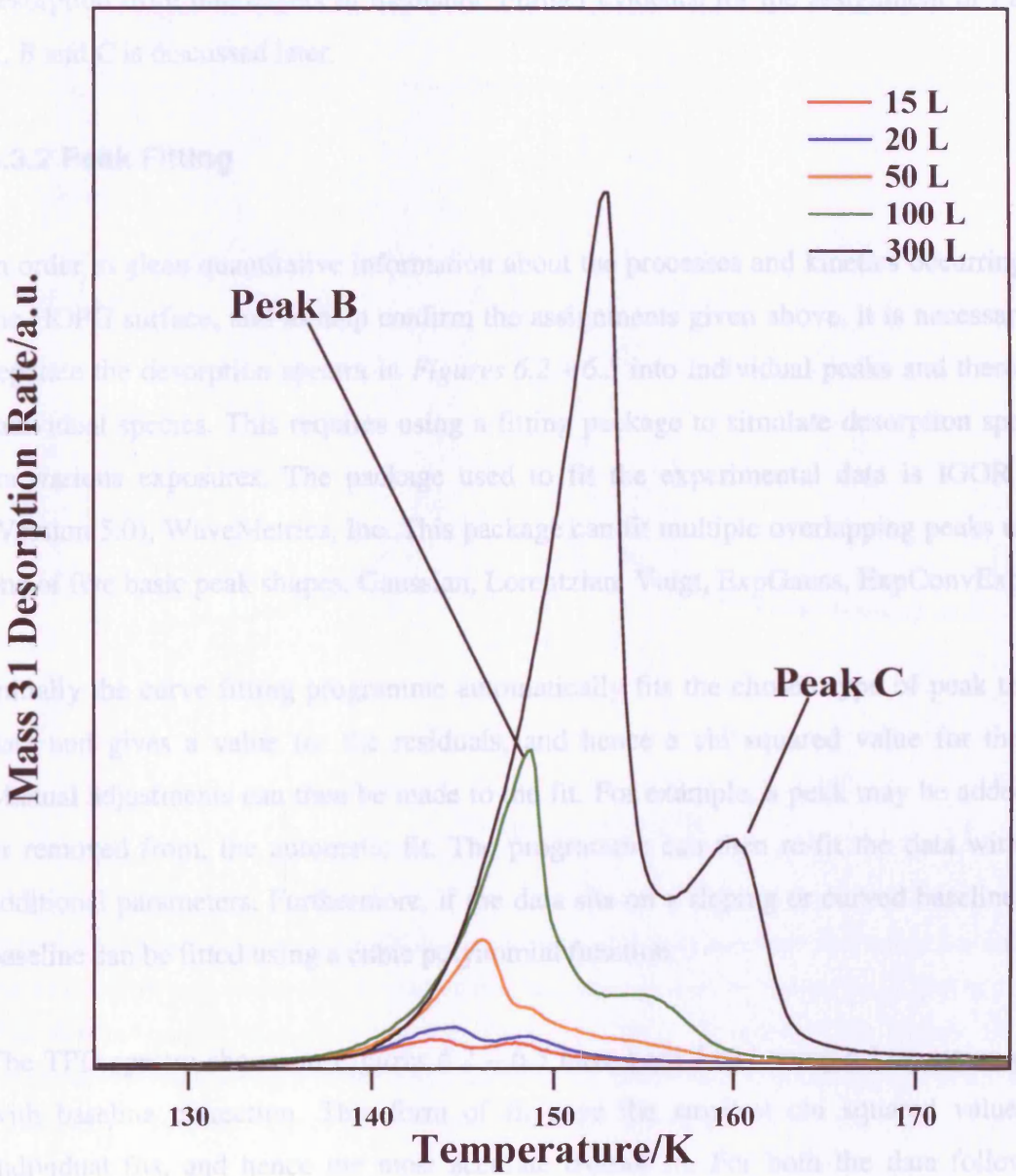

Figure 6.5: TPD spectra following methanol adsorption on HOPG at 130 K. The figure shows spectra following exposures of 15 L, 20 L, 50 L, 100 L and 300 L.

6.3.1 Assignment of Peaks

For adsorption at 100 K and 130 K, *Peak A* is the first peak to be observed at low exposures. Hence, the species giving rise to this peak must be closest to the surface and is therefore assigned to desorption from a monolayer of methanol. *Peaks B* and *C* cannot be saturated and are observed after *Peak A*. They are therefore both assigned to

desorption from multilayers of methanol. Further evidence for the assignment of *Peaks A*, *B* and *C* is discussed later.

6.3.2 Peak Fitting

In order to glean quantitative information about the processes and kinetics occurring on the HOPG surface, and to help confirm the assignments given above, it is necessary to separate the desorption spectra in *Figures 6.2 - 6.5* into individual peaks and therefore individual species. This requires using a fitting package to simulate desorption spectra for various exposures. The package used to fit the experimental data is IGOR Pro (Version 5.0), WaveMetrics, Inc. This package can fit multiple overlapping peaks using one of five basic peak shapes: Gaussian, Lorentzian, Voigt, ExpGauss, ExpConvExp.

Initially the curve fitting programme automatically fits the chosen type of peak to the data and gives a value for the residuals, and hence a chi squared value for the fit. Manual adjustments can then be made to the fit. For example, a peak may be added to, or removed from, the automatic fit. The programme can then re-fit the data with the additional parameters. Furthermore, if the data sits on a sloping or curved baseline, the baseline can be fitted using a cubic polynomial function.

The TPD spectra shown in *Figures 6.2 – 6.5* have been fitted using a Lorentzian peak with baseline correction. This form of fit gave the smallest chi squared value for individual fits, and hence the most accurate overall fit. For both the data following adsorption at 100 K and 130 K, the number of peaks used in the fit reflects the number of peaks observed in the TPD spectrum. Hence, for the 2 L and 3 L spectra only one peak is used (*Peak A*), while two peaks are used for the 5 L exposure up to the 20 L exposure (*Peaks A* and *B*). For exposures from 50 L and above it was no longer possible to distinguish *Peak A* from *Peak B* so only two peaks are used to model *Peaks B* and *C*. An example of a fit to the 15 L exposure TPD data recorded following adsorption at 100 K (*Peaks A* and *B*) is given in *Figure 6.6*. It can be seen from the figure that the fits are very good with respect to the experimental data. The quality of this fit is representative of the quality of all of the fits.

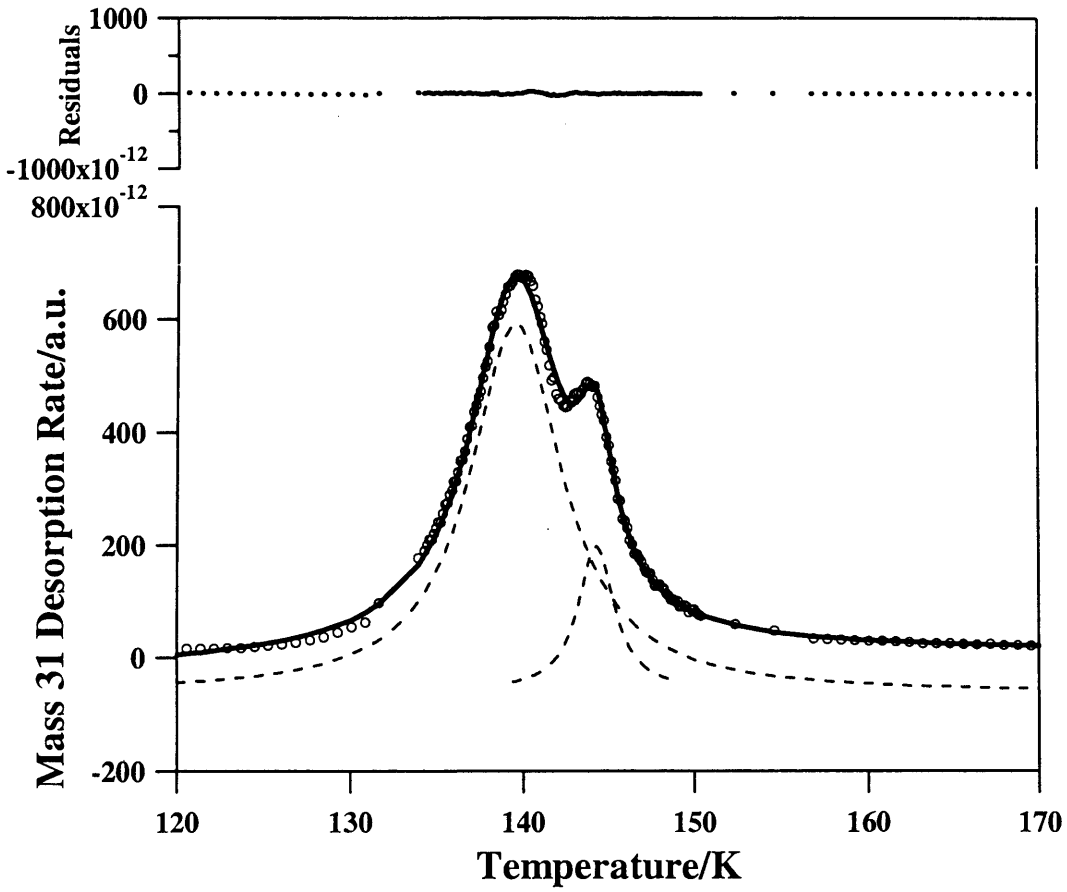

Figure 6.6: Figure showing the IGOR Pro fitting using two baseline corrected Lorentzian functions to fit experimental TPD data for a 15 L exposure of methanol on HOPG at 100 K. The dashed curves represent the individual Lorentzian functions; the circles are the experimental data points and the solid curve is the combined fit to the experimental data. The residual for each data point is shown above the spectra.

To determine the accuracy of the fitted data with respect to the experimental data, the integrated areas under the measured and fitted TPD curves have also been calculated and are given in *Table 6.1*, along with the chi squared value for the fit for the 100 K TPD spectra. This fitting process was repeated for two different sets of experimental data recorded under the same experimental conditions. This allowed a further test of the integrity of the fits and of the calculated areas of individual peaks. In all cases good agreement was noted between the measured and fitted TPD curves for adsorption of methanol on HOPG.

Table 6.1: Table showing the integrated areas of the experimental data and the fitted data over identical temperature intervals for methanol adsorbed on HOPG at 100 K. The chi squared value for the fitted data and the percentage error of the fitted data with relation to the experimental data are also given.

Exposure / L	Integrated area of recorded spectra / a.u.	Integrated area of fitted spectra / a.u.	Chi squared value for the fit	% error of fit data
2	3.71×10^{-10}	3.70×10^{-10}	8.78×10^{-23}	-0.15
3	8.33×10^{-10}	8.42×10^{-10}	2.32×10^{-22}	1.07
5	1.77×10^{-9}	1.76×10^{-9}	9.17×10^{-22}	-0.79
7	2.43×10^{-9}	2.28×10^{-9}	1.41×10^{-21}	-2.16
10	4.63×10^{-9}	4.66×10^{-9}	1.12×10^{-20}	0.81
15	6.53×10^{-9}	6.59×10^{-9}	1.45×10^{-20}	0.87
20	8.51×10^{-9}	8.65×10^{-9}	5.52×10^{-20}	1.66
50	1.88×10^{-8}	1.92×10^{-8}	1.11×10^{-18}	1.88
100	3.55×10^{-8}	3.60×10^{-8}	1.27×10^{-17}	1.42
300	1.00×10^{-7}	1.02×10^{-7}	2.78×10^{-16}	1.44

The integrated areas for the recorded spectra were calculated by subtracting the background intensity from the spectrum and then using the trapezium rule over a temperature interval where the peak intensity is appreciable. This is generally over a temperature interval of 122 K to 171 K. The integrated areas for the fitted spectra are given as parameters by the IGOR Pro package.

Table 6.1 clearly shows that as the exposure is increased the chi squared value increases, hence showing that the lower exposures are fitted more accurately. This is a result of the difficulty in trying to fit *Peak C*. The IGOR Pro package does not allow a mixture of peaks to be fitted to the recorded spectra; hence all peaks are modelled as Lorentzians. The Lorentzian fits were used as they gave the lowest chi squared values for all spectra. The fits for high exposures are still accurate enough since the percentage error between the area of the fitted data and the area of the experimental data is very

small. Fits to the TPD spectra recorded following adsorption at 130 K follow a similar pattern to the fits to the TPD spectra recorded following adsorption at 100 K, with lower exposures having smaller chi squared values than higher exposures, but with small overall percentage errors.

A series of simulated spectra, resulting from the fits for the TPD data recorded following adsorption at 100 K are shown in *Figures 6.7* and *6.8*. A comparison of *Figures 6.7* and *6.8* with *Figures 6.2* and *6.3* shows the good agreement between the simulated spectra and the experimental data. An anomaly in the fitted data is that at the highest exposures, spectra do not share a common leading edge. This is a result of the fitting procedure only allowing one type of peak shape to be used during simulations.

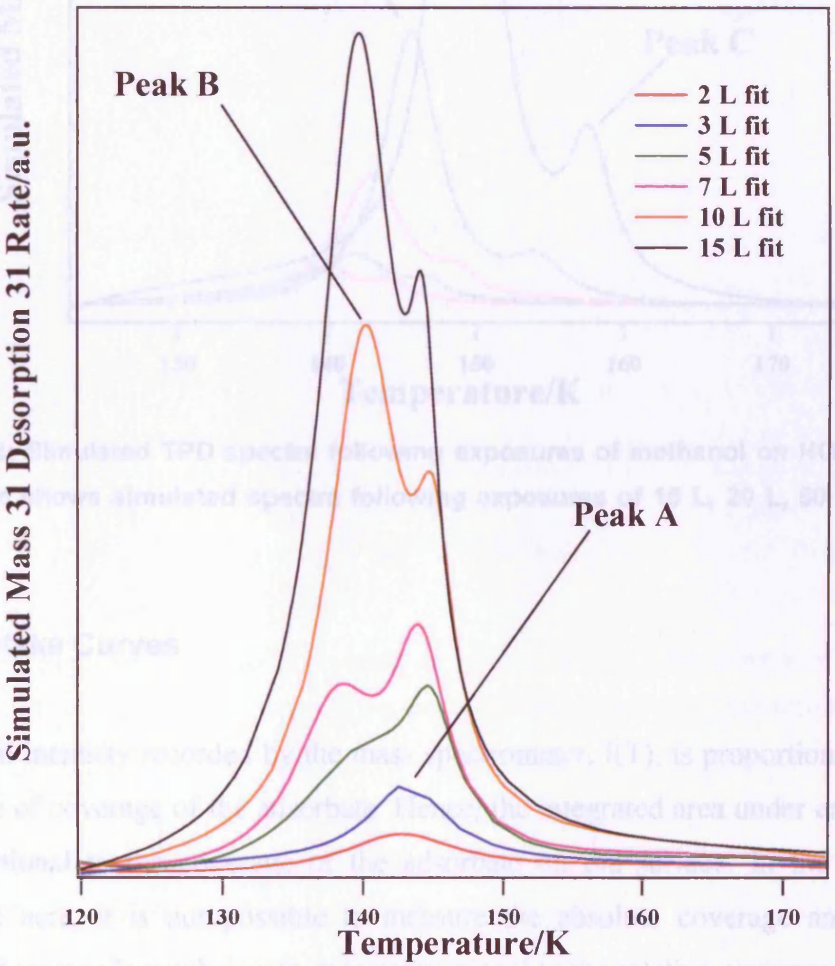

Figure 6.7: Simulated TPD spectra following exposures of methanol on HOPG at 100 K. The figure shows simulated spectra following exposures of 2 L, 3 L, 5 L, 7 L, 10 L and 15 L.

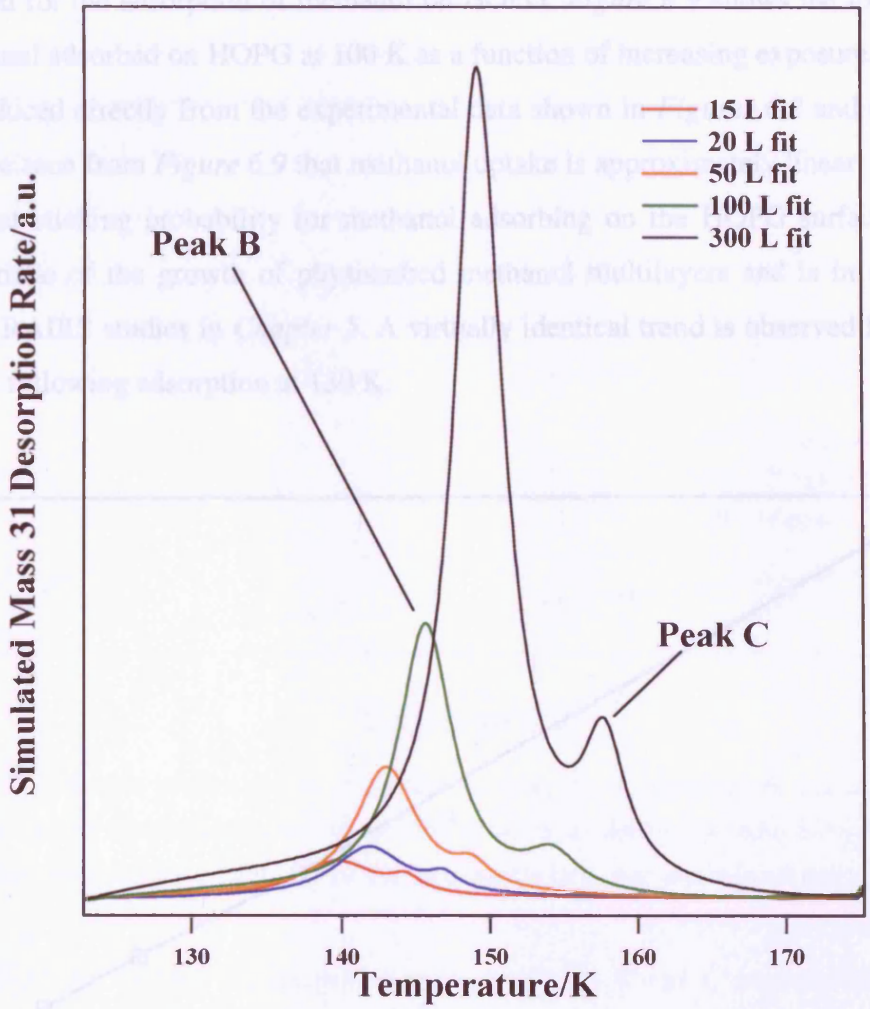

Figure 6.8: Simulated TPD spectra following exposures of methanol on HOPG at 100 K. The figure shows simulated spectra following exposures of 15 L, 20 L, 50 L, 100 L and 300 L.

6.3.3 Uptake Curves

The signal intensity recorded by the mass spectrometer, I(T), is proportional to the rate of change of coverage of the adsorbate. Hence, the integrated area under each spectrum is proportional to the coverage of the adsorbate on the surface. In the experiments described here, it is not possible to measure the absolute coverage and hence the integrated area under each spectrum is proportional to the relative coverage of adsorbate on the surface. Furthermore, the area under each individual peak is proportional to the relative coverage of the species giving rise to that peak. In this way, uptake curves can

be plotted for the adsorption of methanol on HOPG. *Figure 6.9* shows the total uptake of methanol adsorbed on HOPG at 100 K as a function of increasing exposure. This plot was produced directly from the experimental data shown in *Figures 6.2* and *6.3*. It can clearly be seen from *Figure 6.9* that methanol uptake is approximately linear, indicating a constant sticking probability for methanol adsorbing on the HOPG surface. This is characteristic of the growth of physisorbed methanol multilayers and is in agreement with the RAIRS studies in *Chapter 5*. A virtually identical trend is observed for spectra recorded following adsorption at 130 K.

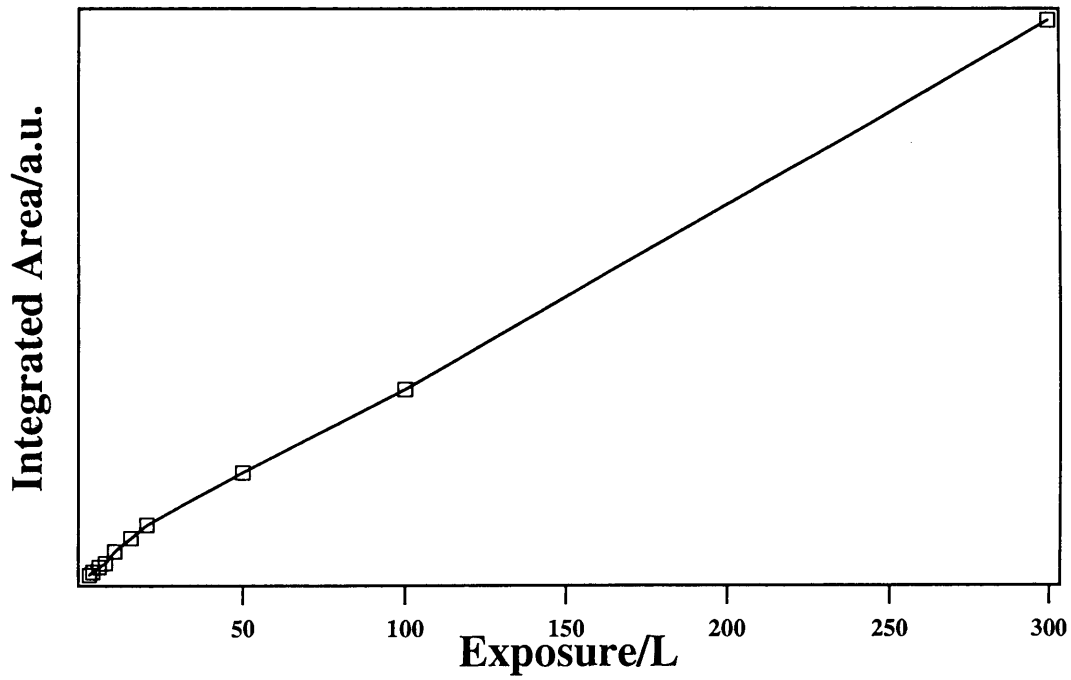

Figure 6.9: Graph showing, as a function of exposure, the total integrated area of the experimentally measured TPD curves obtained following methanol adsorption on HOPG at 100 K.

As mentioned above, it is also possible to determine the integrated area, and hence the relative coverage, for individual species as a function of exposure. *Figure 6.10* shows the integrated areas of *Peaks A*, *B* and *C* plotted as a function of exposure. Individual peak areas can only be determined by using the fitted spectra and the plot shows the average of two sets of data. Similar trends are observed for fits to spectra following methanol adsorption on HOPG at 130 K.

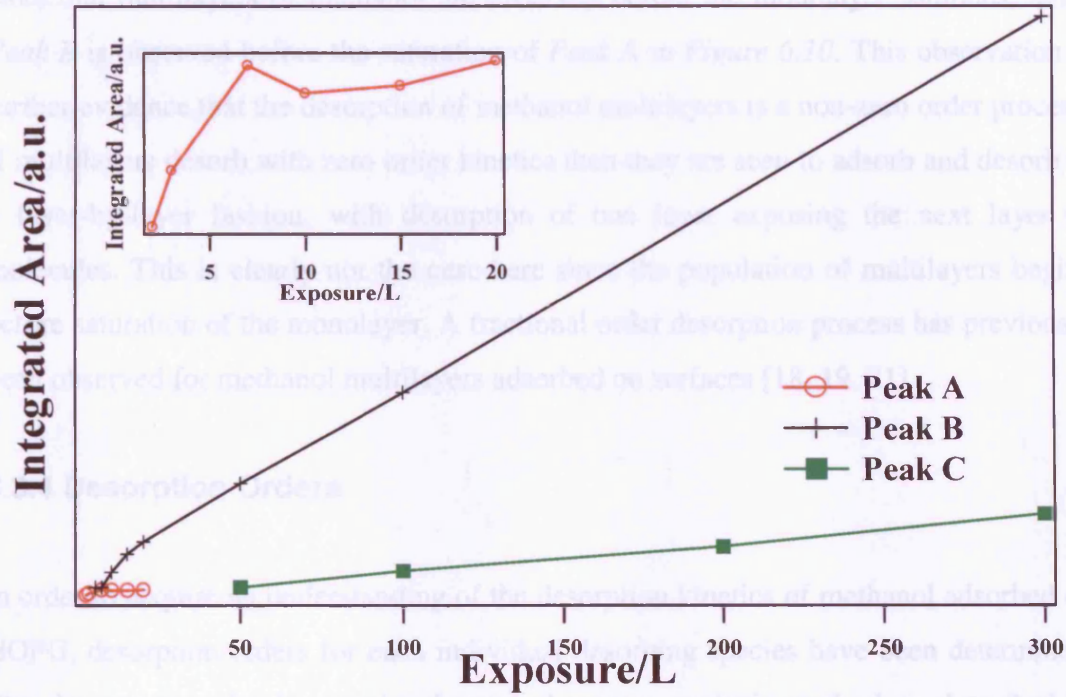

Figure 6.10: Graph showing the integrated areas, as a function of exposure, of the individual peaks that make up the fitted TPD spectra for methanol adsorption on HOPG at 100 K. The inset shows a close up of the data for Peak A, the monolayer peak.

Figure 6.10 shows that the integrated areas of *Peaks B* and *C* increase linearly with exposure. This implies that the relative coverage of the species associated with *Peaks B* and *C* increases linearly with exposure, and that neither species can be saturated. This is in agreement with the assignment of *Peaks B* and *C* to the desorption of multilayers of methanol from the surface.

The inset in *Figure 6.10* shows a close-up of the integrated area, as a function of exposure, of *Peak A*. As the exposure is increased from 2 L to 7 L the integrated area, and hence the relative coverage, increases. However, for exposures of 10 L and above, the integrated area appears to saturate. This confirms the assignment of *Peak A* to desorption from the monolayer. A similar trend is noted for methanol adsorption on HOPG at 130 K, however the monolayer peak, *Peak A*, saturates at a higher exposure. This again is a result of the lower sticking probability at the higher adsorption temperature.

Note that multilayers of methanol are observed before the monolayer saturates, since *Peak B* is observed before the saturation of *Peak A* in *Figure 6.10*. This observation is further evidence that the desorption of methanol multilayers is a non-zero order process. If multilayers desorb with zero order kinetics then they are seen to adsorb and desorb in a layer-by-layer fashion, with desorption of one layer exposing the next layer of molecules. This is clearly not the case here since the population of multilayers begins before saturation of the monolayer. A fractional order desorption process has previously been observed for methanol multilayers adsorbed on surfaces [18, 19, 21].

6.3.4 Desorption Orders

In order to acquire an understanding of the desorption kinetics of methanol adsorbed on HOPG, desorption orders for each individual desorbing species have been determined. The desorption order is calculated using the same analysis method as described in *Section 4.4.1*. Using *Equation 4.6* a plot of $\ln[I(T)]_x$ against $\ln[\theta_{rel}]_x$ (where $[I(T)]_x$ is the QMS signal intensity at a fixed temperature T_x and $[\theta_{rel}]_x$ is the relative coverage at a temperature T_x) gives a straight line with a gradient of n, the desorption order [22]. As before, it has been assumed that the pre-exponential factor does not vary with coverage or temperature, since all of the adsorbed methanol is physisorbed on the surface. The validity of this assumption will be demonstrated later. Furthermore, it has been assumed that the desorption energy does not vary with coverage or temperature. The validity of this assumption will be again demonstrated later when a weak coverage, and no temperature, dependence will be shown for the desorption energy. *Figure 6.11* shows a plot of $\ln[I(T)]_x$ against $\ln[\theta_{rel}]_x$ for a T_x of 140 K for methanol adsorption on HOPG at 100 K.

This value of T_x was chosen to ensure sufficient intensity in both the monolayer peak (*Peak* A) and the multilayer peak (*Peak B*) for all exposures. It can clearly be seen from *Figure 6.11* that there is a change in gradient for exposures below 10 L and for above 10 L, and hence two different desorption orders are observed. This change in gradient can be explained by looking at *Figures 6.2* and *6.3*, which show that at low exposures (< 10 L) the chosen T_x value passes through *Peak A*, the monolayer peak, while for

exposures above 10 L the chosen T_x value passes through *Peak B*, the multilayer peak. Hence *Figure 6.11* shows that multilayers of methanol have a different order of desorption from the monolayer. In order to check the accuracy of the desorption orders for the monolayer and multilayer, this process was repeated for a variety of T_x values. The gradients obtained from the plots, and hence the desorption orders, for the monolayer and multilayer peaks at a range of T_x values are given in *Table 6.2*. These plots were performed for several experiments and provided consistent results.

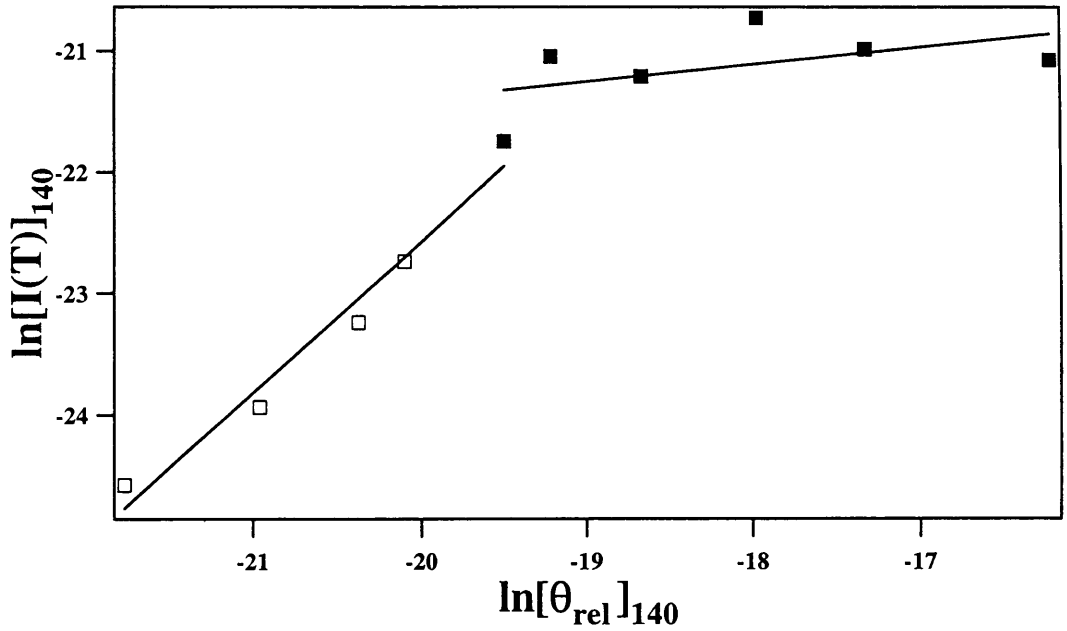

Figure 6.11: A plot of $\ln[I(T)]_x$ against $\ln[\theta_{rel}]_x$ for a T_x of 140 K for various exposures of methanol adsorbed on HOPG at 100 K. The open squares indicate exposures below 10 L and the filled squares indicate exposures above 10 L.

Table 6.2: Table showing desorption orders for the monolayer and multilayer species, for a variety of T_x values, for methanol adsorbed on HOPG at 100 K.

T_x value	Desorption order for *Peak A* (monolayer)	Desorption order for *Peak B* (multilayer)
140 K	1.28	0.17
142.5 K	1.09	0.46
145 K	1.31	0.41

Table 6.2 shows that *Peak A* has a desorption order of 1.23 ± 0.14. This confirms the assignment of this peak to desorption of the monolayer. Since methanol is believed to adsorb reversibly, a first order desorption process would be expected. A desorption order of 1 has previously been used to model methanol desorption from the monolayer on $Al_2O_3\{0001\}$ [21]. A first order process assumes that each individual desorbing molecule is not influenced by surrounding molecules on the surface. The desorption order of 1.23 ± 0.14 for monolayer methanol adsorbed on HOPG is slightly higher than the expected value of 1, however this can be explained by interactions within the monolayer such as hydrogen bonding.

Table 6.2 shows that *Peak B*, the multilayer peak, has a desorption order of 0.35 ± 0.21. This is in excellent agreement with previous studies, which have also determined desorption from the multilayer to be a fractional order process [18, 19, 21]. The observation of a fractional order desorption process for the multilayer is confirmed by the spectra in *Figure 6.3*, which show that increasing exposures of methanol adsorbed on HOPG do not share a common leading edge, as would be expected for perfect zero order desorption. The observed fractional order for desorption of the multilayer can be attributed to hydrogen bonding within the layer. Further evidence for hydrogen bonding within multilayers of methanol is provided by the broadness of the O-H stretch in the RAIR spectra shown in *Chapter 5*. Similar analysis was carried out for the TPD spectra recorded following adsorption at 130 K and virtually identical values for the desorption orders are obtained.

Note that no quantitative analysis has been carried out for *Peak C* since there is only a small amount of data for this peak. Furthermore it is believed that this peak occurs as a result of a phase change during the TPD heating process, and hence evaluating a desorption order for this peak is not relevant. This is discussed further later.

6.3.5 Desorption Energies

Desorption energies for the monolayer and the multilayer can also be calculated for methanol adsorbed on HOPG. In this way, it is possible to gain an indication of the

binding strength of the methanol both within the monolayer and the multilayer. Note that the complete analysis technique, described in *Section 4.4.2*, could not be used to determine desorption energies for the fitted data of the monolayer and multilayer desorption peaks. This is due to the fitted data causing spurious data points when selecting a fixed relative coverage term, θ'_{rel}. An alternative method for determining the desorption energies has therefore been used here. Once again, this method uses the Polanyi-Wigner equation (*Equation 6.1*).

$$r_{des} = -\frac{\partial\theta}{\partial t} = \upsilon_n \theta^n \exp\left[\frac{-E_{des}}{RT_S}\right] \qquad \textit{Equation 6.1}$$

Taking logs and rearranging *Equation 6.1* leads to

$$\ln I(T) \propto n \ln \upsilon_n + n \ln \theta_{rel} - \frac{E_{des}}{RT_S} \qquad \textit{Equation 6.2}$$

Further rearrangement leads to

$$\ln I(T) - n \ln \theta_{rel} \propto n \ln \upsilon_n - \frac{E_{des}}{RT_S} \qquad \textit{Equation 6.3}$$

Hence, plotting a graph of ln $I(T)$ – n ln θ_{rel} against 1/T leads to a straight line with a gradient of $-E_{des}/R$, provided that the pre-exponential factor does not vary with temperature or coverage. Once again this is a valid assumption since RAIR spectra (*Chapter 5*) indicated that methanol is physisorbed at all coverages. The validity of this assumption will be demonstrated later. A typical plot to calculate a desorption energy for the multilayer of methanol adsorbed on HOPG at 100 K is shown in *Figure 6.12*. Note that this plot can only be constructed from the fitted data as it is necessary to separate the TPD spectra into individual peaks. This plot was constructed for both the monolayer and the multilayer using the range of n values shown in *Table 6.2*. Plots were also performed for several sets of TPD data in order to obtain an average value for the desorption energies.

Figure 6.13 shows how the desorption energy for the monolayer varies as a function of methanol exposure on HOPG at 100 K. The data points represent the average desorption energy calculated from several sets of TPD data and the error bars indicate errors arising from the uncertainty in the value of the desorption order.

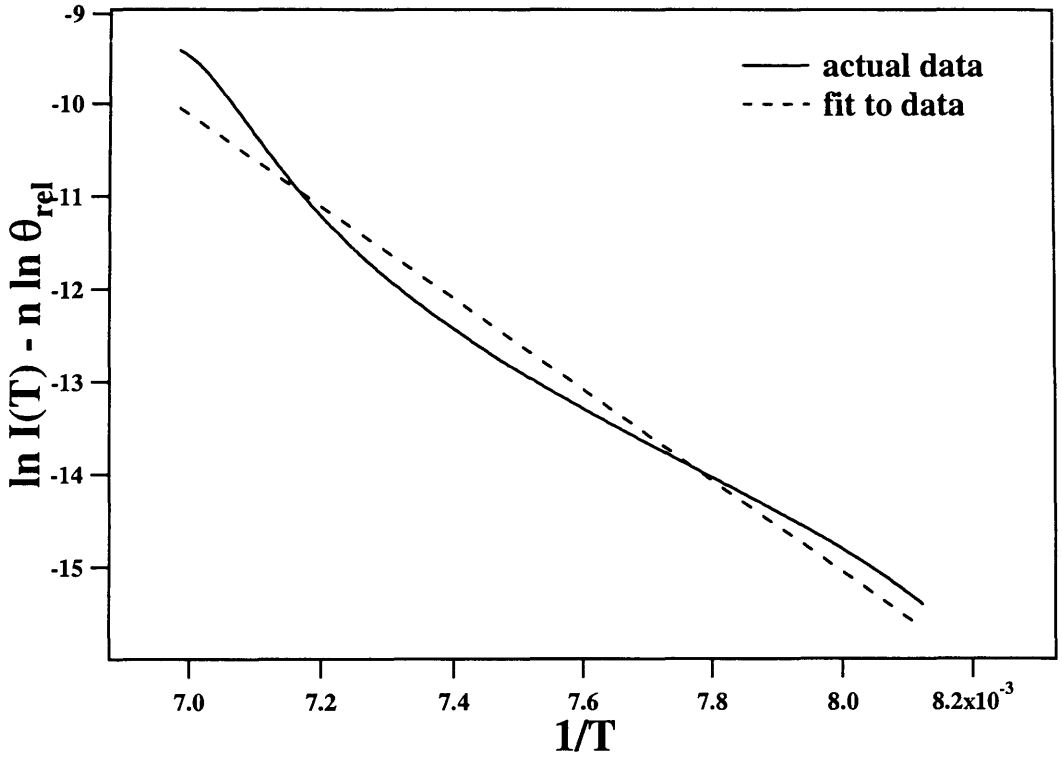

Figure 6.12: A plot of ln *I(T)* – *n* ln θ_{rel} against *1/T* for the multilayer of 50 L of methanol adsorbed on HOPG at 100 K. The plot has an *n* value of 0.35. The solid line represents the plot and the dashed line is a straight line fit to the data.

As the exposure is increased from 2 L to 20 L the desorption energy increases from approximately 33 kJ mol^{-1} to 48 kJ mol^{-1}. This corresponds to either a strongly physisorbed species or a weakly chemisorbed species. The RAIR spectra presented in *Chapter 5* suggested that no chemisorbed species were present on the surface, so it is therefore inferred that the methanol monolayer is strongly physisorbed on the surface. The increase in desorption energy with increasing exposure indicates that, as the exposure is increased, the monolayer is more strongly bound. This is in agreement with previous conclusions that suggest that hydrogen bonding can take place as the coverage of the methanol monolayer increases.

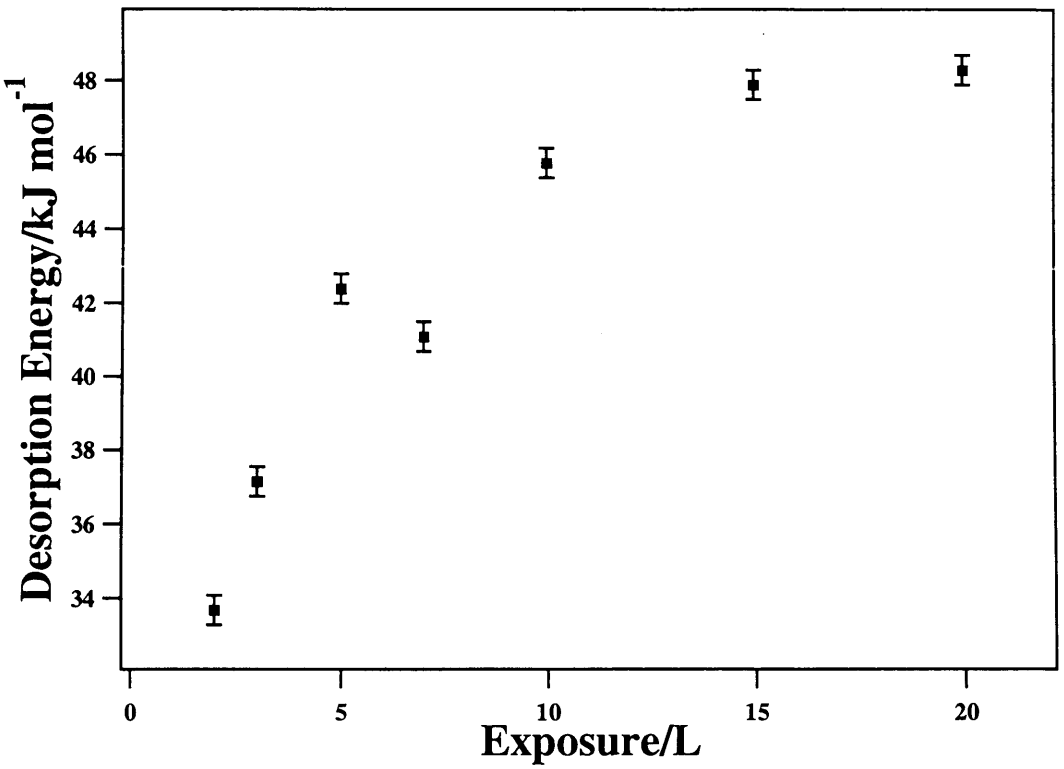

Figure 6.13: A plot of desorption energy against exposure for the desorption of monolayer methanol adsorbed on HOPG at 100 K.

Figure 6.14 shows how the desorption energy for the multilayer varies as a function of methanol exposure on HOPG at 100 K. Once again, the data points represent the average desorption energy calculated from several sets of TPD data and the error bars indicate errors arising from the uncertainty in the value of the desorption order.

Similar to the monolayer desorption energies, desorption energies for the multilayer also increase with increasing exposure. As the exposure is increased the desorption energy increases from 31 kJ mol^{-1} to 40 kJ mol^{-1}. This corresponds to desorption of a physisorbed species, and is in good agreement with a previous study of multilayer methanol adsorbed on Pd{100}, which reported desorption energies of 30.2 kJ mol^{-1} and 37.7 kJ mol^{-1} for two physisorbed species [19]. A study of multilayer methanol adsorbed on Al_2O_3{0001} also reported a desorption energy of 46.5 $kJmol^{-1}$ [21]. Furthermore, there is good agreement between the calculated values for the desorption energy of multilayer methanol from HOPG and the enthalpy of sublimation of methanol, which is 44.9 kJ mol^{-1} [21].

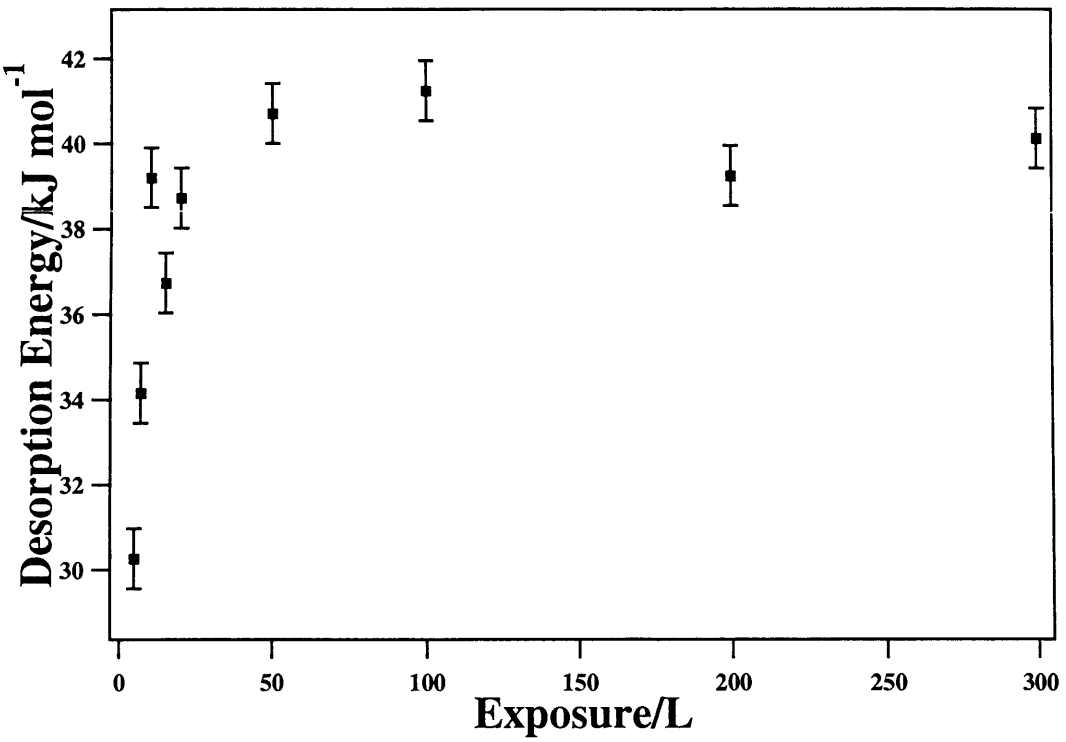

Figure 6.14: A plot of desorption energy against exposure for multilayer desorption of methanol adsorbed on HOPG at 100 K.

Figure 6.14 also suggests that there are two possible regimes for the adsorption of multilayer methanol on HOPG. At lower exposures, there is a rapid increase in desorption energy as the exposure is increased. However, for exposures of 15 L and above the increase in desorption energy seems to plateau. A possible explanation for this is the formation of an intermediate or "sandwich" layer. Previous studies have shown the growth of a "sandwich" phase of methanol [9] between the monolayer and the bulk methanol multilayer. The growth of the sandwich layer is a result of the lattice mis-match between the bulk methanol and the methanol adsorbed directly on the surface. Hence, it is suggested that the sharp increase in desorption energy at low exposures is a result of the rapid development of hydrogen bonds during the growth of an intermediate sandwich layer. The less rapid increase in desorption energy, at higher exposures, is due to the growth of the bulk methanol, in which the amount of hydrogen bonding changes less rapidly with increasing exposure.

6.3.6 Pre-exponential Factors

Pre-exponential factors have also been calculated for the desorption of both monolayer and multilayer methanol adsorbed on HOPG at 100 K. As for water adsorption on HOPG (*Chapter 4*) it is not possible to determine the pre-exponential factors directly from an Arrhenius plot, since the absolute coverage is not known. Pre-exponential factors have therefore been calculated using the same method as described in *Section 4.4.3*. Note that the pre-exponential factors are calculated using the fitted data for the monolayer and multilayer, not the raw data.

The inset in *Figure 6.11* shows that the monolayer saturates following an exposure of 10 L. This is equivalent to an array of methanol molecules arranged in a hydrogen bonded network. To evaluate the number of methanol molecules per unit area (from *Equation 4.9*), it is assumed that a methanol molecule and its associated hydrogen bond occupies a surface area of 2.73×10^{-19} m^2 (derived using values from [23] and *http://www.colby.edu/chemistry/webmo/methanol.html*). The actual coverage for a 10 L exposure is then ~ 0.1 ML (from *Equation 4.8*). The total uptake of methanol molecules on HOPG is approximately constant as a function of exposure (*Figure 6.9*), hence the number of adsorbates per unit area can be directly related to the area under the 10 L TPD curve in *Figure 6.7*. In this way a scaling factor can be used as before to convert all QMS intensities, and hence relative coverages, to actual coverages. The area under the 10 L TPD curve in *Figure 6.7* is 4.66×10^{-9} a.u., which corresponds to an absolute coverage of 3.66×10^{18} molec m^{-2}. Hence, all relative coverage values have been scaled by a factor of 7.9×10^{26} to allow conversion to absolute coverage values. This allows calculation of the pre-exponential factor for both monolayer and multilayer desorption of methanol from HOPG using an identical method to that for water.

In order to verify the validity of the assumptions used in this calculation several checks were carried out as before. *Figure 6.10* suggests that saturation of the first layer (a coverage of 0.1 ML) occurs following an exposure of 10 L. To test this, a 0.1 ML coverage was assumed to have occurred following various exposures of methanol from 5 L to 20 L. This also accounts for any errors that may have occurred in the estimate

relating to the surface area occupied by a methanol molecule. *Table 6.3* shows the effect of varying the exposure corresponding to 0.1 ML coverage on the pre-exponential factors for the monolayer and the multilayer. Desorption orders of 0.35 and 1.23 and desorption energies of 38 kJ mol^{-1} and 41 kJ mol^{-1} have been used for the multilayer and monolayer respectively in evaluating these pre-exponential factors.

Table 6.3: Table showing the effect of altering the exposure corresponding to a 0.1 ML coverage, which equates to saturation of the first layer, on the pre-exponential factor for methanol adsorbed on HOPG at 100 K. Desorption orders of 0.35 and 1.23 and desorption energies of 38 kJ mol^{-1} and 41 kJ mol^{-1} have been used for the multilayer and monolayer respectively.

Exposure/L	Monolayer pre-exponential factor*/s^{-1}	Multilayer pre-exponential factor†/molec m^{-2} s^{-1}
5	7.5×10^{9}	1.1×10^{26}
10	9.3×10^{9}	6.1×10^{25}
20	1.0×10^{10}	4.1×10^{25}

Further tests included propagating the errors associated with the desorption orders and the desorption energies calculated in *Sections 6.3.4* and *6.3.5* through the calculation of the pre-exponential factors for both monolayer and multilayer desorption. The results of these calculations are shown in *Tables 6.4* and *6.5*.

It can be seen from *Tables 6.3* to *6.5* that the pre-exponential factor for monolayer desorption of methanol from HOPG has a value of $10^{9.9\pm3.0}$ s^{-1} and multilayer desorption has a value of $10^{25.8\pm3.0}$ molec m^{-2} s^{-1}. Similar to the findings for water adsorption on HOPG shown in *Chapter 4*, the largest sources of error in calculating the pre-exponential factors is in the propagation of the errors associated with the desorption orders (*Table 6.4*) and desorption energies (*Table 6.5*). This suggests that determination of accurate desorption orders and accurate desorption energies is vital for calculating

* The units used for the pre-exponential factors are those expected for first order desorption for the monolayer.
† The units used for the pre-exponential factors are those expected for zero order desorption for the multilayer.

pre-exponential factors. The value for the pre-exponential factor for methanol multilayers shows good agreement with the calculated pre-exponential factors for multilayers of water (*Chapter 4*) and ammonia (*Chapter 7*). The pre-exponential value for the multilayer is also close to typical values for zero order desorption, as would be expected for fractional order desorption. The monolayer pre-exponential value is lower than would be expected for a pseudo-first order desorption process (typically 10^{13} to 10^{15} s^{-1}). However, these typical values apply to chemisorbed adsorbates and not physisorbed adsorbates as observed for the methanol monolayer on HOPG.

Table 6.4: Table showing the effect of altering the desorption order on the pre-exponential factor for monolayer and multilayer methanol adsorbed on HOPG at 100 K. It has been assumed that a 10 L exposure is equivalent to a coverage of 0.1 ML. Desorption energies of 41 kJ mol^{-1} and 38 kJ mol^{-1} have been used for the multilayer and monolayer respectively.

Monolayer		Multilayer	
Desorption order	Pre-exponential factor/s^{-1}	Desorption order	Pre-exponential factor/molec m^{-2} s^{-1}
1.09	2.1×10^{12}	0.14	4.9×10^{28}
1.23	9.3×10^{9}	0.35	6.1×10^{25}
1.37	4.6×10^{7}	0.56	7.7×10^{22}

Table 6.5: Table showing the effect of altering the desorption energy on the pre-exponential factor for monolayer and multiayer methanol adsorbed on HOPG at 100 K. It has been assumed that a 10 L exposure is equivalent to a 0.1 ML coverage. Desorption orders of 1.23 and 0.35 have been used for the monolayer and multilayer respectively.

Monolayer		Multilayer	
Desorption energy /kJ mol^{-1}	Pre-exponential factor/s^{-1}	Desorption order /kJ mol^{-1}	Pre-exponential factor/molec m^{-2} s^{-1}
33	1.3×10^{7}	31	2.0×10^{22}
41	9.3×10^{9}	35	1.0×10^{24}
48	3.5×10^{10}	38	6.1×10^{25}

6.3.7 Model for the Adsorption of Methanol on HOPG

Using the data presented here and in *Chapter 5*, it is now possible to construct a model for the adsorption of methanol on HOPG. RAIR spectra, shown in *Chapter 5*, showed that methanol is physisorbed on HOPG at all exposures. However it is not possible to distinguish between the adsorption of monolayer and multilayer methanol with RAIRS. RAIR spectra also show that it is possible to form crystalline methanol if specific criteria are met. In contrast, TPD spectra show that it is possible to distinguish the monolayer (*Peak A*) from the multilayer (*Peaks B* and *C*). However, the exact nature of the desorbing multilayer that gives rise to *Peaks B* and *C* has still to be confirmed.

A possible assignment for *Peak C* uses information obtained from the RAIR spectra. In the RAIR spectra crystalline methanol is observed either upon annealing the surface following adsorption at 97 K, or following adsorption to high exposures at 130 K. *Peak C* is only observed at high methanol exposures ($\geq$ 50 L) in both the 100 K and 130 K TPD spectra. This peak is therefore assigned to desorption of the crystalline phase of methanol. No crystalline methanol is formed upon adsorption at 100 K, irrespective of exposure. However, during the TPD process some of the methanol multilayer is converted to crystalline methanol and desorbs as a separate peak. It is the external influence of heating during TPD experiments that causes the appearance of this peak. This assignment of *Peak C* to the desorption of crystalline methanol is in agreement with the RAIR spectra presented in *Chapter 5*, since crystalline methanol could not be formed for exposures < 50 L in RAIRS studies, and *Peak C* is only observed for exposures $\geq$ 50 L in the TPD spectra.

Further evidence for the assignment of *Peak C* to formation, and subsequent desorption, of crystalline methanol arises from RAIRS and TPD studies following adsorption at 130 K. RAIR spectra showed that adsorption of methanol to high exposures (< 50 L) at 130 K yielded crystalline methanol. In the TPD spectra, the crystalline peak, *Peak C*, is more pronounced following adsorption at 130 K compared to corresponding exposures of methanol adsorbed at 100 K. The difference in appearance of the crystalline peak for corresponding exposures at 100 K and 130 K is attributed to the likelihood that some

crystalline methanol is being formed during adsorption at 130 K but not at 100 K. However, similar to adsorption at 100 K, this peak is predominantly a result of multilayer methanol being converted to crystalline methanol during the TPD process. Since the crystalline peak is thought to be observed primarily as a result of the TPD process, no quantitative analysis was carried out for this peak.

With this assignment, the following model can be employed to describe methanol adsorption on HOPG. At low exposures a physisorbed monolayer forms on the surface, for adsorption at both 100 K and 130 K. This is supported by the observation of a single peak (*Peak A* in *Figure 6.2*) in TPD studies at low exposures. Subsequent adsorption leads to the formation of an intermediate sandwich layer, and subsequently the growth of amorphous multilayers. The desorption of the sandwich layer and the amorphous multilayer are observed in TPD studies as *Peak B* in *Figures 6.2* and *6.3*. It is not possible to distinguish the sandwich layer from the multilayer in either TPD studies or RAIR spectra due to the similarity in structure. If the multilayers are grown thick enough (exposures > 50 L), annealing results in some of the amorphous methanol being converted to crystalline methanol. This is observed in both RAIR spectra and TPD studies and is shown schematically in *Figure 6.15*. It should be stressed that the desorption of crystalline methanol in the TPD spectra following adsorption at 100 K is entirely a consequence of the TPD process itself. The conversion of amorphous methanol to crystalline methanol, by annealing methanol multilayers, has also been observed on Pt{111} [16] using RAIRS.

If adsorption takes place at 130 K, methanol multilayers grow in both crystalline and amorphous phases. This is demonstrated by the RAIR spectra seen in *Chapter 5* (*Figures 5.9* and *5.10*) recorded following methanol adsorption at 130 K to high exposures, which showed sharper absorption peaks, due to crystalline methanol, superimposed on a broad base, due to adsorbed amorphous methanol. This is also observed in TPD spectra, as *Peak C* is more pronounced following adsorption at 130 K than at 100 K.

An alternative model for the growth of methanol adlayers on Ag{111} at 110 K has been suggested by Jenniskens and co-workers [14]. This model suggested that crystalline methanol desorbs at a lower temperature than amorphous methanol. If this was the case for methanol adsorbed on HOPG, *Peak B* would be assigned to the desorption of crystalline methanol and *Peak C* would be assigned to the desorption of amorphous methanol. However, *Peak B* is observed in TPD studies for exposures of 5 L and above for adsorption at both 100 K and 130 K. This is in clear disagreement with the RAIR spectra, in which crystalline methanol is only observed for exposures of 50 L and above. Hence *Peak B* is assigned to desorption from amorphous multilayers and *Peak C* is assigned to desorption of crystalline methanol.

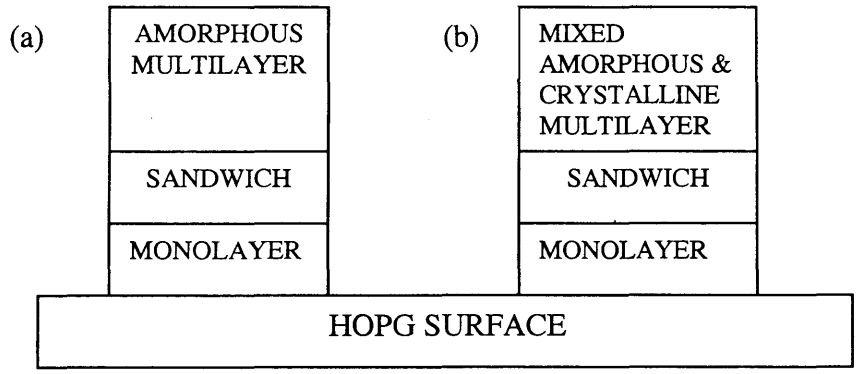

Figure 6.15: Schematic model of the adsorption of methanol on HOPG. Figure (a) shows the adsorption of the sandwich and amorphous multilayer on the monolayer and figure (b) shows the effect on the surface shown in figure (a) of annealing and/or of the temperature ramp during TPD.

6.4 Conclusions

TPD studies show three distinct peaks for desorption of methanol following adsorption at 100 K and 130 K. At low exposures a single peak is observed which is assigned to desorption from the monolayer. Increasing exposure of methanol leads to the appearance of an additional desorption feature, which can be assigned to the desorption of multilayer methanol. At high exposures a third peak is observed, which is assigned to the desorption of crystalline methanol. For adsorption at 100 K, the observation of the crystalline peak is attributed to the TPD process itself, rather than to the adsorption of

crystalline methanol. For adsorption at 130 K, some of the crystalline methanol is formed during adsorption and the remainder is converted from amorphous methanol in the TPD process. The monolayer has a desorption order of 1.23 ± 0.14 and a corresponding desorption energy between 33 and 48 kJ mol^{-1}. The desorption energy increases as the exposure is increased, most likely as a result of hydrogen bonding within the monolayer. The multilayer has a desorption order of 0.35 ± 0.21, with a corresponding desorption energy between 31 and 40 kJ mol^{-1}. This is in good agreement with previous observations for multilayers of methanol adsorbed on a variety of surfaces [18, 19, 21]. Similar to the monolayer, desorption energies for the multilayer increase with increasing exposure, and this is again attributed to an increase in hydrogen bonding with increasing coverage. Pre-exponential factors for monolayer and multilayer methanol desorption from HOPG have values of $10^{9.9\pm3.0}$ s^{-1} and of $10^{25.8\pm3.0}$ molec m^{-2} s^{-1} respectively. A model for the adsorption of methanol on HOPG has been suggested in accordance with observations of both the RAIRS and the TPD studies.

6.5 References

[1] Netzer, F.P. and Ramsey, M.G., Crit. Rev. Sol. St. Mat. Sci., **17** (1992) p. 397.

[2] Shekhar, R. and Barteau, M.A., Catal. Lett., **31** (1995) p. 221.

[3] Barros, R.B., Garcia, A.R., and Ilharco, L.M., J. Phys. Chem. B, **108** (2004) p. 4831.

[4] Demuth, J.E. and Ibach, H., Chem. Phys. Lett., **60** (1979) p. 395.

[5] Mavrikakis, M. and Barteau, M.A., J. Mol. Cat. A: Chem., **131** (1998) p. 131.

[6] Camplin, J.P. and McCash, E.M., Surf. Sci., **360** (1996) p. 229.

[7] Sim, W.S., Gardner, P., and King, D.A., J. Phys. Chem., **99** (1995) p. 16002.

[8] Wachs, I.E. and Madix, R.J., J. Catal., **53** (1978) p. 208.

[9] Pratt, S.J., Escott, D.K., and King, D.A., J. Chem. Phys., **119** (2003) p. 10867.

[10] Bhattacharya, A.K., Chesters, M.A., Pemble, M.E., and Sheppard, N., Surf. Sci., **206** (1988) p. L845.

[11] Barros, R.B., Garcia, A.R., and Ilharco, L.M., Surf. Sci., **502-503** (2002) p. 156.

[12] Hrbek, J., De Paola, R.A., and Hoffmann, F.M., J. Chem. Phys., **81** (1984) p. 2818.

[13] Sardar, S.A., Syed, J.A., Tanaka, K., Netzer, F.P., and Ramsey, M.G., Surf. Sci., **519** (2002) p. 218.

[14] Jenniskens, H.G., Dorlandt, P.W.F., Kadodwala, M.F., and Kleyn, A.W., Surf. Sci., **358** (1996) p. 624.

[15] Peremans, A., Maseri, F., Darville, J., and Gilles, J.M., J. Vac. Sci. Technol. A-Vac. Surf. Films, **8** (1990) p. 3224.

[16] Ehlers, D.H., Spitzer, A., and Luth, H., Surf. Sci., **160** (1985) p. 57.

[17] Peremans, A., Maseri, F., Darville, J., and Gilles, J.M., Surf. Sci., **227** (1990) p. 73.

[18] Wu, M., Truoung, C.M., and Goodman, D.W., J. Phys. Chem., **97** (1993) p. 9425.

[19] Christmann, K. and Demuth, J.E., J. Chem. Phys., **76** (1982) p. 6308.

[20] Christmann, K. and Demuth, J.E., J. Chem. Phys., **76** (1982) p. 6318.

[21] Nishimura, S.Y., Gibbons, R.F., and Tro, N.J., J. Phys. Chem. B, **102** (1998) p. 6831.

[22] de Jong, A.M. and Niemantsverdriet, J.W., Surf. Sci., **233** (1990) p. 355.

[23] Govind, N., Andzelm, J., Reindel, K., and Fitzgerald, G., Int. J. Mol. Sci., **3** (2002) p. 423.

Chapter 7: Ammonia Adsorption on Highly Oriented Pyrolitic Graphite

7.1 Introduction

In the past, radio observations of ammonia (NH_3) have been used to identify many properties of dense molecular clouds [1]. However, these observations are limited to gas phase ammonia and have generally ignored the effect of dust grains. This leads to severe conceptual inconsistencies, since it is known that dust grains can provide an opportunity for freeze-out of ammonia molecules at low temperatures [2]. This has been demonstrated by the observation of ammonia in interstellar ices [3, 4]. Ammonia is also believed to be an important carrier of nitrogen in the interstellar medium (ISM), so is thought to be intimately involved in reactions involving nitrogen. Hence a complete understanding of the interaction of ammonia with dust grains is required to accurately model the chemistry of the ISM. However, there have been no previous studies of ammonia adsorption and desorption from suitable interstellar dust analogues. This chapter presents a study of ammonia adsorption on highly oriented pyrolitic graphite (HOPG).

The only previous study of ammonia adsorption on a carbon surface has been carried out by Ellison and co-workers [5]. This study showed the adsorption of ammonia on single-walled carbon nanotubes (SWNTs) at room temperature. A broad feature, assigned to the N-H stretching vibration, was observed with a maximum at 3318 cm^{-1} and three distinct shoulders. Additionally, bands were observed at 1618 cm^{-1} and 1248 cm^{-1} which were assigned to the asymmetric and symmetric deformation modes respectively. Multilayer growth of ammonia on SWNTs was not observed at this adsorption temperature.

In contrast, the adsorption and decomposition of ammonia (NH_3) on metal surfaces has attracted much attention [6]. This subject is of considerable interest since ammonia has

important applications in processes such as heterogeneous catalysis [7]. Examples include the Ostwald process, where ammonia is passed over a platinum catalyst in HNO_3 synthesis; the Andrussow process, where HCN is synthesised by passing ammonia, methane and oxygen over a platinum-rhodium catalyst [8], and the Haber-Bosch process in which ammonia is produced by passing nitrogen and hydrogen over an iron catalyst. Additionally, ammonia can bond to metal atoms in organometallic compounds and on surfaces via the electron lone pair on the nitrogen atom, and hence is a prototypical example of a weak donor ligand.

Previous studies of the adsorption of ammonia have been predominantly on single crystal transition metal surfaces using a wide variety of techniques such as temperature programmed desorption (TPD) [9-18], low energy electron diffraction (LEED) [10, 11, 13, 18], electron stimulated desorption ion angular distribution (ESDIAD) measurements [10, 13, 19], work function change ($\Delta\varphi$) [9, 13], electron energy loss spectroscopy (EELS) [12, 18, 20] and reflection absorption infrared spectroscopy (RAIRS) [15, 17]. The adsorption behaviour of ammonia on different metal surfaces has been summarised by Thornburg and Madix [21].

TPD studies of ammonia adsorption have been performed on a range of metal surfaces and several similarities are observed [9-12, 19]. At low temperatures (80 - 90 K), adsorption is completely reversible. In general, a three peak structure is observed in the TPD spectrum. At low exposures an initial peak, α, is observed between 150 K and 350 K, which is assigned to desorption from a monolayer. On several surfaces the α peak is separated into two peaks, α_1 and α_2, which are assigned to desorption of ammonia adsorbed in different sites [12, 13]. As the ammonia exposure is increased the α peak shifts to lower desorption temperatures, a direct consequence of repulsive lateral interactions between the adsorbates. As the exposure is further increased, a second peak, β, is observed at approximately 140 K. This peak is assigned to desorption of a second layer of ammonia. At the highest exposures a third peak, γ, is also observed at approximately 110 K, which is assigned to desorption of multilayers of ammonia. *Table 7.1* summarises the desorption temperatures of the α, β and γ TPD peaks of ammonia desorbing from a range of metal surfaces.

Table 7.1: Table showing the range of desorption temperatures for the α, β and γ ammonia TPD peaks on a range of metal surfaces. Note that for Rh{111}, the dosing temperature was above the desorption temperature of the γ peak.

Surface	Desorption Temperature		
	α	β	γ
Ru{1121} [12]	~ 300 K	140 K	100 K
Ru{001}[13]	180 – 315 K	140 K	115 K
Ag{311}[19]	230 K	160 K	120 K
Ni{111} [10]	150 – 300 K	120 K	100 K
Rh{111} [11]	155 – 320 K	130 K	-

In contrast, a TPD study of ammonia adsorption on Au{111} [16] showed a simpler two peak structure consisting of a monolayer desorption peak (115 – 145 K) and a multilayer desorption peak (100 K). As with other metal surfaces, the monolayer peak could be saturated and the peak maximum shifted to lower temperatures as the exposure was increased. The multilayer peak could not be saturated. Similarly, two peaks were also observed for the desorption of monolayer (~170 K) and multilayer (~95 K) ammonia from an Al{111} surface [17].

Szulczewski and White [14, 15] studied the thermal desorption of ammonia (NH_3 and ND_3) from Ag{111}, and in contrast to Au{111} and Al{111}, two peaks were observed for desorption from the monolayer, for both NH_3 and ND_3, at 120 K and 145 K. Increasing the exposure of ammonia led to a multilayer peak at 104 K. As expected, the multilayer peak could not be saturated and demonstrated zero-order desorption kinetics. No peak was observed for the desorption of second layer ammonia.

Several vibrational studies of ammonia adsorption on metal substrates have also been reported. Xu and Goodman studied ammonia adsorption on palladium, epitaxially grown on Mo{110} [18], using HREELS at 90 K. Initially, loss features were observed at 290 cm^{-1} and 1100 cm^{-1} which were assigned to the Pd-N stretch and the symmetric deformation (umbrella) mode of the adsorbed ammonia respectively. As the exposure

was increased, the symmetric deformation mode shifted down in frequency and additional loss features were observed between 3200 and 3500 cm^{-1}. These were assigned to N-H stretching modes. HREEL spectra of multilayer ammonia showed loss features at 420 cm^{-1} (frustrated libration), 1100 cm^{-1} (symmetric deformation), 1620 cm^{-1} (asymmetric deformation), 3360 cm^{-1} (symmetric stretch) and 3400 cm^{-1} (asymmetric stretch) [18].

HREELS studies of ammonia adsorption on Ru{1121} and Ru{001} have also shown similar findings [12, 20]. Initial exposure led to chemisorbed ammonia adsorbed on the surface, characterised by the symmetric deformation mode at approximately 1150 cm^{-1}. Increasing exposure, on both Ru{1121} and Ru{001}, led to a down shift in the frequency of the symmetric deformation. In both cases multilayer ammonia was also seen, with the observed vibrational bands in agreement with those for solid ammonia [22-24].

Pradier and co-workers investigated ammonia adsorption on Cu{110} [25] using RAIRS. RAIR spectra recorded at room temperature showed the ammonia symmetric deformation mode at approximately 1180 cm^{-1}. No symmetric or asymmetric stretches were observed for the adsorbed ammonia, indicating low coverage and the absence of multilayers. The absence of the asymmetric deformation indicated that the ammonia was adsorbed with its C_{3v}-axis normal to the surface. Similar findings have been reported for low coverages of ammonia adsorbed on Al{111} [17].

Several groups have also studied the decomposition of ammonia on single crystal metal surfaces [12, 17, 26-34]. The decomposition of ammonia is an endothermic process (ΔH = 46.4 kJ mol^{-1}) [35], and it is generally considered to be rate limited by the recombinative desorption of N_2. Early transition metals tend to be more active for the decomposition of ammonia, however these metals are limited by either the relatively high desorption temperature of N_2, or the tendency for the species to deactivate via nitride formation.

7.2 Experimental

All experiments were performed in the UHV chamber described in *Chapter 2*. As before, sample cleanness was achieved using the techniques described earlier. Both RAIRS and TPD experiments investigating the adsorption of ammonia (99.98% purity, BOC Gases) were performed by back filling the chamber via a high precision leak valve, in a controlled manner. All exposures are measured in Langmuir (L), where an exposure of 1 L is equivalent to back filling the chamber to a pressure of 1×10^{-6} mbar for 1 second. Exposures were not corrected for ion gauge sensitivity. RAIRS and TPD experiments were performed as already described in *Chapter 3*. All TPD spectra were recorded at a heating rate of 0.20 ($\pm$ 0.005) K s^{-1}.

7.3 RAIRS Results

RAIR spectra following adsorption of ammonia on the HOPG surface at 94 K are shown in *Figure 7.1*. The lowest exposure of the surface to ammonia leads to the appearance of one band at 1076 cm^{-1}. With increasing exposure this band is observed to grow in intensity, however there is no shift in frequency. This band remains the most intense feature in all spectra.

Following an exposure of 15 L, a second band is observed at 3380 cm^{-1}. Similar to the lower frequency band, this peak grows in intensity with increasing exposure but does not undergo a frequency shift. For exposures above 100 L, two further bands are observed at 1120 cm^{-1} and 1652 cm^{-1}. Further increasing the exposure leads to an increase in intensity of both bands, although these bands are significantly less intense than the two bands at 1076 cm^{-1} and 3380 cm^{-1}. Finally, for exposures of 300 L and above, an additional weak feature is observed at 3299 cm^{-1}. A further increase in exposure leads to an increase in intensity of all bands but does not lead to the observation of any additional features. No frequency shift is observed for any of the vibrational bands, nor is it possible to saturate the bands.

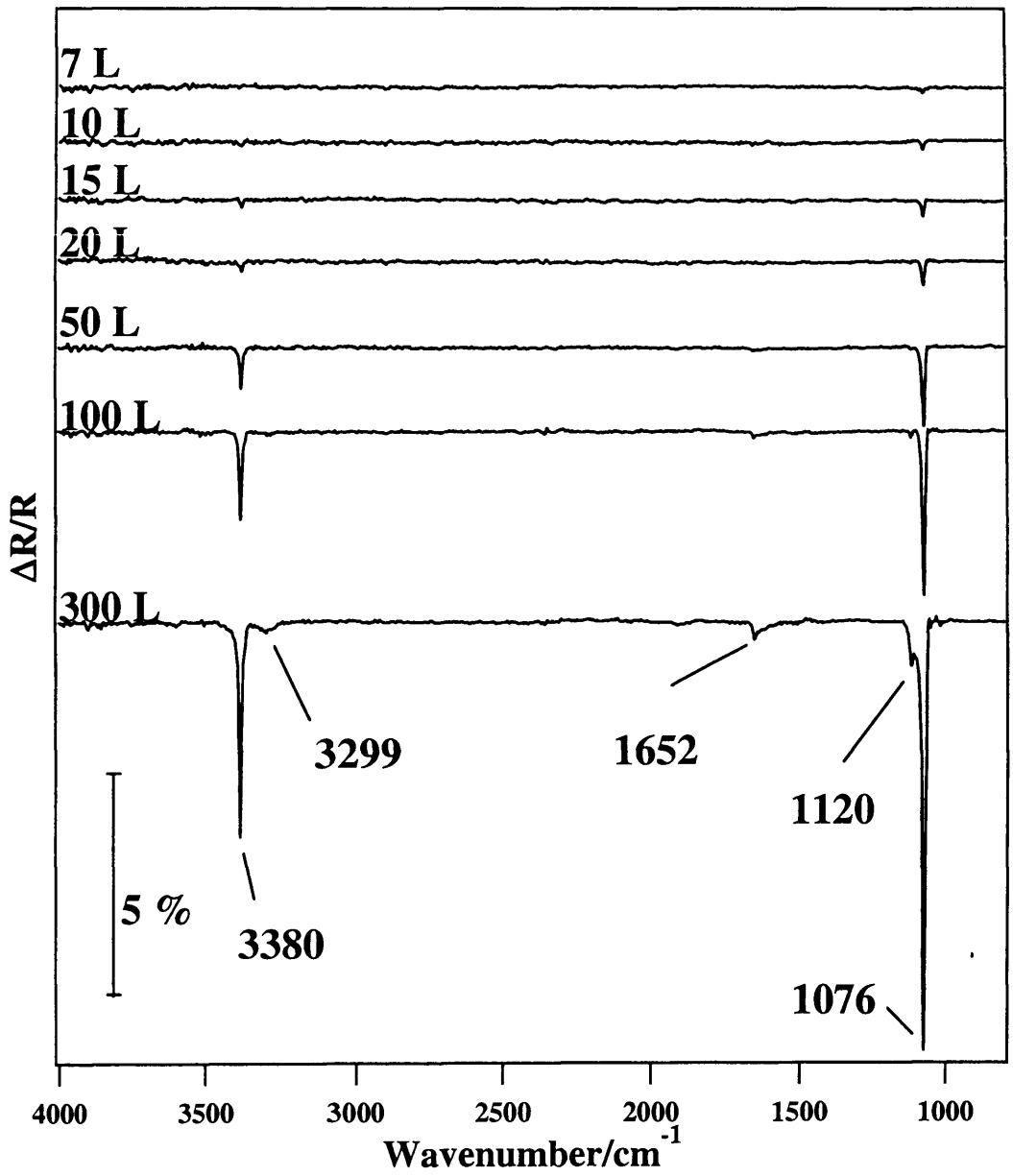

Figure 7.1: RAIR spectra of increasing exposures of ammonia adsorbed on HOPG at 94 K. Exposures of ammonia are indicated on individual spectra.

Figure 7.2 shows a series of spectra resulting from the annealing of the adsorbed ammonia adlayer (300 L exposure) to various temperatures.

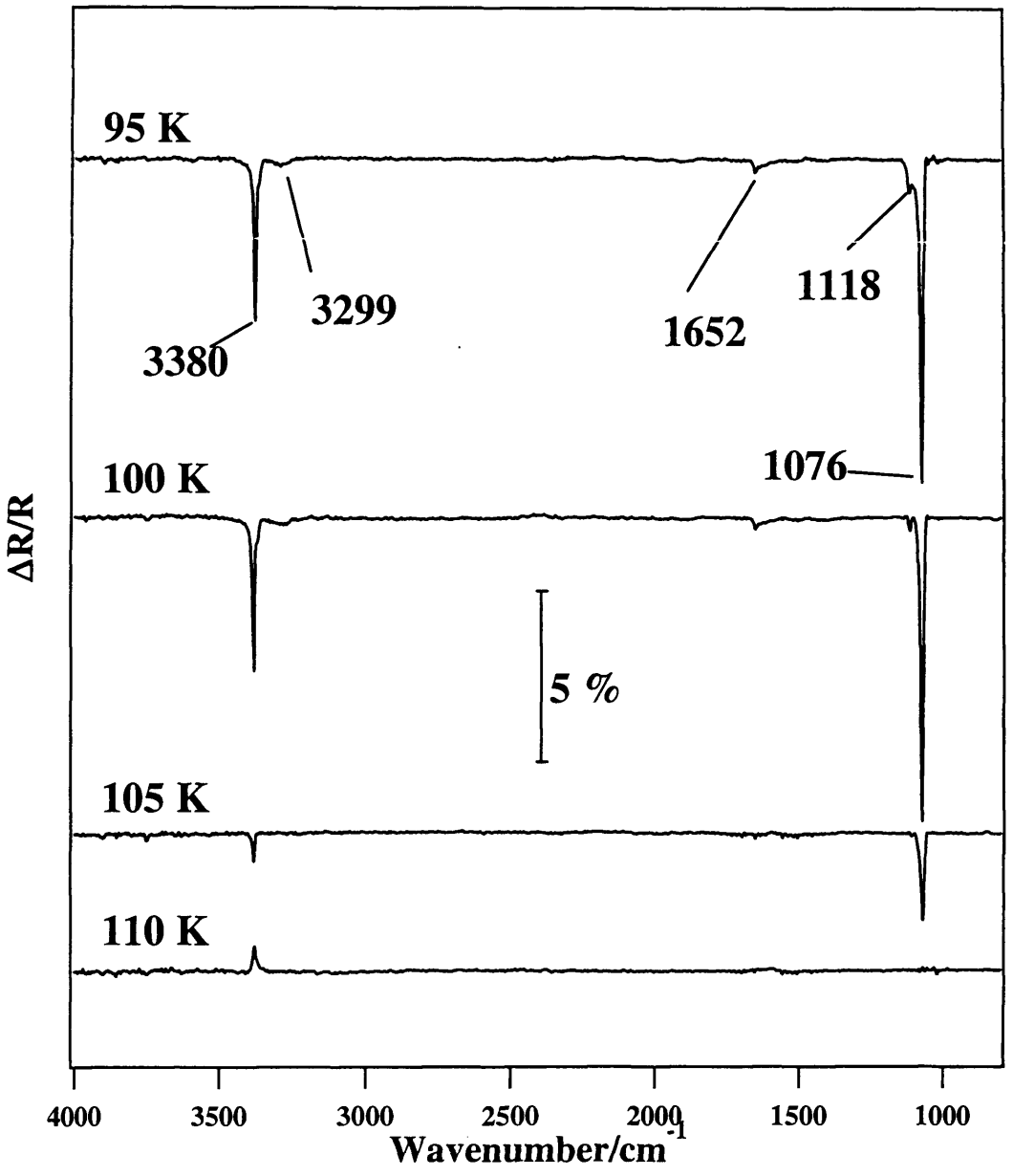

Figure 7.2: RAIR spectra showing the sequential heating of an ammonia adlayer (300 L exposure) adsorbed on HOPG at 94 K. The temperatures to which the ammonia adlayer was annealed are indicated on the individual spectra.

Heating the ammonia adlayer to 100 K does not lead to the loss of any spectral features, however a decrease in intensity is observed in all vibrational bands. Furthermore, there is no shift in the frequency of the observed bands when the ammonia adlayer is heated. Annealing the adlayer to 105 K leads to the loss of the spectral features at 1118 cm^{-1}, 1652 cm^{-1} and 3299 cm^{-1}. Additionally the bands observed at 1076 cm^{-1} and 3380 cm^{-1}

become considerably less intense. Further annealing of the adlayer to 110 K and above leads to the loss of all spectral features. Note that for spectra recorded after annealing the adlayer above 110 K, a weak upward pointing peak is observed at 3380 cm^{-1}. This is most likely due to the adsorption of a small amount of ammonia on the surface as the sample cools down after cleaning. Hence, some ammonia is already adsorbed on the HOPG sample when the reference spectrum is recorded. When the ammonia adlayer is then annealed above 110 K, all ammonia adsorbed on the HOPG is desorbed and an upward peak is observed in the spectrum. Similar upward peaks have been noted by Kim and co-workers for ammonia adsorption on Al{111} [17].

The bands observed in the spectra shown in *Figure 7.1* are comparable in frequency to those recorded for multilayer ammonia adsorbed on a number of surfaces [15, 19, 20, 36, 37] and with those for solid ammonia [22-24], and can therefore be assigned confidently. The bands observed at 1076 cm^{-1}, 1652 cm^{-1}, 3380 cm^{-1} and 3299 cm^{-1} are assigned to the symmetric deformation (umbrella) mode, the asymmetric deformation, the asymmetric stretch and the symmetric stretch of multilayers of ammonia. *Table 7.2* compares the observed multilayer bands recorded here with multilayer bands observed for ammonia adsorbed on a variety of surfaces. All vibrational bands observed in *Figures 7.1* and *7.2* are attributed to physisorbed multilayers of ammonia. The assignment of the band observed at 1118 cm^{-1} will be discussed later.

Annealing the adlayer (*Figure 7.2*) does not lead to the appearance of any new spectral features, implying that there is no structural change within the ammonia adlayer as a result of annealing. Furthermore, annealing the adlayer to 110 K or above leads to the disappearance of all spectral features. This is consistent with previous EELS studies, which have shown that physisorbed multilayers of ammonia desorb at a similar temperature [18, 20].

Assignment of the vibrational bands observed in *Figures 7.1* and *7.2* to multilayers of physisorbed ammonia is confirmed by TPD spectra presented later (*Figure 7.3*). *Figure 7.1* shows that vibrational bands are only observed for exposures of 7 L and above of ammonia. At comparable exposures in the TPD spectra, it will be shown that the

dominant desorption feature is due to multilayers of ammonia. Hence, by comparing the TPD and RAIR spectra it is proposed that the vibrational bands observed in *Figures 7.1* and *7.2* are due to the formation of physisorbed multilayers of ammonia only.

Table 7.2: Table showing the assignment of the vibrational bands observed for ammonia adsorbed on HOPG at 94 K in comparison to multilayer ammonia adsorbed on Ru{001}, Ag{111}, Pt{111} and solid ammonia. For the solid ammonia, a range of values is given for each band based on several IR and Raman studies at temperatures ranging from 18 K to 151 K.

Vibrational Mode	**Multilayer NH_3/ HOPG /cm^{-1}**	NH_3/Ru{001} [20] /cm^{-1}	NH_3/Ag{111} [14] /cm^{-1}	NH_3/Pt{111} [37] /cm^{-1}	Solid NH_3 [23] /cm^{-1}
Symmetric deformation, δ_s	**1076**	1100	1079	1120	1057-1080
Asymmetric deformation, δ_a	**1652**	1640	1652	1640	1630-1679
Symmetric stretch, ν_s	**3299**	3230	3210	Not observed	3160-3330
Asymmetric stretch, ν_a	**3380**	3380	3377	3320	3370-3378

On single crystal metal surfaces a chemisorbed monolayer and a second layer have been observed [12, 18, 20] when ammonia is adsorbed on the surface. However, it is not possible to observe the monolayer or second layer species of ammonia on the HOPG surface in the RAIR spectra presented in *Figures 7.1* and *7.2*. A possible explanation for this is that absorption bands for monolayer adsorption on HOPG are so weak that they cannot be observed.

The appearance of a vibrational band at 1118 cm^{-1} for high exposures of ammonia adsorbed on HOPG (*Figure 7.1*) may be explained by considering different phases of solid ammonia. Solid ammonia exists in three phases: a highly disordered amorphous

phase (< 50 K), an intermediate metastable phase (~50 – 80 K) and an ordered crystalline phase (> 80 K) [24]. Crystalline ammonia, the thermodynamically stable phase of solid ammonia, is characterised by very sharp symmetric deformation and asymmetric stretching bands at 1057 cm^{-1} and 3375 cm^{-1}. A similar observation is noted in *Figures 7.1* and *7.2* and hence leads to the suggestion that the ammonia multilayers on the HOPG surface are in the crystalline phase. This assignment is consistent with the dosing temperature of 94 K, as crystalline ammonia should be formed at this temperature. Infrared studies of metastable ammonia have shown more complex spectra with clear band splitting observed for the symmetric deformation, and to a lesser extent within the asymmetric stretch [24]. This band splitting arises from two preferred molecular orientations within the metastable state. The observation of a vibrational band at 1118 cm^{-1} is therefore assigned to the presence of a small amount of metastable ammonia being present within the multilayer. The presence of the metastable ammonia leads to the appearance of two peaks, separated by ~40 cm^{-1}, for the symmetric deformation mode. This is consistent with previous studies [24].

7.4 TPD Results

A series of TPD spectra for increasing exposures of ammonia on HOPG at 88 K are shown in *Figure 7.3*. At the lowest exposure of ammonia one peak, *Peak A,* is observed with a desorption temperature of approximately 94 K. As the exposure is increased to 3 L and 5 L this peak shifts up in temperature to 96 K and appears to saturate. By 5 L, a second peak, *Peak B*, is observed at 97 K, initially as a high temperature shoulder on *Peak A*. As the exposure is increased to 7 L both peaks become equal in intensity. Further increasing the exposure to 10 L and 15 L leads to *Peak B* dominating the lower temperature peak until it is not possible to distinguish between the two peaks. This combined peak then continues to shift up in temperature as the ammonia exposure is increased.

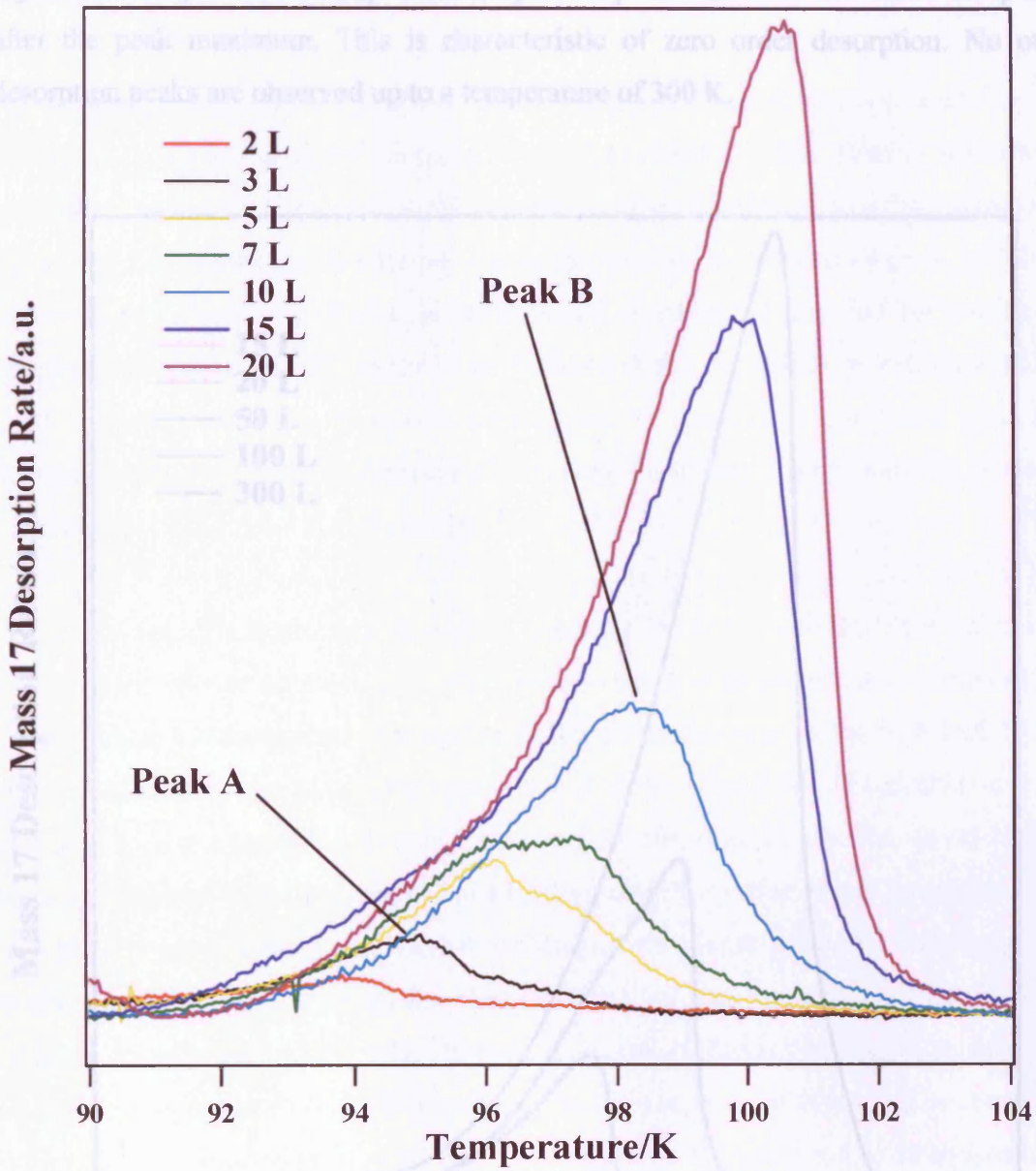

Figure 7.3: TPD spectra recorded following exposures of ammonia adsorbed on HOPG at 88 K. The figure shows spectra following exposures of 2 L, 3 L, 5 L, 7 L, 10 L, 15 L and 20 L.

TPD spectra following higher exposures of ammonia on HOPG are shown in *Figure 7.4*. At an exposure of 20 L, the combined peak, which is predominantly *Peak B*, has a peak temperature of 101 K. The peak maximum continues to shift up in temperature as the exposure is increased, reaching 107 K for an exposure of 300 L. This combined peak could not be saturated at high exposures. Note that the desorption peak has an

asymmetric shape with a steady increase up to the peak maximum and then a sharp drop after the peak maximum. This is characteristic of zero order desorption. No other desorption peaks are observed up to a temperature of 300 K.

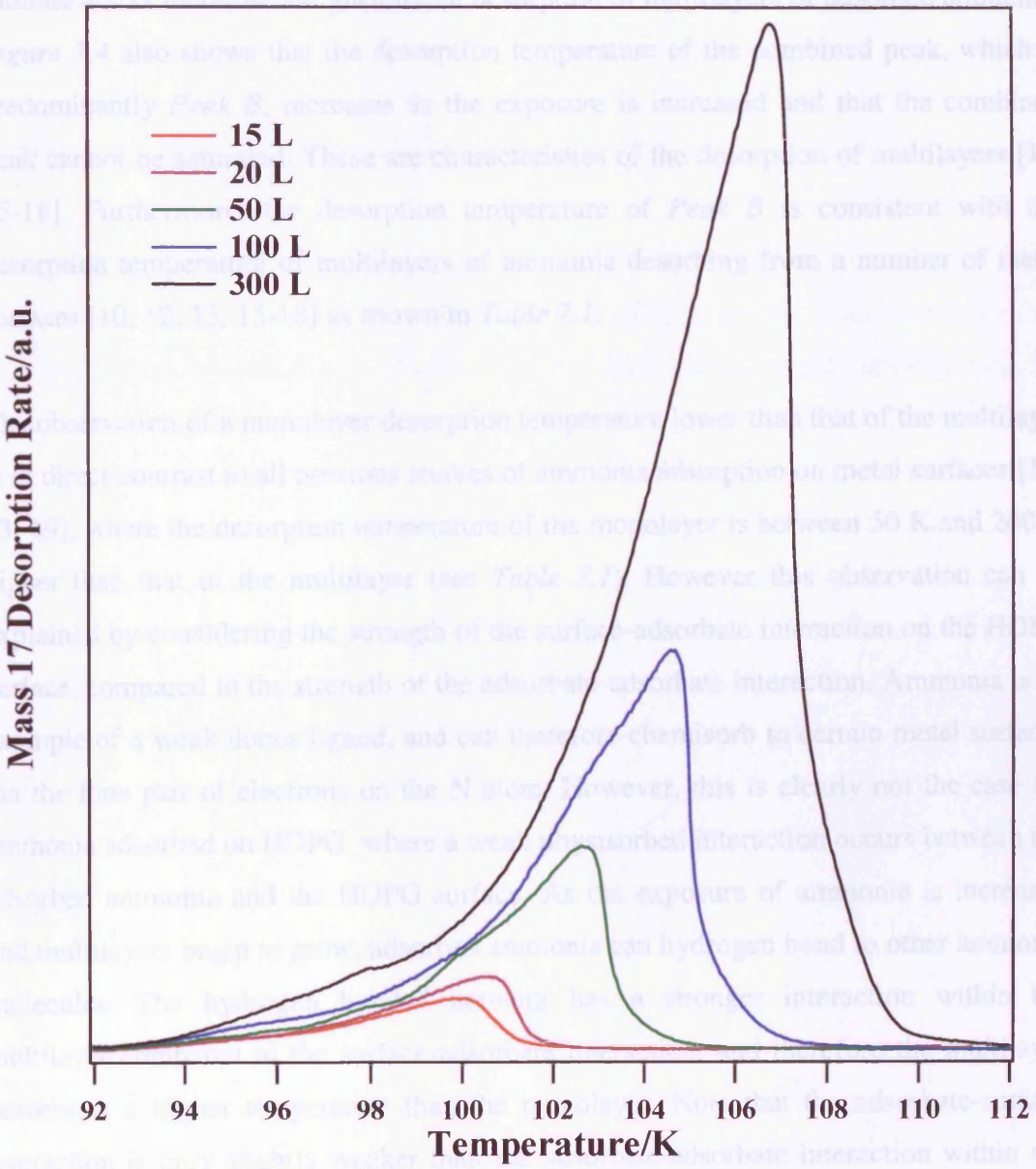

Figure 7.4: TPD spectra recorded following exposures of ammonia adsorbed on HOPG at 88 K. The figure shows spectra recorded following exposures of 15 L, 20 L, 50 L, 100 L and 300 L.

7.4.1 Assignment of Peaks

At the lowest exposures only *Peak A* is observed, hence this species must be due to the desorption of a monolayer of ammonia. *Peak B* is observed after *Peak A* appears to saturate and is therefore assigned to the desorption of multilayers of adsorbed ammonia. *Figure 7.4* also shows that the desorption temperature of the combined peak, which is predominantly *Peak B*, increases as the exposure is increased and that the combined peak cannot be saturated. These are characteristics of the desorption of multilayers [13, 15-18]. Furthermore, the desorption temperature of *Peak B* is consistent with the desorption temperature of multilayers of ammonia desorbing from a number of metal surfaces [10, 12, 13, 15-18] as shown in *Table 7.1*.

The observation of a monolayer desorption temperature lower than that of the multilayer is in direct contrast to all previous studies of ammonia adsorption on metal surfaces [10-13, 19], where the desorption temperature of the monolayer is between 50 K and 200 K higher than that of the multilayer (see *Table 7.1*). However this observation can be explained by considering the strength of the surface-adsorbate interaction on the HOPG surface, compared to the strength of the adsorbate-adsorbate interaction. Ammonia is an example of a weak donor ligand, and can therefore chemisorb to certain metal surfaces via the lone pair of electrons on the N atom. However, this is clearly not the case for ammonia adsorbed on HOPG, where a weak physisorbed interaction occurs between the adsorbed ammonia and the HOPG surface. As the exposure of ammonia is increased and multilayers begin to grow, adsorbed ammonia can hydrogen bond to other ammonia molecules. The hydrogen bonded network has a stronger interaction within the multilayer compared to the surface-adsorbate interaction, and therefore the multilayer desorbs at a higher temperature than the monolayer. Note that the adsorbate-surface interaction is only slightly weaker than the adsorbate-adsorbate interaction within the multilayer, since the monolayer has a desorption temperature of only a few Kelvin lower than the multilayer.

An attempt was made to separate the monolayer desorption peak from the multilayer desorption peak using a fitting programme in order to confirm the above assignments.

However, the quality of the fits was inadequate and hence was not used in the quantitative analysis. To minimise the error caused by not separating the monolayer and the multilayer contribution, analysis has only been carried out for desorption from the multilayer and for exposures of 10 L and above. As seen in *Figure 7.3*, 10 L is the lowest exposure where the multilayer is the dominant contribution to the desorption trace.

7.4.2 Uptake Curves and Desorption Order

As already shown, the signal intensity recorded by the mass spectrometer, I(T), is proportional to the rate of change of coverage of the adsorbate. Hence, the integrated area under each spectrum is proportional to the relative coverage of adsorbate on the surface. As before, an estimate of the actual coverage is made when calculating the pre-exponential factor. *Figure 7.5* shows the total uptake of ammonia adsorbed on HOPG at 88 K.

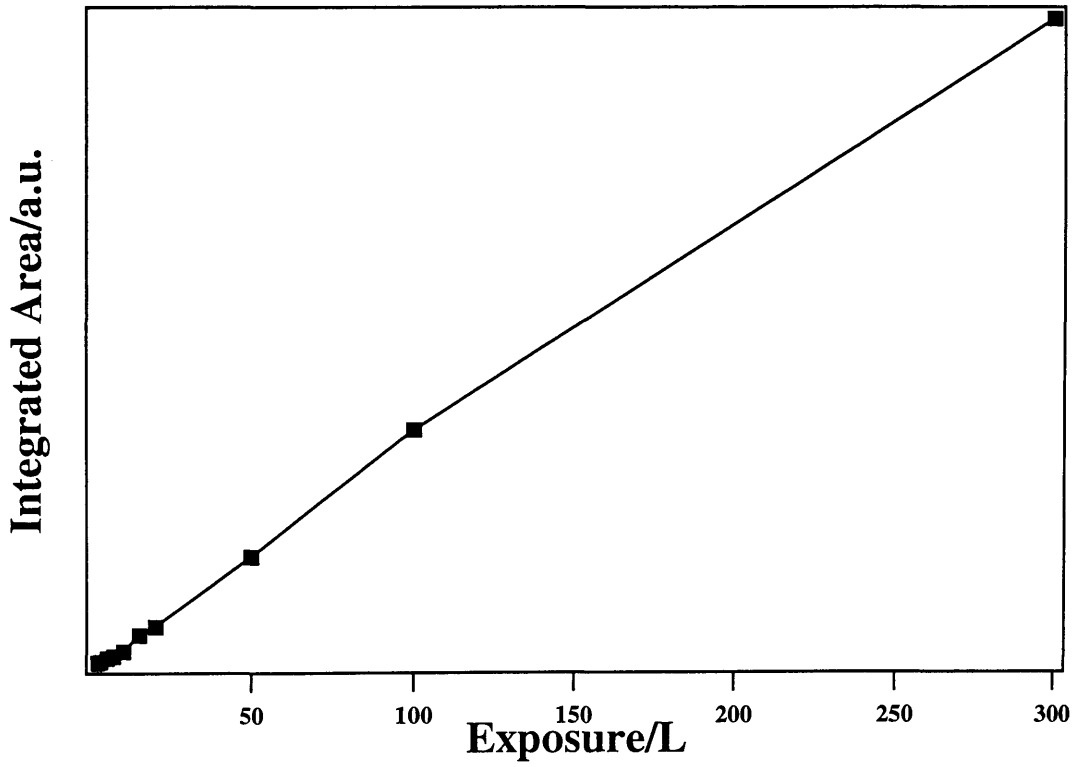

Figure 7.5: Graph showing, as a function of exposure, the total integrated area of the TPD curves obtained following ammonia adsorption on HOPG at 88 K.

The integrated areas were calculated by subtracting the background intensity from the spectrum and using the trapezium rule over a temperature interval where the peak intensity is appreciable. This is generally over a temperature interval of 89 K to 113 K. It can clearly be seen from *Figure 7.5* that the ammonia uptake is approximately linear, indicating a constant sticking probability for the adsorption of ammonia on the HOPG surface. This is characteristic of the growth of physisorbed ammonia multilayers and is in agreement with the RAIRS data and the TPD assignments described earlier.

The desorption order can be calculated for the desorption of ammonia from HOPG by using the same method as was used for water and methanol. Using *Equation 4.6* a plot of $\ln[I(T)]_x$ against $\ln[\theta_{rel}]_x$ (where $[I(T)]_x$ is the QMS signal intensity at a fixed temperature T_x and $[\theta_{rel}]_x$ is the relative coverage at the temperature T_x) gives a straight line with gradient of n, the desorption order. An example of this plot for a T_x value of 96 K is shown in *Figure 7.6*. This process was repeated for a range of fixed temperatures and the gradients obtained from the plots, and hence the desorption orders, for multilayers of ammonia adsorbed on HOPG are given in *Table 7.3*.

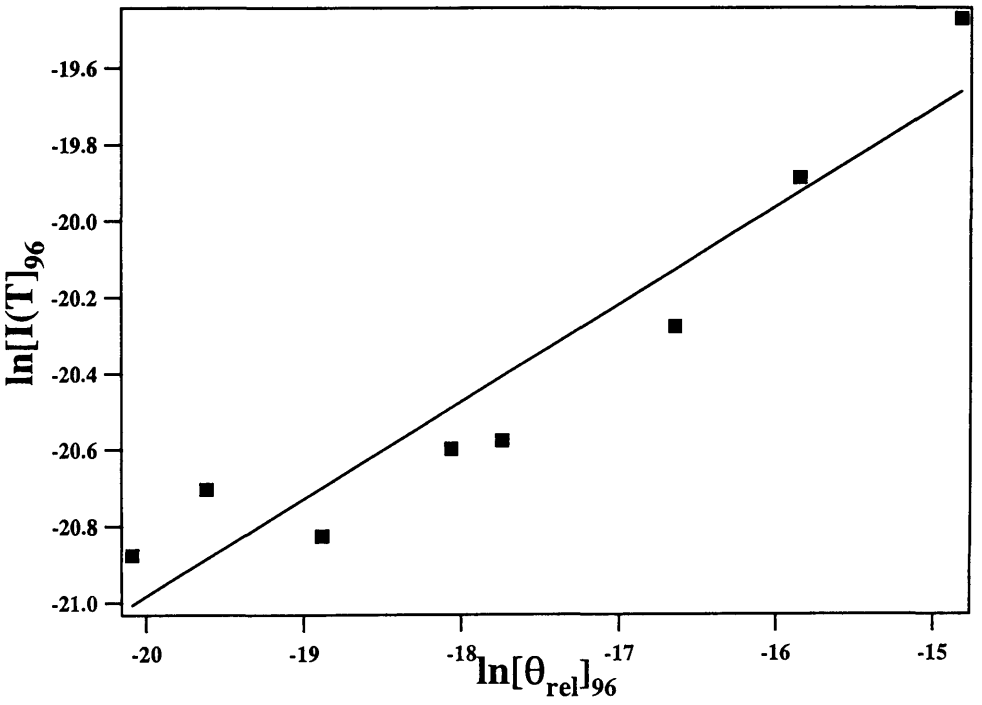

Figure 7.6: A plot of $\ln[I(T)]_x$ against $\ln[\theta_{rel}]_{Tx}$ for a T_x value of 96 K for exposures of 10 L and above of ammonia adsorbed on HOPG at 88 K.

Table 7.3 shows that multilayer ammonia has a desorption order of 0.25 ± 0.05. Previous studies of multilayer ammonia adsorbed on metal surfaces have shown characteristics of zero order desorption [15, 16], with desorption traces of varying exposures sharing a common leading edge. However, *Figure 7.4* shows that increasing exposures of ammonia adsorbed on HOPG do not appear to share a common leading edge. This can be attributed to hydrogen bonding within the multilayer. This phenomenon has been observed in other hydrogen bonded systems [38, 39] including water and methanol adsorbed on HOPG (see earlier chapters). Furthermore, the combined peak shown in *Figure 7.4* is not solely attributed to desorption of the multilayer. The small contribution of the monolayer peak further results in the TPD spectra not sharing leading edges.

Table 7.3: Table showing the calculated desorption orders for multilayer ammonia adsorbed on HOPG at 88 K for a variety of T_x values.

T_x value/K	Desorption order for multilayer ammonia
94	0.24
95	0.25
96	0.25
97	0.30
98	0.26
99	0.20

7.4.3 Desorption Energy

It is also possible to calculate the desorption energy for ammonia multilayers adsorbed on HOPG. In this way it is possible to gain an indication of the binding strength within the ammonia multilayer. The desorption energy has been calculated using the complete analysis technique, the only technique for determining desorption energies without making any assumptions [40, 41]. The analysis carried out for determining the desorption energy for ammonia multilayers adsorbed on HOPG is identical to that described in *Section 4.4.2*, and uses the TPD spectra shown in *Figures 7.3* and *7.4*.

Figure 7.7 shows relative coverage against surface temperature profiles for various exposures of ammonia adsorbed on HOPG.

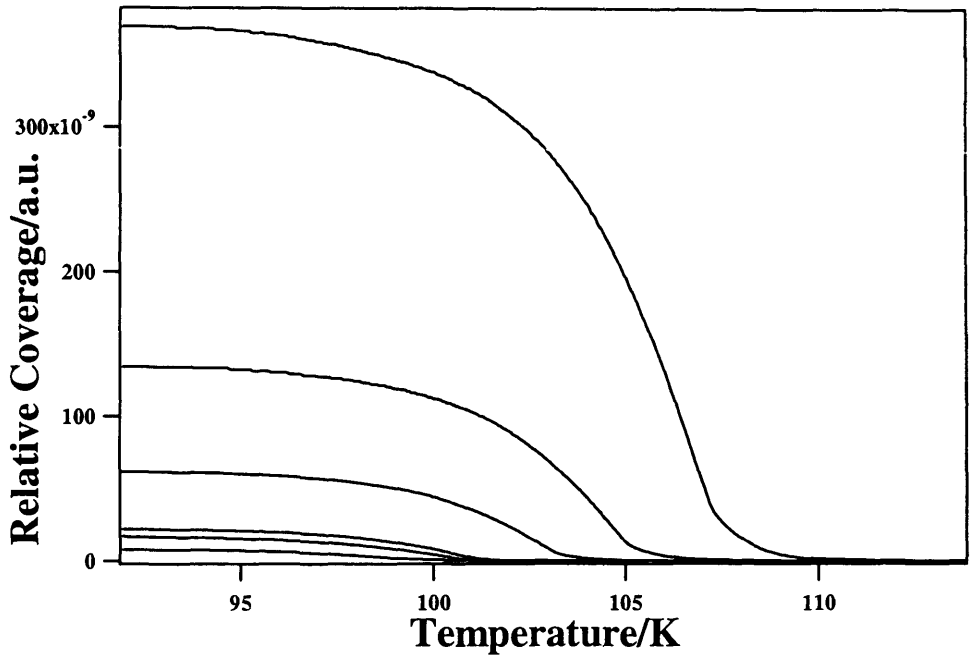

Figure 7.7: Figure showing the relative coverage plotted as a function of surface temperature for ammonia adsorbed on HOPG at 88 K. The plots (from top to bottom) correspond to exposures of 300 L, 100 L, 50 L, 20 L, 15 L and 10 L.

Using the same method as used for water (*Section 4.4.2*) it is then possible to construct Arrhenius plots for a range of fixed relative coverage, θ'_{rel}, values. An Arrhenius plot for a relative coverage value of 7×10^{-9} a.u. is given in *Figure 7.8*. The resulting desorption energy, obtained from the gradient of this graph, is 24.3 kJ mol^{-1}. This process was repeated for several values of θ'_{rel} and *Table 7.4* lists the desorption energies obtained.

Table 7.4 shows good agreement in the calculated desorption energies for multilayer ammonia adsorbed on HOPG obtained for a range of fixed relative coverage values. The table gives an average desorption energy of 23.2 ± 1.2 kJ mol^{-1} for multilayer ammonia adsorption on HOPG at 88 K. This corresponds to the formation of a weakly physisorbed species and is in agreement with previous studies, where desorption energies of 25 kJ mol^{-1} and 23.8 kJ mol^{-1} were reported for multilayer ammonia desorption from Ru{1121} [12] and Ag{111} [15] respectively. Furthermore, this

desorption value is in excellent agreement with the reported enthalpy of sublimation of ammonia of 23.4 kJ mol^{-1} [42].

Table 7.4: Table showing desorption energies for multilayer ammonia adsorbed on HOPG obtained by the complete analysis technique for a range of fixed relative coverage values.

Fixed Relative Coverage Value, θ'_{rel}/a.u.	Desorption Energy/kJ mol^{-1}
7×10^{-9}	24.3
1.5×10^{-8}	22.0
2×10^{-8}	23.3

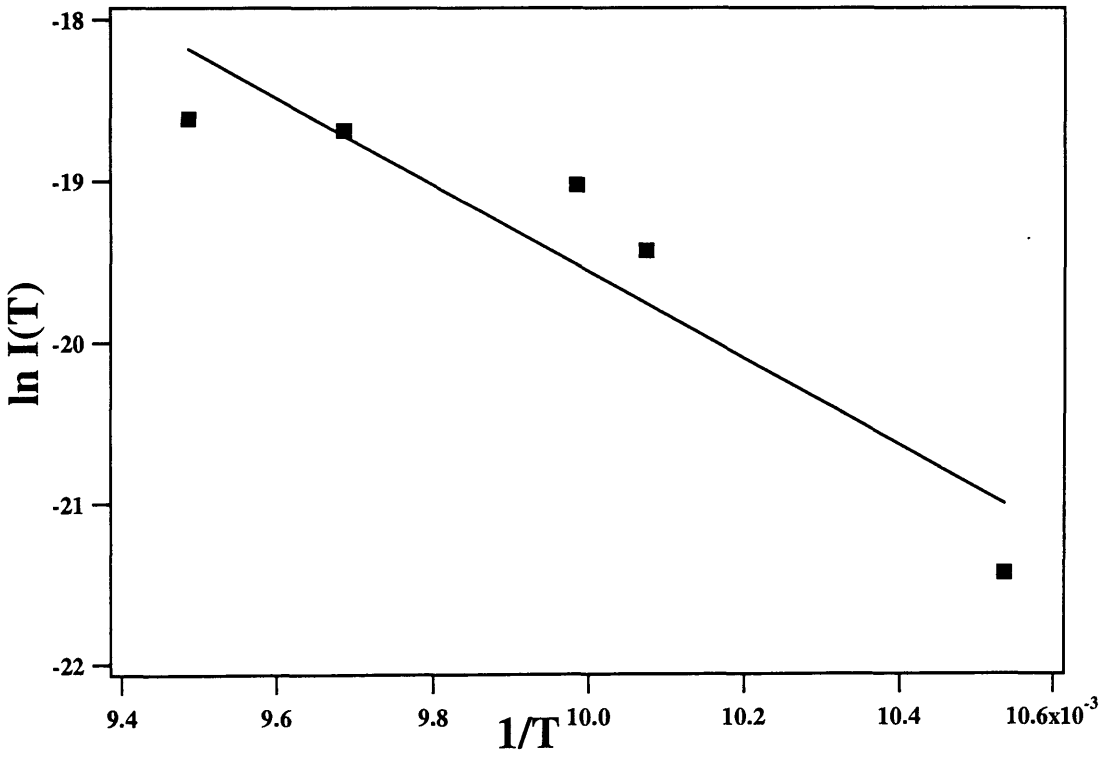

Figure 7.8: An Arrhenius plot used to obtain the desorption energy for multilayer ammonia adsorbed on HOPG at 88 K. The Intensity I(T) and the Temperature T are measured for a fixed relative coverage value of 7×10^{-9} a.u.

7.4.4 Pre-exponential Factor

As for water and methanol, to gain a full understanding of the kinetics of the desorption of ammonia from HOPG, a pre-exponential factor needs to be evaluated. As before, the pre-exponential factor is calculated using the same analysis method as described in *Section 4.4.3* and also in *Section 6.3.6*.

In order to calculate the number of adsorbates present on the surface, and hence to calculate the coverage, a few approximations need to be made. By looking at *Figure 7.3*, it is proposed that the first layer of ammonia adsorbed on HOPG is saturated following an exposure of 7 L. This exposure was chosen since the monolayer peak appears to saturate at this exposure (*Figure 7.3*). The saturated first layer consists of an array of ammonia molecules arranged in a hydrogen bonded network. To evaluate the number of ammonia molecules per unit area, it is assumed that an ammonia molecule and its associated hydrogen bond occupies a surface area of 1.21×10^{-19} m^2 (derived using values from [43]). The actual coverage following a 7 L exposure is then ~0.2 ML (from *Equation 4.8*). As shown in *Section 7.4.2* the total uptake of ammonia molecules on HOPG is approximately constant as a function of exposure (*Figure 7.5*), hence the number of adsorbates per unit area can be directly related to the area under the 7 L TPD curve in *Figure 7.3*. In this way a scaling factor can then be used, as before, to convert all QMS intensities, and hence relative coverages, to actual coverages. The area under the 7 L TPD curve in *Figure 7.3* is 4×10^{-9} a.u., which corresponds to an absolute coverage of 8.26×10^{18} molec m^{-2}. Hence, all relative coverage values have been scaled by a factor of 2×10^{27} to allow conversion to absolute coverage values. This then allows the calculation of the pre-exponential factors for multilayer desorption of ammonia from HOPG.

In order to verify the validity of the assumptions stated above several checks were carried out in a similar way to checks performed for water and methanol. A possible source of error is the assumption that the monolayer saturates at 7 L exposure, which corresponds to a 0.2 ML coverage. To test this assumption, a 0.2 ML coverage was assumed to have taken place for a variety of exposures from 3 L to 15 L. *Table 7.5* lists

the pre-exponential factors obtained by varying the exposure corresponding to a 0.2 ML coverage.

Table 7.5: Table showing the effect of altering the exposure corresponding to a 0.2 L coverage, which equates to saturation of the first layer, on the pre-exponential factor for ammonia adsorbed on HOPG at 88 K.

Exposure/L	Pre-exponential Factor*/molec m^{-2} s^{-1}
3	5×10^{25}
7	8×10^{25}
15	1×10^{26}

Table 7.5 shows a list of assumed saturation coverage values and the resulting pre-exponential factors. From *Table 7.5* a value of $10^{25.0\pm0.3}$ molec m^{-2} s^{-1} is given for the pre-exponential factor for multilayer ammonia desorption from HOPG. This value is in good agreement with the assignment of the observation of multilayers of ammonia. Furthermore, it is in good agreement with the pre-exponential values calculated for water (*Chapter 4*) and methanol (*Chapter 6*). The errors associated with the order of desorption and the desorption energy calculated in *Sections 7.4.3* and *7.4.3* respectively were also propagated through the calculation and led to pre-exponential values within the error value given above.

7.5 Conclusions

RAIRS and TPD studies have been carried out to investigate the adsorption of ammonia on HOPG at 94 K and 88 K respectively. RAIR spectra show that ammonia adsorbs molecularly in a physisorbed state on HOPG. Sub-monolayer ammonia could not be observed in the RAIR spectra. Increasing exposures of ammonia on HOPG result in the appearance of several bands, consistent with previous studies of the formation of multilayers of ammonia. The ammonia multilayer is predominantly crystalline, however at the highest exposures a small amount of metastable ammonia is also present,

* The units used for the pre-exponential factors are those expected for zero order desorption for the multilayer.

indicated by splitting in the symmetric deformation mode observed in the RAIR spectra. Annealing the ammonia adlayer does not lead to the appearance of any new spectral features, but simply causes the desorption of all adsorbed ammonia by 110 K.

TPD studies show the appearance of two distinct peaks following ammonia adsorption at 88 K. At the lowest exposure a single peak is observed at 94 K which is assigned to desorption from the monolayer. A higher temperature peak is observed at higher exposures which is attributed to desorption of multilayers of ammonia. The monolayer and the multilayer peak merge into one peak as the exposure is increased until it is no longer possible to distinguish them. The combined peak is dominated by the multilayer peak and cannot be saturated. Both the monolayer and the multilayer species are weakly physisorbed on the surface, with the surface-adsorbate interaction being slightly weaker than the hydrogen bonded adsorbate-adsorbate interaction. A desorption order of 0.25 ± 0.05 and a pre-exponential factor of $10^{25.0\pm0.3}$ molec m^{-2} s^{-1} have been calculated for multilayers of ammonia adsorbed on HOPG. Furthermore, the multilayer has a desorption energy of 23.2 ± 1.2 kJ mol^{-1}, which is in excellent agreement with previous studies of ammonia multilayers adsorbed on metal surfaces.

7.6 References

[1] Fuller, G.A. and Myers, P.C., in *Physical Processes In Interstellar Clouds*, G.E. Morfill and M. Scholer, Editors. 1987, D. Reidel Publishing.

[2] Sandford, S.A. and Allamandola, L.J., Astrophys. J., **417** (1993) p. 815.

[3] Whittet, D.C.B., in *Dust and Chemistry in Astronomy*, T.J. Millar and D.A. Williams, Editors. 1993, Institute of Physics Publishing.

[4] Whittet, D.C.B., *Dust in the Galactic Environment*. Series in Astronomy and Astrophysics. 2003: Institute of Physics Publishing.

[5] Ellison, M.D., Crotty, M.J., Koh, D., Spray, R.L., and Tate, K.E., J. Phys. Chem. B, **108** (2004) p. 7938.

[6] Laksono, E., Galtayries, A., Argile, C., and Marcus, P., Surf. Sci., **530** (2003) p. 37.

[7] Satterfield, C.N., *Heterogeneous Catalysis in Industrial Practice*. 2nd ed. 1991, New York: McGraw-Hill.

[8] Pan, B.Y.K. and Roth, R.G., Ind. Eng. Chem. Process Des. Dev., **7** (1968) p. 53.

[9] Benndorf, C. and Madey, T.E., Chem. Phys. Lett., **101** (1983) p. 59.

[10] Netzer, F.P. and Madey, T.E., Surf. Sci., **119** (1982) p. 422.

[11] van Hardveld, R.M., van Santen, R.A., and Niemantsverdriet, J.W., Surf. Sci., **369** (1996) p. 23.

[12] Jacobi, K., Wang, Y., Fan, C.Y., and Dietrich, H., J. Chem. Phys., **115** (2001) p. 4306.

[13] Benndorf, C. and Madey, T.E., Surf. Sci., **135** (1983) p. 164.

[14] Szulczewski, G.J. and White, J.M., J. Vac. Sci. Technol. A-Vac. Surf. Films, **15** (1997) p. 1526.

[15] Szulczewski, G.J. and White, J.M., Surf. Sci., **406** (1998) p. 194.

[16] Kay, B.D., Lykke, K.R., Creighton, J.R., and Ward, S.J., J. Chem. Phys., **91** (1989) p. 5120.

[17] Kim, C.S., Bermudez, V.M., and Russell, J.N., Surf. Sci., **389** (1997) p. 162.

[18] Xu, C. and Goodman, D.W., J. Phys. Chem. B, **102** (1998) p. 4392.

[19] Ceyer, S.T. and Yates Jr., J.T., Surf. Sci., **155** (1985) p. 584.

[20] Parmeter, J.E., Wang, Y., Mullins, C.B., and Weinberg, W.H., J. Chem. Phys., **88** (1988) p. 5225.

[21] Thornburg, D.M. and Madix, R.J., Surf. Sci., **220** (1989) p. 268.

[22] Bromberg, A., Kimel, S., and Ron, A., Chem. Phys. Lett., **46** (1977) p. 262.

[23] Binbrek, O.S. and Anderson, A., Chem. Phys. Lett., **15** (1972) p. 421.

[24] Holt, J.S., Sadoskas, D., and Pursell, C.J., J. Chem. Phys., **120** (2004) p. 7153.

[25] Pradier, C.M., Adamski, A., Methivier, C., and Louis-Rose, I., J. Mol. Catal. A-Chem., **186** (2002) p. 193.

[26] Ertl, G. and Huber, M., J. Catal., **61** (1980) p. 537.

[27] Bradley, J.M., Hopkinson, A., and King, D.A., Surf. Sci., **371** (1997) p. 255.

[28] Metkemeijer, R. and Achard, P., Int. J. Hydrog. Energy, **19** (1994) p. 535.

[29] Sun, Y.K., Wang, Y.Q., Mullins, C.B., and Weinberg, W.H., Langmuir, **7** (1991) p. 1689.

[30] Rosenzweig, Z. and Asscher, M., Surf. Sci., **225** (1990) p. 249.

[31] Gohndrone, J.M., Olsen, C.W., Backman, A.L., Gow, T.R., Yagasaki, E., and Masel, R.I., J. Vac. Sci. Technol. A-Vac. Surf. Films, **7** (1989) p. 1986.

[32] Tsai, W. and Weinberg, W.H., J. Phys. Chem., **91** (1987) p. 5302.

[33] Bassignana, I.C., Wagemann, K., Kuppers, J., and Ertl, G., Surf. Sci., **175** (1986) p. 22.

[34] Egawa, C., Nishida, T., Naito, S., and Tamaru, K., **80** (1984) p. 1595.

[35] Santra, A.K., Min, B.K., Yi, C.W., Luo, K., Choudhary, T.V., and Goodman, D.W., J. Phys. Chem. B, **106** (2002) p. 340.

[36] Gland, J.L., Sexton, B.A., and Mitchell, G.E., Surf. Sci., **115** (1982) p. 623.

[37] Sexton, B.A. and Mitchell, G.E., Surf. Sci., **99** (1980) p. 523.

[38] Nishimura, S.Y., Gibbons, R.F., and Tro, N.J., J. Phys. Chem. B, **102** (1998) p. 6831.

[39] Wu, M., Truoung, C.M., and Goodman, D.W., J. Phys. Chem., **97** (1993) p. 9425.

[40] de Jong, A.M. and Niemantsverdriet, J.W., Surf. Sci., **233** (1990) p. 355.

[41] Kolasinski, K.W., *Surface Science: Foundations of Catalysis and Nanoscience.* 2002: John Wiley and Sons Ltd.

[42] *CRC Handbook of Chemistry and Physics.* 1995, Boca Raton, FL: CRC Press.

[43] Hara, Y., Hashimoto, N.T., and Nagaoka, M., Chem. Phys. Lett., **348** (2001) p. 107.

Chapter 8: Astrochemical Implications of the TPD Studies

8.1 Introduction

This thesis presents information on the adsorption and desorption of water, methanol and ammonia on a highly oriented pyrolitic graphite (HOPG) surface at ~100 K. The motivation for these studies, outlined in *Chapter 1*, arises from the data needs of the astronomical community relating to gas-grain interactions in the interstellar medium (ISM). In order to fulfil the astronomers' data needs, the kinetic parameters, extracted in *Chapters 4* to *7*, need to be applied to real astrophysical conditions. For some surface science studies, application to real world situations involves bridging the pressure gap from ultra high vacuum (UHV) to atmospheric conditions [1]. However, this is not the case for the application of surface science studies to astrophysical environments, where pressures are typically a few orders of magnitude lower than UHV studies.

To apply the kinetic parameters derived in *Chapters 4* to *7* to problems of relevance to astronomers, desorption simulations need to be run on timescales relevant to the ISM. Furthermore, these simulations need to be applied to interstellar ices of appropriate thicknesses. Using these parameters, it is then possible to calculate astronomically useful quantities, such as the residence time of molecular species on dust grains as a function of temperature. The simulations presented in this chapter can then be directly compared to previous desorption studies of astrochemically relevant molecules. This study is the first to construct simulations using kinetic parameters derived directly from experimental data on grain-like surfaces.

8.2 Verification of Desorption Parameters

To test the accuracy of the kinetic parameters (desorption order, desorption energies and pre-exponential factors), simulations of the experimental TPD spectra, described in

Chapters 4 to *7*, were carried out. These simulations involved replicating the TPD spectra using the Polanyi-Wigner equation [1] and the kinetic parameters shown in *Table 8.1*.

To simulate TPD spectra for all three adsorption systems, an initial coverage has to be specified for each simulated TPD spectrum. This was estimated using the areas under the experimental TPD spectra, which are proportional to the relative coverage at that exposure. The areas under the TPD curves were then scaled to absolute coverages using a scaling factor in a similar manner to that described in *Section 4.4.3*. A comparison of the experimental and simulated TPD spectra for ammonia adsorbed on HOPG at 88 K is shown in *Figure 8.1*. It can clearly be seen that there is excellent agreement between the simulated TPD spectra and the experimental data. Similar agreement was observed for the desorption of both water and methanol adsorbed on HOPG at ~100 K.

Table 8.1: Table showing the kinetic parameters used in the Polanyi-Wigner equation to simulate TPD spectra for the adsorption of water, methanol and ammonia on HOPG at ~100 K.

	Desorption order	Desorption Energy / kJ mol^{-1}	Pre-exponential Factor* / molec m^{-2} s^{-1}
Water	0.24	39.9	1×10^{27}
Ammonia	0.25	23.2	8×10^{25}
Methanol Multilayer	0.35	41.0	6×10^{25}
Methanol monolayer	1.23	48.0	$9 \times 10^{9\dagger}$

* The units for the pre-exponential factor for water, ammonia and methanol multilayers are those expected for zero order desorption, despite the fractional desorption order used in the simulations.
† The units for the pre-exponential factor for monolayer methanol are those expected for first order desorption (s^{-1}), despite the fractional desorption order used in the simulations.

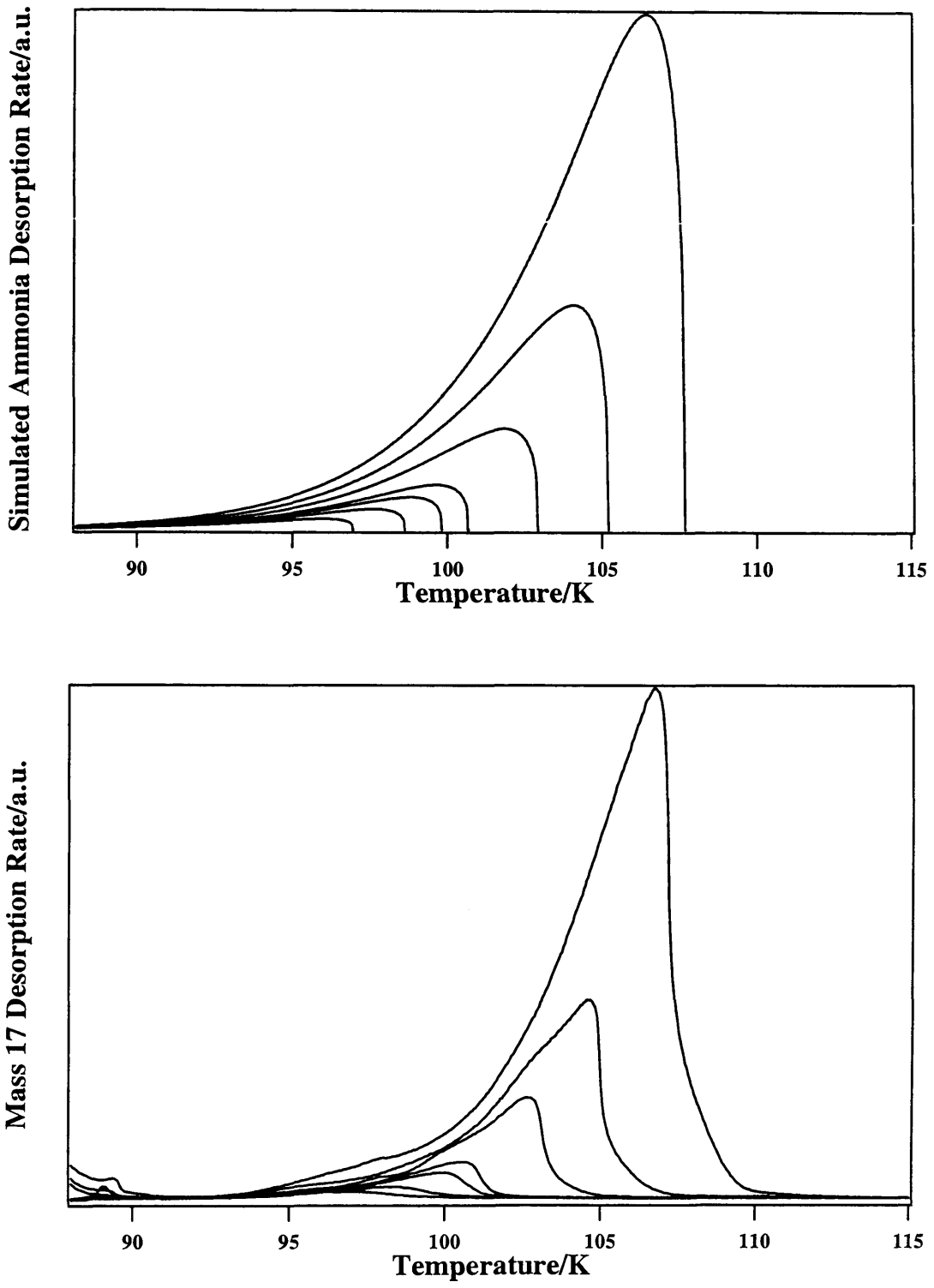

Figure 8.1: A comparison of experimental TPD spectra and simulated TPD spectra for ammonia adsorbed on HOPG at 88 K. The bottom figure shows TPD spectra recorded following increasing exposures of ammonia on HOPG. The top figure shows the simulated TPD spectra for adsorbed ammonia on HOPG.

8.3 Effects of Heating Rate Variation

The main discrepancy between the conditions in laboratory based experiments and in the ISM is the timescale within which adsorption and desorption occur. During the process of star formation, the rate at which the temperature rises is dependent on the mass of the star. Hence, high mass stars will have a faster heating rate than low mass stars. It has been shown that a dust grain in a hot core is typically heated at a rate of approximately 1 K century^{-1} [2, 3]. Although this is short on astronomical timescales, it is clearly impractical in laboratory based studies. Typical heating rates in TPD experiments vary from 0.05 K s^{-1} to 100 K s^{-1} [4]. In order to bridge this timescale gap, "TPD peaks" have been simulated to show the effect that varying the heating rate has on the desorption temperature. This simulation is based upon a method developed by Collings and co-workers [5], and involves simulating the rate of change of gas phase concentration of the desorbing species as a function of temperature. In this way, the simulations produce traces which resemble typical TPD "peaks". Constructing the simulation is a two step process involving the rate of desorption from the surface and the rate of pumping out of the system. This can be expressed as

$$\frac{d[NH_3(g)]}{dt} = k_d\theta^n - k_p[NH_3(g)] \qquad \textit{Equation 8.1}$$

where $[NH_3(g)]$ is the gas phase ammonia concentration, θ is the surface coverage, n is the order of desorption, k_p is the constant pumping speed, and k_d is the rate of desorption, described in *Equation 8.2*.

$$k_d = \nu_n \exp\left[\frac{-E_{des}}{RT_s}\right] \qquad \textit{Equation 8.2}$$

In *Equation 8.2* ν_n is the pre-exponential factor, E_{des} is the desorption energy, R is the gas constant and T_s is the surface temperature. The pumping speed used in each simulated TPD spectrum is scaled in proportion to the heating rate, with a heating rate of 10 K s^{-1} having a pumping speed of 300 s^{-1}. This is to ensure that the simulations

produce TPD peaks on a comparable scale. *Figure 8.2* shows the effect of varying the heating rate from 1 K century^{-1} to 10 K s^{-1} on the desorption of ammonia, water and methanol multilayers.

The spectra shown in *Figure 8.2* are simulated using the kinetic parameters specified in *Table 8.1* and using an initial coverage of 9.5 × 10^{2i} molec m^{-2}. This coverage corresponds to a water ice thickness of 0.3 μm, comparable to the thickness of interstellar ices [5]. *Figure 8.2* clearly shows that a change in heating rate causes a marked change in the desorption temperature of all three species. By slowing the heating rate from the experimental rate to 1 K century^{-1}, the desorption peaks shift down in temperature by 59 K for ammonia, by 79 K for water and by 65 K for the methanol multilayer. The desorption temperatures for a selection of heating rates for the three species are shown in *Table 8.2*.

The results of this study can be directly compared to a previous simulation of water desorption from a Au substrate by Collings and co-workers [5]. The parameters used in the study by Collings and co-workers are given in *Table 8.3*. Both studies show good agreement in the desorption temperature of water at astrochemically relevant heating rates, despite the fact that the two studies were performed on different surfaces. At a heating rate of 1 K century^{-1}, desorption temperatures of 103 K and 105 K are evaluated by this study and by Collings and co-workers [5] respectively. This suggests that the desorption temperature of water ice at astrochemically relevant heating rates is independent of the substrate used to model the dust grain. This is extremely important since the nature of dust grains in the ISM is not certain.

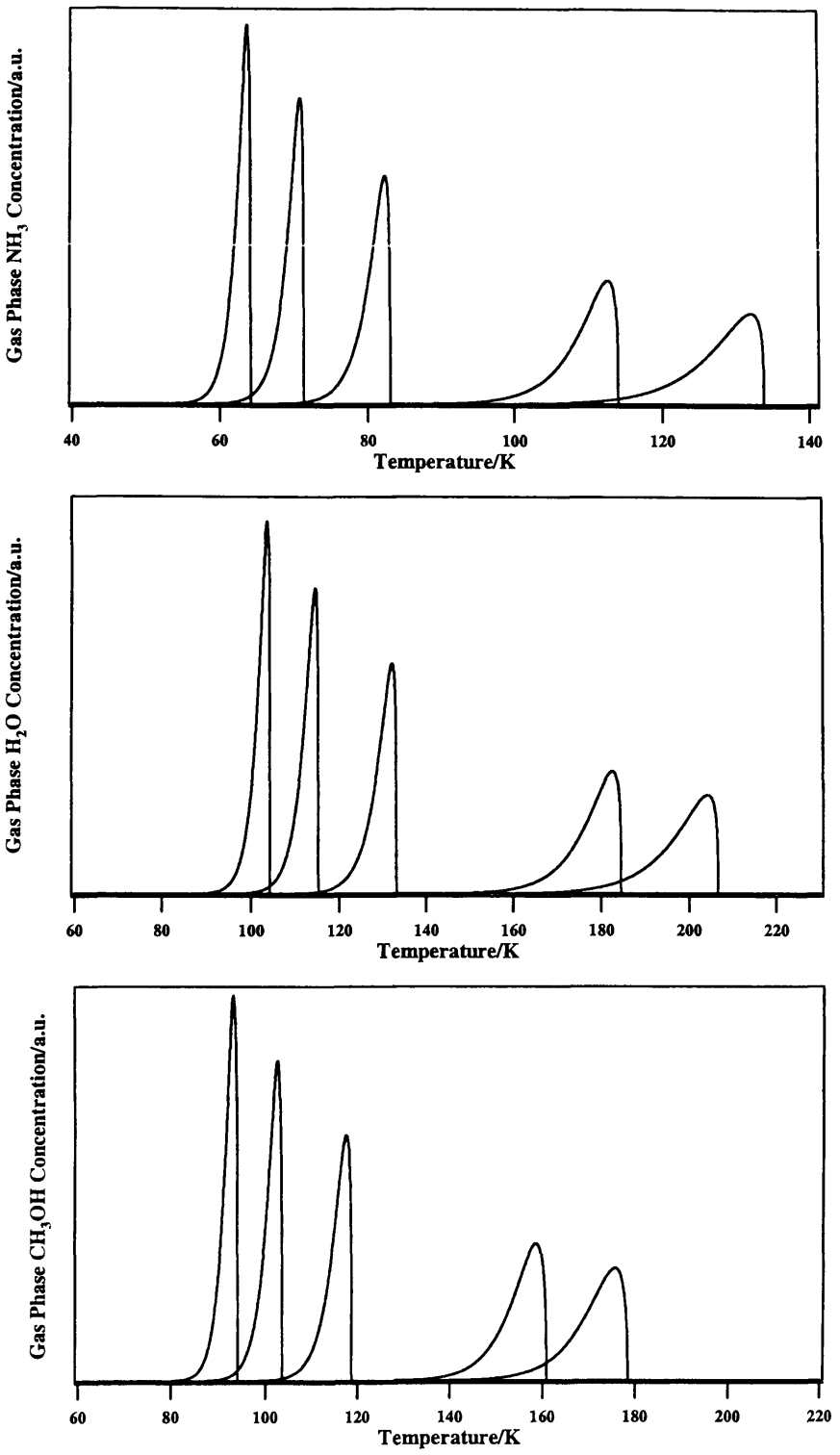

Figure 8.2: Simulated TPD profiles for ammonia, water and methanol from HOPG as a function of heating rate. The spectra (from left to right) have a heating rate and pumping speed of 1 K century^{-1} and 9.5 × 10^{-9} s^{-1}, 1 K year^{-1} and 9.5 × 10^{-7} s^{-1}, 1 K day^{-1} and 3.5 × 10^{-5} s^{-1}, 0.2 K s^{-1} and 6 s^{-1} (0.5 K s^{-1} and 15 s^{-1} for water and methanol multilayers), 10 K s^{-1} and 300 s^{-1} respectively.

Table 8.2: Table showing the effect of different heating rates on the desorption temperature for water, ammonia and methanol desorbing from HOPG.

Heating rate	Desorption Temperature/K		
	Water	Ammonia	Methanol Multilayer
10 K s^{-1}	204	132	175
Experimental[‡]	182	112	158
1 K $year^{-1}$	114	71	104
1 K $century^{-1}$	103	63	93

Table 8.3: Table showing a comparison of the kinetic parameters for water used in this study and in a study by Collings and co-workers [5, 6].

	This study	Collings and co-workers [5, 6]
Desorption Order	0.24	0
Pre-exponential/molec m^{-2} s^{-1}	1×10^{27}	1×10^{34}
Desorption energy/kJ mol^{-1}	39.9	48.0
Initial coverage/molec m^{-2}	9.5×10^{21}	9.5×10^{21}

A simulation has also been carried out to investigate the effect of varying the heating rate on the desorption temperature of the methanol monolayer. This simulation uses the kinetic parameters specified in *Table 8.1* and an initial coverage of 3×10^{18} molec m^{-2}. This coverage corresponds to saturation of the monolayer as estimated in *Section 6.3.6*. *Figure 8.3* shows the effect of varying the heating rate on the desorption temperature of the methanol monolayer. By slowing the heating rate from the experimental rate of 0.5 K s^{-1} to 1 K $century^{-1}$, the desorption peak shifts from 165 K to 104 K.

[‡] The experimental heating rate is 0.2 K s^{-1} for ammonia desorption and 0.5 K s^{-1} for both water and methanol desorption.

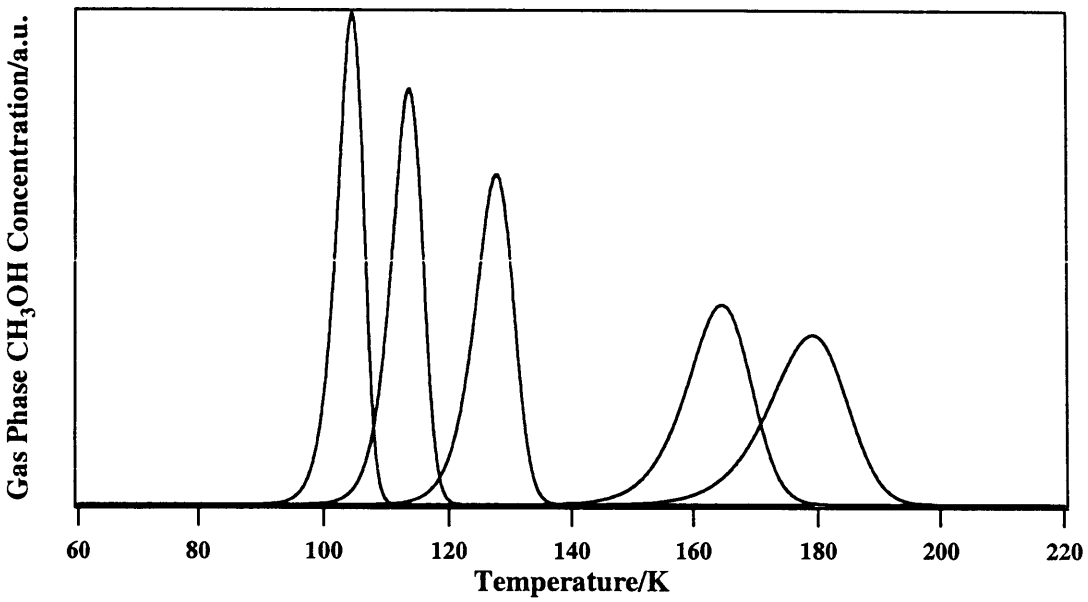

Figure 8.3: Simulated desorption profiles for a monolayer of methanol desorbing from HOPG as a function of heating rate. The spectra (from left to right) have a heating rate and pumping speed of 1 K century^{-1} and 9.5 × 10^{-9} s^{-1}, 1 K year^{-1} and 9.5 × 10^{-7} s^{-1}, 1 K day^{-1} and 3.5 × 10^{-5} s^{-1}, 0.5 K s^{-1} and 15 s^{-1}, 10 K s^{-1} and 300 s^{-1} respectively.

The simulations presented above can also be adjusted to more astrochemically relevant environments. In the ISM, there are no pumping effects so the above simulation has also been run ignoring the effect of pumping. In this case, the gas phase concentration is simply equal to the total number of molecules desorbed from the grain surface. As there is no pumping mechanism in this model, the gas phase concentration will saturate when all of the molecules have desorbed from the surface. *Figure 8.4* shows the gas phase concentration of ammonia, water and methanol multilayers desorbed from HOPG as a function of heating rate and temperature. The simulations use the same parameters shown in *Table 8.1* and heating rates from 1 K century^{-1} to 10 K s^{-1}. The simulations were run for an initial surface coverage of 9.5 × 10^{21} molecule m^{-2}, hence the cumulative gas phase desorption saturates at 9.5 × 10^{21} molecule m^{-2}. Note that, for each desorption spectrum shown in *Figure 8.2*, the temperature of the desorption peak is identical to the temperature at which desorption to the gas phase is complete for the corresponding heating rate, as shown in *Figure 8.4*.

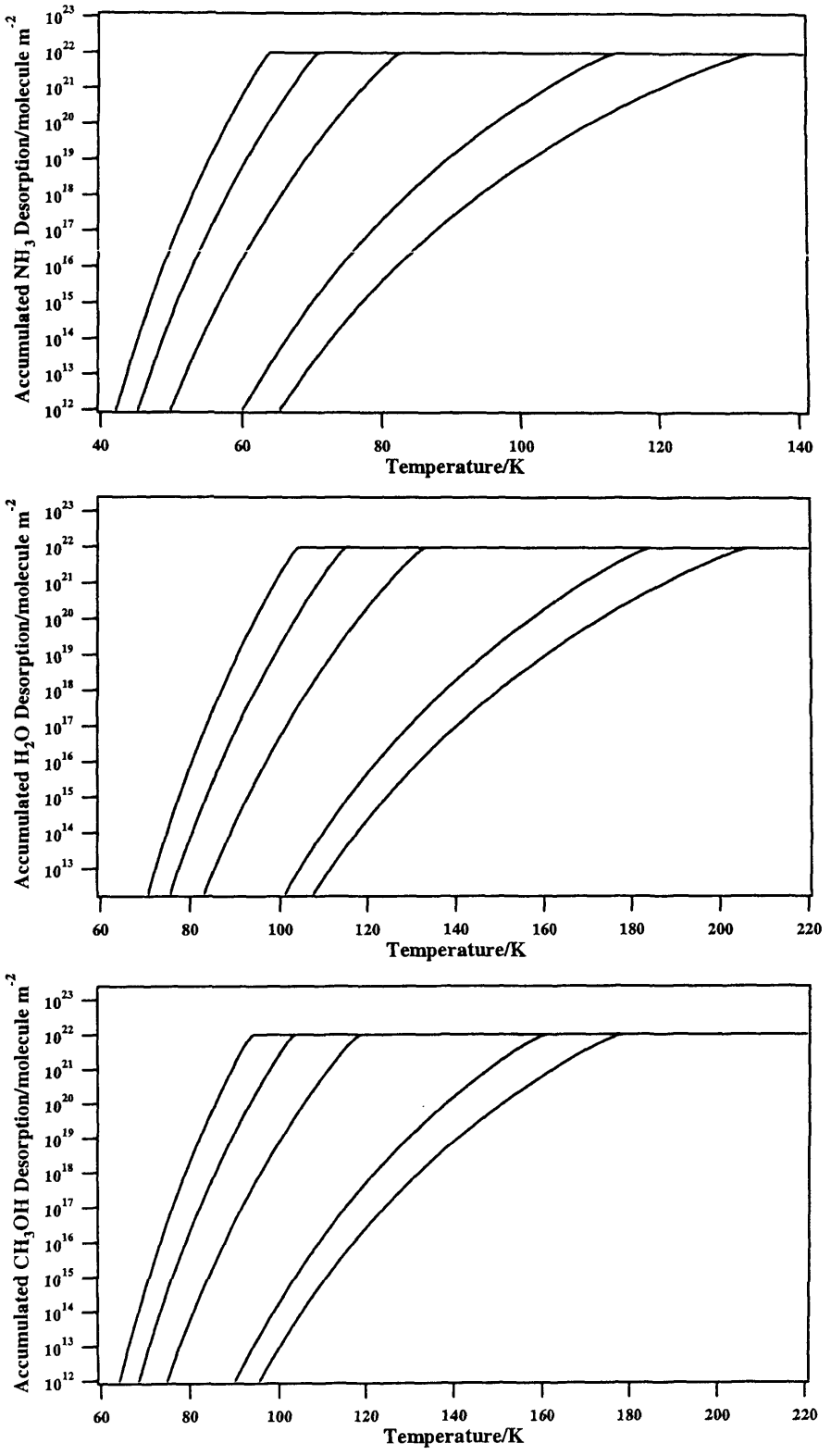

Figure 8.4: Simulated cumulative desorption to the gas phase for ammonia, water and methanol multilayers desorbing from HOPG as a function of heating rate. The spectra (from left to right) have a heating rate of 1 K century^{-1}, 1 K year^{-1}, 1 K day^{-1}, 0.2 K s^{-1} (0.5 K s^{-1} for water and methanol) and 10 K s^{-1}.

The data shown in *Figure 8.4* can be directly compared with previous simulations of water desorption performed by Collings and co-workers [5] *Table 8.3* shows that Collings and co-workers simulated multilayer water desorption from a Au substrate as a perfect zero order process [5]. A feature of a zeroth order desorption process is that, for a given heating rate, desorption profiles for varying coverages can be laid on top of each other. Hence simulations, such as *Figure 8.4*, can be extrapolated for ice layers of any thickness. A consequence of this is that thicker water ice layers will desorb at a higher temperature [5]. However, the simulations presented in this thesis for the desorption of water multilayers (and methanol and ammonia) have used a fractional order desorption, as determined in *Chapters 4* to *7*. By using a fractional order desorption process it is not possible to overlay desorption traces of differing coverages (and hence ice thicknesses). The effect of differing initial ammonia coverages for a fractional order desorption process is shown in *Figure 8.5*. *Figure 8.5* shows that differing film thicknesses lead to different desorption traces for a fractional order process. This demonstrates the importance of using the correct order in modelling desorption, since use of incorrect desorption order will give incorrect coverage dependence in the simulations.

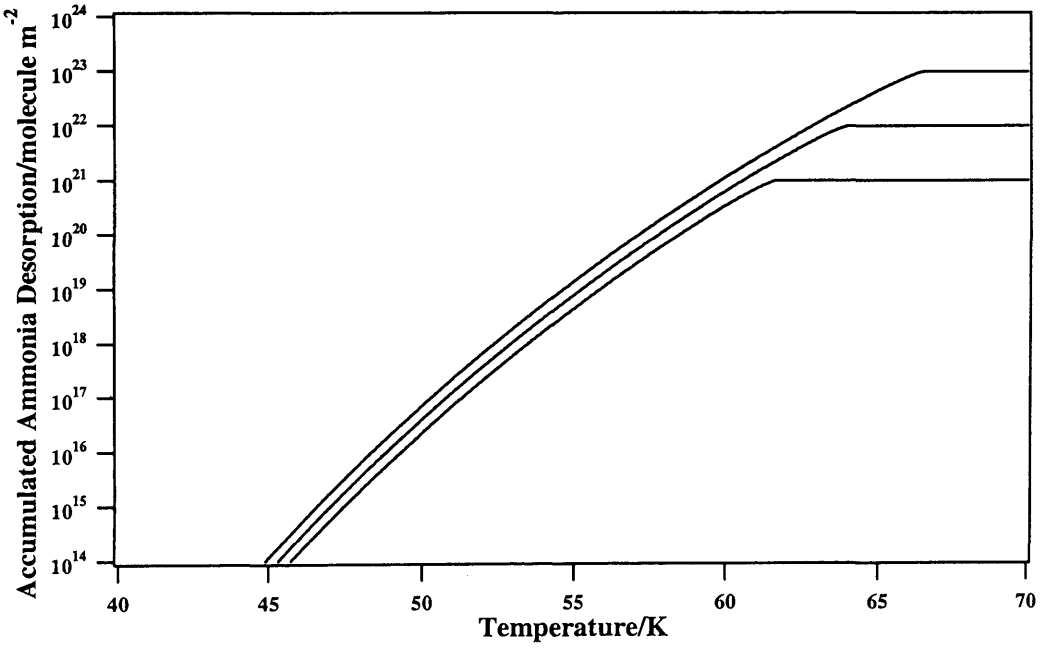

Figure 8.5: The effect on cumulative ammonia desorption to the gas phase of using different thickness ice films for a fractional order desorption process. The simulated spectra (from top to bottom) represent initial coverages of 9.5 × 10^{22} molecule m^{-2}, 9.5 × 10^{21} molecule m^{-2} and 9.5 × 10^{20} molecule m^{-2} of ammonia on HOPG. The heating rate is 1 K $century^{-1}$.

Whilst water desorption has previously been investigated by Collings and co-workers [5, 6], the only previous investigations of methanol and ammonia from astrophysically relevant surfaces were performed by Sandford and Allamandola [7, 8]. Sandford and Allamandola evaluated kinetic parameters for the desorption of astrochemically relevant molecules indirectly from spectroscopic data. The parameters obtained from these experiments are shown in *Table 8.4*. Their investigations assumed a first order desorption process and evaluated desorption energies by monitoring relative changes in the integrated intensity of surface infrared features during isothermal desorption. It has been clearly been shown in this thesis that multilayer desorption is not a first order process, and that incorrect assignment of the desorption order leads to evaluation of incorrect pre-exponential factors. Sandford and Allamandola's method of determining kinetic parameters is based on several assumptions, and ignores any non-equilibrium effects such as re-adsorption and crystallisation. In Sandford and Allamandola's study re-adsorption is highly possible, while re-adsorption in TPD studies is negligible, where the pumping speed is significantly greater than the rate of re-adsorption [6]. Furthermore the results presented in this thesis, have shown that crystallisation effects are extremely important during the desorption of water and methanol. The effects of using these parameters on astrochemical models will be discussed in depth later.

Table 8.4: Table listing the kinetic parameters evaluated by Sandford and Allamandola [7, 8] for water, ammonia and methanol desorption from their respective ices.

	Desorption order	Desorption Energy / kJ mol^{-1}	Pre-exponential Factor / s^{-1}
Water [8]	1	42.2	2.0×10^{12}
Ammonia [7]	1	25.6	8.0×10^{12}
Methanol [7]	1	35.2	2.2×10^{12}

8.3 Gas Phase Depletion and Residence Times

An important consequence of gas-grain interactions in the ISM is that molecules are depleted from the gas phase when they are adsorbed on dust grains. The rate of depletion from the gas phase is an important consideration in modelling the true column density of molecules present in dark clouds, such as water, methanol and ammonia [7]. The residence time of the molecule on the dust grain (and hence the rate of depletion) can be calculated as a function of grain temperature by using the kinetic parameters shown in *Table 8.1*. The residence time is equal to $1/k_d$, where k_d is defined in *Equation 8.2*. In order to compare the simulations presented in this thesis with previous studies which have performed simulations with differing orders of desorption, residence times are presented as the half-life of the surface population. The half-life is defined as the time taken for the surface population to fall to half its original value. In all cases except for a first order desorption process, the half-life will depend on the initial surface concentration of molecules. In these cases the surface concentration was fixed at 1.15×10^{21} molecule m^{-2}, in agreement with previous studies [6]. This concentration is equivalent to ~100 layers of water, which is the number of molecules expected to accrete on a dust grain during the lifetime of a dark cloud [9].

The half-life of water molecules within water multilayers as a function of temperature is shown in *Table 8.5*. *Table 8.5* also lists the half-life of water molecules on water ice surfaces determined using the kinetic parameters evaluated by Fraser and co-workers [6] and Sandford and Allamandola [8]. In both of these studies water desorption from the multilayer (or desorption of water from water ice) was modelled as desorption from a crystalline structure and an amorphous structure. However, the simulations performed in this study relate only to desorption from crystalline ice, since the kinetic parameters in *Table 8.1* were evaluated for the desorption of crystalline water ice (*Chapter 4*). Therefore, all discussion of desorption of water molecules from water ice implies desorption from crystalline water ice.

Table 8.5: Table showing the half-life of water molecules on water ice surfaces as a function of temperature evaluated in this study, by Fraser and co-workers [6] and by Sandford and Allamandola [8].

Temperature/K	Half-life, $t_{1/2}$/years		
	This Study	Fraser and co-workers [6]	Sandford and Allamandola [8]
10	$\mathbf{2.6 \times 10^{189}}$	8.8×10^{231}	6.8×10^{200}
20	$\mathbf{1.6 \times 10^{85}}$	8.6×10^{105}	5.5×10^{90}
30	$\mathbf{2.9 \times 10^{50}}$	8.5×10^{63}	1.1×10^{54}
40	$\mathbf{1.2 \times 10^{33}}$	8.4×10^{42}	4.9×10^{35}
50	$\mathbf{4.7 \times 10^{22}}$	2.1×10^{30}	4.8×10^{24}
60	$\mathbf{5.3 \times 10^{15}}$	8.4×10^{21}	2.2×10^{17}
70	$\mathbf{5.7 \times 10^{10}}$	8.4×10^{15}	1.3×10^{12}
80	$\mathbf{1.1 \times 10^{7}}$	2.7×10^{11}	1.5×10^{8}
90	$\mathbf{1.4 \times 10^{4}}$	8.4×10^{7}	1.3×10^{5}
100	$\mathbf{6.7 \times 10^{1}}$	1.3×10^{5}	4.6×10^{2}
110	$\mathbf{8.5 \times 10^{-1}}$	6.8×10^{2}	4.6×10^{0}
120	$\mathbf{2.3 \times 10^{-2}}$	8.4×10^{0}	9.8×10^{-2}
130	$\mathbf{1.0 \times 10^{-3}}$	2.0×10^{-1}	3.8×10^{-3}
140	$\mathbf{7.4 \times 10^{-5}}$	8.4×10^{-3}	2.3×10^{-4}
150	$\mathbf{7.6 \times 10^{-6}}$	5.3×10^{-4}	2.1×10^{-5}

Table 8.5 shows that there is a significant difference in the half-life of water molecules on water ice surfaces across the three studies. This study has shown that water would remain on the surface for an appreciable time up to a temperature of 90 - 100 K, while Fraser and co-workers noted a temperature of 110 - 120 K [6] and Sandford and Allamandola a temperature of 100 - 110 K [8]. This difference can, once again, be explained by looking at the differing kinetic parameters used in the simulations, especially the order of desorption, and how they were obtained. This study modelled desorption as a fractional order process, while the study by Fraser and co-workers modelled desorption as a zero order process and Sandford and Allamandola modelled the desorption as a first order process, which is clearly inaccurate. The study of Fraser and co-workers assumed a zero order desorption process by comparing the shapes of zero order desorption simulations with experimentally recorded data [6]. Sandford and Allamandola determined the kinetic parameters indirectly by spectroscopic measurements and assumed a first order rate law applied [8]. However, in this study the

desorption order has been directly evaluated from the experimental data as shown in *Chapter 4.4.1*, hence fewer assumptions have been made than in previous studies. In contrast to the desorption temperatures calculated in *Section 8.2*, it seems that the nature of the grain surface might be important in describing the difference in residence times presented in this study and by Fraser and co-workers [6].

Similar analysis has been carried out to calculate the half-life of multilayers of ammonia adsorbed on dust grains. *Table 8.6* lists the half-life of ammonia calculated in this study and in a previous study by Sandford and Allamandola [7].

Table 8.6: Table showing the half life of ammonia molecules on ammonia ice as a function of temperature evaluated in this study and by Sandford and Allamandola [7].

Temperature/K	Half-life, $t_{1/2}$/years	
	This study	Sandford and Allamandola [7]
10	$\mathbf{1.9 \times 10^{103}}$	2.2×10^{113}
15	$\mathbf{7.5 \times 10^{62}}$	6.8×10^{68}
20	$\mathbf{4.7 \times 10^{42}}$	3.8×10^{46}
25	$\mathbf{3.6 \times 10^{30}}$	1.7×10^{33}
30	$\mathbf{3.0 \times 10^{22}}$	2.1×10^{24}
35	$\mathbf{5.1 \times 10^{16}}$	9.1×10^{17}
40	$\mathbf{2.4 \times 10^{12}}$	1.6×10^{13}
45	$\mathbf{1.0 \times 10^{9}}$	3.0×10^{9}
50	$\mathbf{2.1 \times 10^{6}}$	3.3×10^{6}
55	$\mathbf{1.3 \times 10^{4}}$	1.2×10^{4}
60	$\mathbf{1.9 \times 10^{2}}$	1.2×10^{2}
65	$\mathbf{5.3 \times 10^{0}}$	2.2×10^{0}
70	$\mathbf{2.5 \times 10^{-1}}$	7.6×10^{-2}
75	$\mathbf{1.7 \times 10^{-2}}$	4.1×10^{-3}
80	$\mathbf{1.7 \times 10^{-3}}$	3.1×10^{-4}
85	$\mathbf{2.2 \times 10^{-4}}$	3.3×10^{-5}
90	$\mathbf{3.5 \times 10^{-5}}$	4.4×10^{-6}

It can be seen from *Table 8.6* that there is generally good agreement between this study and the study of Sandford and Allamandola [7], with both studies showing that ammonia can remain on the surface of dust grains up to temperatures of ~60 K. This

agreement is rather surprising since the two studies employ different methodologies and different kinetic parameters.

Table 8.7 shows similar analysis carried out to calculate the half-life of methanol molecules on methanol ice. Note that the simulation for the residence time of methanol in this study is constructed using the kinetic parameters determined from fitted data as described in *Chapter 6.3*. In contrast to the ammonia, there is a discrepancy between the calculated half-life of methanol in this study and that obtained by Sandford and Allamandola [7]. This study shows that methanol can remain on the surface of dust grains at temperatures up to approximately 90 K, while Sandford and Allamandola calculated a temperature of 80 K. This discrepancy, which arises from the different kinetic parameters between the two studies, may have an effect on the modelling of star forming regions.

Table 8.7: Table showing the half life of methanol molecules on methanol ice as a function of temperature evaluated in this study and by Sandford and Allamandola [7].

Temperature/K	Half-life, $t_{1/2}$/years	
	This study	Sandford and Allamandola [7]
10	$\mathbf{4.2 \times 10^{178}}$	8.4×10^{163}
20	$\mathbf{2.3 \times 10^{79}}$	9.2×10^{71}
30	$\mathbf{1.9 \times 10^{46}}$	2.0×10^{41}
40	$\mathbf{5.6 \times 10^{29}}$	9.6×10^{25}
50	$\mathbf{6.6 \times 10^{19}}$	6.1×10^{16}
60	$\mathbf{1.6 \times 10^{13}}$	4.5×10^{10}
70	$\mathbf{3.0 \times 10^{8}}$	1.9×10^{06}
80	$\mathbf{8.6 \times 10^{4}}$	9.8×10^{2}
90	$\mathbf{1.5 \times 10^{2}}$	2.7×10^{0}
100	$\mathbf{9.3 \times 10^{-1}}$	2.5×10^{-2}
110	$\mathbf{1.5 \times 10^{-2}}$	5.2×10^{-4}
120	$\mathbf{4.6 \times 10^{-4}}$	2.1×10^{-5}
130	$\mathbf{2.4 \times 10^{-5}}$	1.4×10^{-6}
140	$\mathbf{2.0 \times 10^{-6}}$	1.4×10^{-7}
150	$\mathbf{2.3 \times 10^{-7}}$	1.8×10^{-8}

Residence times have also been evaluated for a monolayer on a bare grain surface. The results of these calculations are shown in *Table 8.8* as a function of grain temperature. It can be seen that there is a difference in residence time between methanol adsorbed on methanol ice and methanol adsorbed on bare HOPG. At all temperatures methanol adsorbed directly on the HOPG will remain on the surface for a longer time than that adsorbed on methanol ice. This implies that the residence time for methanol molecules in interstellar ices will vary depending on the amount of methanol present and to what extent it interacts with the grain surface itself.

Table 8.8: Table showing the half life of methanol molecules on methanol ice and on HOPG as a function of temperature.

Temperature/K	Half-life, $t_{1/2}$/years	
	Methanol on methanol ice	Methanol on HOPG
10	4.2×10^{178}	2.5×10^{226}
20	2.3×10^{79}	3.2×10^{201}
30	1.9×10^{46}	5.2×10^{59}
40	5.6×10^{29}	6.7×10^{38}
50	6.6×10^{19}	1.9×10^{26}
60	1.6×10^{13}	8.5×10^{17}
70	3.0×10^{8}	9.1×10^{11}
80	8.6×10^{4}	3.0×10^{7}
90	1.5×10^{2}	1.0×10^{4}
100	9.3×10^{-1}	1.6×10^{1}
110	1.5×10^{-2}	8.6×10^{-2}
120	4.6×10^{-4}	1.1×10^{-3}
130	2.4×10^{-5}	2.7×10^{-5}
140	2.0×10^{-6}	1.1×10^{-6}
150	2.3×10^{-7}	7.1×10^{-8}

8.4 Conclusions

In this chapter simulations of desorption processes have been created in astrophysical environments, using the kinetic parameters obtained in *Chapters 4* to *7*. It has been shown that applying heating rates applicable to regions of the ISM, such as hot cores, has a marked effect on the desorption temperature of water, methanol and ammonia. All three species show a down shift in desorption temperature as the heating rate is changed

from laboratory values to astronomically relevant heating rates. Since all three species obey a fractional order desorption process, an intimate knowledge of the ice thickness is required to accurately model the desorption profiles of interstellar ices. It has also been shown that the desorption temperature of water at astronomical heating rates is in good agreement with a previous study [5], hence suggesting that the identity of the grain analogue may not be important when evaluating kinetic data concerning desorption of water ice.

The residence time of water, methanol and ammonia on their respective ice surfaces has also been calculated as a function of temperature. The residence time of ammonia is in agreement with previous studies, while methanol is depleted from the gas phase until temperatures higher than previously evaluated. In contrast, simulations for water ice show desorption to occur at a lower temperature than previous studies. These discrepancies can be attributed to the different kinetic parameters used in each of the individual studies. The residence time has also been calculated for methanol on a bare HOPG surface and has been shown to differ from the residence time of methanol on methanol ice. This suggests that the identity of the grain analogue may be important in calculating residence times.

8.5 Future Work

An initial extension of these studies would be to investigate the effects on the desorption parameters of using mixed ices. All the studies presented in this thesis are based on pure ice systems using only one adsorbate, be it water, methanol or ammonia. However, interstellar ices are known to be a mixture of several different species, all of which will interact with each other to various degrees. This has been shown in TPD investigations by Collings and co-workers [5]. The study of mixed ices can be used to investigate the effect of co-adsorption of molecules, as well as sequential adsorption. Once the effects of mixed ices on the desorption parameters have been evaluated, the results can then be applied to gain a better understanding of star forming regions.

A further extension to this work would be to determine whether adsorption at lower astrophysically relevant temperatures has any effect on the desorption parameters. The data shown in this thesis was recorded following adsorption at ~100 K, hence these investigations could be repeated at 10 – 20 K. However it is anticipated that lower adsorption temperatures will not affect the results obtained, at least for the pure ice systems investigated here.

8.6 References

[1] Kolasinski, K.W., *Surface Science: Foundations of Catalysis and Nanoscience.* 2002: John Wiley and Sons Ltd.

[2] Viti, S. and Williams, D.A., Mon. Not. R. Astron. Soc., **305** (1999) p. 755.

[3] Viti, S., Collings, M.P., Dever, J.W., McCoustra, M.R.S., and Williams, D.A., Mon. Not. R. Astron. Soc., **354** (2004) p. 1141.

[4] Attard, G. and Barnes, C., *Surfaces.* Oxford Chemistry Primers, ed. R.G. Compton. 1998: Oxford University Press.

[5] Collings, M.P., Anderson, M.A., Chen, R., Dever, J.W., Viti, S., Williams, D.A., and McCoustra, M.R.S., Mon. Not. Roy. Astron. Soc., **354** (2004) p. 1133.

[6] Fraser, H.J., Collings, M.P., McCoustra, M.R.S., and Williams, D.A., Mon. Not. Roy. Astron. Soc., **327** (2001) p. 1165.

[7] Sandford, S.A. and Allamandola, L.J., Astrophys. J., **417** (1993) p. 815.

[8] Sandford, S.A. and Allamandola, L.J., Icarus, **76** (1988) p. 201.

[9] Hasegawa, T.L. and Herbst, E., Mon. Not. R. Astron. Soc., **261** (1993) p. 83.